Master of Science Thesis

Study on Optimal Trajectories and Energy Management Capabilities of a Winged Re-Entry Vehicle during the Terminal Area

Sven De Ridder

July 6, 2009

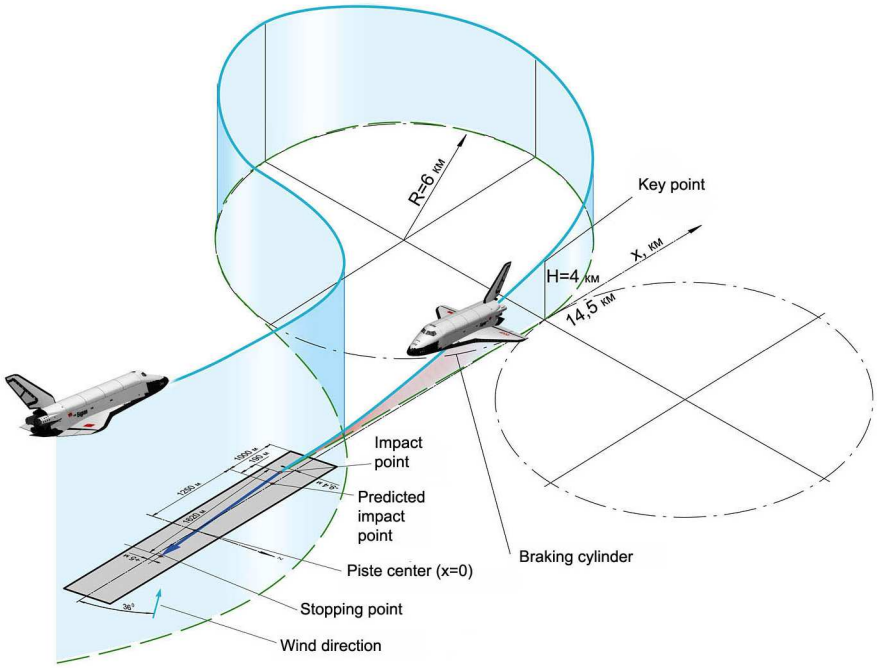

Faculty of Aerospace Engineering · Delft University of Technology

TU Delft

Study on Optimal Trajectories and Energy Management Capabilities of a Winged Re-Entry Vehicle during the Terminal Area

Master of Science Thesis

For obtaining the degree of Master of Science in Aerospace Engineering
at Delft University of Technology

Sven De Ridder

July 6, 2009

Faculty of Aerospace Engineering · Delft University of Technology

Delft University Of Technology
Department Of
Astrodynamics and Satellite Systems

Members of the graduation commission:

Head of department:

prof. ir. B.A.C. Ambrosius
Delft University of Technology

Supervisor:

dr. ir. E. Mooij
Delft University of Technology

Reader:

ir. R. Noomen
Delft University of Technology

Reader:

prof. dr. ir. W. Bosschaerts
Royal Military Academy RMA, Belgium

Reader:

dr. ir. G. Ortega
European Space Agency ESA/ESTEC

Preface

This thesis report describes the work undertaken to obtain the Master of Science degree at the faculty of Aerospace Engineering, at Delft University of Technology, the Netherlands. In the next decades, new launch vehicles will be used to launch payload and humans into space. Improved guidance technologies are indispensable for these new vehicles. I very much enjoyed working on such a challenging and interesting topic related to the re-entry guidance of reusable launch vehicles.

I would like to thank my supervisor, dr. ir. E. Mooij, for his valuable support, stimulating input and pleasant working environment. Further, special thanks to ir. R. Noomen, dr. ir. G. Ortega and prof. dr. ir. W. Bosschaerts for making time to participate in the graduation commission. I would also like to thank prof. ir. B.A.C. Ambrosius for his help during the orientation of my graduation project.

A special thanks to my parents, grandparents and sister for giving me the opportunity to study in the Netherlands and for all their support. I would also like to thank my fellow graduation students on 'the ninth floor' and friends for the pleasant and wonderful stay in Delft. And last but not least, I would like thank my girlfriend, Ellen Scharpé, for being so patient and for giving me so many support during the study.

Sven De Ridder
Delft, July 2009

Contents

Summary

Launchers are indispensable in space flight and space exploration. Nowadays, launching payload or humans into space is very expensive and highly inflexible. To reduce the costs of space transportation, advanced fully reusable launch vehicle have to be designed. Lift producing re-entry vehicles are able to make a controlled re-entry and gliding flight and hence, are more suitable to be used as a reusable vehicle. Next to reducing the costs, other objectives include significant improvements in the vehicle safety and reliability. This can be achieved by designing advanced guidance and control technologies.

The unpowered entry of a winged re-entry vehicle, such as the HORUS-2B, consists of a hypersonic atmospheric re-entry phase, a Terminal Area Energy Management (TAEM) phase and a approach and landing phase. The TAEM is the subject of this thesis study. During the TAEM, the vehicle is brought to the correct interface position with the landing phase, on the extension of the centerline of the runway with the correct amount of energy and the correct heading. The most characteristic feature of the TAEM phase is the so-called Heading Alignment Cylinder (HAC). The vehicle performs a turn around the HAC to align with the runway. During actual re-entry flights, flight conditions at the beginning of the terminal area will not always be nominal and several variations in entry position, energy, heading angle and flight-path angle can occur. Therefore, the main question of this thesis work is formulated as: **Can the safe return of a winged re-entry vehicle through the terminal area be guaranteed for a wide range of initial conditions?**

The guidance system of the Space Shuttle uses reference trajectories, which are pre-flight computed, in combination with tracking algorithms. An important disadvantage of this guidance system is that the flexibility of the pre-flight computed reference profiles, to off-nominal conditions, is limited. To solve this problem, several terminal area studies have investigated the adaption of the reference trajectories based on the initial state (onboard planning). In these guidance systems, off-nominal conditions are dealt with by adapting the lateral ground track, while the longitudinal strategy remains the same. Another possibility to deal with off-nominal conditions is to use a predicting capability based guidance algorithm. Such a system does not need any reference trajectory. The commanded control variables are determined based on estimating the required energy to reach the runway and hence, the key feature of this type of guidance is the energy estimator. The implementation of an automatic HAC selection scheme would increase the flexibility to off-nominal conditions.

To design an energy estimator and a planning algorithm, it is important to know the correct vertical corridor of the vehicle. This vertical corridor determines the capabilities of the

vehicle in terms of the maximum range that it can fly and the maximum dive that it can perform. Therefore, optimal longitudinal strategies are calculated using a genetic algorithm. Although is commonly stated that a maximum lift-to-drag ratio results in a maximum range flight in the vertical plane, the obtained optimal solutions indicate that it is possible to obtain larger ranges. Because of the large computational times, it is not feasible to use an on-board optimizer based on a genetic algorithm. Therefore, the obtained optimal solutions are analyzed in the energy space and the obtained information is used to design guidance laws, which approximate the optimal solutions. The energy-state approximation states that the vehicle has to intercept the minimum-drag flight path and has to follow this drag valley until the final flare maneuver. This approximation is a valid approximation for a subsonic maximum range flight of HORUS. But in case HORUS starts at a supersonic velocity, the energy-state approximation using equilibrium flight conditions, is no longer valid because the transient maneuvers have a large impact on the optimal maximum-range trajectory of a winged re-entry vehicle with poor gliding capabilities at supersonic velocities. Further, the energy-state approximation is also valid to approximate the influence of a subsonic turn on the optimal longitudinal strategy. An optimal turn is performed at a larger angle of attack and a lower velocity, with respect to a wings-level flight. A different turn radius results in a different drag valley. The optimal maximum dive is performed by flying at a low dynamic pressure, because of the large encountered drag in this flight regime. An important conclusion from the optimal trajectories is that it is not possible to use a single, fixed dynamic-pressure profile as the longitudinal strategy in case the maximum range or the minimum range must be predicted for off-nominal conditions.

Using information from the energy-state analysis, guidance laws are designed using a simple PD control scheme. For a subsonic maximum range flight, it is not possible to use the same set of gains for different initial states because than, incorrect trajectories are followed. A different initial state requires a different set of optimal gains. Using robust design, a suboptimal set of gains is found that can be used for several initial states. The obtained suboptimal gains for the subsonic maximum range flight in a vertical plane can also be used during an optimal turning flight. For a supersonic maximum range flight, it is possible to find an optimal set of gains for a specific initial supersonic state. The attempt to design a single set of gains for several initial states, using the robust design method, did not succeed. For a supersonic maximum range flight, it is necessary to optimize the gains for each initial state. For a maximum dive flight, it is also possible to use a PD control law. By using several simulation, a good set of gains was obtained.

Based on simulations using the designed guidance laws, it is found that, although it is common to specify a single value for the minimum required energy to reach a specific range, the maximum range differs for initial states with the same initial energy. The maximum range also depends on the combination of the components of the initial energy (altitude and velocity). The same holds for the maximum energy boundary determined by the maximum dive capabilities. All the combinations for which it is possible to fly a desired range, without overshoot or undershoot, form an energy area in the energy space. This energy area is the cross-section of the energy tube at the desired range.

The energy-tube concept is used in a HAC planning algorithm. The HAC position is adapted until the initial state in the energy space is positioned in the middle of the energy tube. The planning algorithm adapts the position of a single cylindrical HAC such that a flight using a nominal longitudinal strategy results in a trajectory with an end point as close as possible to the runway threshold. The energy estimator consists of numerically propagating the trajectory,

using the nominal longitudinal strategy. Using the HAC planner, terminal area trajectories are analyzed to investigate if HORUS can safely reach the runway for various initial conditions. For some initial conditions, the HAC planner is unable to find and optimal HAC, which results in a trajectory that ends at the runway threshold, using a nominal longitudinal strategy. But it is still possible to safely reach the runway, if a different longitudinal strategy is used. Therefore, the main conclusion of this thesis study is: **It is possible to guarantee the safe return of a winged re-entry vehicle through the terminal area for a wide range of initial conditions, if an onboard HAC planning is used, in combination with a variable longitudinal strategy determined by the output of the energy estimator.**

Nomenclature

Latin Symbols

C_D	drag force coefficient	-
C_L	lift force coefficient	-
g_δ	acceleration due to gravity in latitudinal direction	m/s^2
g_r	acceleration due to gravity in radial direction	m/s^2
J_2	gravity-field coefficient	-
q_{dyn}	dynamic pressure	N/m^2
R_e	equatorial radius	m
R_{HAC}	HAC radius	m
R_p	polar radius	m
R_s	surface radius	m
S_{ref}	aerodynamic reference area	m^2
V_e	equivalent airspeed	m/s
V_{ST}	stall speed	m/s
$\mathbf{F}$	force vector	N
$\mathbf{g}$	gravitational acceleration vector	m/s^2
$\mathbf{r}$	position vector	m
$\mathbf{u}$	control vector	-
$\mathbf{V}$	velocity vector	m/s
a	speed of sound	m/s
D	drag force	N
e	error	-
h	height (geometric altitude	m
K	control gain	-

L	lift force	N
L/D	lift-to-drag ratio	-
M	Mach number	-
m	mass	kg
n	load factor	-
p	atmospheric pressure	N/m^2
R	modulus of position vector	m
s	Laplace variable	-
t	time	s
V	modulus of velocity vector	m/s
X,Y,Z	axes	-

Greek Symbols

α	angle of attack	rad
β	angle of sideslip	rad
χ	heading	rad
δ	geocentric latitude	rad
δ^*	geographic latitude	rad
δ_b	body flap deflection	rad
δ_e	elevator/elevon deflection	rad
δ_r	rudder deflection	rad
δ_{sb}	speedbrake deflection	rad
γ	flight-path angle	rad
ω_n	undamped natural frequency	rad/s
ρ	atmospheric density	kg/m^3
σ	bank angle	rad
τ	geocentric latitude	rad
ζ	damping ratio	-

Superscripts

$_0$	initial condition
$_{cm}$	centre of mass
$_d$	derivative
$_G$	groundspeed-based
$_I$	inertial
$_l$	left
$_p$	proportional

$_{ref}$	reference
$_{RW}$	runway-based
$_{r}$	right

Abbreviations

AAEC	Area of Allowable Entry Conditions
ALI	Approach and Landing Interface
ASTRA	Advanced Systems and Technology for future RLV Application
CED	Cylinder of Energy Dispersion
CNES	Centre National d'Etudes Spatiales
COESA	Committee On Extension to the Standard Atmosphere
CoM	Centre of Mass
ESA	European Space Agency
ESTEC	European Space research and TEchnology Centre
FBL	Feedback Linearization
FESTIP	Future European Space Transportation Investigation Program
FLPP	Future Launcher Preparatory Programme
GNC	Guidance, Navigation and Control
HAC	Heading Alignment Cylinder
HORUS	Hypersonic ORbital Upper Stage
HTHL	Horizontal Take-off and Horizontal Landing
ISA	International Standard Atmosphere
ISO	International Organization for Standardization
IXV	Intermediate eXperimental Vehicle
MRAC	Model Reference Adaptive Control
NASA	National Aeronautics and Space Administration
NDI	Nonlinear Dynamic Inversion
NGL	Next Generation Launcher
PID	Proportional, Integral and Derivative
RLV	Reusable Launch Vehicle
SSTO	Single-Stage-To-Orbit
TAEM	Terminal Area Energy Management
TEG	Terminal Entry Gate
TEP	Terminal Entry Point
TSTO	Two-Stage-To-Orbit

Chapter 1

Introduction

This thesis deals with reusable launch vehicles and more specific with the re-entry flight of such vehicles. The main topic of the current study is the terminal area, which is a particular flight phase in the re-entry flight. Major fields of interest include the study of optimal trajectories, energy management capabilities of these type of vehicles and new guidance and control technologies to improve the safety and reliability.
The scope of the thesis is discussed in section 1.1, including a discussion on reusable launch vehicles and the terminal area. Section 1.2 describes the layout of the thesis in which the thesis statement, the limitations of the study and a document overview are given.

1.1 Scope

Launchers are indispensable in space flight and space exploration. Without them, no space activity would be possible. Many benefits that we now take for granted in our lives would not exist: satellites providing telephone and telecommunications connection, weather forecasting, precise location determination, and so on. Moreover, no human space exploration would exist and the Moon would still be untouched by human life.
Nowadays, two possibilities exist to launch payload or humans into space, which are both very expensive and highly inflexible. It can either be launched by a conventional expendable launcher like the Ariane 5, or it can be carried by the semi-reusable U.S. Space Shuttle. With every launch, a considerable amount of material and thus manufacturing and processing effort, is wasted. To reduce the costs of space transportation, advanced fully reusable launch vehicles have to be designed. To have such a fully reusable system, the vehicle must be brought back to Earth in a controlled way and it must be able to make a pinpoint landing on a runway. Lift producing vehicles have a larger controllability with respect to re-entry capsules and are able to land on a predetermined location. Lift producing re-entry vehicles are able to make such a controlled re-entry and gliding flight and hence, are more suitable to be used as a reusable vehicle.
Reducing the costs is not the only reason for designing new, reusable launch vehicles. Other objectives include significant improvements in the vehicle safety and reliability. Perhaps the most important goal is to reduce the probability of catastrophic failure. Advanced guidance and control technologies will greatly improve the overall safety and reliability of future reusable

launch vehicles (Kluever & Horneman, 2005).

The Future Launcher Preparatory Programme (FLPP) of the European Space Agency (ESA) is dedicated to the preparation of this future reusable launch vehicles. The program started in 2004 and aims to a have a Next Generation Launcher (NGL) operational around 2020. The major objective is to develop technical concepts for launchers such that an autonomous European access to space is guaranteed. The FLPP program also includes in-flight tests to validate the required technology. The Intermediate eXperimental Vehicle (IXV) is used to validate key re-entry technologies such as the thermal protection system, aerothermodynamic simulation models and guidance, navigation and control algorithms. The aim of the IXV is to make a controlled Earth re-entry flight, aided by active aerodynamic control surfaces. The flight of IXV is planned in 2012. Although IXV will descend by parachute after the entry in the Earth's atmosphere, ESA is also performing studies related to a gliding re-entry and more specific to the terminal area, see documents (Filipe, 2008a) and (Filipe, 2008b).

Below, reusable launch vehicles are described in more detail, followed by a discussion on the general re-entry sequence of such vehicles.

1.1.1 Reusable launch vehicles

A reusable launch vehicle is a vehicle that can be used more than once. From the mid-eighties onwards, many different concepts of reusable launch systems have been studied throughout the world. The concepts can be divided into several classes according to the number of stages required to get into Earth's orbit (Single-Stage-To-Orbit (SSTO) or Two-Stage-To-Orbit (TSTO)), the method of take-off and landing (vertical or horizontal) and the type of propulsion system (rocket engines or air-breathing engines).

Figure 1.1: The Martin Aircraft Company X-24 (courtesy of NASA)

A reusable vehicle that wants to make a horizontal landing like an aircraft needs to be able to produce sufficient lift. Two different concepts can be used to produce lift: a lifting body or winged vehicles. A lifting body is a vehicle configuration where the body itself produces the lift and hence, no conventional wings are presents. On the other hand, a winged vehicle has a

fuselage and wings like a conventional aircraft. An example of a lifting body, the X-24, is given in figure 1.1. The US Space Shuttle is an example of a winged vehicle. Both lifting bodies and winged re-entry vehicles have a low lift-to-drag ratio, poor gliding capabilities and the descent is unpowered. But they are able to make a controlled re-entry and subsequent gliding flight and hence, can land on a predetermined location.

A distinction is also made between orbital and sub-orbital reusable launchers. In a sub-orbital space flight, the vehicle reaches space, but is not capable of completing one orbital revolution around the Earth. A flight that reaches an altitude of 100 km above sea level and then falls back to Earth is considered a sub-orbital spaceflight. The apogee reaches space, but the perigee distance is to low. In an orbital flight, the vehicle is capable of completing at least one orbital revolution. The perigee distance of the orbit during an orbital flight must at least have an value of 100 km.

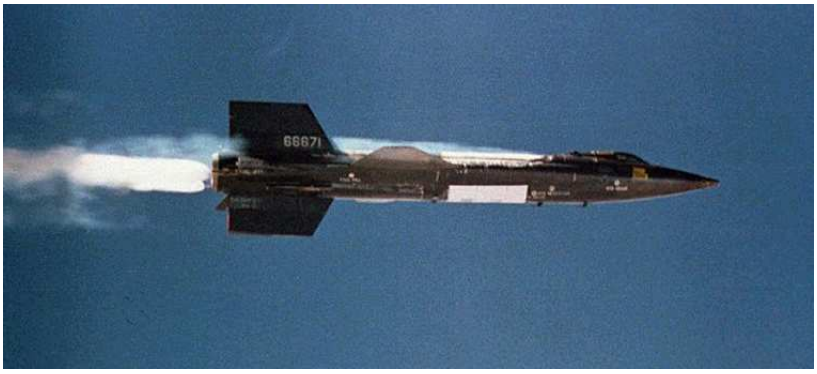

Figure 1.2: The North American X-15 (courtesy of NASA)

Examples of a sub-orbital space vehicle includes the X-15, SpaceShipOne and Hopper. The X-15, see figure 1.2, was developped by North American and the first flight of this manned rocket plane took place in 1959. The X-15 was carried underneath a wing of a B-52 until a sufficient altitude was reached. Then it was dropped, its engine was ignited and the X-15 was launched. The X-15 can be categorized as horizontal take-off and horizontal landing (HTHL) TSTO vehicle.

On October 4, 2004, the Scaled Composite company made history by becoming the first private company that was able to launch a manned space-vehicle into space twice within a span of a 14-day period. With this achievement, it won the ten million dollar Ansari X-price. SpaceShipOne is the vehicle that reaches space and is carried as a second stage underneath the White Knight. A similar launch sequence to the X-15 is used and also SpaceShipOne is an HTHL TSTO vehicle. Figure 1.3 shows SpaceShipOne underneath the White knight.

Hopper evolved from the Future European Space Transportation Investigation Programme (FESTIP) and was elaborated in the scope of the Advanced Systems and Technology for future RLV Application (ASTRA) program funded by the German national agency (Buechner, 2003). The FESTIP investigation aimed at defining the most cost-effective and most efficient concept of a reusable space transportation system. The Hopper is a HTHL TSTO semi-reusable launch vehicle, comprising of a reusable primary stage, the RLV Hopper, and an expendable upper stage, the HUS. This expendable upper stage is staged internally in the primary stage to have

only one aerodynamically affected flight configuration and is deployed at an altitude of 130 km. The horizontal launch is supported by a rail guided sled. Figure 1.4 shows the Hopper RLV together with payload inside Hopper.

Figure 1.3: SpaceShipOne underneath the White Knight [http://www.scaled/com]

At this moment, no true orbital reusable launch system exists. The closest example is the partially reusable US Space Shuttle. The Shuttle's orbiter and the two solid rocket boosters are reused after several months of refurbishment, while the large external fuel tank is expandable. The Shuttle system is very expensive. In total, 5 Space Shuttles and 2 test Shuttles were build. The first Space Shuttle, Columbia, was launched into space on April 12, 1981.

Another example is the Russian Buran-Energia, which was developed as an answer to the American Shuttle. The Buran made only one flight on November 15, 1988. The program was finally stopped 1993 due to financial problems. During the first and only flight, Buran was launched by the Energia, made two revolutions around the Earth and landed on the cosmodrome at Baikonur (Kirpischikov, 2007). Although the appearance of both the Space Shuttle and the Buran is similar, the Buran-Energia is entirely a Soviet design and thus, many differences exist. The main difference is that the Buran can fly in an automatic mode without any pilot on-board during the whole mission. Also, the Buran itself does not have engines that assist the launch. All thrust is provided by the Energia.

Other orbital reusable launch systems include Hermes and Kliper. Hermes was a proposed mini shuttle designed by the French Centre National d'Etudes Spatiales (CNES) and ESA. It was to be launched on top of an Ariane 5 launcher. The program was canceled in 1993.
As soon as the Russian economy started emerging from the post-Soviet transition, developers started the search for a new vehicle to replace the current used Soyuz spacecraft. The RKK Energia company has been working on a new vehicle called Kliper or Clipper (Zak, 2006). Both a purely lifting-body and a winged version are investigated. In July 2006, the Russian government and Russian Space Agency canceled the funding agreement and decided to collaborate with the European Space Agency to design a capsule-type replacement of the Soyuz. Meanwhile, Energia has announced that it will seek for private funding to develop and build the

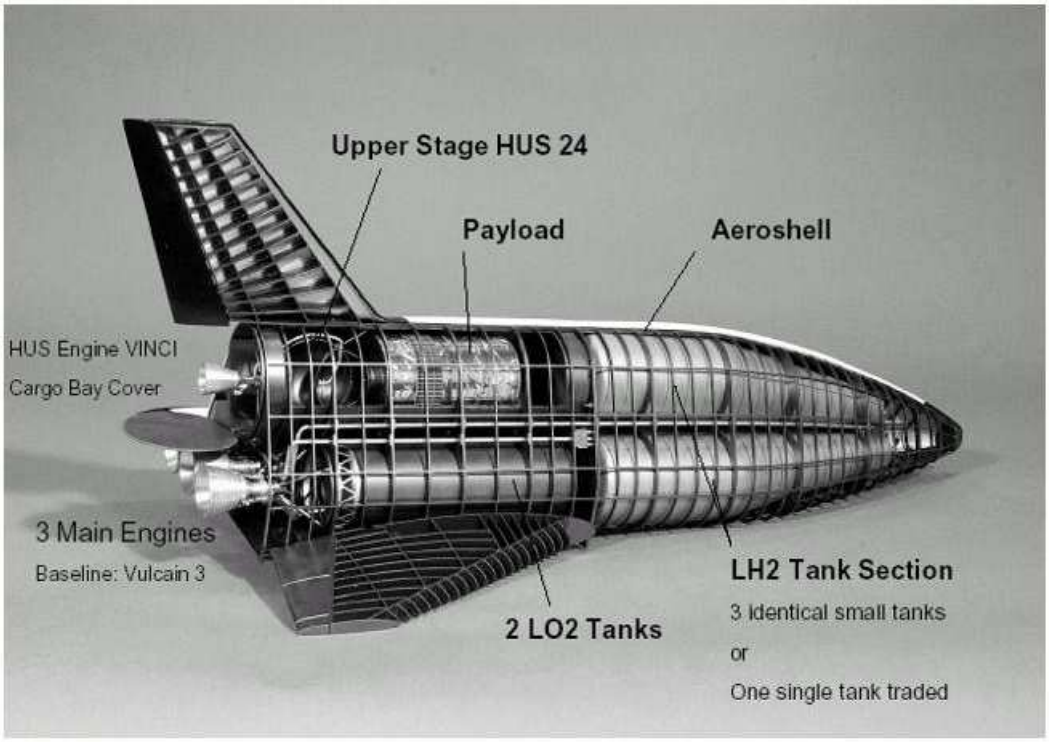

Figure 1.4: Hopper model cut-away view (Belau & Sommer, 2006)

winged Kliper spacecraft.

Next to the full-scale launch vehicles that can bring payload and crew into space, also a lot of technology demonstrator programs exist that serve as test beds for new technologies. The Phoenix flight demonstrator is 1:7 scale model of the Hopper vehicle. The Phoenix is developed and build by EADS Astrium Space Transportation in Bremen (Buechner, 2003). Test flight were performed in 2004 to demonstrate guidance, navigation and control technologies for the approach and landing phase. Other technology demonstrators include the American experimental vehicles X-33, X-34, X-37, X-38, X-42, etc. The IXV is a European technology demonstrator for re-entry technology.

In this thesis study, another vehicle called the HORUS (Cucinelli, 1987) is chosen as the reference vehicle to be consistent with previous re-entry studies as presented in (Mooij, 1998). Moreover, its complete aerodynamic data is available for use. HORUS-2B was originally designed as a fully reusable second stage of the Ariane-5 launcher. Another version, that serves as the second stage of the Saenger space plane concept, also exists.

1.1.2 Re-entry and Terminal Area Energy Management

A space vehicle in an orbit around the Earth has a large potential and kinetic energy. When the vehicle wants to return to the Earth, it has to reduce this large energy to the level of potential energy that the vehicle has after landing on the surface of the Earth. This is done by means of energy dissipation due to the friction of the vehicle during its flight through the atmosphere (Wakker, 2002).

Generally, it is assumed that the atmosphere starts at an altitude of 120 km. After a de-orbit maneuver, the vehicle re-enters into the atmosphere. A typical re-entry flight consists of three phases:

- **Hypersonic atmospheric re-entry phase**
  The hypersonic atmospheric re-entry starts at an altitude of 120 km and ends at an altitude of about 25 km. During this phase, the vehicle flies with a high angle of attack and resembles a typical blunt re-entry vehicle. The vehicles decelerates from an initial velocity of Mach 24 down to Mach 2.5. This phase is characterized by a high heating rate and temperatures can be as high as 1500°C. The highest temperatures are reached on the nose of the vehicle, at bottom of the vehicle and on the leading edges of the wings. Figure 1.5(a) shows an artist impression of this re-entry phase.

- **Terminal Area Energy Management phase**
  During the Terminal Area Energy Management (TAEM) phase, the vehicle is brought to the correct interface position with the landing phase, on the extension of the centerline of the runway with the correct amount of energy (velocity and altitude) and the correct heading.

- **Approach and landing phase**
  The last phase, the approach and landing phase, is responsible for the final part of the runway approach and the actual landing. The interface between the TAEM phase and the landing phase is called the Approach and Landing Interface (ALI). Figure 1.5(b) shows the landing of the Space Shuttle.

(a) (b)

Figure 1.5: (a) Artist impression of the hypersonic atmospheric re-entry [http://www.vionline.com] (b) Landing of the Space Shuttle (courtesy of NASA

The terminal area is the subject of this thesis work. The terminal area is used to manage the vehicle's energy while aligning the vehicle with the runway threshold. During the TAEM phase, the flight is unpowered, the vehicle flies through the transonic flight regime and the flight characteristics of the vehicle change significantly. The most characteristic feature of the TAEM is a Heading Alignment Cylinder (HAC). Such an imaginary cylinder touches the extension of the centerline of the runway and the vehicle will perform a turn around the mantle wall of this cylinder to get aligned with the centerline of the runway. Two of these cylinders might exist, one at each side of the runway centerline. During the TAEM phase, the amount of energy is regulated such that the vehicle will arrive at the HAC and ALI with the correct amount of energy. To dissipate more energy, the flight path can be enlarged by making S-turns. Making

a turn in itself (the banked flight situation) will also contribute to an increase of the energy dissipation. Other ways are to fly faster by flying at a steeper descent angle and to use speed-brakes. Figure 1.6 shows a sketch of a typical trajectory during the TAEM phase of the Space Shuttle.

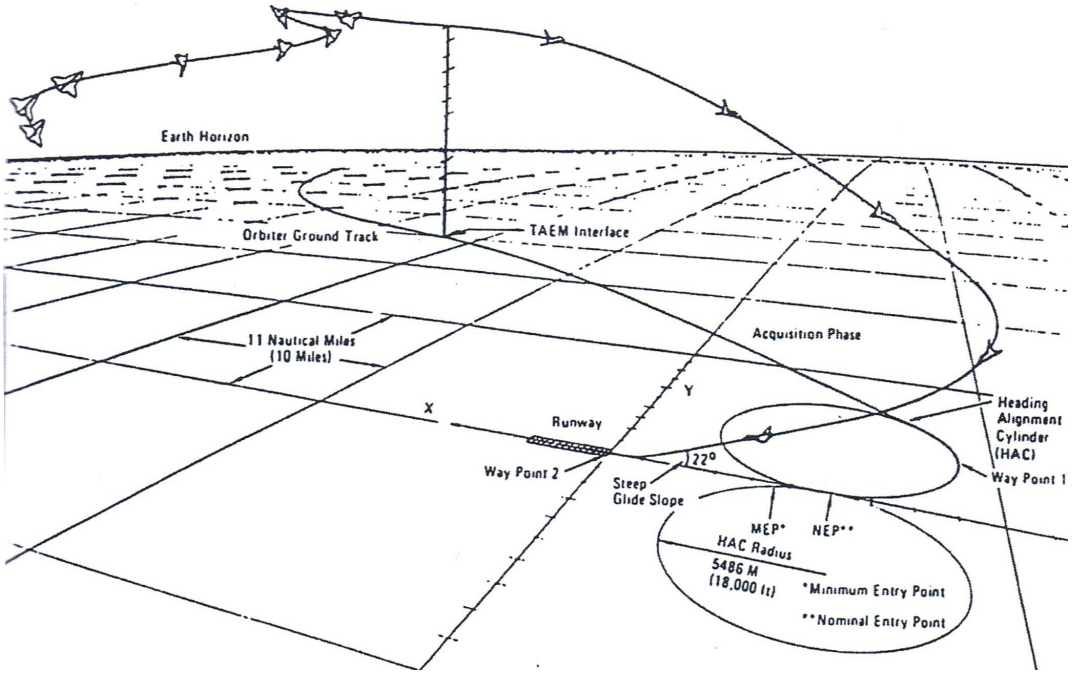

Figure 1.6: Flight of the Shuttle in the TAEM phase (Wakker, 2002)

When one or more engines fail during the ascent, the vehicle must abort the flight and return to a landing site. During this return, the energy of the vehicle must also be regulated such that the runway is reached with the correct amount of energy. Also in this case, a terminal area is present.

For a normal re-entry flight, analysis and pre-flight simulations indicate a single starting point or a relatively small area from which the vehicle might start the TAEM phase. It is the task of the hypersonic re-entry guidance to bring the vehicle to this Terminal Entry Point (TEP) or Terminal Entry Gate (TEG). A different situation occurs when during the ascent-phase, something goes wrong and the flight has to be aborted. It cannot be guaranteed that the vehicle will enter the TAEM phase through the same small TEG. Moreover, not all landing sites or runways have the same orientation and hence, it is not possible to specify the same TEG with respect to different runways. The terminal area may start in any position on an entry circle around the landing site.

In terminal area studies, nominal conditions are used to analyze terminal area trajectories. But in reality, the conditions will not be nominal and several variations can be present. Hence, these off-nominal conditions must be taken into account. Off-nominal conditions include both variations in the initial conditions (energy level, heading angle and flight-path angle) and variations in the models (density, wind, vehicle characteristics). In this thesis, the focus is on the variations in the initial conditions. Hence, next to to the position at the start of the terminal

area (on the entry circle), the TEG is also determined by the variations in initial conditions for which the vehicle is able to reach the runway. These observations lead to the thesis statement.

1.2 Layout of thesis

1.2.1 Thesis statement

The main question or problem definition of this thesis work is formulated as follows:

Can the safe return of a winged re-entry vehicle through the terminal area be guaranteed for a wide range of initial conditions?

To find an answer to this question it is required to analyze optimal descent trajectories of a winged re-entry vehicle, with means to establish and possibly explain the influence of off-nominal conditions on the trajectory and on the energy management capabilities of the vehicle. Hence, the problem definition has been translated into four study goals:

- investigate current terminal area studies and identify their strong and weak points.
- calculate optimal trajectories and analyze the influence of changing initial conditions on these trajectories in terms of energy.
- assess the use of guidance systems to approximate the optimal trajectories.
- analyze the energy management capabilities in case of both nominal and off-nominal conditions, using the obtained optimal strategies and determine the TEG.

These study goals require a simulation tool and an optimizer, with which the trajectory and related performance characteristics can be computed with sufficient accuracy. In order to be able to design a simulation tool, it is important to understand the flight mechanics of reusable launch vehicles during a gliding flight. Also the principles of the guidance, navigation and control system must be studied.

1.2.2 Limitations of study

Several limitations apply to different aspect of the current terminal area study. Throughout the thesis work, several simplifications are introduced. This section gives a short overview of the used simplifications.

flight dynamics

- vehicle is considered to be a point mass
- no wind or gusts

GNC system

- ideal navigation system: measured state is equal to the actual state
- ideal control system and actuators: no delay in obtaining the commanded state
- no filters on the input to the guidance system
- guidance system runs at the same frequency as the simulator

vehicle

- use of available models from literature
- no changes in aerodynamic data
- no changes in the weight of the vehicle
- no changes in banking capabilities

optimization

- no local optimization

1.2.3 Overview of document

- **chapter 2**
  Chapter 2 describes the equations of motion of a rigid body with a constant mass under the influence of aerodynamic and gravitational forces in the atmosphere of the Earth without wind. Only the translational motion is considered. This forms the mathematical core of the flight-simulation model.
- **chapter 3**
  The used reference vehicle, the HORUS-2B, is described in chapter 3. The reference configuration and data as presented is sufficient to study trajectories and energy management principles in the terminal area. Also the guidance, navigation and control system is described in this chapter. The final part of this chapter describes the simulation model, which is used to study the terminal area.
- **chapter 4**
  Optimization is an essential part of the thesis. In chapter 4, a general overview of optimization techniques is given, followed by a discussion on optimization problems related to the terminal area. This chapter also introduces the optimization method used during the thesis work: genetic algorithms. The last part of this chapter describes the actual optimization tool based on genetic algorithms, OPTIDUS, as used in the current study.
- **chapter 5**
  Chapter 5 is related to terminal area guidance systems. First, the basic terminal area guidance principles and methods are described, followed by an overview of the available systems. Many terminal area guidance systems have been designed and the obtained conclusions are used to define concrete areas of interest for the current study.

- **chapter 6**
  In several terminal area studies, it is common to assume a steady-state. In this chapter, a discussion on the performance of a winged re-entry vehicle is given, based on the steady-state approximation. These results will be used as a comparison for the optimized results.

- **chapter 7**
  In chapter 7, optimal terminal-area trajectories are calculated using a genetic algorithm. Because a genetic algorithm is a global optimizer with relatively poor convergence properties, small improvements could still be made, but the obtained accuracy is enough to define general optimal trends. Optimization problems that are considered include the maximum-range problem, the maximum-dive problem and the optimal-turning problem.

- **chapter 8**
  In chapter 8, the obtained optimal results from chapter 7 are studied in terms of energy. The energy-state approximation is used to characterize the optimal maximum range solutions in the energy space. The energy-state approximation is also extended to characterize the maximum-dive problem and the optimal-turning problem.

- **chapter 9**
  It is time consuming to calculate an optimal trajectory using a genetic algorithm and hence, the genetic algorithm cannot be used in an on-board guidance system. Chapter 9 considers the design of guidance laws that are able to generate commands such that the resulting trajectory approximates the optimal solutions. Use is made of the characterization results from chapter 8. The guidance laws as described in this chapter only consider the longitudinal motion of the vehicle.

- **chapter 10**
  Using the maximum-range and maximum-dive strategies, the energy-tube concept is defined in chapter 10. This energy tube concept is used to describe the energy management capabilities of the vehicle.

- **chapter 11**
  Chapter 11 describes a HAC planning algorithm based on the energy tube concept. Also the used ground-track geometry, the lateral guidance and the nominal longitudinal strategy are described in this chapter.

- **chapter 12**
  In chapter 12, the HAC planning algorithm is used to analyze the energy management capabilities of the vehicle in case of off-nominal conditions. The planning algorithm calculates an optimal position of the HAC based on the initial state. The analysis, as performed in this chapter, is used to answer the main question of this thesis study.

- **chapter 13**
  Chapter 13 states the conclusions and recommendations.

Chapter 2

Flight mechanics

Flight mechanics describes the motion of a flying vehicle in a general sense. To investigate optimal trajectories and the capabilities of the vehicle, it is required to understand the principles that influence the motion of a vehicle. This chapter introduces some mathematical models that are used to determine the motion of a vehicle in the Earth's atmosphere. These models, in combination with the vehicle model described in chapter 3, can be used to design a flight-simulation model. The mission objective for a vehicle that returns from space is land at the targeted runway. The motion can be controlled such that the vehicle remains targeted at its landing site. To steer the vehicle towards its target, a guidance system is required.
First, several reference frames that are used in describing the motion of a vehicle are introduced in section 2.1. Section 2.2 discusses the sets of variables that are used to describe the state of the vehicle. The flight environment is described in section 2.3 and includes a discussion on the shape of the Earth and the atmosphere. Section 2.4 presents the external forces that influence the motion of a vehicle. The external motions include the aerodynamic forces and the gravitational forces. The vehicle is considered as a point mass and the corresponding equations of motion that describe the translational motion are presented in section 2.5. Approximations that are commonly used in flight performance studies, the steady-state approximation and the energy-state approximation, are introduced in section 2.6.

2.1 Reference frames

In deriving the equations of motion of a unpowered re-entry vehicle in the Earth's atmosphere several reference frames are used in order to allow for the definition of the state variables and the external moments. These reference frames are discussed this section. The frames are all considered to be right handed and Cartesian.

2.1.1 Reference frames with origin at the CoM of the Earth

The origin of the following reference frames are all located at the Centre of Mass (CoM) of the Earth.

Inertial geocentric reference frame, index I

The Z_I axis is pointing north. The OX_IY_I plane coincides with the equatorial plane of the Earth. The X_I axis points toward the vernal equinox and defines the zero-longitude meridian at zero time. The Y_I axis completes the right handed reference system. Note that this reference frame is actually a pseudo-inertial reference frame due to the motion of the Earth itself. However, the accelerations due to the motion of the Earth are small compared to the accelerations of the vehicle under consideration and hence, this frame can be considered to be inertial. Figure 2.1(a) shows the inertial geocentric reference frame.

Rotating geocentric reference frame, index R

The frame is fixed to the Earth and hence rotates with the same angular velocity as the Earth. The Z_R axis is pointing north and coincides with the Z_I axis. The X_R axis intersects the equator at zero longitude and hence, crosses the Greenwich meridian. The Y_R axis lies in the equatorial plane and completes the right-handed system, see figure 2.1(b).

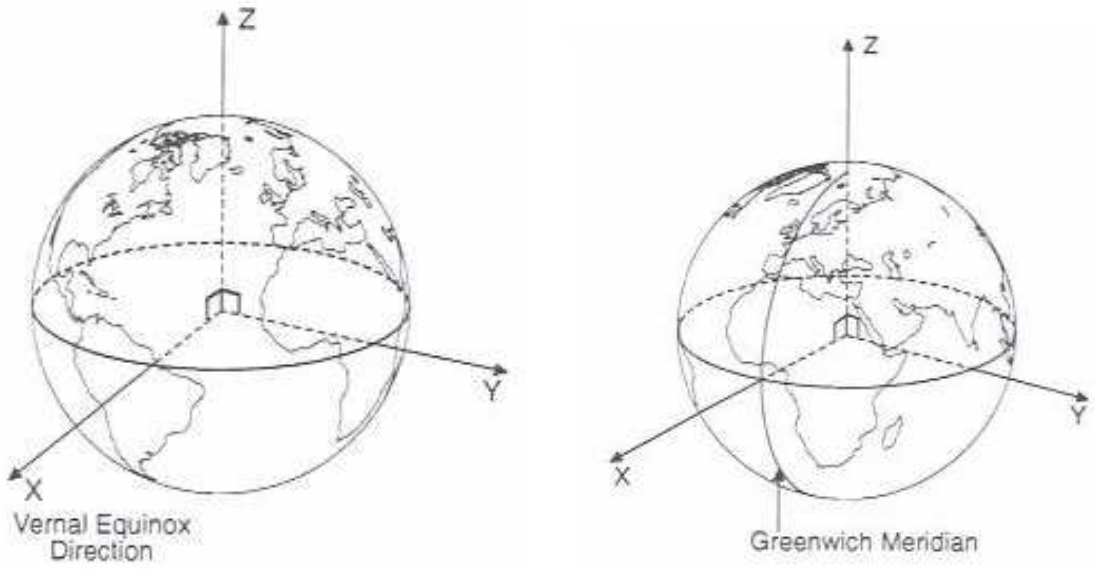

(a) (b)

Figure 2.1: (a) inertial geocentric reference frame (b) rotating geocentric reference frame (Wertz, 2001)

2.1.2 Reference frames with origin at the CoM of the vehicle

The origin of the following reference frames are all located at the CoM of the vehicle. Further, it is assumed that the vehicle has a plane of symmetry in longitudinal direction.

Body-fixed reference frame, index B

The body-fixed reference frame is fixed with respect to the vehicle. The X_B lies in the plane of symmetry, points out of the nose of the vehicle and is positive in forward direction. The Z_B axis also lies in the plane of symmetry and is positive in downward direction. The Y_B

axis is perpendicular to the plane of symmetry and completes the right-handed system, see figure 2.2(a). A rotation about the X_B, Y_B and Z_B axis are called roll, pitch and yaw, respectively.

Vertical reference frame, index V

The Z_V axis points toward the CoM of the Earth along the radial component of the gravitational acceleration. The X_V axis lies in a meridian plane, is perpendicular to Z_V and points to the northern hemisphere. The Y_V completes the right-handed reference frame. The $X_V Y_V$-plane represents the local horizontal plane. Note that this is actually only true when the Earth would be a true sphere. A small error is introduced when using an elliptical Earth shape.

Trajectory reference frame groundspeed based, index TG

The X_{TG} axis is directed along the velocity vector relative to the rotating geocentric reference frame or the velocity vector relative to the ground. Z_{TG} lies in the vertical plane, pointing downward and perpendicular to the X_{TG} axis. Y_{TG} completes the right-handed system.

Aerodynamic reference frame groundspeed based, index AG

The X_{AG} axis is directed along the velocity vector relative to the rotating geocentric reference frame, so the X_{AG} axis is collinear with the X_{TG} axis. The Z_{AG} axis is collinear with the aerodynamic lift force (based on ground speed), but directed in opposite direction. The X_{AG} axis completes the right handed system. Note the TG and the AG frame are coincident when the vehicle is not banking. Figure 2.2(b) indicates the aerodynamic reference frame.

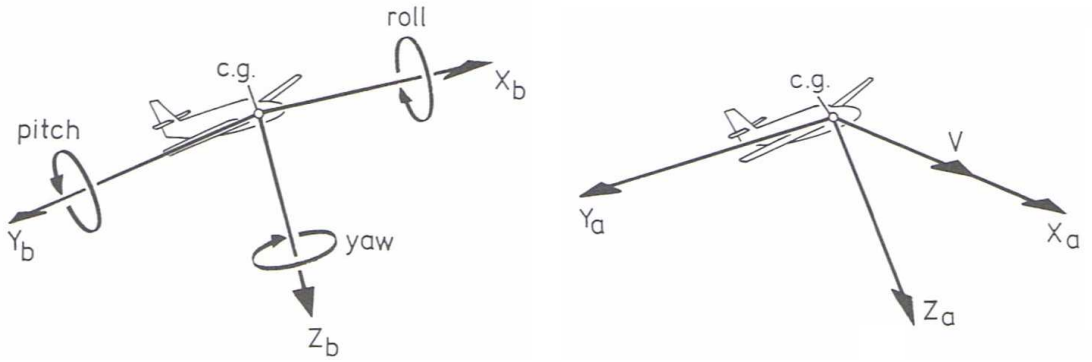

Figure 2.2: (a) body-fixed reference frame (b) aerodynamic reference frame (Ruijgrok, 1996)

The reference frames as described above are not the only existing reference frames with the origin at the CoM of the vehicle. One can also think of a propulsion reference frame, an airspeed based trajectory reference frame, an airspeed based aerodynamic reference frame and a wind reference frame. Since no propulsion is used during the terminal area, the propulsion reference frame is not described in this section. The other reference frames are also not considered, because wind is not considered. Assuming a zero wind condition, the airspeed (velocity relative to the atmosphere) is equal to the groundspeed. Hence, the definitions of the reference frames based on the airspeed are equal to the definitions based on the groundspeed. During this study the velocity refers to the groundspeed, but is also equal to the airspeed.

2.1.3 Reference frame with origin at the runway threshold

Runway reference frame, index RW

The runway reference frame is useful to express the position of the vehicle with respect to the runway. The origin of this reference frame is the intersection between the runway threshold and the centerline of the runway. The Z_{RW} axis is directed perpendicular to the Earth surface and is positive in the upward direction. The X_{RW} axis is directed along the centerline of the runway and is positive in the nominal landing direction. The Y_{RW} axis completes the right handed system. The top view of this reference frame is depicted in figure 2.3.

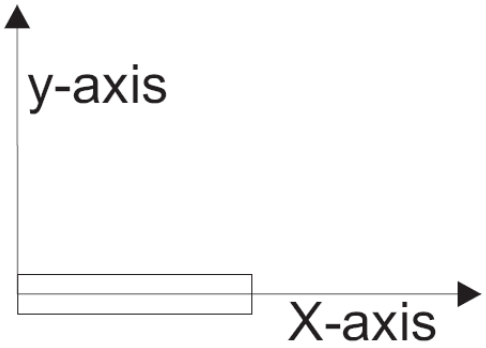

Figure 2.3: Runway reference frame

2.2 State variables

2.2.1 Position and velocity

In the study of the motion of vehicles within the atmosphere, the state variables for position and velocity can be expressed in either Cartesian or spherical components. Using Cartesian coordinates, the position and velocity can be expressed with respect to the I- or R-frame using x,y,z coordinates and in principle, it is possible to study all kinds of motion. Using spherical coordinates, singularities can occur when a vehicle crosses the poles or when the flight-path angle is equal to $\pm$ 90°(vertical flight as during a rocket launch or the parachute descent of a capsule). But during the terminal area, none of these situations occur and hence, the use of Cartesian components is not required. Moreover, the use of spherical components has the advantage that the results are directly interpretable. Therefore, the spherical representation is used throughout this study.

Using spherical coordinates, a vector is specified by its length and two angles. Using this spherical representation, the components of the position vector **r** and the velocity vector **V** defined with respect to the R-frame are illustrated in figure 2.4 and are given as:

- Position: distance R, longitude τ and latitude δ
- Velocity: relative velocity V, flight-path angle γ and heading χ

The distance, R, is the distance from the centre of the Earth to the CoM of the vehicle. The longitude, τ, is measured from the X_R axis, in the equatorial plane and positively eastward

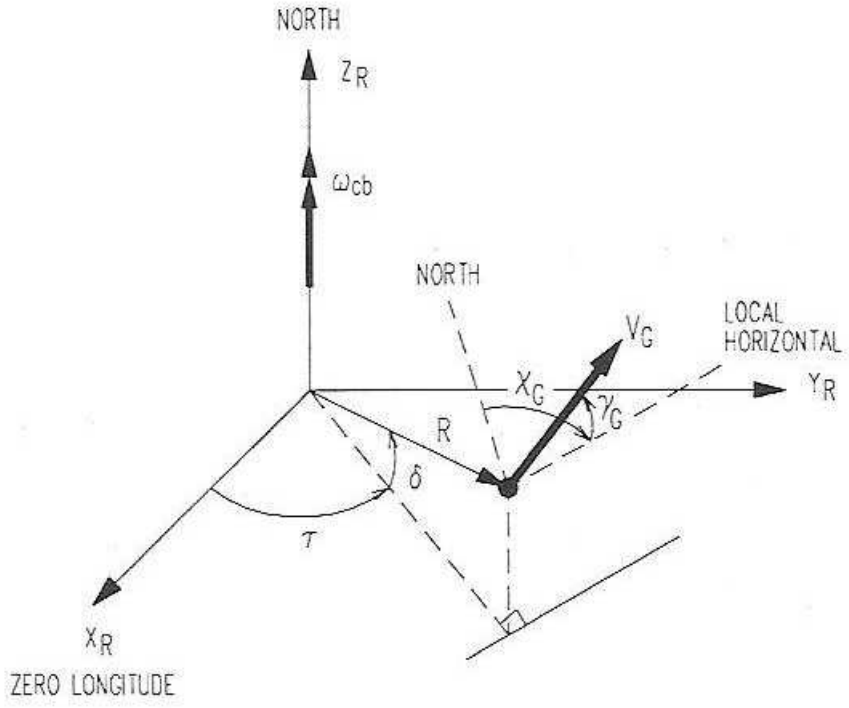

Figure 2.4: Definition of the six spherical flight parameters (Mooij, 1998)

($0° \leq \tau \leq 360°$). The latitude, χ, is measured from the equatorial plane along the appropriate meridian and positively northward ($-90° \leq \delta \leq 90°$).

The relative velocity V is the velocity of the vehicle expressed with respect to the rotating geocentric reference frame and is equal to the velocity of the vehicle with respect to the ground. The flight-path angle, γ, is the angle between the velocity vector $\mathbf{V}$ and the local horizontal plane. The flight-path angle ranges from $-90°$ to $90°$ and is negative when the velocity vector is below the local horizon. The heading angle, χ, is defined as the angle between the projection of $\mathbf{V}$ on the horizontal plane and the local north direction. The heading angle ranges from $-180°$ to $180°$. When $\chi = 90°$, the vehicle is moving parallel to the equator to the east.

2.2.2 Attitude

The attitude of the vehicle is defined as the orientation of the body-fixed reference frame with respect to an external reference frame. This can be done by using a set of Euler angles or quaternions. The use of Euler angles can result in singularities. The use of quaternions eliminates the chance of singularities, but require a fourth parameter. Quaternions must be used for spacecraft which can rotate over the full range, but for a winged re-entry vehicle during the terminal area, situations that lead to singularities do no not occur. Moreover, in contrast to the Euler angles, quaternions are difficult to interpret physically and hence it is chosen to use a specific set of Euler angles for the terminal area study, which are called the aerodynamic angles:

- angle of attack, α

- angle of sideslip, β
- bank angle, σ

The angle of attack, α, is positive for a nose-up attitude and ranges from $-180°$ to $180°$. The bank angle, σ, is positive when banking to the right and ranges from $-180°$ to $180°$. The angle of sideslip, β, is positive for nose-left attitude and ranges from $-180°$ to $180°$. During this thesis study, a coordinated motion of the vehicle is assumed and hence a zero-sideslip condition. These aerodynamic angles are showed in figure 2.5.

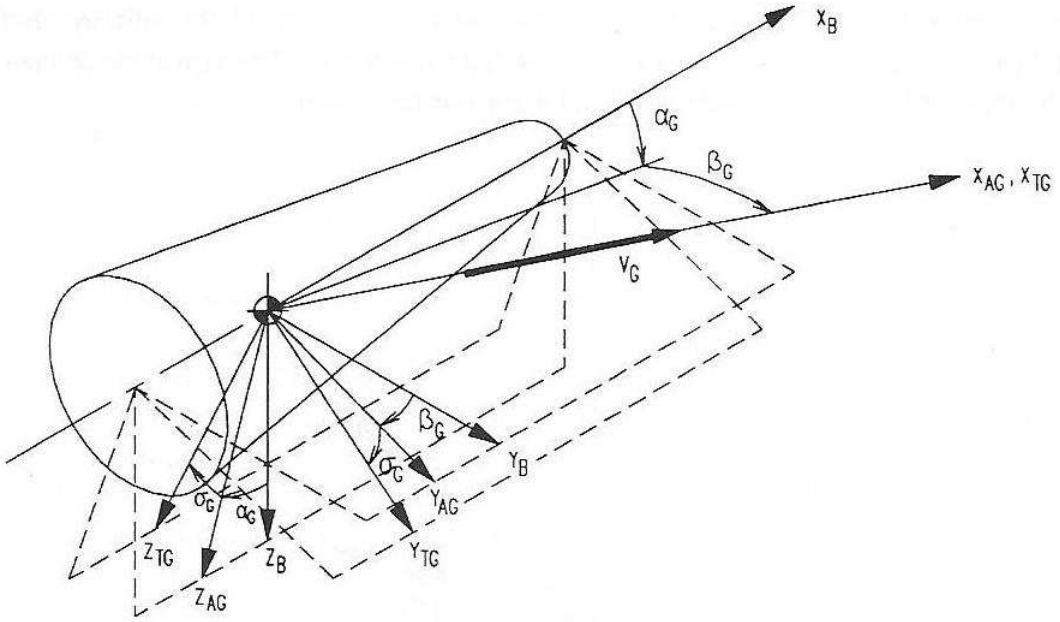

Figure 2.5: Definition of aerodynamic attitude angles α, β and σ (Mooij, 1998)

Since only the translational motion of the vehicle will be considered in this study, no information on the angular rates is given here. The interested reader is referred to (Mooij, 1997). The aerodynamic angles as given above define a transformation matrix that can be used to transform between the body fixed reference frame and the trajectory reference frame. The angle-of-attack and the angle of sideslip give the orientation of the aerodynamic reference frame with respect to the body-fixed reference frame, while the bank gives the orientation of the trajectory reference frame with respect to the aerodynamic reference frame. Many transformation matrices exist for transformations between the different references frames or between different sets of state variables. These transformations are beyond the scope of this study and again, the interested reader is referred to (Mooij, 1997).

2.3 Flight environment

The environment for the flight simulations of a re-entry vehicle consists of the Earth and its atmosphere. This section defines the parameters related to the environment.

2.3.1 Shape of the Earth

The Earth rotates about the Z_R-axis with an angular velocity of about 7.2921150×10^{-5} rad/s. Due to this rotation, the shape of the Earth deviates from a perfect circle. For the purpose of flight simulation, the shape of the Earth may be approximated as an ellipsoid of revolution, with its minor axis along the Earth's polar axis (Mooij, 1998). This reference ellipsoid is defined by a parameter called the ellipticity e, which is specified as:

$$e = 1 - \frac{R_p}{R_e} \tag{2.1}$$

where R_p is the Earth radius at the pole and R_e is the Earth radius at the equator. For the Earth, R_p is bout 21 km smaller than R_e. Figure 2.6 indicates a cross-section of the ellipsoid representing the Earth. The ellipticity can be used to derive an expression for the radius R_s at an arbitrary point along the surface, see (Mooij, 1998). However, this expression depends on the geodetic (geographic) latitude δ^*. The latitude, as defined in the previous section to specify the position, corresponds to a geocentric latitude. The geodetic latitude is not the same as the geocentric latitude, see figure 2.6. An iterative process is required to solve for δ^*, which is expensive in terms of computation time. However, the difference between the geocentric and the geodetic latitude is small and hence, the accuracy gained with the iterative procedure is small. Therefore, the geodetic altitude will be assumed to be equal to the geocentric latitude, $\delta^* = \delta$ (Mooij, 1998). Using this in combination with a first order approximation, R_s can be expressed as (Mooij, 1998):

$$R_s = R_e(1 - e\, sin^2\delta) \tag{2.2}$$

This expression can be used to determine the height h of the vehicle above the surface of the Earth:

$$h = R - R_s \tag{2.3}$$

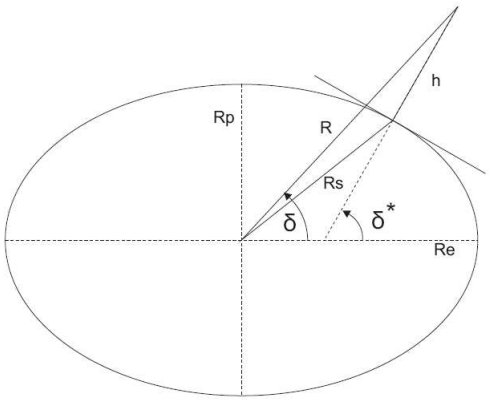

Figure 2.6: Geocentric latitude δ and geodetic latitude δ^*

2.3.2 Atmosphere

The real atmosphere never remains constant and a considerable variation of temperature, pressure and density is present at any time, height and place on Earth (Ruijgrok, 1996). Over the years, a number of standard atmospheres has been developed and these may be seen as expected

mean circumstances. Such an atmospheric model must be able to represent the vertical run of pressure, density and temperature.

A common model as used in airplane performance studies and that describes the variation of pressure, temperature and density is the International Standard Atmosphere (ISA), published by the International Organization for Standardization (ISO). This model consists of table of values at various altitudes and some formulas. The model presents data up to an geopotential altitude of 32 km. The ISA model is used in other terminal area studies, see (Helmersson, 1988b) and (Camara, 2003).

Another accepted standard as used for re-entry problems is the U.S. Standard Atmosphere 1976 published by the Committee on Extension to the Standard Atmosphere. This model covers the atmosphere from Earth's surface to an altitude of 1000 km at a latitude of 45°N. The US76 model is used in (Mooij, 1998) to study the hypersonic re-entry of HORUS. Hence, during this study, the same US76 model will be used to be consistent. The complete description of the US76 model can be found in (NOAA, NASA, & USAF, 1976). More information can also be found in (Regan & Anandakrishnan, 1993).

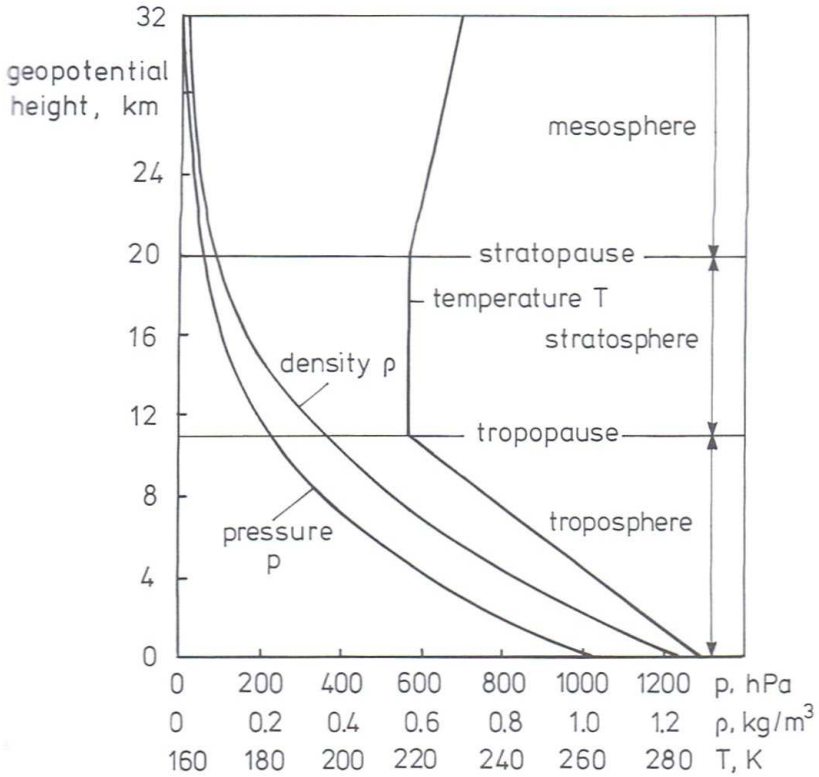

Figure 2.7: Variation of pressure, density and temperature in IAS (Ruijgrok, 1996)

Up to an altitude of 32 km, the US76 is identical to the ISA. Figure 2.7 presents the variation of the pressure, temperature and the density as a function of the geopential altitude in the ISA. The model is divided into three different layers: the troposphere, the stratosphere and the mesosphere. The ISA atmosphere is based on the assumption that the air is a perfect gas, which is supposed to contain no moisture or dust. A second assumption is that the atmosphere is motionless with respect to the Earth. All the quantities are given as a function of the geopen-

tial altitude instead of the measurable geometric altitude. The geopotential altitude is based upon the assumption that the gravitational acceleration is constant with altitude, rather than obeying the inverse-square law (Regan & Anandakrishnan, 1993). Both altitudes as equal to zero at sea level and the geopotential altitude is the height in a uniform gravity field at which the potential energy is the same as the geometrical altitude in a variable gravity field. At an geopotential altitude of 32.0 km, the geometric altitude is equal to 32.1619 km and hence, the difference between the two quantities is small.

2.4 External forces

Two types of external forces are acting on a gliding re-entry vehicle: aerodynamic forces and gravity forces.

2.4.1 Aerodynamic forces

Aerodynamic forces develop whenever there exists relative motion between the fluid and the immersed body (Vinh, 1981). The aerodynamic forces are generated by the relative motion and the interaction between the vehicle and the surrounding air. The aerodynamic forces acting on a moving vehicle arise from pressure forces and viscous forces. The total aerodynamic force can be split into three components: the lift force L, the side force S and the drag force D. Because of the no-side slip assumption throughout this report, the side force is always equal to zero and hence, only the lift force and drag force are important. These forces are defined with respect to the aerodynamic reference frame and the forces are positive in the negative axis direction. The aerodynamic forces are given as:

$$L = C_L \, q_{dyn} \, S_{ref} \tag{2.4}$$

$$D = C_D \, q_{dyn} \, S_{ref} \tag{2.5}$$

with the variables:

- $q_{dyn} = \frac{1}{2}\rho V^2$ = dynamic pressure (N/m^2)
- ρ = atmospheric density (kg/m^3)
- V_A = velocity with respect to the surrounding air (m/s)
- S_{ref} = aerodynamic reference area (m^2)

The aerodynamic lift and drag coefficients C_L and C_D are not constant but depend on the vehicle configuration, control surface deflections, Mach number, Reynolds number, attitude of the vehicle (the angle of attack) and the altitude. The Mach number is defined as:

$$M = \frac{V}{a} \tag{2.6}$$

where a is the local speed of sound. Another quantity related to velocity that will be used in this study, is the equivalent airspeed V_e, which is related to the true airspeed at a particular altitude by:

$$V = V_e \sqrt{\frac{\rho_0}{\rho}} \tag{2.7}$$

The aerodynamic forces must be expressed in the airspeed-based, aerodynamic reference frame. But because, the groundspeed is equal to the airspeed (no wind), the groundspeed can be substituted in the equations and hence, these equations are then expressed in the groundspeed based, aerodynamic reference frame and can be used directly for the spherical equations of translational motion.

The total drag of the vehicle can be divided into two components: the drag of the wing and the sum of the drag of other components of the vehicle. The wing drag can be further divided into the induced drag and the profile drag. The induced drag is related to the lift produced by the wings. The profile drag consists of the pressure drag, the skin friction drag and the wave drag. The wave drag is only present at supersonic velocities and is equal to zero for subsonic airspeeds below the critical Mach number. The pressure drag is due to flow separation is also called form drag. For a three-dimensional body such as a complete vehicle, the sum of the skin friction drag and the pressure drag is frequently called parasite drag.

2.4.2 Gravitational forces

The gravitational force acting on a vehicle is specified as:

$$\mathbf{F_g} = m\mathbf{g} \tag{2.8}$$

where m is the mass of the vehicle (kg) and $\mathbf{g}$ is the gravitational acceleration vector (m/s^2).

To model $\mathbf{g}$, the Earth is thought as an ellipsoid with mass symmetry about the polar axis (Mooij, 1998). Spherical equations of motions are used for the translational motion and hence, $\mathbf{g}$ is expressed in spherical components:

$$\mathbf{g} = (g_r \ 0 \ g_\delta)^T \tag{2.9}$$

These spherical components of the gravity vector are given in a new vehicle based frame. The X-axis is positive pointing downward to the center of the Earth. The Z-axis lies in the local horizontal plane and is positive in the northern direction. The Y-axis completes the right-handed system. Because of the assumption of the rotational symmetry of the Earth, there is no component of the gravity vector out if the meridian plane (Y-component). The components of the gravity field are given as (Mooij, 1998), (Regan & Anandakrishnan, 1993):

$$g_r = \frac{\mu}{R^2}\left[1 - \frac{3}{2}J_2\left(\frac{R_e}{R}\right)^2(3sin^2\delta - 1)\right] \tag{2.10}$$

$$g_\delta = -3J_2\frac{\mu}{R^2}\left(\frac{R_e}{R}\right)^2 sin\delta cos\delta \tag{2.11}$$

In these expressions, only the second coefficient of the harmonic expansion of the gravity field, J_2, is taken into account. The harmonic coefficients express the form of the Earth and the J_2 coefficient is related to the oblateness or the flattening of the Earth. For the Earth, J_2 is equal to $0.1082626925638815 \times 10^{-2}$ (Wertz, 2001). Higher order coefficients are a thousand times smaller and hence, can be ignored. More information about the other coefficients can be found in (Regan & Anandakrishnan, 1993). Other parameters as used in the above expressions are defined as:

- μ = gravitational parameter; Earth = $398600.4418 \times 10^9 \ m^3/s^2$ (Wertz, 2001)

- R = distance to the center of the Earth (m)
- R_e = mean equatorial radius of the Earth = 6378137 m (Wertz, 2001)
- δ = geocentric latitude (rad)

2.5 The equations of translational motion

The motion of a non-elastic body with a constant mass can be divided into the motion of the CoM and the one around this CoM. The equations describing the first part are called the equations of translational motion and gives the information about the position and the velocity in three directions. The second part of the motion is describes by the equations of rotational motion, which give information on the angular rates around the three axes. The complete set of equations incorporates 6 degrees of freedom (6 d.o.f). For the purpose of trajectory design and guidance system design, it is sufficient to consider the vehicle as a point mass and hence, only the translational equations of motion (3 d.o.f) are used in this thesis study. Below, a summary is given of these equations of translational motion. The derivation can be found in (Mooij, 1998) and (Mooij, 1997).

2.5.1 Translational motion with respect to inertial space

Assume an arbitrary non-elastic vehicle with constant mass or a vehicle represented by a point mass, moving in the Earth's environment. This vehicle is subjected to the sum of the external forces $\mathbf{F_I}$. The position vector of the CoM of the vehicle is given by $\mathbf{r_{cm}}$. The velocity of the vehicle is given by $\mathbf{V_I}$. These vectors are given with respect to the inertial reference frame, the I-frame. Using Newton's second law of motion, the translational motion of the point mass or non-elastic vehicle with a constant mass under the influence of an external force can be described by with respect to the I-frame:

$$\mathbf{F_I} = m\frac{d^2\mathbf{r_{cm}}}{dt^2} \tag{2.12}$$

This equation is the dynamic equation or the force equation and describes the motion of a body under the influence of external forces. The corresponding change in position can be described by the kinematic equation:

$$\frac{d\mathbf{r_{cm}}}{dt} = \mathbf{V_I} \tag{2.13}$$

2.5.2 Translational motion with respect to a rotating frame

The equations as given above are given with respect to an inertial reference frame. But it is more convenient to specify the equations in the R-frame because then it is easy to follow the motion of the vehicle projected onto the surface of the Earth. Newton's second law as given in equation 2.12, can be adjusted to be valid for a point mass with respect to the rotating R-frame:

$$m\frac{d\mathbf{V_R}}{dt} = \mathbf{F_R} - 2m\omega_\mathbf{R} \times \mathbf{V_R} - m\omega_\mathbf{R} \times (\omega_\mathbf{R} \times \mathbf{r_{cm}}) \tag{2.14}$$

where $\mathbf{V_R}$ is the velocity of the vehicle with respect to the R-frame. The apparent acceleration of the vehicle in the R-frame is specified by $d\mathbf{V_R}/dt$. The rotational rate of the R-frame is

equal to the rotation rate of the Earth and is given by $\omega_{\mathbf{R}}$. The equation shows that due to the rotation of the Earth, two additional forces or acceleration occur: the Coriolis force (second term on the right) due to the motion of the vehicle in a rotating frame and the centripetal force (third term on the right) due to the angular rotation of the rotating frame. The acceleration related to the centripetal force is also called the apparent or transport acceleration.

The kinematic equation in the R-frame becomes:

$$\frac{d\mathbf{r_{cm}}}{dt} = \mathbf{V_R} \tag{2.15}$$

The position and the velocity can be expressed in both Cartesian or spherical coordinates. It was already stated that spherical components have the advantage that the results are directly interpretable. Using spherical components, the position vector $\mathbf{r_{cm}}$ can be expressed by its magnitude r, its longitude τ and latitude δ, while the velocity is expressed by the V, the flight path angle γ and the heading angle χ. To express the kinetic and the kinematic equations in terms of the these components, a new rotating coordinate system is introduced, see figure 2.8. The x-axis is directed along the position vector $\mathbf{r}$. The y-axis lies in the equatorial plane, orthogonal to the x-axis and from it toward the eastward direction. The z-axis completes the right handed system. The several components of equations 2.14 and 2.15 must be expressed in this new reference frame. Using this new intermediate reference frame, the force equations and kinematic equations as specified below are given for a non-elastic gliding vehicle with a constant mass. The elaborate derivation can be found in (Mooij, 1998) and (Mooij, 1997), and will not be repeated here.

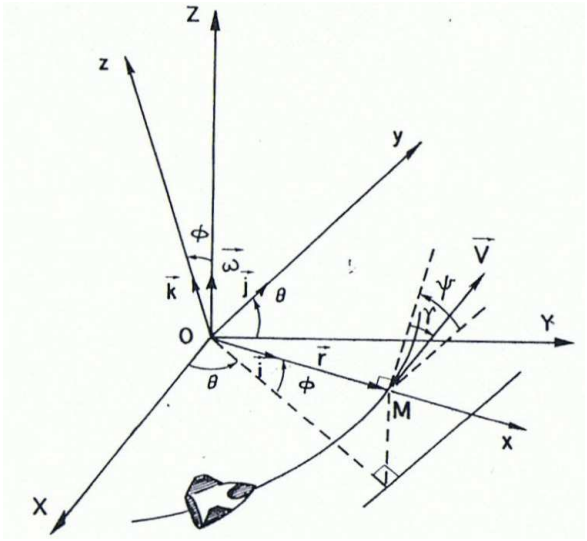

Figure 2.8: Coordinate system for equations of motion (Vinh, 1981); $\tau = \theta$, $\delta = \phi$

Dynamic equations

$$\dot{V} = \frac{F_V}{m} + \omega^2 R cos\delta(sin\gamma cos\delta - cos\gamma sin\delta cos\chi) \tag{2.16}$$

$$V\dot{\gamma} = \frac{F_\gamma}{m} + 2\omega V cos\delta sin\chi + \frac{V^2}{R}cos\gamma + \omega^2 R cos\delta(cos\delta cos\gamma + sin\gamma sin\delta cos\chi) \quad (2.17)$$

$$Vcos\gamma\dot{\chi} = \frac{F_\chi}{m} + 2\omega V(sin\delta cos\gamma - cos\delta sin\gamma cos\chi) + \frac{V^2}{R}cos^2\gamma tan\delta sin\chi + \omega^2 R cos\delta sin\delta sin\chi \quad (2.18)$$

with the forces given as:

$$F_V = -D - mg_r sin\gamma + mg_\delta cos\gamma cos\chi \quad (2.19)$$

$$F_\gamma = Lcos\sigma - mg_r cos\gamma + mg_\delta sin\gamma cos\chi \quad (2.20)$$

$$F_\chi = Lsin\sigma - mg_\delta sin\chi \quad (2.21)$$

Kinematic equations

$$\dot{R} = Vsin\gamma \quad (2.22)$$

$$\dot{\tau} = \frac{Vsin\chi cos\gamma}{rcos\delta} \quad (2.23)$$

$$\dot{\delta} = \frac{Vcos\chi cos\gamma}{r} \quad (2.24)$$

The equations as stated above describe the motion with respect to a rotating Earth represented by a reference ellipsoid. These equations were used in (Mooij, 1998) for the hypersonic re-entry phase of HORUS. To use a single model for the re-entry and the terminal area, these equations are also used in this study. The integration is performed using these equations, such that the position and velocity are obtained in spherical components. After the integration, the spherical components of position are transformed to the runway coordinate frame for plotting and interpretation purposes. The transformation equations are based on figure 2.9 and are given as:

$$x_{RW} = R_s(\tau - \tau_{RW}) \quad (2.25)$$

$$y_{RW} = R_s(\delta - \delta_{RW}) \quad (2.26)$$

$$z_{RW} = R - R_s \quad (2.27)$$

If the coordinates τ_{RW} and δ_{RW} of the runway threshold are known, the x- and y-coordinate of HORUS with respect to the runway threshold can be calculated. For this thesis study, an existing runway in Kourou, French Guyana, is used.

2.5.3 Translational motion with respect to a flat, non-rotating Earth

In some studies related to the terminal area, a simplified version is used of the equations as stated above, see for example (Buechner, 2003) or (Kluever & Horneman, 2005). Moreover, these simplified equations are also used when deriving approximation theorems for the point performance of HORUS. These simplified equation are stated in this section. A common used simplification is the use of a flat, non-rotating Earth.

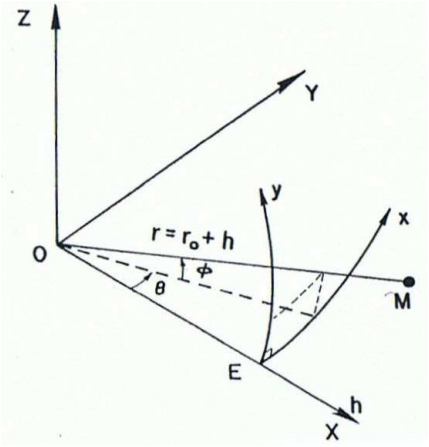

Figure 2.9: Topocentric coordinate system (Vinh, 1981); $\tau = \theta$, $\delta = \phi$, R = r, $R_e = r_0$

The rotation of the Earth is responsible for two extra terms in the force equation: the centrifugal acceleration and the Coriolis acceleration. The centripetal acceleration depends on the direction of the position vector and hence, the latitude. The acceleration is zero at the poles and maximum at the equator. Assuming an altitude of 25 km above the equator, the maximum magnitude of the centripetal acceleration $\omega^2 R$ is equal to 0.034 m/s^2. The Coriolis acceleration depends on the magnitude and the direction of the velocity of the vehicle with respect to the Earth. The magnitude of this Coriolis acceleration has an important effect in a high-speed, long-range flight. The acceleration is zero when the flight path is parallel to a meridian (flying North or South) and is maximum when flying parallel to the equator. Assuming a flight situation at an altitude of 25 km and with a velocity of M = 2.5 parallel to the equator, the maximum Coriolis acceleration $2\omega V$ is equal to 0.109 m/s^2. For an accurate result, both accelerations should be taken into account. But because a terminal area flight is not a long range flight and because of the small values of the accelerations compared to the gravitational acceleration, these accelerations are often ignored in terminal area studies by assuming a non-rotating Earth, $\omega = 0$.

Assuming the Earth is a perfect sphere, the J_2 terms in the expressions for the gravitational acceleration components become zero. The g_δ term is eliminated and only a radial component g_r is present. This radial component is inversely proportional to the square of the distance from the center of the Earth. In a flat Earth assumption, it is appropriate to consider g_r, or simply g as constant. Since atmospheric flights are conducted in a relative thin layer of the atmosphere as compared by the radius of the Earth, g can be considered as a constant (Vinh, 1981).

Next, also the term $\frac{V^2}{R}$ can be neglected in the force equation because even for a vehicle flying at twice the speed of sound at sea level, the ratio is in the same order as the Coriolis acceleration (Vinh, 1981). Using all these simplifications and expressing the position in x-, y- and z-coordinates, gives the following set of equations:

$$\dot{h} = V sin\gamma \tag{2.28}$$

$$\dot{x} = V sin\chi cos\gamma \tag{2.29}$$

$$\dot{y} = V cos\chi cos\gamma \tag{2.30}$$

$$\dot{V} = -\frac{D}{m} - g sin\gamma \tag{2.31}$$

$$V\dot{\gamma} = \frac{L cos\sigma}{m} - g cos\gamma \tag{2.32}$$

$$V\dot{\chi} = \frac{Lsin\sigma}{mcos\gamma} \tag{2.33}$$

These equations are used throughout the literature to study the terminal area phase of a winged re-entry vehicle. But it can be seen that some assumptions are made in deriving these equations. Each assumption on its own has only a minor effect and causes only small inaccuracies. But the accumulated effect of these assumptions is larger and for an accurate result, the equations of motion for the flight over a rotating spherical Earth must be used. As already stated, these more complex equations are used during this thesis study to simulate the trajectory of HORUS. The simplified equations, on the other hand, are used to derive approximation theorems for the performance of HORUS.

2.6 Approximations for performance prediction

The equations that describe the translation motion of the vehicle, can be used to study optimal trajectories and the performance of the vehicle. Solving the complete trajectory corresponds with determining the path performance or the integral performance and requires numerical methods. This results in the most accurate solution, but is also computationally the most complex. To overcome the problems of computational complexity encountered in optimal control problems or performance analysis, efforts have been made to generate near optimal solutions. Moreover, experience in actual flight, as well as comparison between various optimal and solutions suboptimal approximations, often displays the fact that the improvement in performance is minimal when the exact optimal trajectory is compared with a suboptimal one obtained by a simple analysis. If a simple analysis is carried out properly, the obtained solution is close to the optimal solution.

Analyzing the complete trajectory using numerical integration of the equations of motion corresponds with an integral performance of the vehicle. An example of an integral performance value is, for example, the maximum range. Point performance, on the other hand, identifies the study of performance parameters, which occur at a given point on the flight path (Ruijgrok, 1996). Point performance refers to instantaneous quantities, such as, for example, minimum drag, minimum flight-path angle or minimum radius of turn. In this thesis, it is studied if using parameters related to the point performance can be used to analyze or approximate the integral performance. Two approximations that are commonly used are the steady-state approximation and the energy-state approximation. Note that the use of a point mass model in itself is an approximation. Also the reduction of the translational equations of motion for a rotating Earth specified by a reference ellipsoid to a flat non-rotating Earth model is already an approximation. This section is concerned with further approximations.

Steady-state approximation

In a steady-state assumption, the accelerations are neglected completely and hence, a stationary flight situation exists. A stationary flight occurs when the direction and the velocity of the vehicle, with respect to the surrounding air, do not change. This is only the case when the forces acting on the vehicle are in equilibrium. So a stationary flight is a flight situation in which the forces (and moments) acting on the vehicle do not change with time, nor in magnitude nor in direction. More information on the steady-state approximation can be found in chapter 6.

Energy-state approximation

An improved approximation is the energy-state approximation, where it is assumed that kinetic and potential energy can be exchanged back and forth in zero time without loss of total energy (Bryson, Desai, & Hoffman, 1968). The total energy may be considered as the state variable of the system, and is continuous. The total mechanical energy is the sum of the potential and the kinetic energy:

$$E_{tot} = E_{pot} + E_{kin} = mgh + \frac{1}{2}mV^2 \tag{2.34}$$

In the energy-state approximation, a constant gravity field is assumed. Using this constant g, all the terms in equation 2.34 can be divided by the weight, and the so-called energy height is obtained. The energy height is the total mechanical energy divided by the weight:

$$E_h = \frac{E}{mg} = h + \frac{1}{2g}V^2 \tag{2.35}$$

More information on the energy-state approximation can be found in chapter 8. In this thesis study, optimal trajectories will be calculated (integral performance) and will be compared with analysis results obtained from a point performance. This is done to investigate whether it is possible to analyze the integral performance without the need of the time consuming integral performance analysis.

Chapter 3

HORUS-2B simulation model

In this thesis study, the HORUS-2B is used as the reference vehicle. All its aerodynamic data are available in literature. Moreover, in previous studies on the flight phase before the terminal area, the hypersonic atmospheric re-entry, this vehicle was used as well, see (Mooij, 1998). The HORUS-2B is derived from Messerschmitt-Bolkow-Blohm GmbH (MBB) funded studies on winged upperstages (Cucinelli, 1987). The used reference configuration is not yet fully optimized with respect to aerodynamic design, flight performance and stability characteristics (Grallert, 1988). But although some improvements can be made on the design, the reference configuration and the accompanying data is sufficient to study the principles of re-entry.
Section 3.1 describes the mission scenario for which the HORUS-2B is designed for. The geometry and the aerodynamic model are described in section 3.2 and 3.3, respectively. Section 3.4 discusses the vehicle constraints. The components of the Guidance, Navigation and Control (GNC) system are described in section 3.5.The simulation tool that is used in this study is presented in section 3.6. This simulation tool is based on flight dynamic models as described in chapter 2 and on the vehicle model as described in this chapter.

3.1 Mission scenario

Initially, the HORUS-2B was designed as a fully reusable second stage to the Ariane-5 launcher. HORUS had no main engines and was thus an unpowered vehicle. In 1985, MBB began renewed studies of the Saenger spaceplane concept, this time a two-stage-to-orbit horizontal take-off concept, see figure 3.1. The first stage consisted of an air-breathing hypersonic vehicle that carried a delta winged second stage, the Hypersonic ORbital Upper Stage (HORUS), augmented with a rocket engine.

Figure 3.2 presents the flight profile of the Saenger concept. The first stage hypersonic booster aircraft is capable of cruising at a velocity of Mach 4. HORUS separates from the lower stage at Mach 6.6 and is boosted into orbit by a rocket engine. In the late 1980s and early 1990s, the German government funded several studies related to this spaceplane concept. In 1994, it was concluded that the further development would become very costly, while the design would reduce costs only 10 to 30 percent below that of the Ariane-5 expendable launcher and hence, the project was canceled.

Figure 3.1: Saenger space plane concept with HORUS as the second stage [www.astronautics.com]

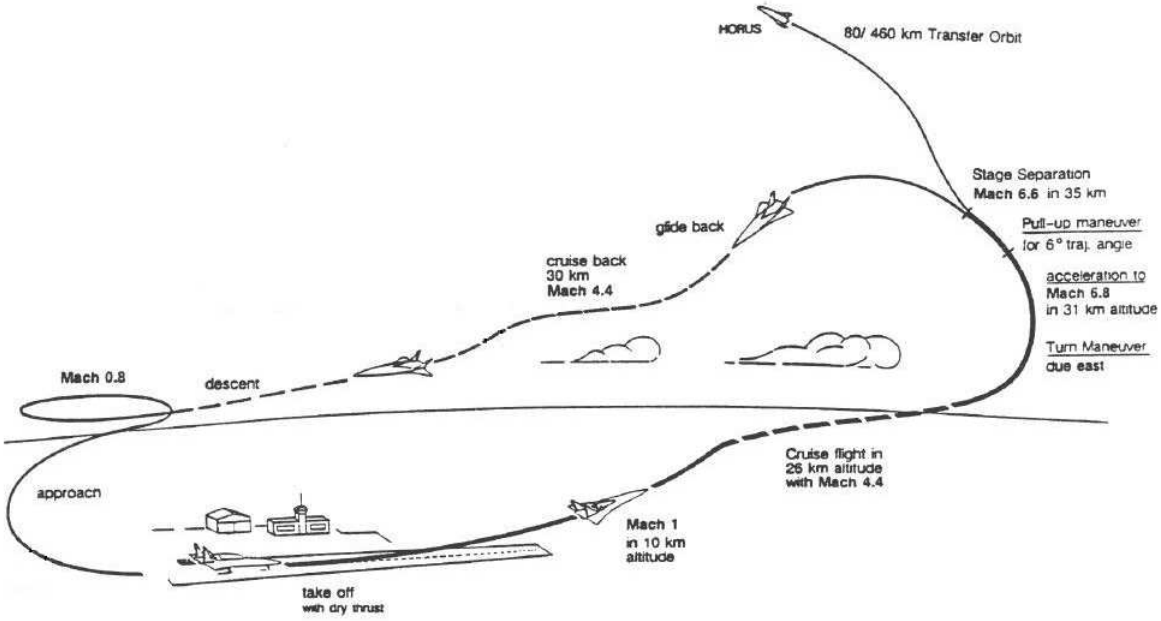

Figure 3.2: Flight profile of Saenger (Mooij, 1998)

During this study, the original unpowered version will be used. The aerodynamic database of this vehicle is given in (Cucinelli, 1987). In the following sections, a summary of the characteristics and aerodynamics of the vehicle is presented.

3.2 Geometry and characteristics

The configuration of HORUS-2B is presented in figure 3.3, while the main vehicle characteristics are summarized in table 3.1. The center of mass is located in the symmetry plane of the vehicle and at a 13 m distance from the nose. The control surfaces of HORUS consists of two rudders, two elevons and one body flap. The sign conventions for the deflection angles are defined as:

- left and right rudder deflection angles $\delta_{r,l}$ and $\delta_{r,r}$: positive outboard
- left and right elevon deflection angles $\delta_{e,l}$ and $\delta_{e,r}$: positive down
- body flap deflection angle δ_b: positive down

The rudders can only be moved outward. So for yaw control, only one rudder is active at a time, while the speedbrake function is activated by deflecting both rudders outward at the same time. An elevon combines the functions of a conventional elevator and ailerons. The commanded aileron and elevon deflections are combined into a single commanded elevon deflection (Mooij, 1998).

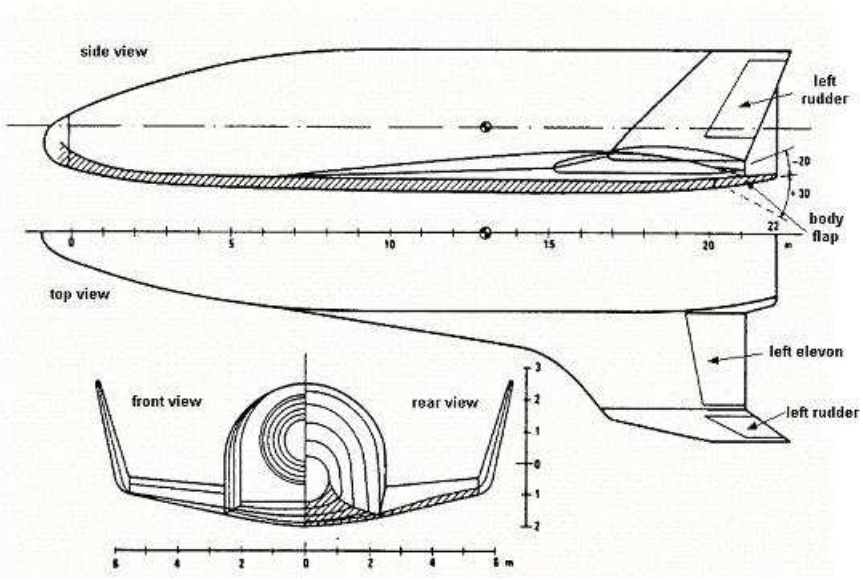

Figure 3.3: HORUS-2B reference vehicle (Mooij, 1998)

More information on the geometry, including inertia properties, can be found in (Cucinelli, 1987).

Table 3.1: Main characteristics of HORUS-2B

total vehicle length	25 m
maximum fuselage width	5.4 m
maximum fuselage height	4.5 m
wing span	13.0 m
wing chord	23.0 m
wing area	110 m^2
re-entry and landing mass	26029 kg

3.3 Aerodynamic model

The HORUS-2B shape has changed significantly during the design phase. The aerodynamic data as presented in (Cucinelli, 1987) relate to version 7 of the HORUS-2B. The presented aerodynamic data set is based on simple calculation methods. No wind tunnel test were made to investigate the validity of the aerodynamic data. Therefore, the presented data should be considered as a rough description of major aerodynamic effects (Cucinelli, 1987).

3.3.1 Aerodynamic data provided by MBB

The aerodynamic data set from (Cucinelli, 1987) is presented in graphical form. It contains the untrimmed aerodynamic coefficients for supersonic and hypersonic flight conditions and the trimmed aerodynamic coefficients for the subsonic and supersonic flight regimes. No data for transonic flight conditions, between M = 0.95 and M = 1.2, are available.

untrimmed data

The untrimmed data set contains six steady coefficients: lift coefficient, drag coefficient, side force coefficient, pitching moment coefficient, yawing moment coefficient and rolling moment coefficient. This corresponds to a six-degrees-of-freedom model. Since during this thesis study only the translational motion in considered, only the lift and drag coefficient will be discussed. The side force is not taken into account because HORUS is a symmetrical vehicle and it is assumed that the sideslip angle is always zero and hence, no side force arises.

The total lift coefficient is given by (Cucinelli, 1987):

$$C_L = C_{L,0} + C_{L,\delta_{e,l}} + C_{L,\delta_b} + C_{L,\delta_{e,r}} \tag{3.1}$$

where $C_{L,0}$ is the clean lift coefficient of the total vehicle without any surface deflections, $C_{L,\delta_{e,l}}$ is the lift coefficient increment due to a deflection of the left elevon, C_{L,δ_b} is the increment due to a deflection of the body flap and $C_{L,\delta_{e,r}}$ is the increment due to a deflection of the right elevon.

The total drag coefficient is given by (Cucinelli, 1987):

$$C_D = C_{D,0} + C_{D,\delta_{r,l}} + C_{D,\delta_{e,l}} + C_{D,\delta_b} + C_{D,\delta_{e,r}} + C_{D,\delta_{r,r}} - C_{D,DH} \tag{3.2}$$

where $C_{D,0}$ is the clean lift coefficient of the total vehicle without any surface deflections, $C_{D,\delta_{r,l}}$ is the drag coefficient increment due to a left rudder deflection, $C_{D,\delta_{e,l}}$ is the increment due to a left elevon deflection, C_{D,δ_b} is the increment due to a body flap deflection, $C_{D,\delta_{e,r}}$ is the increment due to a right elevon deflection, $C_{D,\delta_{r,r}}$ is the increment due to a right rudder deflection and $C_{D,DH}$ is the drag altitude decrement. The coefficients are valid for trajectory calculations below an altitude of 20 km. In order to use these data for altitudes higher than 20 km, a drag altitude decrement must be subtracted (Cucinelli, 1987). Hence the last term that contributes to the total drag coefficient.

The untrimmed aerodynamic coefficients in graphical form can be found in (Cucinelli, 1987).

trimmed data

For trajectory calculations down to Mach 0.2, a trimmed data set is available. The vehicle is trimmed in the longitudinal direction, which means that the moment around the pitch axis (y-axis), C_M, is reduced to zero. The trimmed data are obtained by using an arbitrary trim rule (Cucinelli, 1987):

- **M > 1**
  The vehicle is trimmed with the body flap as far as possible. If necessary, the rest is done with the wing flaps (elevons)

- **M < 1**
  The vehicle is trimmed with the wing flaps. The body flap is fixed to a maximum up position (-20°)

Using the untrimmed data set, the clean lift and drag coefficients, together with the resulting moment around the pitch axis, can be determined for a specific angle-of-attack and Mach number. Knowing the pitch moment and the trim law as stated above, the deflections and the corresponding extra lift and drag terms can be determined to eliminate the pitch moment. Using equation 3.1 and 3.2, the trimmed lift and drag coefficients are obtained. This was done by MBB and the results as graphically presented in (Cucinelli, 1987) are shown in appendix A. Because the trimmed drag coefficient are obtained using a subtraction of the drag altitude decrement, the trimmed drag data is valid at altitudes higher than 20 km. For altitudes lower than 20 km, the drag altitude decrement should be added. This corresponds with higher drag coefficients at lower altitudes (where the density is larger). The data points from the graphs as presented in appendix A are used as the vehicle model for HORUS. Values in between these data points are obtained through linear interpolation.

A speedbrake deflection is modeled as an increase in drag, while it is assumed that the lift remains unchanged. A reasoning for this is stated below and is based on (Camara, 2003). Assume that the vehicle is in a trimmed condition and deflects the speedbrakes. By doing so, the lift force is decreased and the drag force is increased. The vehicle is no longer in a trimmed condition. In order to get a new trimmed situation, the body flaps and/or elevons have to be further deflected which will produce an increase of the lift. So it is assumed that the lift that was destroyed by the speedbrakes is compensated by the extra lift created by the body flap and elevon deflections required for a new trimmed condition.

Note that a trimmed, banked flight situation requires small rudder and aileron deflections. These deflections are not taken into account by MBB in determining the trimmed data. Moreover, to go from one point to another point along the flight path, control surface deflections are required to change the attitude. These will cause an extra change in the lift and drag coefficients. These extra terms are not taken into account during the simulations. Hence, for a more accurate simulation and to check if the obtained trajectories using the 3 d.o.f. equations of motion with the trimmed data set is flyable, the full untrimmed aerodynamic model is required in combination with a control system. This is recommended for further studies.

3.3.2 Transonic data

During the terminal area, the vehicle passes through the transonic speed regime and hence, aerodynamic data between M = 0.95 and M = 1.2 is required. Therefore, the aerodynamic data of the X-38 were used from (Alenia, 2003) to study the trend in the lift and drag coefficients in the required Mach interval between M = 0.95 and M = 1.2. It is very difficult to find exact solutions for HORUS in this interval, because in the transonic region, complex aerodynamic phenomena occur. But by using the trends from the X-38 data, an engineering guess is made.

For HORUS, the angle of attack in this Mach interval cannot be larger than 10°, see the next section, and hence, the investigation was limited to an α between 0°and 10°. The untrimmed data of the X-38 contained information about aerodynamic coefficients for several α. From this untrimmed data of the X-38, trimmed values of the lift coefficient and lift-to-drag ratio were

calculated for an angle of attack of 4°and 10°. The variations of these quantities as a function of Mach is shown in figure 3.4. In the required Mach interval, data is specified for M 1.05 and M 1.1.

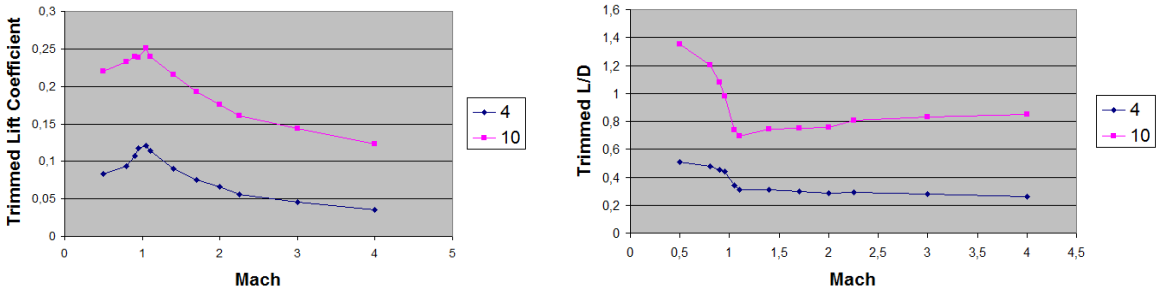

(a) (b)

Figure 3.4: Variation of the lift coefficient and lift-to-drag ratio of the X-38 as a function of the Mach number and for an angle-of-attack of 4°and 10°.

Figure 3.5 shows the variation of the lift coefficient and the lift-to-drag ratio of HORUS over the entire Mach range for an angle of attack of 5°and 10°. The subsonic data points till M = 0.95 and supersonic data from M = 1.2 are already specified by MBB (Cucinelli, 1987). The two data points in the red circles indicate the data points for M = 1.05 and M = 1.1 that are obtained by using similar trends as indicated in figure 3.4 for the X-38, in the required Mach interval. For the lift coefficients, the values are chosen such that the jump in this Mach interval is included. Using a simple interpolation between M = 0.95 and M = 1.2 would not include this jump. Also for the lift-to-drag ratio, the values are chosen such that the same trends are obtained from figure 3.4. The chosen lift coefficient and lift-to-drag ratio values for an angle of attack of 5°and 10°are indicated in table 3.2. The values for other angles of attack

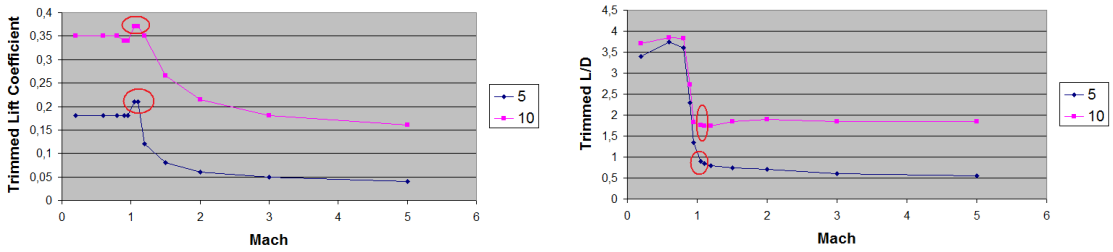

(a) (b)

Figure 3.5: Variation of the lift coefficient and lift-to-drag ratio of HORUS as a function of the Mach number and for an angle-of-attack of 5°and 10°. The red circles indicate the estimated data points for M = 1.05 and M = 1.1.

are also indicated in this table. These are again based on the trends observed in the data of the X-38. Figure 3.6 and 3.7 show respectively the variation of the trimmed lift coefficient and the trimmed lift-to-drag ratio as a function of α for HORUS in the required Mach interval of the transonic region. These transonic data points, in combination with the data as given in appendix A, will be used in this study as the model for HORUS.

Using the available data of the X-38 and knowing that it is very difficult to obtain the exact solution, the presented data are the best guess that was possible. Although uncertainties

Table 3.2: Transonic data points of the trimmed lift coefficient and the trimmed lift-to-drag ratio, for M 1.05 and M 1.1. Data is obtained by analyzing the data for the X-38.

	lift coefficient		Lift-to-drag ratio	
α [deg]	**M = 1.05**	**M = 1.1**	**M = 1.05**	**M = 1.1**
0.0	0.02	0.02	0.05	0.05
2.5	0.12	0.12	0.45	0.4
5.0	0.21	0.21	0.90	0.85
7.5	0.30	0.3	1.40	1.35
10.0	0.37	0.37	1.76	1.74

on the aerodynamic database are present, the data are sufficient to study the terminal area. For further studies, a more accurate vehicle model is required, not only for the transonic region but also for the subsonic and supersonic region, as stated in (Cucinelli, 1987). It means that more calculations and wind tunnel tests are required.

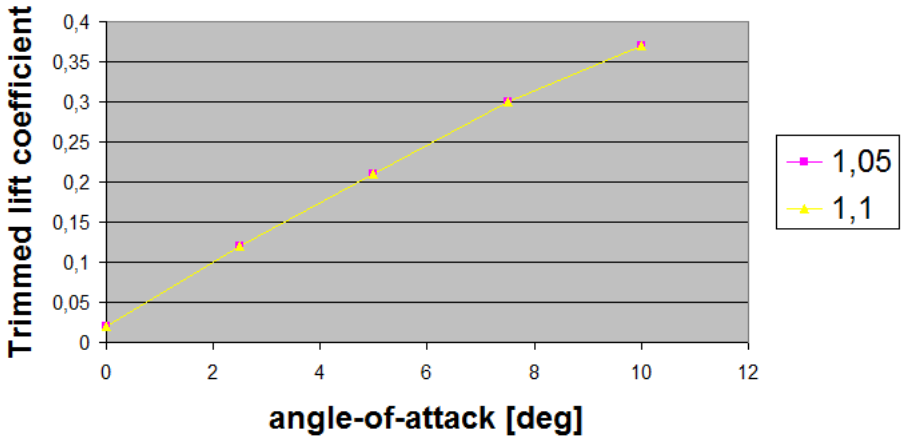

Figure 3.6: Trimmed lift coefficient for HORUS in the transonic regime for M 1.05 and M 1.1

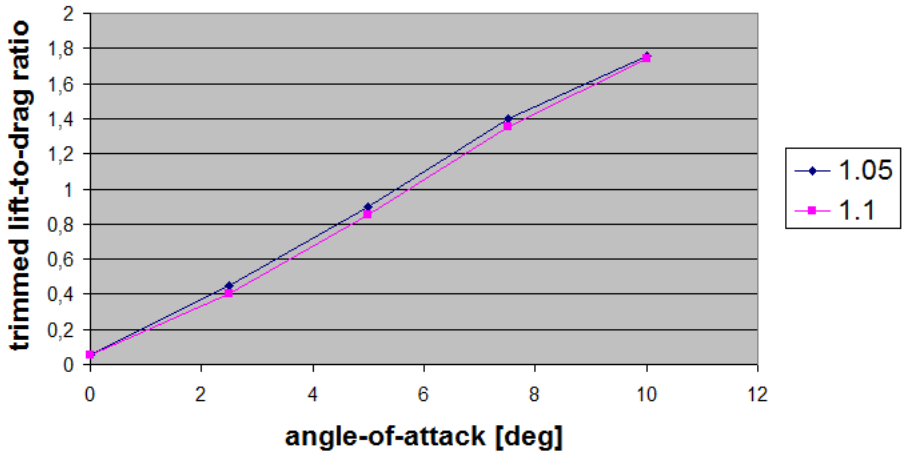

Figure 3.7: Trimmed lift-to-drag ratio for HORUS in the transonic regime for M 1.05 and M 1.1

3.4 Vehicle constraints

The design and analysis of terminal area missions is driven vehicle requirements. These requirements are derived from the vehicle structural limitations and from the trimming and maneuverability restrictions imposed by flight dynamics (Costa, 2003). The constraints encountered during the terminal area can be summarized as:

- maximum dynamic pressure, $q_{dyn,max}$
- maximum load factor, n_z
- speedbrake deflection, δ_{sb}
- angle-of-attack corridor
- maximum bank angle, σ_{max}

Flight envelope

The flight envelope described the area of altitude and airspeed where a vehicle is constrained to operate and defines the altitude-speed operating limit. (Ruijgrok, 1996). For airplanes, several boundaries can be recognized in a flight envelope: the stall limit, the maximum design dive speed, the maximum design diving Mach number and the maximum flight altitude. For a winged re-entry vehicle, the latter two boundaries are of no use. The maximum speed is expressed by the maximum dynamic pressure, but not by specifying a maximum Mach number. Since a re-entry vehicle comes from outer space, the altitude boundary is eliminated as well. The remaining two boundaries for a winged re-entry vehicle in the terminal area are the stalling speed and maximum velocity or maximum dynamic pressure.

The maximum dynamic pressure is associated with the structural safety of the vehicle. No value for HORUS was found in the literature. In a terminal area study of the Hopper vehicle, a conservative value of 10 kPa was used, see (Buechner, 2003). Based on this number, a somewhat less conservative number of 15 kPa is used for HORUS in this study to be able to investigate a larger number of possible trajectories.

The stalling speed is defined as the minimum speed at which the lift equals the weight or the minimum steady speed in free air under one-g conditions (Ruijgrok, 1996). Hence, it is the lowest speed at which a force equilibrium is possible. The stalling speed V_{ST} can be calculated from the aerodynamic data of the vehicle using equation 3.3. This equation indicates that in a banked flight situation, the stalling speed is higher than in a wings-level flight situation.

$$V_{ST} = \sqrt{\frac{mg}{S}\frac{2}{\rho}\frac{1}{C_{L\,max}}\frac{cos\gamma}{cos\sigma}} \tag{3.3}$$

From the aerodynamic data as presented in appendix A, one can see that the maximum lift coefficient changes with the Mach number. The stalling speed can be calculated for a particular altitude by starting with an arbitrary sufficiently high velocity and lowering this velocity until the required lift coefficient for a steady glide condition is equal to the maximum lift coefficient. At this point, it is not possible to lower the velocity any further because the required lift coefficient for a steady state condition will be larger than the available maximum lift coefficient.

Figure 3.8 presents the calculated flight envelope boundaries in the (V,h) space or the energy space. The figure also contains several Mach lines, which indicate different Mach regimes. The stall speed limits as indicated in this figure is the stall speed during a wings-level flight. During a turn with a specific bank angle, this limit shifts to the right (higher velocities). Also, the stall speed is calculated for a vehicle mass of 26029 kg. If this mass would change, a new stall speed limit must be calculated. Important to note is that in theory, HORUS is capable of flying outside the stall limit. The stall limit represents the lowest velocity in a steady-state flight situation. A vehicle can conduct a transient or dynamical maneuver in which the velocity gets lower than the steady state stall speed. A wing over is an example of such a maneuver. But because such maneuvers are unlikely to be used for HORUS, these will not be studied and hence, the stall speed limit is used as a constraint in the simulations.

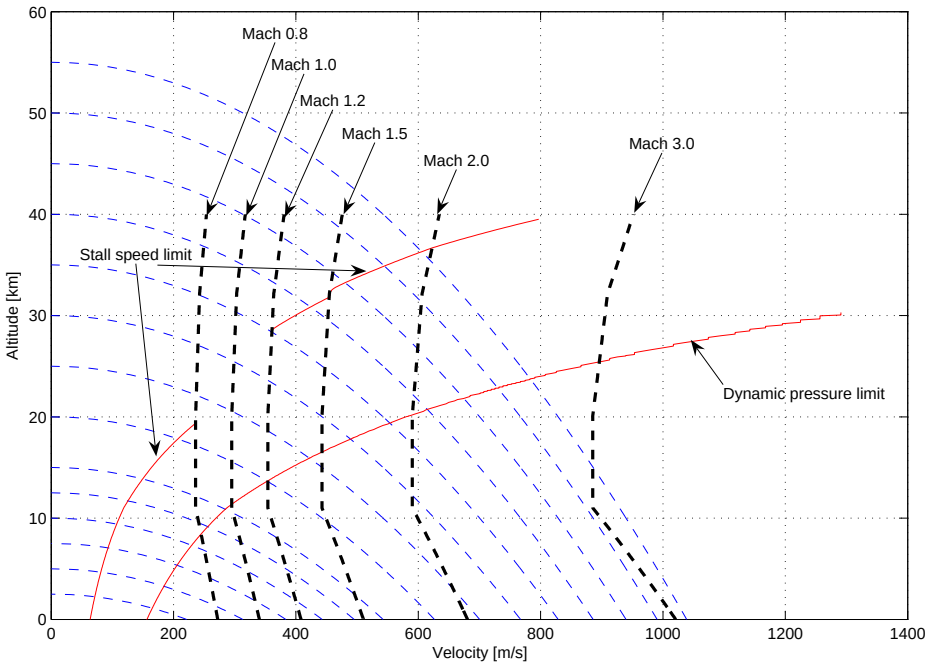

Figure 3.8: Flight envelope of HORUS consisting of the stall limit and the maximum dynamic pressure. DASHED BLUE: indicate lines of constant energy height.

Load factor

In describing the air loads on a vehicle, the load factor is used. This parameter refers to the ratio of the resultant aerodynamic force to the weight of the airplane, for a specific velocity (Ruijgrok, 1996). The increase in lift is of prime significance and hence, the load factor is usually obtained by dividing the lift by the weight of the vehicle:

$$n = \frac{L}{mg} \tag{3.4}$$

Loads applied to an airborne vehicle are produced through accelerations of the vehicle as a result of a control action (maneuvering loads) or by encountering atmospheric turbulence (gust

loads). Since no wind or gusts are included in the current study, no gust loads will be taken into account. Maneuvering loads arise from a change in angle of attack. Also during a turn, the angle of attack will be increased to have force equilibrium in a banked flight situation and hence, the load factor will increase. Normally, the allowable maneuvering load changes with the velocity, resulting in a maneuvering load envelope. Since, this load envelope is not available for HORUS, a constant value for the maximum load factor of 2.5 is used in this study.

Speedbrake deflection

The deflection of the speedbrakes are also connected with the structural safety and with allowed hinge moments. The speedbrakes of HORUS are only used at subsonic velocities, $M < 0.95$.

Angle-of-attack corridor

The elevon deflection used for trim purposes is limited to leave sufficient elevon deflection to control the vehicle. Therefore, the allowable angle-of-attack interval is constrained due to limitations in trim range. As given in (Cucinelli, 1987), these restrictions are a function of Mach number. Figure 3.9 presents the restrictions on the angle-of-attack with a linear interpolation between the data points, based on (Cucinelli, 1987). In the transonic regime, a narrow angle-of-attack corridor exists. In this regime, the angle of attack cannot be larger than 10°. Table 3.3 presents the used data points.

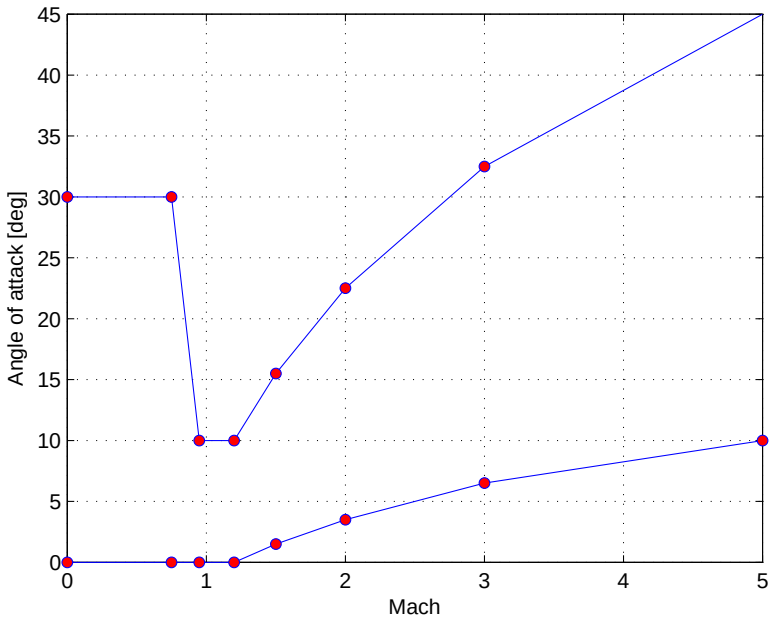

Figure 3.9: Angle-of-attack boundaries due to trim considerations, based on (Cucinelli, 1987)

Bank angle limit

No bank-angle limits for HORUS are found in the literature. But to use realistic bank-angle limits during this study, a scheme similar to the Space Shuttle is used. When the Mach number

Table 3.3: Data points as used in the angle-of-attack boundaries

Mach	0.00	0.75	0.95	1.20	1.50	2.00	3.00	5.00
α_{max}	30.0	30.0	10.0	10.0	15.5	22.5	32.5	45.0
α_{min}	0.0	0.0	0.0	0.0	1.5	3.5	6.5	10.0

is larger than 0.95, the maximum bank angle is set to 30°. Below a Mach number of 0.75, the maximum bank angle depends on the phase in which HORUS is. Table 3.4 indicates these phase-dependent values for the maximum bank angle. More information on the different phase during the terminal area can be found in section 11.2. Between M = 0.75 and M = 0.95, a linear interpolation is used. Next to the maximum value of the bank angle, a limit is also imposed on the rate of change of the bank angle. During the simulations, the change in bank angle is limited to 15°/s.

Table 3.4: Phase dependent bank angle limits for M < 0.75

phase	**bank angle limit [deg]**
acquisition	50.0
heading alignment	60.0
pre-final	30.0
2nd acquisition	60.0

3.5 Guidance, Navigation and Control

In the previous sections, equations were presented that describe the motion of a re-entry vehicle with a constant mass, under the influence of aerodynamic and gravitational forces in the Earth's atmosphere. The current section describes how the motion of the vehicle can be influenced such that a desired trajectory is followed. A vehicle's flight software has to direct the vehicle from its initial position to its desired position. Therefore, it is equipped with a guidance system. This system is part of the Guidance, Navigation and Control (GNC) system. Although the guidance, navigation and control of a vehicle are three individual topics, they are closely related and are considered as one system. First, the general principles of GNC are discussed, followed by describing the simplified GNC model as used during the current study.

3.5.1 Working principle of GNC system

The basic principle of the GNC system is that the guidance produces a commanded state based on the input from the navigational system, and the control system transfers this commanded state to actuator commands. Figure 3.10 shows a schematic overview of the GNC system. The guidance loop from navigation system to guidance system is called the outer loop and the control loop from navigation system to control system is called the inner loop. Below, the different functions are described in more detail. The discussion is based on (Mooij, 1998) and (Bletsos, 2007).

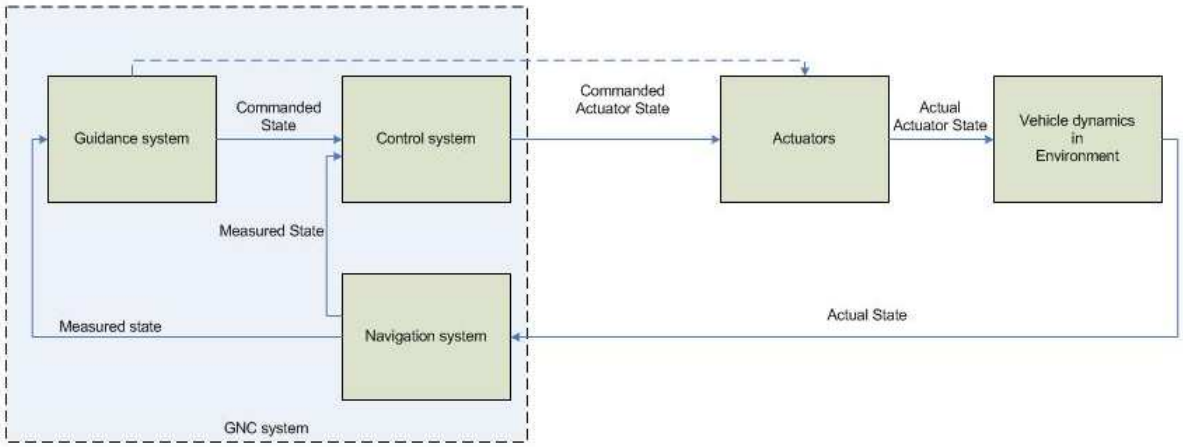

Figure 3.10: Overview of a GNC system

Guidance

Two types of guidance exist: open-loop guidance and closed-loop guidance. Open-loop guidance generates commands without taking into account the actual state of the vehicle. Closed-loop guidance, on the other hand, generates commands based on the measured state. If the vehicle state and environmental conditions were exactly known and did not change, open-loop guidance could be used. But in reality, unknown variations in the state of the vehicle and the environment forces the use of a closed-loop guidance in which the measured state of the vehicle is used as feedback. Also non-linearities and delays in the response can cause deviations and hence, forces the use of a closed-loop guidance.

Figure 3.10 shows a closed-loop guidance system and the guidance system generates steering commands based on the difference between the measured state and the desired reference state. The system takes into account the trajectory constraints and the desired final state (Mooij, 1998). The guidance system must generate state commands which will results in a trajectory that reaches target conditions despite continuous changes in the vehicular and environmental conditions. Next to the commanded state, the guidance system can also generate some commanded actuator states such as trim deflections and speed brake deflections. These are not used as an input for the controller, but are immediately fed to the actuators. As already stated, the guidance system and its guidance algorithms need information about the current state of the vehicle. This is provided by the navigation system.

Navigation

The navigation system measures the actual state of the vehicle and produces a measured state. This is done using sensor information and predefined theoretical models. Due to several errors resulting from measurement inaccuracies or model mispredictions, the measured state is not equal to the actual state. The state of the vehicle consists of the position, velocity, attitude and angular rates. Other parameters required by the guidance and/or control system may include the forces and moments, information about the environment and deduced parameters like the total energy of the vehicle and components of the lift vector (Mooij, 1998).

Control

The control system transforms the commanded state generated by the guidance system in commanded actuator (control surfaces) deflections based on the difference between the measured state and the commanded state. Thus, it is the task of the control system to carry out the steering commands as given by the guidance system, such that the actual state approaches the desired and commanded state in a certain, limited amount of time, and to assure that the state remains stable (Mooij, 1998). Again, information about the state of the vehicle is provided by the navigation system.

3.5.2 Simplified GNC system

The total GNC system is very complex. During this study, only the guidance system will be considered in more detail. Therefore, a perfect navigation system and control system will be assumed. These assumptions considerably simplify the GNC system, see figure 3.11.

As stated above, due to several errors in the navigation system, the measured state is not equal to the actual state. A perfect navigation system implies that these errors are neglected and hence, the measured state is equal to the actual state vehicle. This means that the actual state of the vehicle can directly be used as the input for the guidance system.

In reality, due to the inertia of the vehicle, the commanded state is not reached immediately but needs a finite amount of time to reach the commanded state. An ideal controller is a controller which generates actuator deflection commands that result directly in the desired attitude of the vehicle. Also, any errors (control and deflection errors) that might occur, are neglected. As the commanded attitude is reached immediately, this means that the actual state is equal to the commanded state.

These assumptions effectively remove the control, the actuator and the navigation block from the system as well as the inner loop because the commanded state, the actual state and the measured state are all equal.

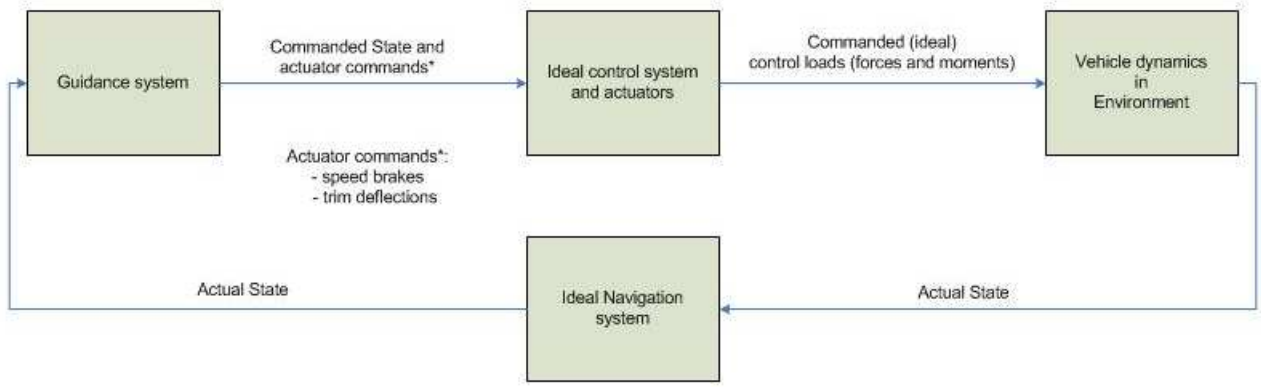

Figure 3.11: Simplified GNC system

3.6 Simulation model to study the terminal area

In reality, the real vehicle is moving the real environment. To study the trajectory of a vehicle in the terminal area and the performance of a guidance system, a simulation model is needed. The simulation model as used in this study is shown in figure 3.12 and relies on state-vector propagation.

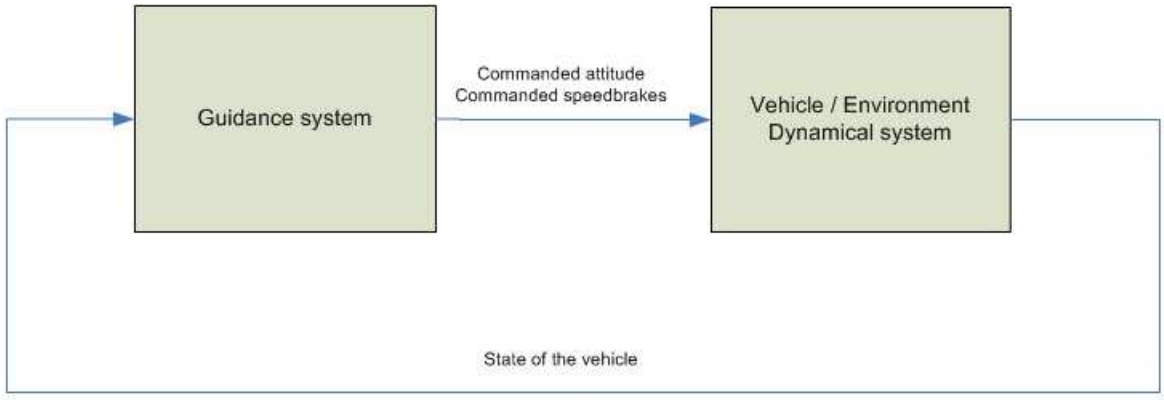

Figure 3.12: Schematic view of simulation model

The guidance system computes the commanded attitude (angle-of-attack and bank angle) and the commanded speedbrake deflection. Using the assumption of an ideal control system, the commanded attitude and speedbrake deflection can be used directly as the input to the model that describes the motion of the vehicle in the Earth's environment. Because of the assumed ideal navigation system, the measured state is equal to the actual state. Hence, the actual state can be used directly as the input to the guidance system. Due to the assumptions as stated in section 3.5.2, both the navigation and the control system are effectively eliminated.

The commanded attitude and the commanded speedbrake deflection specified by the guidance system is used to calculate the lift and drag coefficients, using the HORUS model as described in this chapter. These coefficients are then used to calculate the forces on the winged re-entry vehicle. Next, the state derivatives (accelerations) due to these forces are computed by substituting the forces in the differential equations of motion, which describe the mathematical model of the vehicle motion, see section 2.5. Also the gravitational forces and parameters resulting from the atmospheric model, as described in section 2.3, are substituted in the equations of motion. By using numerical integration of the state derivatives, a new state can be calculated which will be used again as an input to the guidance system. In this study, the RK45 method is used as the interpolation method, see appendix B for more information.

Note that during the trajectory optimization as described in chapter 7, the guidance system as depicted in figure 3.12 is in essence an open-loop guidance system. The control variables are specified as a pre-flight or pre-simulation determined vector. These values are used during the simulation without altering these values. The actual state of the vehicle does not influence the command vector. However, during the design of guidance algorithms as described in chapter 9, the guidance algorithm does calculate the commands based on the actual state and hence, can be considered as a closed-loop system.

Chapter 4

Optimization

Optimization is an essential part in the thesis study. First, optimal terminal area trajectories must be calculated. Then, guidance algorithms are optimized to approximate the optimal trajectories. During the literature study preceding this thesis work, an extensive discussion was presented on optimization techniques. In this chapter, a summary of this discussion is given. In section 4.1, the general optimization problem is discussed. Section 4.2 gives an overview of numerical optimization techniques. Different types of optimization problems related to the terminal area are discussed section 4.3. During the terminal area study, a genetic algorithm is used as the optimizer. More information on this optimizer is given in section 4.4. Finally, the actual optimization problem, OPTIDUS, is discussed in section 4.5.

4.1 General optimization problem

The general optimization problem is to find a set of parameters $\bar{x}$ or design variables, which minimize or maximize a system characteristic that is dependent on $\bar{x}$. The vector $\bar{x}$ is defined as:

$$\bar{x} = (x_1, x_2, ..., x_n)^T \tag{4.1}$$

The objective function $f(\bar{x})$ to be minimized or maximized might be subject to constraints in the form of equality constraints and inequality constraints. These constraints limit the solution space and determine the feasible solution space $\mathbf{X}$. The design variables $\bar{x}$ can also be bounded by lower and upper limits.

The minimization problem has the following form:

$$min\ f(\bar{x}) \tag{4.2}$$

subjected to respectively the equality constraints and the inequality constraints:

$$g_i(\bar{x}) = 0,\ for\ i = 1, 2, ...j \tag{4.3}$$

$$g_i(\bar{x}) \geq 0,\ for\ i = j+1, ..., m \tag{4.4}$$

where j is the number of equality constraints and $m - j$ is the number of inequality constraints. The number of equality constraints is always smaller or equal to the number of parameters x_i. Although the optimization problem has been stated as a minimization problem, there is no fundamental difference between minimization and maximization.

A distinction is made between static and dynamic optimization problems. Static optimization is frequently referred to as parameter optimization. In contrast to dynamic optimization, the system variables $\bar{x}$ of a static optimization are not time varying (Visser, 2007).
The optimization problems related to the terminal area are dynamic, so focus will be on this type. More information on static optimization can be found in (Visser, 2007).

Except for simple problems which can be solved analytically, the solution to more complex problems can only be obtained by using a numerical method. The terminal area is a complex problem so numerical optimization techniques will be used. The next section gives an overview of the different numerical optimization techniques.

4.2 Overview of numerical optimization techniques

This section gives a short overview of optimization techniques that can be used to solve general optimization problems. In the next section, more information is given on optimization problems related to terminal area studies.

The numerical optimization techniques can be split into two major classes: local and global optimization techniques. The difference between a local and global optimizer can be explained using figures 4.1(a) and 4.2(b).

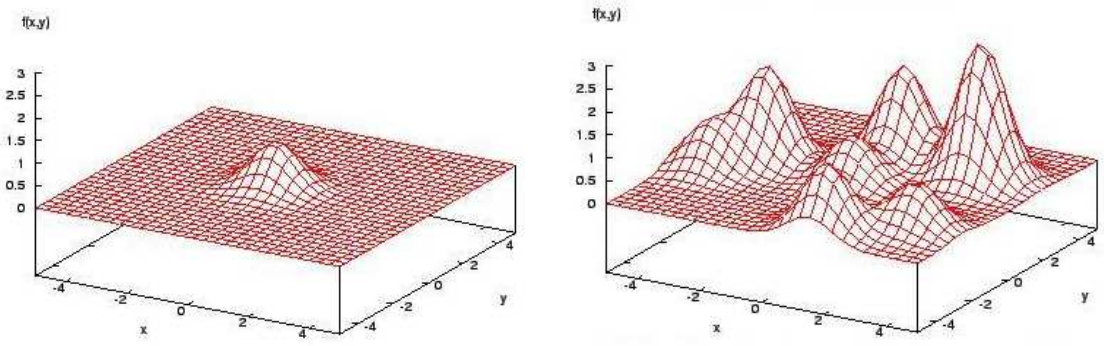

(a) (b)

Figure 4.1: Difference between local and global optimum. [http://www.msm.cam.ac.uk/phase-trans/2006/ga_html_files/ga.html]

A local optimizer will have no problem in finding the optimum of the function as shown in 4.1(a). For more complex functions as indicated in figure 4.2(b), a local optimizer may miss the target (the highest peak) when the search algorithm starts in the neighborhood of a lower peak. Global optimizers have the potential to find the global optimum.

Both local and global optimization techniques can be further classified into different methods, based on (Noomen, 2007):

- Local optimisation techniques
  - Gradient based methods or calculus based methods
    - Steepest Descent
    - Newton's method
- Global optimisation techniques
  - Enumerative methods
    - Nested do-loop
    - Dynamic Programming
    - Genetic Algorithms
    - Simulated annealing
    - Particular Swarm optimisation
    - Differential evolution
  - Random methods
    - Monte Carlo

4.2.1 Local optimization techniques

Although the local optimization techniques are restricted to a certain region in the solution space, in general they are more accurate than the global techniques. A local optimizer solves the optimization problem as described by equations 4.2, 4.3 and 4.4 by calculating improvements of some initially estimated $\bar{x}_0$ to converge toward an optimal design parameter set or design vector of $\bar{x}$. All numerical methods to solve optimization problems incorporate some type of iteration. This iteration can be stopped when some criterion is met. Improving an initial solution guess toward the optimum is done using gradient information hence the name Gradient Techniques.

The steepest descent or gradient descent and Newton's method are the two most widely used gradient based techniques. In a steepest descent method, only first-order partial derivatives of the objective function at the current guess (Jacobian matrix) are used to obtain the direction of search. This direction is called the direction of steepest descent. In Newton's method, also second-order derivative information (Hessian) is used and the corresponding direction of search is called the Newton direction. Newton's method works well for relatively simple problems with a sufficient accurate initial guess of the solution. More complex optimization problems and optimization problems where a good initial guess is not available should be solved using more robust schemes, such as a Quasi-Newton method (Demeyer, 2007).

Problems described by equation 4.2 and subjected to constraints as given by equations 4.3 and 4.4 can be solved numerically by using the gradient techniques described above. Problems of this type where the objective function and the constraints are nonlinear functions of the design variables are called NonLinear Programming (NLP) problems. Optimal Control concerns the optimization of a trajectory and may be seen as an extension of NLP problem. More information about NLP can be found in (Betts, 1998) and (Visser, 2007).

4.2.2 Global optimization techniques

Global optimization techniques are not restricted to a certain region in the solution space and have the task of finding the absolute best value. They can be used to find the highest peak shown in figure 4.2(b) or to bring the solution as close as possible to this peak, without getting stuck at a smaller peak.

Random methods

Random methods search for the optimum using random trial and error. A random set of possible solutions is initiated and all these are evaluated with respect to the objective function. The solution which optimizes the objective function is saved and accepted as the best solution. A global Monte Carlo is an example of a random search method.

Random methods have two disadvantages. In these methods, randomness is the driving force. Another disadvantage is that random methods may need many simulations. This make the method inefficient for large problems (Goldberg, 1989). It is often more efficient to use pseudo-random methods. These methods are discussed in the next section.

Note that also a local Monte Carlo analysis exists. In this case, the MC method is performed around the best solution obtained from another global optimizer. The optimal solution is refined by making small changes to the best solution and save the best set of small changes.

Enumerative methods

The basic idea behind enumerative methods is straightforward: calculate the value of the objective function at every point (if the search space is discrete) in the search space one by one and save the best solution. This method is called a (nested) do-loop and is a simple but inefficient method for large problems, because of the large search space (Goldberg, 1989). To solve for this inefficiency, more advanced methods were obtained.

As indicated above in the overview scheme, several advanced methods exist.
Dynamic programming breaks the problem down into problems of moderate size and complexity, but it still requires a large amount of storage capability and therefore is unattractive for large problems.
Differential evolution (DE) is based on updating each element of the population of feasible solutions by using the weighted difference of two or more other randomly population elements (Vinko, Izzo, & Bombardelli, 2007).
Particle Swarm Optimization (PSO) is also a population-based algorithm inspired by the social behavior of bird or fish flocks. Each element evolves by taking the combination of the current global best solution and the individual best solution into account (Vinko et al., 2007).
Genetic Algorithms (GA) are based on biological evolution. The fittest individuals survive and the weakest are removed from the population. The goodness of an individual in the population is measured by its fitness value (value of objective function). A GA evaluates the fitness of each individual in the population and if no convergence is yet reached, individuals are selected for reproduction to generate new offspring. More information on genetic algorithms can be found in section 4.4.
Simulated Annealing (SA) mimics the annealing of metal and uses random processes to help

guiding the search for minimal energy states.

It is important to note randomized techniques such as GA and SA are to be separated from the random search method (Goldberg, 1989). In randomized techniques, random choice is used in a directed search process while random search methods take undirected random points.

4.3 Optimization problems for the terminal area study

In the terminal area study as described further in this thesis, two types of optimization problems are encountered:

- optimization of the trajectory
- optimization of the guidance algorithm

Both optimization problems are discussed below.

4.3.1 Optimization of the trajectory

The problem of trajectory optimization is a non-linear problem which is described by ordinary differential equations, in the following state-variable form (Visser, 2007):

$$\dot{\bar{x}} = \bar{f}[\bar{x}\,(t)\,, \bar{u}\,(t)\,, t] \tag{4.5}$$

where $\bar{x}(t)$ contains the state variables and $\bar{u}(t)$ contains the control variables.

Both the state and the control variables may be subjected to certain physical constrains. These constraints are called the path constraints. A control history which satisfies the control constraints is called an admissible control and a state trajectory which satisfies the state variable constraints is called an admissible trajectory (Visser, 2007). Also boundary constraints are present, which specify the initial conditions and the required final conditions.

Starting from an initial state and applying a control $\bar{u}(t)$ causes the system to follow some trajectory and by using a performance criteria, a unique real number is assigned to each trajectory. The trajectory optimization problem or optimal control problem can be stated as follows (Visser, 2007):
From among all admissible control functions $\bar{u}$, find the one which optimizes the performance criteria, subjected to the dynamic constraints and all initial and terminal boundary conditions that may be specified.

The particular control function $\bar{u}^*(t)$ that minimizes J is called an optimal control and the corresponding state history $\bar{x}^*(t)$ is called an optimal trajectory. In an optimization scheme, the design variables (here the control functions) are usually the input to the state equations which describe the dynamics of the system. After an evaluation of these equations, the objective function is evaluated to judge the acceptability of the set of proposed design variables.

Local trajectory optimization

In optimal control theory, local trajectory optimization techniques are used to determine an optimal trajectory for a specific initial state. The optimal control problem may be interpreted as an extension of the nonlinear programming problem to an infinite number of variables (Betts, 1998). Optimal control theory determines the optimal $\bar{u}^*(t)$ for a specified initial state. This is an open-loop, because this $\bar{u}^*(t)$ is obtained for one specific initial state. Any point directly on the obtained optimal trajectory can serve as the initial state and use the same $\bar{u}^*(t)$. But if a control vector needs to be found to take the system to the required final conditions starting at a point not directly on the optimal path, a new optimal problem must be solved with a new initial state.

Direct and indirect methods are two methods which are widely used to solve an open-loop trajectory optimization problem. In a direct approach, the optimization problem is interpreted directly as a nonlinear programming problem. A direct method discretizes the control variables and/or state variables and directly computes the state variables and hence the performance index and the constraints (Mora & Martin, 1995). An indirect method avoids the parameterization by using a calculus of variations approach (or Pontryagin approach) to the optimization problem. This leads to the Two Point Boundary Value Problem (TPBVP). Both direct and indirect methods start with an initial guess and use an iterative process in which the search direction is found with one of the methods as described in section 4.2.1, in combination with shooting, multiple shooting or collocation methods. In this thesis, a global optimization technique is used to calculate the open-loop optimal trajectory and hence, no further information is given about local trajectory optimization techniques. The interested reader can find more information on direct and indirect methods in (Visser, 2007), (Betts, 1998), (Mora & Martin, 1995), (Alemany & Braun, 2007) and (Demeyer, 2007).

Global trajectory optimization

Local optimization techniques require an initial guess and the accuracy of the obtained optimal solution depends on this initial guess. A global optimizer can be used to generate this initial guess which is already in the neighborhood of the real optimum. Since no global optimizer has been used yet for terminal area studies, it is not possible to say which global optimizer is the best one for this type of problem. In the past few years, the Astrodynamics and Satellite section has gained a good knowledge about genetic algorithms, so therefore a GA will be used as the global optimizer for the thesis work. OPTIDUS is an optimization tool, using a evolution algorithm method, which is developed at the Astrodynamics and Satellite section.

Although a GA was never used to optimize terminal area trajectories, it was used to an atmospheric re-entry problem, corresponding to the phase before the TAEM phase. In (Yokoyama & Suzuki, 2003), a modified genetic algorithm is used to find an appropriate initial solution which is then used as an input to a gradient based direct method. The modified GA uses a different approach for the selection method instead of the conventional fitness function. The used direct method is a Direct Collocation (DC) method with sequential quadratic programming. After testing the method for a simple problem, it was used to optimize the re-entry trajectory of a space plane. Figure 4.2 shows the calculated optimal values for the angle-of-attack, the bank angle and the heating rate as a function of time for both the GA and the DC. These results indicate that the modified GA approaches the vicinity of the optimal solution and is reliable to find an initial solution for a local gradient-based trajectory optimizer. In the GA, the control variables were

represented as discrete values at specific time intervals. The control variables at an arbitrary time in between two discrete values are determined by a cubic spline interpolation method.

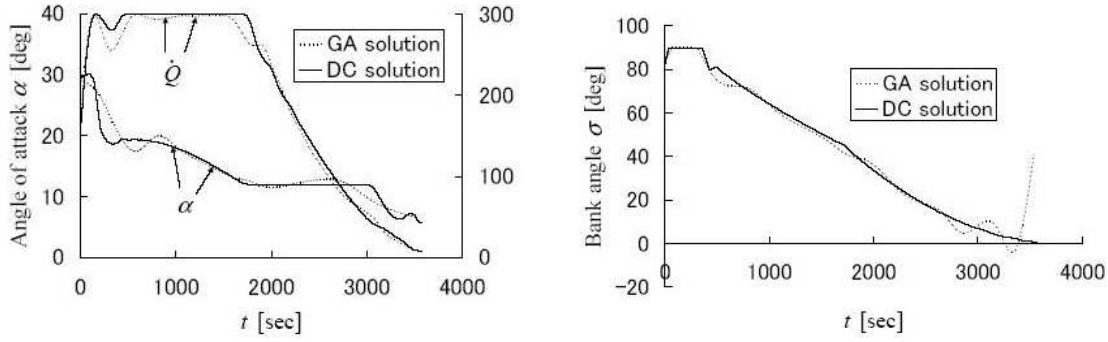

(a) (b)

Figure 4.2: (a) Time history of the angle-of-attack and heating rate (b) time history of the bank angle (Yokoyama & Suzuki, 2003)

During this thesis work, time does not permit to implement both a genetic algorithm and a local optimizer. Hence, all the optimizations will be done solely by using a GA. Only for one specific case, a simple local Monte Carlo will be used to slightly improve the results, see section 8.1.2.

4.3.2 Optimization of the guidance algorithm

The optimal control variables that will be found by using a GA are still open-loop because they are only valid for a specific initial state and all states situated on the optimal trajectory. A new initial state requires the calculation of a new optimal trajectory and corresponding control variables. It would be better if a control vector $\bar{u}^*(t)$ would be found which is not only a function of time but also a function of the initial state. Such a control vector is called an optimal feedback control law and is in closed-loop form. Thus the optimal open-loop control is optimal only for a particular initial state value, whereas, if the optimal feedback control law is known, the optimal control history starting from any state value can be generated (Visser, 2007).

Most off-line or simulation applications do not require a closed-loop control solution. Hence the open-loop GA can be used to for initial simulations of winged re-entry vehicles and analyzing and estimating their performance. The influence of off-nominal situations on the control history and the trajectory can be studied by calculating a new open-loop trajectory for these new conditions. However, in on-line real time applications, closed-loop controllers are required. Closed-loop controllers use information on how the process evolves and therefore are able to reduce the effect of changes in initial conditions, disturbances and variations during the flight. Open loop-controllers do not have access to any information concerning the process except for what is available before control starts and compensation for the effect of disturbances is therefore not possible (Visser, 2007).

Dynamic programming is a method introduced by Bellman and can be used to obtain such an optimal feedback control law. But the great drawback of dynamic programming is, as Bellman himself calls it, the curse of dimensionality. Even for moderate complicated problems, the

solution requires an enormous amount of storage space. So although this optimization technique gives the required control variables as a function of time and many different initial states, it is practically not possible to use this technique for the terminal area problems. The development of exact optimal feedback control laws is usually out of reach for nonlinear systems of any practical significance (Visser, 2007).

Another solution is to use a reference trajectory in combination with a tracking algorithm. This tracker algorithm consists of a guidance law that takes into account disturbances during the flight and variations in the initial states. Based on information during the flight, the guidance law will generate commands such that the reference trajectory is followed as close as possible. Guidance systems are discussed in more in detail in chapter 9. The guidance law contains gains and these gains will be optimized by the GA. Based on the optimal trajectories resulting from the open-loop GA simulations, a reference trajectory is selected and gains are optimized such that this trajectory is followed as close as possible. The reference trajectory may be either obtained on-board (on-board planning algorithm) or pre-flight by off-line open-loop calculations that are stored in an on-board computer.

In case of off-nominal conditions (changes in initial state), the guidance system must still be able to calculate the correct commands. A robust guidance system is a guidance system that can handle a large amount of off-nominal conditions. The robustness of the system can be investigated by performing a sensitivity analysis. Two approaches to this sensitivity analysis can be used. A first option is to do simulations with off-nominal conditions, using the guidance system obtained for the nominal trajectory and to investigate the end conditions. If the guidance system is still able to calculate the correct commands, the guidance system is robust. Another option is to calculate a new optimal trajectory for the off-nominal conditions and to calculate new gains based on this new optimal trajectory. If these gains are close to the earlier obtained nominal gains, the system is robust. But large differences between the gains means that even a small deviation in initial conditions requires a new guidance system (new gains). For each new initial condition, a new guidance controller is needed and hence, a single guidance system (single set of gains) is not a robust system. So an optimal system for a specific set of initial conditions might not be a robust system. A technique called robust design is an optimization process based on off-nominal conditions and can be used to design a robust guidance. In robust design, the optimization and the sensitivity analysis are performed simultaneously. This technique, in combination with a GA, and results in sub-optimal gains that can be easily implemented on-line and allows HORUS to fly as close as possible to the optimal trajectory when off-nominal conditions occur. The optimization of the gains of the guidance law is described in chapter 9.

4.4 Genetic algorithms

Evolution based algorithms have a population of potential solutions and by using a selection process based on the fitness of individuals and some genetic operators, a new and fitter population is obtained. A Genetic Algorithm (GA) is such an evolution based algorithm. It mimics the nature its own search system, evolution, to find an optimum. The working principle of a GA is based on the principle of *survival of the fittest*. Genetic Algorithms (GAs) are global function optimizers and can be used to find a global optimum value of a discrete parameter or of a set of discrete parameters. During the thesis, only single-objective optimization is used. The goal is to optimize a single cost function or objective function during each optimization run. Hence, multi-objective optimization will not be part of the discussion below.

This section, section 4.4, gives an basic overview of the different elements that are present in a GA. Section 4.5 gives an overview of the elements as used in OPTIDUS.

4.4.1 Basic scheme of GAs

It is already stated that GAs mimics nature's evolution. This can be illustrated using an example as given by (Michalewicz, 1996). Take a population of rabbits at a given time. Some rabbits are faster and smarter than others and these rabbits have a lesser chance of being eaten by foxes, so more of them survive in comparison with slower and dumber rabbits (selection). But of course, some of the slower and dumber rabbits will also survive. The surviving population starts breeding and genetic material is mixed (crossover). In addition, once in a while a bit of genetic material is mutated (mutation). The resulting baby rabbits (offspring) will on average be faster and smarter than the previous generation.

This principle can be applied in the optimization problem. A GA starts with generating an initial population. Using several operators, the fittest individuals of the population are chosen to produce offspring. After several generations, the population has evolved in fitter individuals and the evolution is stopped when a stopping criteria is met. Figure 4.3 gives a schematic representation of these basic steps of GA.

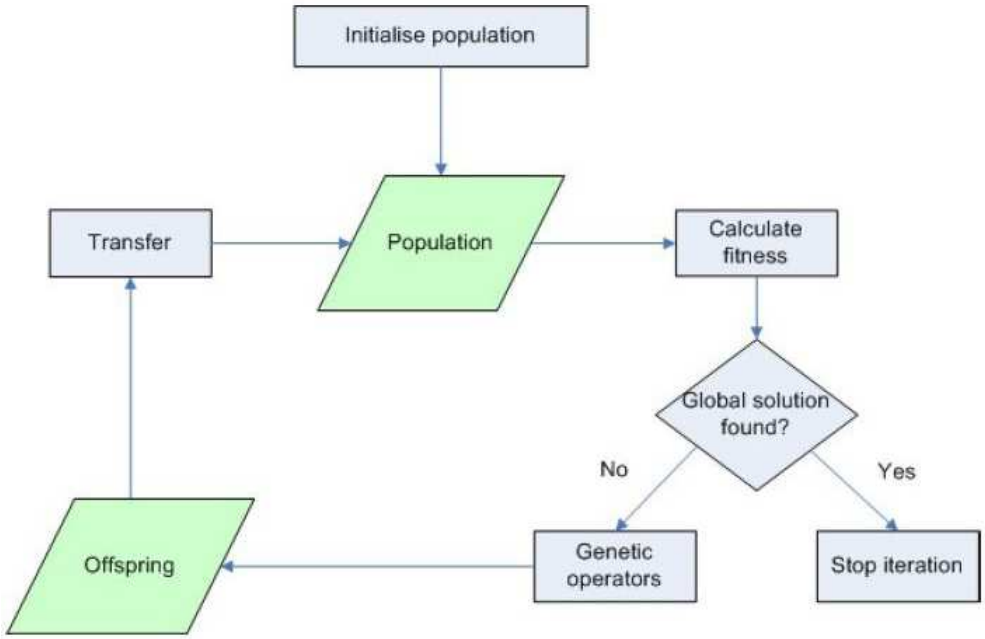

Figure 4.3: Schematic overview of basic steps of GA (Noomen, 2007)

A population consists of several individuals. Individuals are often called strings, genotypes or chromosomes (Michalewicz, 1996). An individual consists of units or genes arranged in linear succession. Other names for genes are features, characters or decoders (Michalewicz, 1996). The place where a gene is located in a chromosome is called the loci (string location).

The initial population of solutions is usually created at random but it can also be created

in a specific region were the optimum must be situated in (by using Monte Carlo). One has to take care that premature convergence does not occur due to specifying the initial population in a solution interval around a local optimum. Another reason for premature convergence is genetic drift. Genetic drift is an evolutionary process of change in the gene frequencies. These gene frequencies can differ throughout subsequent generations due to the stochastic nature of selection in which purely chance events determine which gene will be carried forward while others disappear. Genetic drift can cause gene variants to disappear completely and thereby reduce the genetic variability. This effect is especially important in small populations.

An evolution run on a population of individuals corresponds with a search through a space of possible solutions. This search requires the balance between exploiting the best solutions and exploring the search space. This is the essential difference between GAs and other global or local optimizers. A Gradient-Descent methods is a strategy which exploits the best solution for possible improvements but it neglects exploration of search space. A random search method on the other hand explores the search space but ignores the exploitation of the promising regions (Michalewicz, 1996).

Although GAs are suitable to find a global optimum, it does not mean that a global optimum is always found. There are two pitfalls: the global optimum can be surrounded by bad solutions (deception) and premature convergence, where convergence will take place too rapidly because only a part of the solution space is exploited, resulting in important information getting lost. In order to get a robust GA, a good balance must be found between the selective pressure and the population diversity. The concept of selective pressure is a measure of importance that is given to strings with a high fitness. High selective pressure means that strings with a high fitness have a large probability of being selected while the probability of being selected for strings with lower fitness is considerably smaller. Low selective pressure means that the difference between the probability of being selected between string with a high fitness and a lower fitness is smaller. The concept of population diversity is measure of how much the solutions or individuals are spread out in the solution or search space. A high population diversity means that the solutions are well spread out. It is not a surprise that these two concepts of selective pressure and population diversity are conflicting. High selective pressure means low population diversity and vice versa. A robust GA is a good balance between these two such that no information or search region is missed in the solution space but is also able to exploit the best solution. In order to control the balance, the user is able to control the selective pressure by using different selection schemes.

4.4.2 Classical genetic algorithm

The foundation of classical genetic algorithms is primarily the work of Holland and is further described in (Goldberg, 1989) and in (Michalewicz, 1996). This section describes some important concepts of GAs. These concepts are extended in the next section.

String representation

The goal is to find the control variables which optimize a function. The control variables are represented in a string. A string consists of different control variables, which are written next to each other. One string represents one combination of the control variables and a single string is one element of the population. The classical GA uses a coded representation of the variables

and represents the variables as a binary string (Goldberg, 1989). The binary representation is sufficient for theoretical analysis and can be used in combination with simple genetic operators, but it has some drawbacks for more complex and high precision problems. For such a problems, the length of binary string can become very large and this increases the computational time. Therefore, a real-coded or Floating-Point (FP) representation will be used for these problems. This FP representation will be discussed in section 4.5.

Initial population size

It was already stated that the initial population is generated randomly. In a classical GA, this corresponds to randomly selecting 0 and 1 for each gene of an individual. An important choice in the generation of an initial population is the size of the population. If the population is too small, the GA may converge too quickly. On the other hand, if it is too large, the waiting time for an improvement might be too long. If a quick estimate of the optimal solution is required, a small population size could be used. But if it is important to find the absolute optimum, larger populations are required. A good balance has to be found. The complexity of the problem itself also influences the choice of the initial population size.

Fitness function

The fitness function is used to evaluate the the quality or performance of an individual and is often equal to the objective function of the problem. In case of trajectory optimization, a simulation is made of the trajectory using the control variables given by a particular individual as an input. The output of the simulation determines the fitness of the individual.

Operators

The classical GA uses three main operators: selection, crossover and mutation. The purpose of these operators is to create new individuals to form a new population based on the old population.

The selection operator is the operator that decides which individuals or strings are going to be part of the mating pool, which is the group of strings that are going to be used by other operators to produce offspring. The selection can be done randomly or can be based on the fitness function. A common selection method in the classical GA is the so-called biased roulette wheel selection. Each individual in the population has a chance of being selected proportional to its fitness. This can be visualized as a roulette wheel where the size of the slots are proportional to the fitness. An individual with a higher fitness has a larger slot size. This is illustrated in figure 4.4 for a population of four individuals. By spinning the wheel, the mating pool is filled with individuals. An ndividual with a higher fitness has more chance of being selected.

The recombination operator is the operator that builds a new population from the individuals in the mating pool. Classical GA uses crossover. Two parents are taken and offspring or children are created by exchanging parts of the string of the parents. This process will be illustrated for a floating point representation in section 4.5. It is possible to use a one point crossover or to use multiple crossing sites. The location of the point or sites is done randomly. The number of crossovers is determined by the recombination probability, which can be specified by the user.

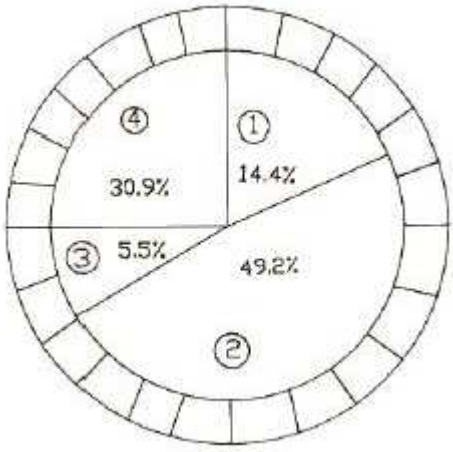

Figure 4.4: Biased roulette wheel selection (Goldberg, 1989)

After the new population has been formed, a mutation operator can be used to alter some genes of some individuals. In a classical GA, this corresponds to changing 0 into 1, or vice versa. Each gene of each individual has the same mutation probability. Mutation produces a slightly different offspring and is a protection system against genetic drift and premature convergence.

Constraint handling

An optimization may be subjected to equality and inequality constraints. The solution space defines a certain region in the search space for which the constraints are met. Several procedures exist to account for these constraints.

One option is to include a penalty function to the objective function. If an individual violates a constraint, then a penalty is subtracted from the fitness function of the individual. This penalty might be a constant value or it might be proportional to the degree of violation. A second option is to introduce the so-called death penalty. Infeasible individual are eliminated from the population. The drawback is that these solutions can never contribute to the production of new generations. A third option is to use special operators and apply a technique called preselection. For each new created individual, it is checked whether this individual is feasible or not.

4.4.3 Modified GAs or Evolution Programs

As already stated, the classical GAs do not perform very well when more complex problems are encountered. Therefore, modified GAs are used for these problems. Modified genetic algorithms are called Evolution Programs (EP). The basic difference between a classical GA and an EP is the manner in which they approach the problem. The classical GA operates on binary strings and requires a modification of the original problem into an appropriate form. The potential solutions (population) have to be transformed to a binary representation and decoders and repair algorithms are required (Michalewicz, 1996). Usually this is not an easy task and when a high accuracy is needed, the length of a binary string can become very large.

Evolution Programs, on the other hand, leave the problem unchanged and modify genetic operators instead. This is the best approach for complex problems.

Floating-point representation

In a modified GA, a real-coded or Floating-Point (FP) representation is used. The variables of an individual are represented in an array of real numbers. Assuming that the control variable is described by six parameters, the FP representation of an individual with six independent variables then looks like:

$$P_1 = [a_1\ b_1\ c_1\ d_1\ e_1\ f_1] \tag{4.6}$$

The most important advantage of a FP representation is that the variables can have a high accuracy without the need of large strings.

Modified selection

The biased roulette wheel selection method (a stochastic selection method) can also be used for the floating-point representation, but the drawback of this method is that it is vulnerable to genetic drift and hence contributes to premature convergence. One way to solve this problem is to count the number of selections of a certain individual. If this exceeds a particular number depending on the fitness of the individual, then this individual can no longer be selected. Another option is to use other selection operators which provide the ability to control the selective pressure. In a ranked based selection method, the individuals are ranked according to there fitness and the selection probability is a function of the rank. Using a tournament selection, a number of individuals are randomly taken out of the population and the fittest individual is selected to produce offspring. Other methods include stochastic sampling and stochastic universal sampling (Michalewicz, 1996).

Modified recombination

The crossover method can also be used as the recombination method in floating-point represented individuals. This is illustrated for a single point crossover. If two individuals, given in the form of equation 4.6, are selected for recombination, the resulting two children look like:

$$C_1 = [a_1\ b_1\ c_1\ d_1|e_2\ f_2] \tag{4.7}$$

$$C_2 = [a_2\ b_2\ c_2\ d_2|e_1\ f_1] \tag{4.8}$$

The point or location where the crossover occurs is chosen randomly. In this example, the point is located after the fourth gene. Also multiple crossing sites are possible.

Other recombination methods include arithmetical crossover and heuristic crossover. Using arithmetical crossover, the offspring is a linear combination of the parent individuals. The value of a gene of a children is between the values of the genes of the parents at the corresponding gene location. The heuristic crossover operator produces only one child and it can be even possible that no offspring is produced at all. This operator uses the value of the fitness or objective function in determining the direction of the search and hence, it contributes to the local fine tuning by searching in the most promising direction.

Modified mutation

Using the floating-point representation, several options exist for a mutation operator. A uniform mutation is similar to the type as used in the classical GA for a binary representation. If a gene in an individual is selected for mutation, it is replaced with a value specified between a specific interval, depending on the control variable constraints. Boundary mutation is similar to uniform mutation, except that if a gene is selected for mutation, the value is replaced by an extreme value of the boundary interval and not a value in between. Using non-uniform mutation, the probability of mutation depends on the position of an element in the individual and the generation number. For this type of mutation, the effect of mutating an element decreases over time.

Other operators

Other operators that are used in EP include immigration and elitism.

Immigration is an operator that brings new individuals into the population. These individual are randomly created and added to the population. The percentage of the new population that will be filled by immigration can be determined by the user. Immigration is used to ensure the diversity of the population and hence helps to avoid premature convergence.

Elitism is an operator that assures that the best individuals or several best individuals are automatically copied to the next generation to keep good individuals in the population. This operator improves local search at the expense of global perspective (Goldberg, 1989).

Varying population size and adaptive GAs

It was already stated that a good balance between population diversity and selective pressure is needed to have a robust GA. A method to influence both population diversity and selective pressure, is to vary the population size. Genetic algorithms using variable population size are called GAVaPS and in this method, the concept of age is introduced. Every individual in the population can be chosen to produce offspring, independent of its fitness. Instead, the age of an individual and its lifetime parameter are used. Age corresponds to the number of generations that the individual is present in the population and the lifetime parameter is assigned to an individual when the individual appears in the population for the first time. The lifetime parameter for a specific individual remains constant throughout the optimization process. Each generation, the age of the individuals is increased by one. When the age exceeds the lifetime of an individual, the individual dies and is removed from the population. In this way, the population size is varied.

There exist several methods to allocate a value to the lifetime parameter. In order to introduce selective pressure, the lifetime allocation should reinforce the individuals with above-average fitness and tune the size of the population to the current stage of the search. The lifetime allocation methods include proportional allocation, linear allocation an bi-linear allocation.

Normally, the user has to specify the probabilities of crossover and mutation, together with the population size. In adaptive GAs, the GA is capable of steering these parameters. So next to a variable population size, also two other parameters which determine the number of crossover and mutation can be varied by the adaptive GA.

Genetic operators to approximate Gradient-Descent

Global optimization methods are suitable for large-scale and complex problems, but they require many function evaluations to obtain acceptable optima. Local methods find only optima close to the starting point. One can try to combine the advantages of both methods to overcome the individual shortcomings (Lee & Roh, 2001). It should be noted that a gradient-descent technique is most effective in linear regions. Most search spaces are non-linear, but many non-linear spaces can be assumed to be linear when considering only a much smaller subspace of the search space. If a genetic algorithm can evolve a solution to the neighborhood of an optimal solution, then a gradient technique can be very effective in finishing the search process (Ranasinghe, 2003).

It was stated earlier that an heuristic crossover operator contributes to the local fine-tuning by searching in the most promising direction. Two other modified operators exist which can be used to approximate a local gradient-descent method. (Lee & Roh, 2001) discuss a modified crossover operator that uses gradient information, while (Ranasinghe, 2003) discusses the use of a Gradient-Descent Mutation (GDM) operator as an extension to the standard mutation operator.

4.5 OPTIDUS

The Optimization Tool for Interplanetary trajectories by Delft University Students or OPTIDUS is an optimization tool which uses an adaptive genetic algorithm. Till now, the main application for this tool was the optimization of interplanetary missions and trajectories. In this thesis, the same OPTIDUS program will be used to optimize trajectories and guidance algorithms for a winged re-entry vehicle in the terminal area. OTIDUS is complete designed by students of the Astrodynamics and Satellite Systems section of the Delft University of Technology. Many students have contributed to this algorithm.

The version of OPTIDUS as described below is the latest version as used in (Spaans, 2009). The GA as designed in (Spaans, 2009), will be used in the rest of this thesis as the standard algorithm to perform optimizations. The internal structure of the algorithm is not changed and is considered as a black box. Figure 4.5 gives a schematic overview of the steps as used in OPTIDUS.

Generating initial population

The algorithm starts with generating an initial population. The individual are generated by using a random generator which generates a random value for each gene in an individual. The random is situated between the control variable boundaries as specified by the user. The population size is also specified by the user. Each generated individual is checked for its fitness. An unfeasible solution is eliminated and a new individual is calculated until a feasible individual is found. Hence, the constraints handling consists of a combination of preselection with the death penalty. The complete initial population consists of feasible solutions.

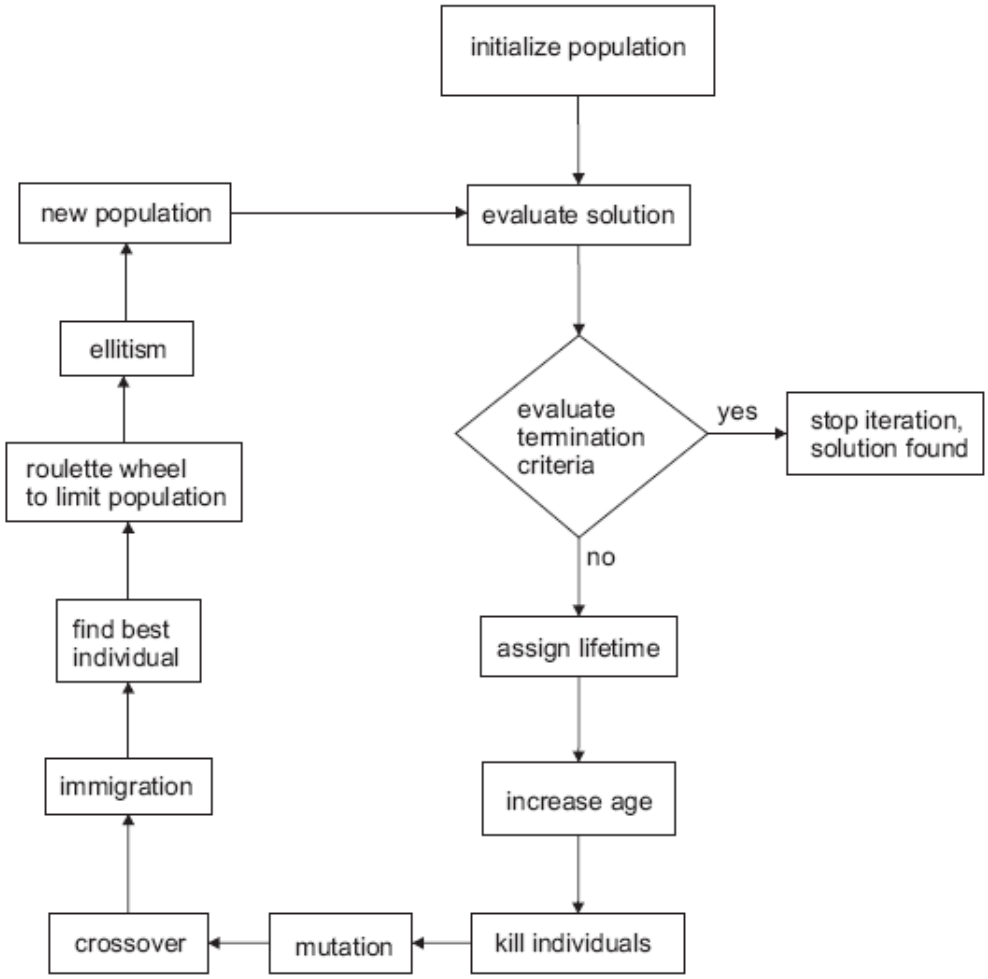

Figure 4.5: Flow diagram of OPTIDUS

Evaluate solutions

The fitness function is used to evaluate the performance of the individuals in a population. A value of the fitness function for a particular individual is obtained by performing a simulation with the control variables given by the individual as an input. The output of the simulation determines the fitness. In this step, the best solution from the population is searched for. The best solution is used to monitor the improvements of the next generations.

Evaluate termination criteria

Three termination criteria are used:

- number of generations without an improvement (convergence criteria)
- maximum number of generations
- maximum number of evaluations of the fitness (trajectory simulations)

If one of these criteria is met, the optimization run is stopped and an optimum is found. Of course, the intention is to stop the simulation only when the first criteria is met, because that determines if the solution has converged or not. The criteria above can be specified by the user.

Assign lifetime

Each individual is assigned a lifetime based on their fitness function. A lifetime is only assigned once to particular individual and occurs when an individual appears in the population for the first time. After the initial population generation, all individual get an assigned lifetime. In the population of next generations, lifetimes are only assigned to new individuals resulting from crossover, immigration and mutation. The lifetime is assigned using a linear allocation method. The minimum and the maximum lifetime can be specified by the user. The individual with the lowest fitness gets the minimum lifetime, while the individual with the best fitness gets the maximum lifetime. The lifetime for individuals in between is assigned using a linear scale.

Increase age and kill individuals

After a new generation is obtained, the age of all the individuals is increased by +1. Next, the age of each individual is compared with the assigned lifetime corresponding to that particular individual. When the age exceeds the lifetime, the individual is killed and eliminated from the population.

Mutation

On the remaining individuals, a possible mutation is performed. Each gene of each individual is tested for mutation by using a random generator. The chance of mutation can be specified by the user. If a gene is selected for mutation, a random generator determines if the current value will be increased or decreased. Another random generator determines the amount of change. This amount of change also depends on the number of generation. The maximum amount of change decreases as the number of generation increases. Hence, the effect of mutating an element decreases over time. This mutation operator corresponds to a non-uniform mutation. After a mutation occurred, the fitness of the individual is calculated to check if the mutated individual is feasible.

Crossover

The number of crossovers is determined by the user specifying a percentage of the population size. For each crossover, two parents are selected by a random generated. These two parents produce two children by using a single point crossover is described in section . The crossover point is also determined by a random generator. If the resulting children are not feasible, then two new parents are randomly selected until two feasible children are produced. Both the parents and the children stay in the population. Hence the population size is increased by 2 times the number of crossovers.

Immigration

In each generation, a number of new individual are introduced. The individuals are calculated in a similar way as described in 'Generating initial population'. The number of new individuals is determined by the user by specifying a percentage of the current population size. This changes the population size.

Roulette wheel selection

At this point, the population size differs from the original size because of the use of the age concept, the use of both the parents and the children and by using immigration. This system leads to a rapid increase of population size. To limit the population size, a roulette wheel was used. Before using this roulette wheel, the current best solution is searched and stored. The slots of the roulette wheel are determined by the fitness of each individual. The required population size determines the number of roulette wheel spinnings. During each spin, one individual is selected to go to the next generation by using a random generator. Note that a particular individual can be selected several times. Also, it is possible that an individual with a low lifetime is selected over an individual with a high lifetime due to the use of a randomness.

Elitism

If the best solution was not selected by the roulette wheel, the elitism operators assures that the best solution goes to the next generation. Hence the population size of a new generation can be at maximum equal to the required population size +1.

After the use of all these operators as stated above, a new generation is obtained and the cycle starts again until one of the termination criteria is met.

Random generator

In several of the steps described above, a random generator is used. The random number generator contains a function that returns a sequence of numbers that appear to be random. This function needs an initial value, called the seed. In case the same seed is used, the random generator will return exactly the same random number. Hence, although the numbers appear to be random, they actually can be predicted once the seed value is known. In the optimization run, the seed is specified before the iterative optimization process starts. If a same seed value is used for two similar trajectory optimizations, the outcome will be the same, because the random numbers are drawn in exactly the same sequence for each generation of the individuals, for selection of the crossover points and so on. If two optimization runs are performed with a different seed value, the outcome of the optimizations will be different. Hence, one seed value may provide better results than another value. This influence of changing the seed value was not investigated during the thesis and an arbitrary value of 8 is used. Knowing this fixed seed value, all the optimization results could be reproduced of needed.

User dependent parameters

Although OPTIDUS is considered as a black box and the internal structure is not changed during this thesis, it contains some parameters that can be adapted by the user. These parameters

were already mentioned in the description of the several steps, but a small summary is provided to get an overview:

- number of generations without an improvement (convergence criteria)
- maximum number of generations
- maximum number of evaluations of the fitness (trajectory simulations)
- population size
- chance of mutation
- number of crossover
- number of immigration
- minimum lifetime
- maximum lifetime

Next to these parameters, it is also possible to specify if a maximization or a minimization of the objective function is required. The first three parameters determine the termination criteria. In this thesis, a value of 90 generations is used as the convergence criterion. If no improvement is obtained for 90 generations, the solution is said to have converged and is used as the optimal solution. If a simulation is stopped because of one of the other criteria, the value for this criteria is increased, such that the convergence criteria is the main criterion to stop the optimization. The last two parameters determine the lifetime of an individual. A value of 3 and 7 were used for the minimum and maximum lifetime, respectively (Spaans, 2009). These parameters are not changed during the thesis. The values of the remaining four parameters are determined in a tuning analysis of the GA, which can be found in section 7.2.

Chapter 5

Terminal area guidance algorithms

The goal of the terminal area guidance is to properly manage the energy of the vehicle while aligning the vehicle with the runway. This is achieved by using a guidance algorithm that calculates guidance parameters that are used to influence the trajectory of the vehicle. These guidance parameters are described in section 5.1. A distinction between guidance systems is made on how the guidance parameters are calculated. This is discussed in section 5.2. Saab Space performed a study on the terminal area of HORUS (Helmersson, 1988b). This system is used as the baseline guidance algorithm in this study and is described in section 5.3. However, some improvements in this guidance system are possible. Therefore, two guidance systems that have actually been used in flight are studied. Section 5.4 describes the algorithm of the Space Shuttle, while the algorithm of the Russian Buran is given in section 5.5. In the last few years, several other terminal area studies have been performed. Section 5.6 describes some of these algorithms which are useful for this thesis study. Finally, section 5.7 summarizes the shortcomings of the HORUS guidance and indicates how these can be solved. Also a rational is give for the study objectives as used in subsequent chapters.

5.1 Guidance parameters

To guide the vehicle along a nominal trajectory, the path of the of the vehicle must be influenced. This can be done by changing the magnitude and direction of the control force which results in an acceleration or deceleration. The only force that is available to deflect the trajectory of an unpowered gliding vehicle is the aerodynamic force. The main components of this aerodynamic force are the lift force and drag force. The aerodynamic force is a function of the aerodynamic shape of the vehicle, its velocity and attitude with respect to incoming air flow and atmospheric properties (Mooij, 1998). An efficient way to change the magnitude of the aerodynamic force is to change the attitude using the angle of attack and to change the aerodynamic shape of the vehicle by using speed brakes. The direction of the lift vector can be changed by rolling the vehicle around its velocity vector (Mooij, 1998). The angle over which the vehicle is rolled, is called the bank angle. By using a bank angle, the lift force is split into a vertical and a horizontal part. For a zero-side slip flight, the angle-of-attack in combination with the bank angle fully determine the attitude of the vehicle.

Summarizing, the guidance system can use three guidance variables to control the aerodynamic force and to guide the vehicle:

- the angle-of-attack, α
- the bank angle, σ
- the speed brake deflection, δ_{sb}

5.2 Guidance methods

The operational principle of the guidance system is based on tracking of a reference trajectory and computing a commanded attitude and speedbrake deflections (Mooij, 1998). Hence, a guidance system consists of two items: a reference input and a controller. First, a comparison is made between the actual and desired state. This serves then as an input for a controller, which generates the required commands. The controller mentioned here as a part of the guidance system is not related to the earlier mentioned control system after the guidance system. It is a filter inside the guidance system which calculates commands based on some error input.

There are two important classes of guidance systems, based on how the reference input is obtained. The first class is based on guidance using nominal trajectories, while the second class is based on guidance using predicting capabilities.

5.2.1 Guidance using nominal trajectories

When using nominal trajectories, an explicit reference trajectory is used. The reference trajectory is used in the form of nominal profiles, for example, the nominal altitude, dynamic pressure or energy as a function of the range. The actual flight state is compared with the nominal reference trajectory and control laws generate commands to bring the actual trajectory to the reference one. Within this class, two options are possible. Either the reference trajectory is calculated prior to the flight and the nominal profiles stored in the flight computer, or the reference trajectory is calculated at the beginning or during the TAEM phase onboard of the vehicle.

Pre-flight calculated reference trajectories

The use of pre-flight calculated reference trajectories assumes small deviations between the actual trajectory and the reference trajectory. Hence, it requires several reference trajectories to be stored in the flight computer in order to cope with variations of the initial state. Also a switching logic must be present to be able to choose the closest reference trajectory (Helmersson, 1988b). The disadvantage of this guidance method is that it requires pre-mission planning to account for all state deviations due to both expected and unexpected situations. This planning can be expensive in terms of time and money. It can even cause delays in the mission execution.

Onboard calculated reference trajectories

When the reference trajectory is calculated onboard the vehicle, a reference trajectory is calculated at the beginning of the terminal area, based on the initial state of the vehicle. The

guidance system consists actually of two parts, a trajectory planner and control laws which generate commands based on the onboard calculated nominal profile. If off-nominal conditions would occur during the terminal area resulting in a large deviation from the current profile, the trajectory could be recalculated and updated based on the new state.

5.2.2 Guidance using predicting capabilities

A guidance system using predicting capabilities does not need any reference trajectory or nominal profiles. The commanded control variables are determined by computing an implicit nominal trajectory at regular intervals, and by comparing this to the actual state of the vehicle. For example, a system calculates the required energy to reach the ALI, compares this with the vehicle's current energy and computes the required commands. The implicit trajectory can be computed in a closed-form approximation (analytical formula) or in a fast-time prediction by solving the equations numerically. This method of predicting capabilities yields a high flexibility regarding variations in the initial state and flight disturbances (Helmersson, 1988b).

The terminal area guidance of the US Space Shuttle uses pre-flight computed reference trajectories. A system using onboard reference trajectory calculation is used in several projects like the X-34 and Hopper. The method of predicting capabilities is used in a guidance system study for HORUS. In the next section, several guidance algorithms will be discussed in more detail. Next to a distinction between pre-flight and onboard reference profile calculation, a distinction can also be made based on the physical quantity that is used as an input. Several quantities can be used: altitude, velocity, dynamic pressure, flight-path angle or total energy. This will also be further discussed in the next sections.

5.3 HORUS guidance designed by Saab Aerospace

In 1988, MBB and Saab Space published a study on re-entry-guidance and control of winged re-entry vehicles. In this study, the HORUS-2B was used as the reference vehicle. Detailed trajectory analyses on the different phases of a re-entry flight were performed, including the terminal area. The proposed TAEM guidance system was based on predicting capabilities. The complete proposed guidance system, including all the mathematical formulas, can be found in (Helmersson, 1988a) and (Helmersson, 1988b). This section gives a summary of the working principles of the guidance system. Also the performance assessment is discussed, leading to several possible improvements.

5.3.1 Different segments of the TAEM

The terminal area trajectory is conceptually divided into four segments, see figure 5.1, and depends on the circuit pattern. Three possible circuit patterns exist: a direct approach (no HAC turn), a left-hand HAC turn or a right-hand HAC turn. In the proposed guidance system, the circuit pattern must be manually chosen in advance. But it is recommended to design an autonomous algorithm that chooses the mode. This will increase flexibility if the initial states are less known (Helmersson, 1988b). The terminal area study performed by Saab Space used a fixed left-circuit mode. Hence, the four segments of a terminal area trajectory are presented in figure 5.1 for a left hand HAC turn. But the principles remain the same for a right-circuit approach.

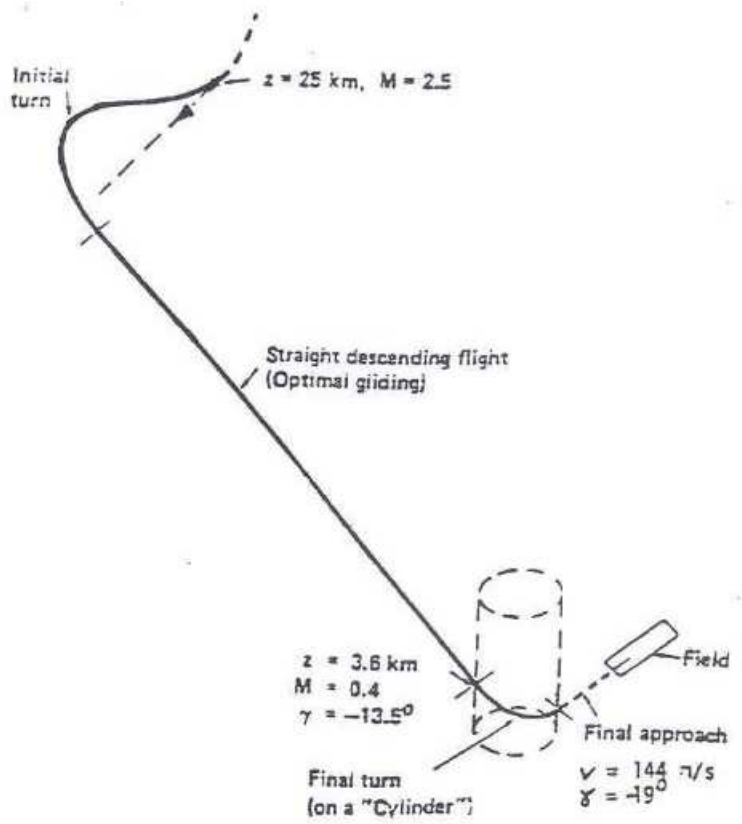

Figure 5.1: Different segments of terminal area trajectory for HORUS (Helmersson, 1988b)

- **Zoom and initial turn**
  The zoom and initial turn is the first segment and starts at the interface with the hypersonic atmospheric re-entry phase. The zoom maneuver reduces the velocity towards the selected stationary glide velocity. The reduction in velocity assures that the forces on the vehicle are not too large when the vehicle enters the denser, lower part of the atmosphere (Helmersson, 1988b). The initial turn or heading adjustment maneuver direct the heading of HORUS towards the HAC.

- **Straight descending flight**
  A straight descending flight is performed until the final turn around the HAC. During this glide, the velocity is reduced from supersonic to subsonic and thus, the vehicle passes through the transonic zone. Due to the limited angle of attack during the transonic regime, the lift force is not large enough to counteract the weight and a falling motion is performed. This segment is flown at an almost constant equivalent airspeed. This constant equivalent airspeed can be the value required for a maximum-range flight, but for the nominal case, a somewhat larger value of 144.0 m/s is selected. The nominal value has a margin of 20 percent relative to the optimal value.

- **Final turn around the HAC**
  The HAC turn aligns the vehicle towards the runway. In the guidance system proposed by Saab Space, a fixed conical HAC is used. The center of the HAC is located 12 km in front of the runway and 2.5 km to the left of the centerline of the runway (left hand HAC turn). The HAC radius is equal to 2 km at sea level and at other altitudes, the

radius is proportional to the inverse of the air density (Helmersson, 1988a). The radius increases with altitude and the HAC is an inverted cone. Further, it is assumed that the HAC turn is performed at a constant equivalent airspeed and with a constant bank angle (Helmersson, 1988b).

- **Straight final approach**
  This final segment reduces the heading errors towards the runway to negligible values. The segments ens at the interface with the landing phase. This landing phase was not covered in the terminal area study performed by Saab Space.

5.3.2 Working principle of the guidance system

The proposed terminal area guidance is a closed-loop system and is based on predicting capabilities. The required energy to reach the runway, according to a nominal strategy or implicit trajectory, is calculated continuously and the proper actions are commanded for dissipating or economizing energy. The implicit trajectory used for energy management is expressed by using analytical formulas. These analytical formulas approximate the required energy during the four terminal area segments.

The guidance system can be divided into four main blocks: a navigational block, an energy block, a load factor block and a conversion block. A scheme of the guidance system is shown in figure 5.2. Further information on each block is given below.

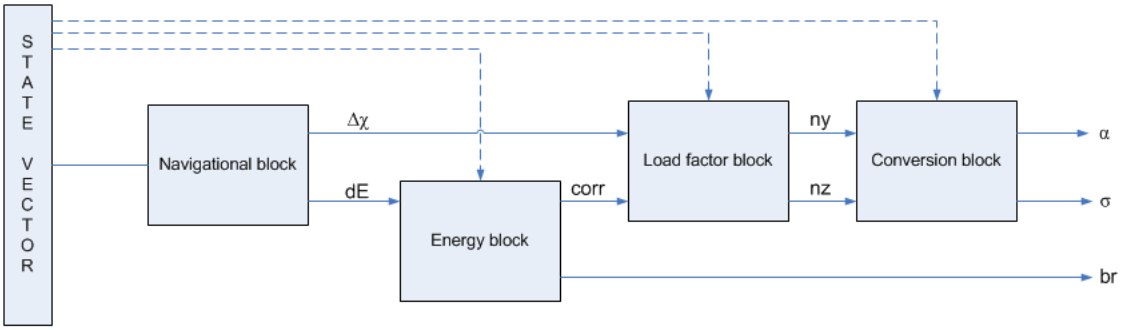

Figure 5.2: TAEM guidance scheme of HORUS

Navigational block

The navigational block uses information about the actual state of the vehicle to determine the energy excess with respect to a nominal trajectory and the required heading change to follow the nominal trajectory.

The required heading change is determined by the current heading and the reference heading. The reference heading is chosen such that the vehicle will join the HAC with a radius corresponding with the altitude at which the HAC is joined, assuming a glide with a constant glide ratio, starting at a linearmy extrapolated position 1 km in front of the actual position. If a correct and accurate reference calculation is required, then an iterative process is needed due to the conical shape of the HAC. The distance in a straight line to the HAC tangent depends

on the HAC radius at the altitude where the HAC is reached. This altitude and corresponding HAC radius depend on the traveled distance. Hence, an iterative process is required. Instead of this iterative scheme, an analytical approximation is used in the proposed guidance system by assuming a radius of the HAC which is equal to the value if the vehicle would arrive at the HAC with the same altitude as it has in the current position. A cylindrical HAC does not have this problem. The calculation of the reference heading is throughout the complete terminal area, except for the final approach. There, the algorithm is based on the heading error with respect to the runway heading and the lateral error with respect to the extension of the runway.

The key element of the proposed guidance system using predicting capabilities is the estimation of the required energy to reach the runway according to a nominal strategy or trajectory. The nominal required energy is not calculated directly, but instead, an energy excess is calculated. The energy excess is composed out of three terms: a speed energy excess, a transonic loss and a turn loss.

- The speed energy excess term accounts for the difference between the actual velocity and the nominal glide velocity ($V_{eq} = 144.0$ m/s).
- The transonic loss term accounts for an energy loss in the transonic region. In the transonic regime around M 1.0, a large increase in drag occurs which is associated with the presence of shock waves. It will be shown in chapter 8 that the drag directly determines the energy variation. The drag increase in the transonic region results in an energy loss, hence the transonic loss term.
- The last component, the turn loss, accounts for the altitude that is lost when the vehicle makes a turn. Because only the loss in altitude in considered, it is assumed in the proposed guidance system that the same nominal equivalent airspeed of 144.0 m/s can be used in a turning flight.

During the final approach, a modified version of the energy estimation is used. The transonic loss is no longer taken into account, while a altitude deviation term is added. This altitude deviation term calculates the difference between the actual altitude and a reference altitude based on a particular glide slope.

These terms determining the total energy excess are all calculated using analytical formulas. In (Helmersson, 1988b), it is stated that the proposed estimation scheme is relatively accurate at subsonic speeds. At supersonic and transonic speeds however, significant errors occur. It is recommended to design a better estimation method. A possible improvement is to use fast time prediction by solving the dynamic equations numerically, in combination with simplified equations of motions and models and with simple integration schemes.

Energy block

The energy block calculates the required commands to dissipate or economize energy, based on the value of the energy excess calculated in the navigational block. Two situations can occur, based on the energy excess:

- **High energy situation**
  In a high energy situation, the actual energy is higher than the nominal required energy

(energy excess) and energy dissipation is required. This dissipation can be done by performing a diverting turn, increasing the flight velocity or by using speedbrake deflections. It is not wise to deviate too much using a diverting turn since the energy needed to reach the runway may drastically increase, even for small adjustments. This is especially important during the end of the terminal area. Hence, the proposed guidance system uses diverting turns at higher altitudes, while the speed brakes are used during the last part of the TAEM. Both the diverting turns and the speedbrake deflections can be used in combination with a velocity increase. In the energy block, an energy correction factor is calculated based on the energy excess. The required diverting turn, velocity change and speedbrake deflection are proportional to this energy correction factor. In the next blocks, the energy correction factor is used to determine the required angle of attack and bank angle. The amount of speedbrake deflection is calculated in the current energy block.

- **Low energy situation**
  If the actual energy is less than the nominal, the optimal path is used until the nominal trajectory is reached. This optimal trajectory yields an energy dissipation which is about 20 percent less than the nominal trajectory. When the nominal trajectory (zero energy excess) is reached again, the speed is increased to 144.0 m/s equivalent airspeed to increase the energy dissipation such the nominal trajectory is followed.

Load factor block and conversion block

The load factor block computes the commanded load factors based on the energy correction factor and the commanded heading change, see figure 5.2. The vertical load factor n_v and the horizontal load factor n_h are calculated by two guidance laws. These algorithms are approximations based on studying optimal trajectories. Saab Space concluded that to fly a maximum range, it is required to fly at a constant equivalent airspeed that corresponds with the maximum lift-to-drag ratio. The same velocity was also used during a turning flight. It is stated in (Helmersson, 1988b) that by using more refined control laws, the maximum range can be extended by 5 km at most. In the conversion block, the load factors from the load factor block are converted to an angle of attack and a bank angle, based on relations that describe the aerodynamic model of HORUS.

5.3.3 Performance assessment

Saab Space performed a number of simulations with the proposed guidance algorithm. Next to the nominal reference case, both initial state and model variations were studied. Variations in the initial state included variations in the initial altitude, initial velocity and initial heading. In case of model variations, variations in the vehicle model (lift and drag coefficients) and atmospheric model (density) were taken into account. An example trajectory is given in figure 5.3, which shows the resulting trajectory for the nominal reference case (nominal initial state and models). A description of the other results can be found in (Helmersson, 1988b). Saab Space concluded that the simulations showed that the proposed guidance scheme is robust and can cope with a wide range of initial state values and with realistic model errors. But during the performance assessment by Saab Space, only one variable was changed at a time while the other were kept constant. The result of a combination of parameter variations was not studied. Moreover, all the simulations were performed for a single initial position in the ground plane (x- and y-coordinate). Also, all simulations used a left-hand approach, which was specified

before the simulations. Saab stated that several automatic selection schemes were investigated to determine if a left or right hand approach was required, but none of them gave results that were reliable. Hence, the HAC was fixed to a left hand approach, which for the chosen initial position results in an overhead approach.

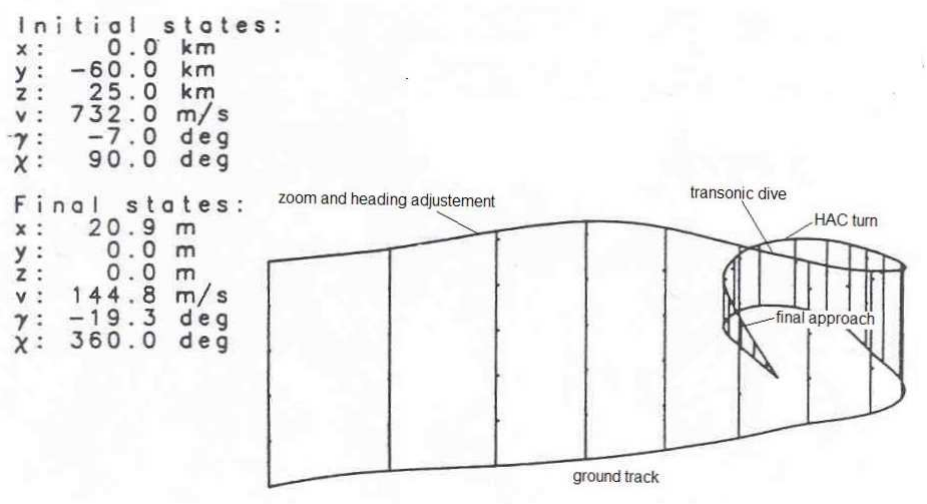

Figure 5.3: Resulting trajectory as flown by HORUS for a nominal initial state and nominal models (Helmersson, 1988b).

The performance analysis of the proposed guidance algorithm was extended in (Linden, 1994). Next to variations in initial altitude and initial heading, variations in the initial xy-positions were investigated. Initial positions can be situated on a circle around the runway with a radius of 83 km. The velocity and flight-path angle were not varied. The sensitivity analysis showed that the guidance algorithm cannot cope with variations in initial course angle at lower altitudes [1]. It was not possible to state a clear range of initial conditions with which the guidance algorithm can cope. Also simulation results related to a HAC selection criterion are described in (Linden, 1994). It was tried to find an automatic selection criterion based on the initial state in the xy-plane and the initial heading angle. The radius of the HAC and its downrange placement with respect to the runway threshold were kept constant. The selection only considered a left or right hand approach. Simulations did not lead to a good selection criterion, though

5.3.4 Possible improvements

The terminal area guidance for HORUS as proposed by Saab Space forms the basis of the terminal area analysis in the current thesis study. The above discussion on the guidance system leads to several possible improvements:

- The method used to determine the energy excess must be refined. The energy estimator can be improved by using a fast-time prediction by solving the equations of motion numerically.

[1] This might be due to the fixed overhead approach HAC. Because of the low energy and the required heading adjustment maneuver, the ground track along the fixed overhead HAC is to large. By making the HAC placement a variable and depending on the initial state, more initial states could be dealt with by the algorithm. More information can be found in chapter 12.

- Improved control laws can be used which can allow the range to be extended by 5 km.
- In the current system, the selection of the left or right approach mode is done manually. A automatic selection law must be designed. Next to the left or right approach mode, the selection law can be extended to adapt also the HAC radius and the downward placement.

Next to the guidance algorithm designed for HORUS, several other guidance algorithms exist. Two algorithm that are used during real flights are the algorithms for the Space Shuttle and the Buran. Several other terminal area studies were also performed. In the next sections, an overview is given of several other guidance algorithm. These guidance algorithms are based on reference profiles. During the discussion, the focus will be on the calculation of these reference profiles and on the placement and geometry of the HAC. Information from these algorithms can be used to tackle the problems related to the HORUS guidance.

5.4 Space Shuttle guidance

The American Space Shuttle has been flying for many years and each flight, its TAEM guidance performs well. So thanks to its age, the Space Shuttle guidance serves as a convenient basis for technology extrapolation. Moreover, some guidance algorithms for new generation vehicles are based on the Space Shuttle guidance, see for example (Kluever & Horneman, 2005). Therefore, it is essential to understand the guidance logic of the Space Shuttle. During the early 1970's, many organizations were involved in the development of the TAEM guidance of the Shuttle and many different options were considered. In 1975, a study contract was given to McDonnell Douglas Astronautics Company in St. Louis to make the final guidance consisting of all the good qualities from several developed algorithms (Moore, 1991). After some fundamental modifications, this guidance algorithm was used for the Shuttle flights. In this section, both the original guidance and the guidance as used during actual Space Shuttle flights is described.

5.4.1 Terminal area flight phases of the Shuttle

The terminal area of a Space Shuttle starts at Mach 2.5, at about 85000 ft ($\approx$ 26km) and finishes at the approach and landing interface at an altitude of 3 km and Mach 0.4 (Moore, 1991). The TAEM phase is divided into four flight phases. These flight phases are illustrated in figure 5.4 and described below. Note that in figure 5.4 the positive y coordinate is to the right of the x axis. This is opposite to the runway coordinate frame as used in this thesis work.

- **S-turn phase**
  The S-turn phase (Phase 0) is used when the Shuttle has an energy excess which cannot be reduced to the proper final interface conditions by means of speed brakes and dynamic pressure modulation only. The shuttle is commanded to turn away from the heading alignment cylinder tangency and when sufficient energy has been dissipated, the acquisition phase is started and the Shuttle is turned to an appropriate tangency to the heading alignment cylinder. During the S-turn, the Shuttle is flown with a maximum dynamic pressure and maximum speed brake deflection (within the limits of the flight conditions) to achieve a maximum energy dissipation rate.
- **Acquisition phase**
  In the acquisition phase (Phase 1), the Shuttle is guided to an appropriate tangency point

to the heading alignment cylinder. In the original TAEM guidance of the Shuttle, the HAC had a radius of 20000 feet. The acquisition phase can be divided into two segments. First, a turn to acquire a heading which is tangent to the HAC is performed. Then follows a wing level flight until the capture of the HAC (Camara, 2003).
During phase 1, the energy is controlled by modulating the dynamic pressure and by modulation the speed brake if the Shuttle is flying in the subsonic regime. Design requirements prevent modulation of the speed brake in the supersonic speed range. The acquisition phase is terminated when the Shuttle is within 4000 feet (about 1220 m) of the HAC. This avoids a large overshoot of the heading alignment cylinder.

- **Heading alignment guidance phase**
  In the heading alignment guidance phase (Phase 2), the Shuttle is controlled to directionally track the heading alignment cylinder. Again, the energy dissipation rate is controlled by dynamic pressure modulation and the speed brake. This phase is continued until the heading is within 20 ° of the final approach plane and then a switch is made to the prefinal guidance phase. The final approach plane is a vertical plane through the extended runway centerline.

- **Prefinal guidance phase**
  During the prefinal guidance phase (Phase 3), the lateral guidance steers the Shuttle toward the final approach plane. The longitudinal guidance controls the speed brake in order to modulate the dynamic pressure and to achieve an equivalent air speed of 290 knots (about 149 m/s) as specified for autoland interface. Also the required glide slope is achieved.

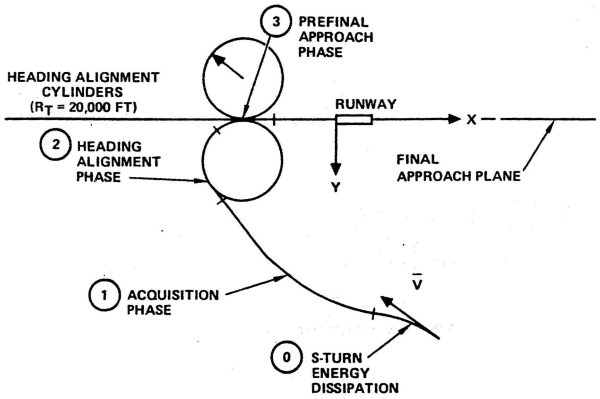

Figure 5.4: TAEM guidance phases of the Space Shuttle (Kraemer & Ehlers, 1975)

The ground track geometry as depicted in figure 5.4 is used in both the original guidance algorithm from McDonnell Douglas and the algorithm during actual Space Shuttle flights. Original options that were studied by other companies during the early 1970's include Racetrack, VOR-TAC, Cylinder, Spiral, see (Moore, 1991) and chapter 11 for more information.

5.4.2 Original guidance system

The original Shuttle TAEM guidance, was developed to do its primary function of energy management with an energy controller (Kraemer & Ehlers, 1975). The guidance system controlled

the unpowered vehicle to an energy-versus-range profile. The longitudinal guidance computes guidance commands in order to modify the energy dissipation, such that the required energy state is reached. The lateral guidance computes the guidance commands to follow a prescribed ground track. The longitudinal and lateral guidance are decoupled. Figure 5.5 shows the original Shuttle TAEM guidance together with the interfaces of the avionics subsystems.

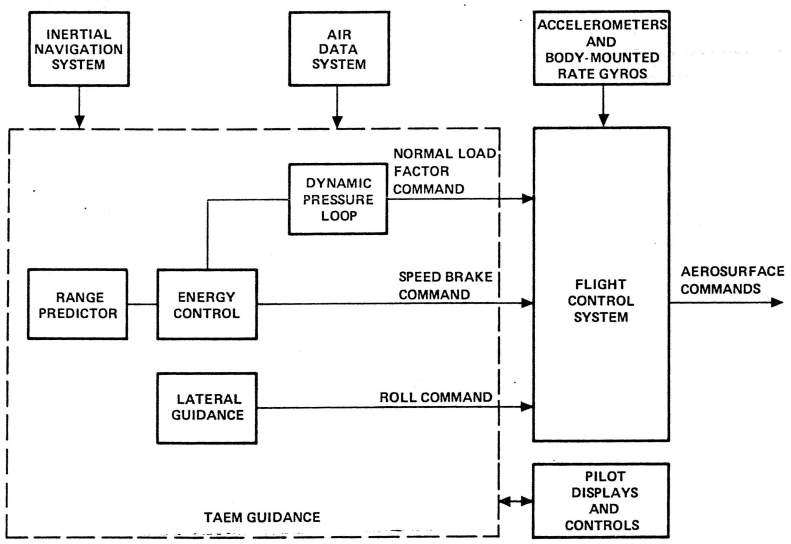

Figure 5.5: Original Shuttle TAEM guidance (Kraemer & Ehlers, 1975)

Energy control and longitudinal control

A ground track ranges predictor estimates the range to go for the different guidance phases and adds the appropriate components to obtain the total ground track. This ground track is used by the Shuttle TAEM guidance system to control the unpowered vehicle to an energy-versus-range profile. This profile uses the energy factor normalized with respect to the weight of the vehicle, which is given as:

$$\frac{E}{W} = h + \frac{V^2}{2g} \tag{5.1}$$

Figure 5.6 shows the energy-versus-range profile. These energy-versus-range profiles were derived from digital simulations. The several curves determine the guidance boundaries. The R_{NOM} profile is derived by using a fixed mid-range speed brake position and a mid-range dynamic pressure in a no wind atmosphere. This profile is the desired nominal energy state as a function of the range to fly. The R_5 represents the maximum energy dissipation rate that can be achieved without the use of an S-turn. If the energy state exceeds this function, the S-turn guidance mode is initiated. If the energy state falls below the $R_{5'}$ function, the S-turn is terminated and the acquisition phase in initiated. The R_3 function is used to relocate the heading alignment cylinder closer to the runway. The relocated HAC closer to the runway is called the Minimum Entry Point (MEP). So two options are available for the placement of the HAC on the x-axis, a nominal or minimum entry point.

To achieve the required energy state, the guidance system must modify the energy dissipation to be above or below the nominal rate. The rate of dissipation of energy with glide range

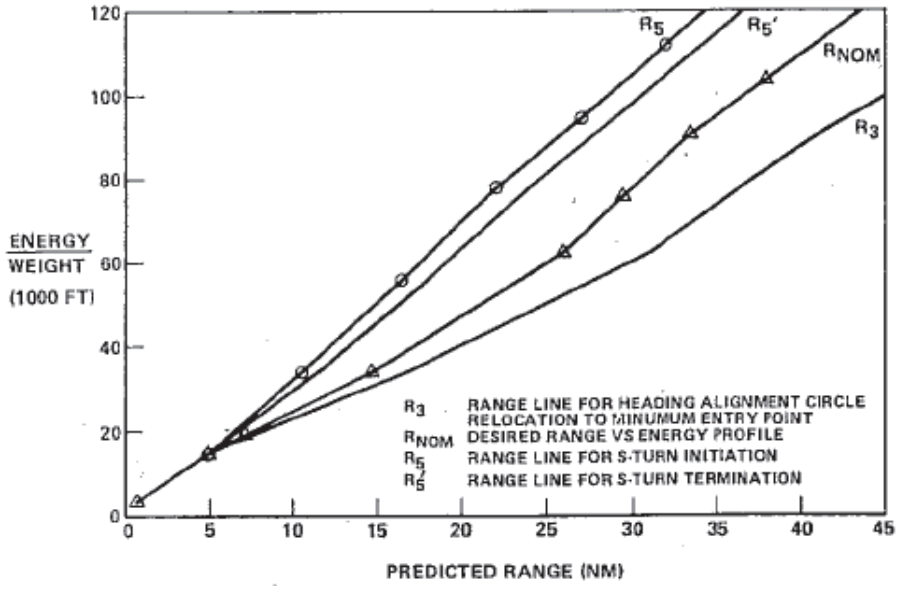

Figure 5.6: Shuttle TAEM energy profiles (Kraemer & Ehlers, 1975)

is derived in (Kraemer & Ehlers, 1975) as:

$$\frac{d\,(E/W)}{dR} = -\frac{D}{W}\frac{1}{cos\gamma} \tag{5.2}$$

This equation is derived in chapter 8 and shows that the rate at which energy dissipates with glide range is proportional to drag and inversely proportional to the cosine of the flight path angle. The longitudinal guidance system compares the current energy gradient to the desired energy gradient and uses the difference to guide the Shuttle to the nominal energy. The desired energy gradient is calculated using the current energy computed value energy to weight and the energy value obtained from the energy profiles as shown in figure 5.6, using a point 2500 ft closer to the runway. The current energy gradient is derived by comparing the energy of the Shuttle at successive sampling times and dividing by the computed ground track distance in that time interval. The profiles from figure 5.6 were obtained for a wings-level flight condition, so no bank maneuvers were taken into account. On the other hand, the current energy gradient takes both the loss in energy due to a wings-level glide and banking maneuvers into account. To be able to compare both energy gradients, a correction is made to the current energy gradient.

The guidance system has three basic means for modifying the energy dissipation rate with respect to range-to-go: a turn away from the runway (S-turn) to increase the range, a modulation of speedbrake deflection and a modulation of dynamic pressure. The angle of attack is obtained through dynamic pressure control. The energy determines the required dynamic pressure and this required dynamic pressure is transformed to an angle-of-attack. The modulation of the speedbrake over its full deflection range is only available in the subsonic speed regime, because of design constraints. So in the supersonic speed regime, the speedbrake cannot be used for energy control. But in the subsonic speed regime it is used effectively for energy rate modulation. In the supersonic region, the speebrake deflection is set to 55 °, while in the subsonic regime it can vary between 0 ° and 87.2 °. During the S-turn phase, all three means to increase the energy dissipation are used in order provide a maximum dissipation. In the acquisition phase and the heading alignment phase, the speed brake is used at subsonic speed

for correcting small energy errors. If the energy is error becomes large, the dynamic pressure is used for energy control. During the prefinal phase, the main objective is to capture the autoland glide slope and to control the airspeed to that required for autoland. In this phase, the two longitudinal channels available for control (normal acceleration and speedbrakes) are used independently (Kraemer & Ehlers, 1975). Now, the normal-acceleration command (through use of the elevator) is used to control the altitude while the speedbrakes are used to control the dynamic pressure [2]. So the guidance, as shown in figure 5.4, is not used in the prefinal phase.

Lateral guidance

The lateral control uses the commanded bank angle to guide vehicle so that it follows a prescribed ground track.
During the S-turn phase, the bank angle is set to 50°. In the acquisition phase, the lateral guidance is designed to control the heading of the Shuttle tangential to the HAC and during the heading-alignment phase, the lateral guidance assures that the vehicle makes a turn around the HAC. During the prefinal phase, the lateral guidance brings the vehicle to the extension of the runway centerline.

Performance of the guidance algorithm

From the discussion above, it can be concluded that the energy-range profiles are the main characteristic that is used to calculate the commands. These profiles were obtained through simulations and are fixed, and the same profiles are used for different initial conditions. Also, banked-flight situations are not taken into account in the profiles and a correction factor must be used in case of banking. The (fixed-radius) HAC can be placed in two downrange positions with respect to the runway threshold.

A closed-loop study was performed in order to evaluate this guidance principle in the presence of various headings, initial positions, winds and turbulence. The results can be found in (Kraemer & Ehlers, 1975). In general, the TAEM systems performance is satisfactory, but for some cases with severe wind conditions, the dynamic pressure was outside the tolerance. Moreover, it is noted that tuning the system to provide tighter energy control and slightly modifying the energy control algorithms is expected to provide results within tolerance with the severe winds.

5.4.3 Algorithm as used during actual flights

The algorithm as used during the first Shuttle flight is described in (Anon., 1980), while (Moore, 1991) gives an overview of modifications to the guidance system for later Shuttle missions. This section gives a summary of the changes with respect to the original guidance system. For detailed information, the reader is referred to the stated documents.

As described above, the original guidance performed the task of energy control by adapting the dynamic pressure and the speedbrakes. The dynamic pressure was regulated with the normal acceleration and hence, the angle of attack. After additional simulations tests, two major

[2] Note that the longitudinal control is just opposite to that used for gliding, where the altitude is controlled with the speebrakes and the velocity with the normal acceleration (or elevator).

problems were found. The first problem was that in presence of severe winds, the results were outside the tolerances. The second problem is related to the oscillatory response characteristics of controlling the dynamic pressure with just the normal acceleration. This was due to the fact that dynamic pressure is also a function of drag, in addition to lift (Moore, 1991).

The modification in which the altitude component of the energy is controlled with the normal acceleration solved both problems. The speedbrake controls the other component of the energy, the dynamic pressure. So the energy controller was changed to a separate altitude controller and dynamic-pressure controller. All Space Shuttle missions use this altitude controller. Reference altitudes are now the main input for computing the commanded normal acceleration, while dynamic-pressure references determine the commanded speedbrake deflection. Figure 5.7 shows a schematic view of the new TAEM guidance. Energy references are still used in the guidance algorithm, but only as a secondary controller to determine the normal acceleration and the speedbrake deflection. Energy is now merely used as a constraint on the output calculated by the main altitude and dynamic pressure controllers. The energy reference profiles as depicted in figure 5.6 are also used to determine the initiation of an S-turn. All the altitude, dynamic pressure and energy reference profiles are calculated pre-flight.

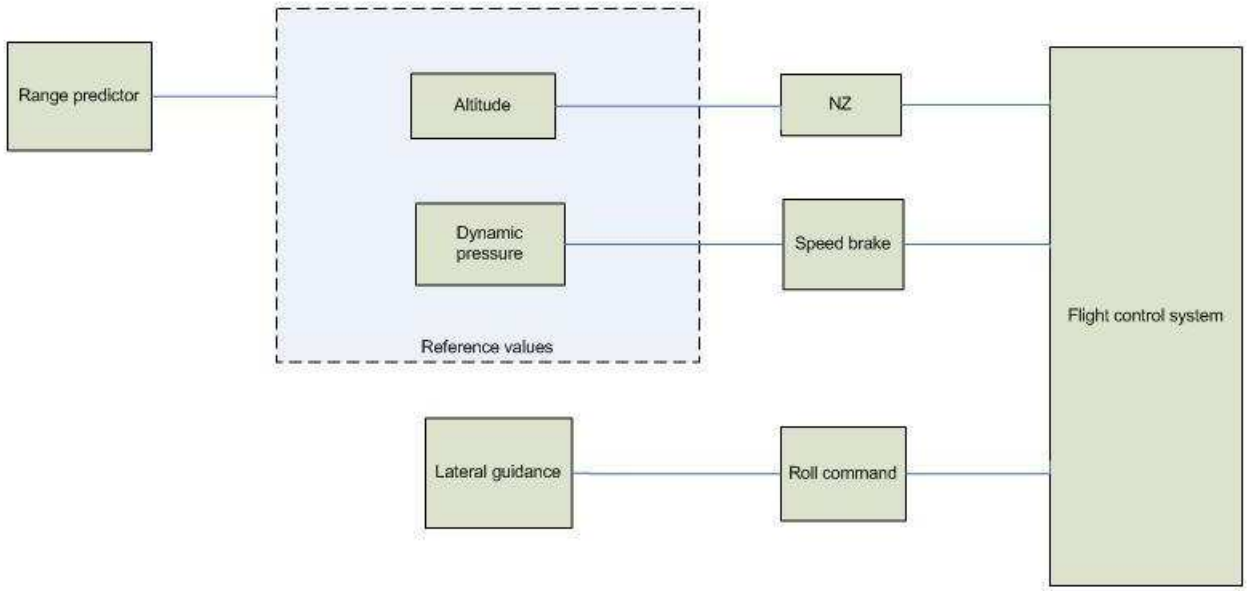

Figure 5.7: Schematic overview of improved Shuttle TAEM guidance

Similar to the original guidance, two options exists for the placement of the HAC in the downrange location with respect to the runway threshold. Normally, the Shuttle arrives in the plane through the extension of the centerline of the runway, the final-approach plane, at a Nominal Entry Point (NEP). But in an energy low situation where the pilots assess that the altitude at the approach and landing interface will not be achieved, the center of the HAC can be moved to the MEP.

During the first Shuttle flight in April 1981, a circular HAC was used with a fixed radius of 20000 ft. During subsequent Shuttle missions, the circular HAC was changed to a spiral

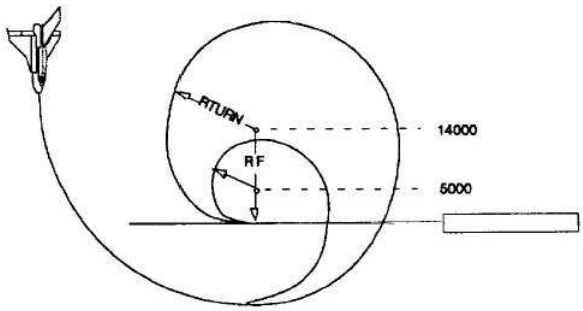

Figure 5.8: Boundaries of the spiral HAC (Moore, 1991)

HAC. In three dimensions, the spiral is a cone so the HAC became a heading alignment cone. The radius at the intersection with the final approach plane or the final radius of the HAC has a nominal value, but can be changed to a smaller value if the altitude goes below a particular reference value, see figure 5.8. Another modification is the use of Optional TAEM Targeting (OTT). OTT provides the option for an OverHead approach (OH) to the runway in addition to a Straight-In approach (SI), see figure 5.9. The objective is to conserve energy for subsonic dissipation in the vicinity of the runway (Moore, 1991). The altitude difference between SI and OH increases the probability for successfully flying either under or over weather disturbances along the landing site approach. The first flight of OTT was on STS-5 in 1982. Combining NEP/MEP and SI/OH results in four possible HAC positions. The choice of HAC placement depends on pre-flight determined energy boundaries. The Shuttle guidance also includes an energy dump phase on approach to the HAC to eliminate a HAC overshoot resulting from from suspersonic HAC turns. This energy dump phases assures a subsonic flight around the HAC.

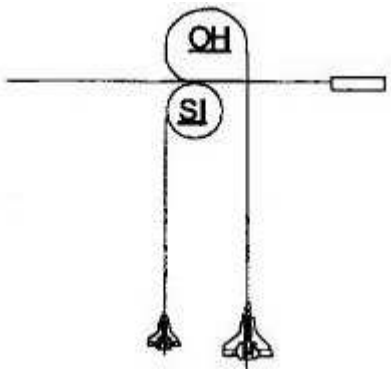

Figure 5.9: Optional TAEM Targeting (Moore, 1991)

An important disadvantage of the Shuttle algorithm is that the flexibility of pre-computed reference profiles to off-nominal conditions is limited. The guidance relies upon considerable pre-mission planning.

5.5 Guidance algorithm of BURAN

The first flight of the BURAN Orbiter has proved the efficiency of the trajectory design principle and guidance algorithm. Despite the strong gusty wind, which was present during the first flight,

the guidance system performed its task perfectly and with high accuracy. Therefore, a similar approach can be used in the development of guidance systems for other winged re-entry vehicles. This section briefly describes the guidance algorithm of the Russian BURAN Orbiter and is based on (Kirpischikov, 2007).

5.5.1 Re-entry of BURAN

The descent and landing phase started in the so called Area of Allowable Entry Conditions (AAEC) at an altitude of 100 km. This AAEC covered a large area and embraced as many numbers of daily orbit circuits as possible in order to provide safety during the orbital flight.

The main feature of the Buran guidance system is centered around the so called trajectory tubes. Descent trajectories are bounded by several restrictions and during the design, a broad set of disturbances must be taken into account, for example, disturbances in atmospheric parameters or vehicle uncertainties. These disturbances have a random character and do not only change from flight to flight, but also during the same flight. So it is impossible to define a fixed descent trajectory. Trajectories design tubes were considered instead and during an actual flight, the trajectory would be within this tube with a certain probability. The tubes were determined with a probability of 0.997.

The descent and landing phase was divided into three stages, all with their own guidance algorithm. The three stages are divided according to altitude of the vehicle:

- Descent Stage: altitude = 100-20 km
- Pre-Landing Maneuvering Stage (PM): altitude = 20-4 km
- Pre-Landing Approach and Landing Stage: altitude = 4-0 km

The TAEM phase for both the HORUS and the Space Shuttle starts approximately at an altitude of 25 km. But the Pre-Landing Maneuvering Stage for BURAN starts at 20 km altitude. This is the reason why in addition to this Pre-Landing Maneuvering Stage, also the final part of the Descent Stage will be discussed.

5.5.2 Final part of Descent Stage

Figure 5.10 shows the tube trajectories and cross-sections of the tube at the final leg of the Descent Phase together with the Cylinder of Energy Dispersion (CED) indicated with the red circle. Number 2 denotes the HAC, 3 denotes the runway, 4 is the flight trajectory that was flown during the first flight of BURAN, and 5 and 6 denote the area were the trajectories tubes end at the interface with the Pre-Landing Maneuvering Stage.

The guidance algorithm will guide the vehicle into a given area of trajectory parameters at a height of 20 km. This area is called the final area and is given in figure 5.10 by the grey region (denoted by 1). In this area, the velocity vector should be directed tangent to the CED with a permissible deviation of 15° at most, the magnitude of the velocity must be within a certain range, and the distance along a great circle arc from the Orbiter's center of mass to the CED tangency point must between 19 and 45 km. These are the trajectory parameters that define the end conditions of the Descent Stage and the initial conditions for the Pre-Landing

Maneuvering Stage.

The algorithm of lateral trajectory control guides the vehicle to a direction equal to one of the two tangents to the CED. Therefore, the trajectory tube is separated into two smaller tubes at an altitude of 35 km. After several simulations, it was calculated that the probability of the Buran proceeding into the left terminal area (with respect to flight direction of the Orbiter) was about 0.3. So there is a 30% change that the vehicle proceeds into the left tube. Consequently, the probability that the vehicle proceeds into the right tube is 0.7.

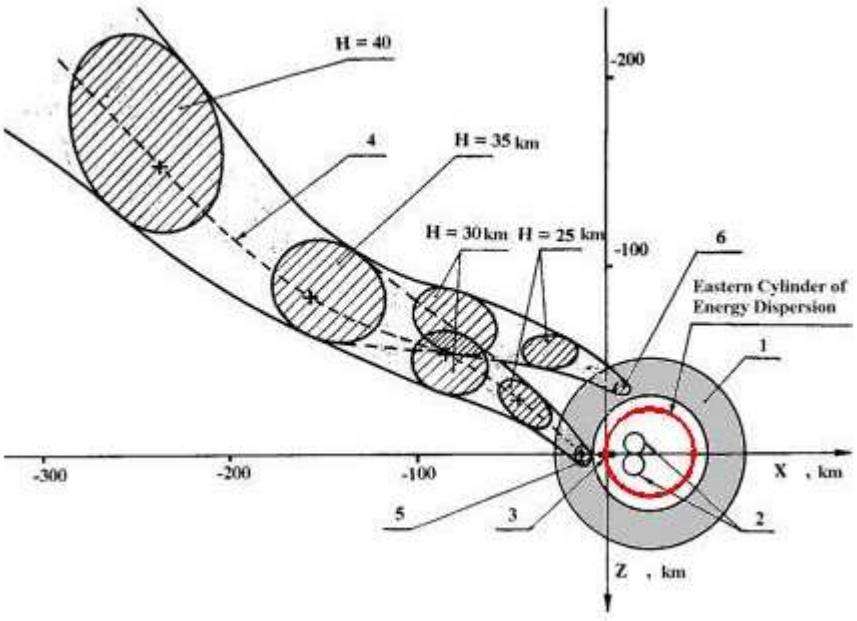

Figure 5.10: Final leg of Descent Phase (Kirpischikov, 2007)

5.5.3 Pre-Landing Maneuvering Stage

The main task of the guidance algorithm at PM is to guide the vehicle from the final area of the Descent Stage to the vicinity of the Key Point. This Key Point is located at an altitude of 4 km above the runway centerline on a distance of approximately 14.5 km from the center of the runway. The boundaries for the state of the Orbiter at the Key Point can be found in (Kirpischikov, 2007). Figure 5.11 shows the trajectories tubes for the Pre-Landing Maneuvering Stage. Two CEPs and two Key Points are shown. These are needed to account for an Eastern or Western wind. All trajectories assume that the vehicle is approaching from the West. At the Pre-Landing Maneuvering Stage, dispersion of excessive energy is done. Generally, this can be done by three methods:

- Change of trajectory by means of turns for matching the current energy vs. range state with the designed state
- Change of dynamic pressure
- Change of lift-to-drag ratio

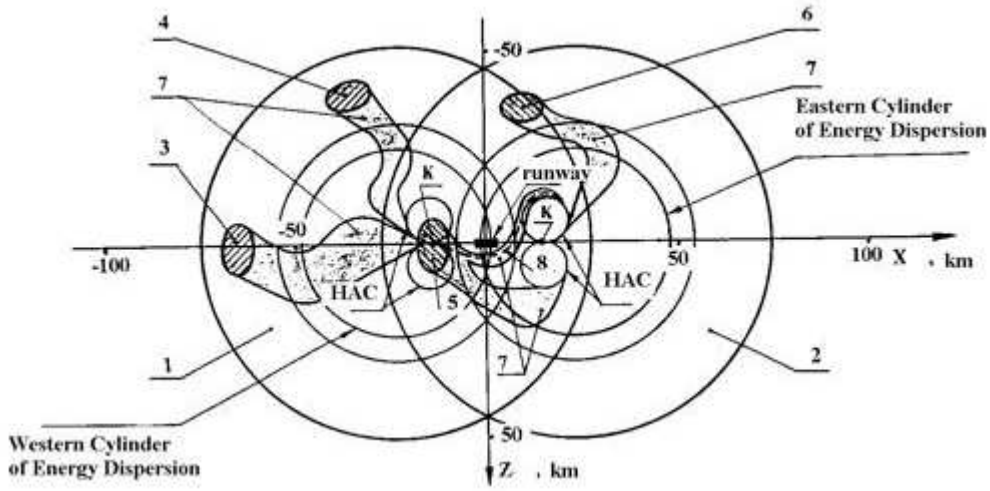

Figure 5.11: Pre-Landing Maneuvering Stage (Kirpischikov, 2007)

For BURAN, a combined method was selected. The basic idea is to change the trajectory extent (by using spiral turns) in combination with a programmed change in the levels of lift-to-drag ratio and dynamic pressure. The change in lift-to-drag ratio is accomplished by deflecting the air brakes. The vehicle should fly at the maximum value for the dynamic pressure as a function of altitude in presence of tailwind in order to intensively disperse energy. Minimum dynamic pressure is needed when a headwind occurs in order to fly with the maximum lift-to-drag ratio (Kirpischikov, 2007) [3].

At the start of the PM stage, the guidance system forms a 3-D reference trajectory based on the energy level and the state of the Orbiter. This reference trajectory connects the initial position with the Key Point, and the projection of this reference trajectory onto the horizontal plane generally consists of five geometrical trajectory parts:

- a turn-way spiral
- corrective turn spiral
- tangent to the HAC
- arc of HAC circle
- a straight line to Key Point

The reference trajectory is calculated as follows. Four possible versions of trajectories in the horizontal plane without a turn-away are determined. But in (Kirpischikov, 2007), it is not mentioned what these four versions look like. For all the trajectories, the programmed function relation between the flight altitude and the range to the Key Point is determined. Then, the reference trajectory is selected out of these four possible trajectories by sequential comparison

[3]Note that this is true for only a part of the Pre-Landing Maneuvering Stage. At the end of this Phase, when flying in a straight line towards the Key Point on the extension of the runway centerline, the dynamic pressure must be higher than the minimum value in the presence of a headwind. It is known from gliding experience that the magnitude of the wind is smaller at the ground than at some altitude. If one flies at minimum speed and the wind drops, the speed of the vehicle is lowered and a stall can occur.

of the required and available Orbiter's energy. The trajectory for which the energy difference is within an acceptable limit is accepted as the nominal reference trajectory.
A turn-away maneuver is performed if the best trajectory without a turn-away is insufficient to dissipate the energy.
The reference trajectory is redefined when the deviation from the reference trajectory is too large and at the end of a turn maneuver (end of turn-away and corrective turn).

During the first and only flight of the BURAN, the Eastern CEP was used (selection was based on wind conditions). It was already stated that after several simulations, the probability to have a trajectory to the right terminal area (with respect to flight direction) was 0.7. This area was also used during the first flight. Starting at this terminal area, two trajectory tubes are possible. One tube goes around the Southern HAC while the other one goes around the Northern HAC. It was evaluated that the Southern HAC would be used with a probability of 0.97 and the Northern HAC with a probability of 0.03. Although a larger chance exists that the Southern HAC is selected, during the first flight of BURAN, conditions dictated the use of the Northern HAC. This is shown in figure 5.12. A final overview of the final part of the Descent

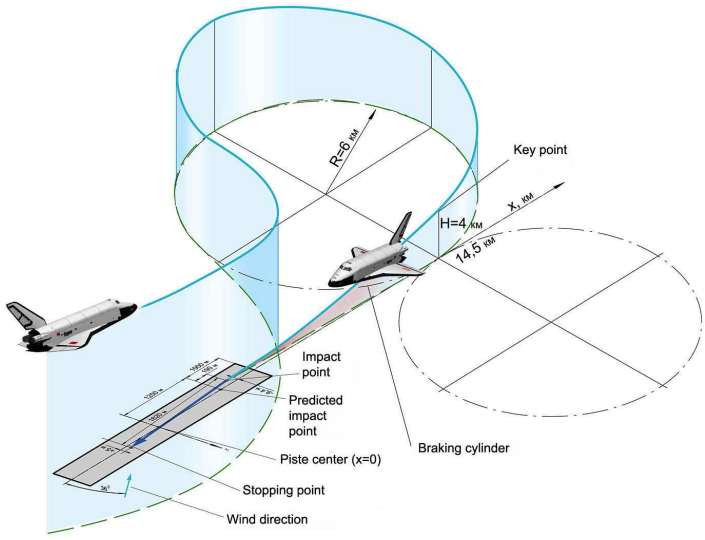

Figure 5.12: Flight of BURAN around the HAC during first flight (Kirpischikov, 2007)

Stage and the Pre-Landing Maneuvering Phase of the first flight of the BURAN is shown in figure 5.13. BURAN's trajectory projected on the ground is indicated by the red line inside the blue trajectories tube. The green circle indicates the different HACs.

5.6 Recent terminal area guidance studies

Over the last years, several terminal area studies have been performed. This section gives an overview of the results that are useful for the current thesis study and that could be used to solve the shortcomings of the HORUS guidance. All the algorithms as described below use explicit reference trajectories.

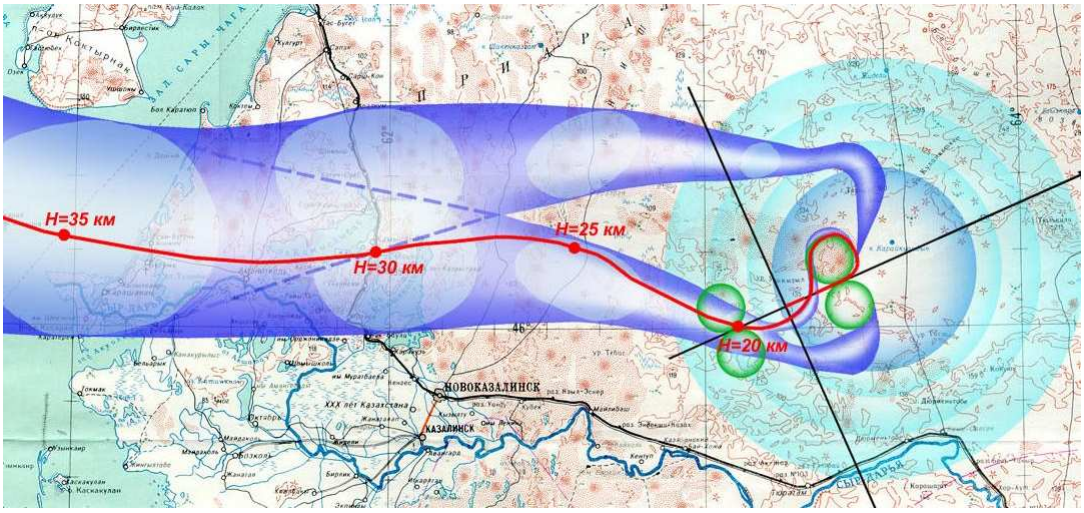

Figure 5.13: Trajectory of BURAN during the first flight (Kirpischikov, 2007)

5.6.1 Trajectory generation strategy for the terminal area of a RLV

A study on terminal area GNC for the Hopper RLV is presented in (Buechner, 2003) and (Costa, 2003). A trajectory planner is described, which includes a ground track planner based on a vertical nominal reference profile.

The computation of the nominal vertical profile is performed based on a vertical corridor, see figure 5.14. The boundaries of this corridor are the maximum range gliding capabilities and the maximum dive capabilities of the vehicle. The TAEM vertical corridor was set up in the dynamic pressure versus altitude state space. The maximum-range glide is computed using the angle of attack for maximum lift-to-drag ratio, whereas the maximum dive corresponds to the minimum range that the vehicle can fly and is calculated by flying at the maximum dynamic pressure. The nominal vertical trajectory is placed in the middle of the corridor and gives a nominal dynamic pressure as a function of the altitude.

Next, this nominal profile is used in a trajectory planning algorithm which calculates an optimal ground track. The entire trajectory planning is based on the vertical profile is shown in figure 5.14. The ground track planning algorithm is based on a concept with the vehicle's turning rate as a design parameter. This method results in a trajectory that respects the interface conditions at both the entry and the landing interface and generates flexible and geometrically non-predefined ground tracks. All the trajectories are flown with the nominal value of the dynamic pressure as given in the dynamic pressure profile. A change in initial conditions leads to a different ground track, while the same vertical or longitudinal nominal profile is still used. This method of adapting the ground track based on the state of the vehicle is a good solution to solve the flexibility problem of the Shuttle in case of off-nominal conditions.

Note that off-nominal conditions are dealt with by only adapting the ground track, while a nominal longitudinal profile is always used. Moreover, the influence of off-nominal conditions on the maximum range and maximum dive, and hence the nominal profile, was not studied.

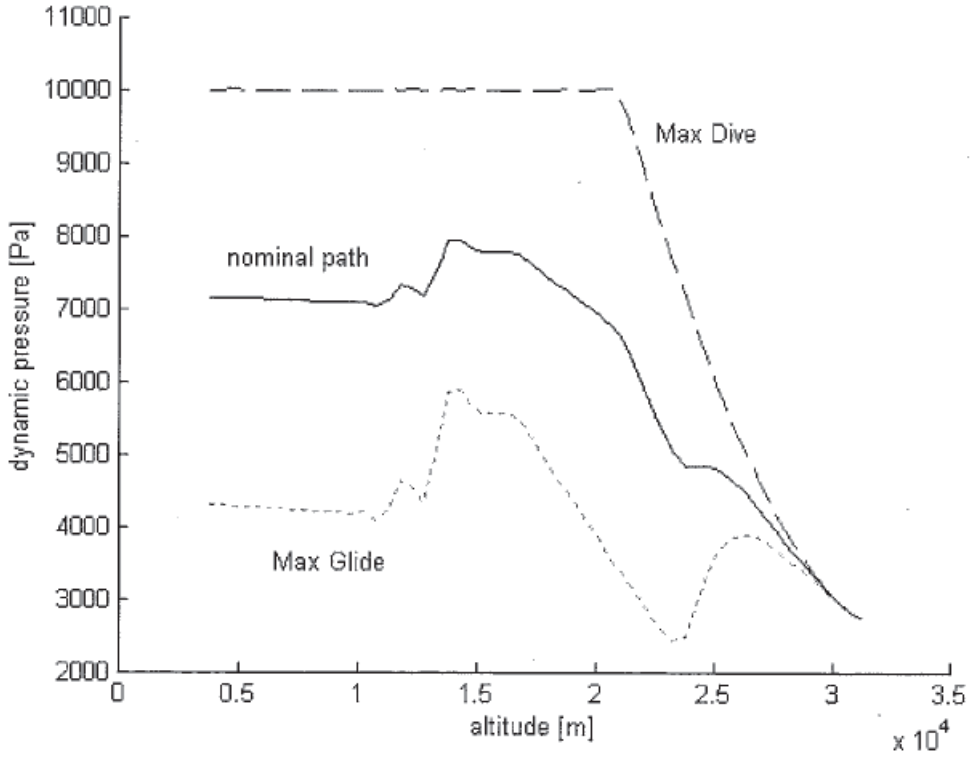

Figure 5.14: TAEM vertical corridor bounded by maximum range and maximum dive (Buechner, 2003)

5.6.2 Terminal trajectory planning and optimization for an unpowered RLV

(Kluever & Horneman, 2005) describes a new guidance scheme for the TAEM phase of an unpowered RLV. The new guidance algorithm uses an on-board trajectory planning algorithm that generates a reference path. Once the reference trajectory is generated, the guidance algorithm generates both open-loop and closed-loop commands to track the calculated reference trajectory.

The planning algorithm is based on a predicted ground track consisting of the same geometrical segments as those of the Shuttle, the energy state and the vehicle's aerodynamic performance. The planning algorithm calculates several feasible trajectories by iterating on three geometric parameters relates to the HAC and by propagating a trajectory along the ground track defined by the three HAC parameters. A conical HAC is used and the three HAC parameters consist of the final radius of the HAC, a coefficient that determines the tightness of the HAC and the downrange position of the HAC. When all the iterations are completed, the best reference geometry and corresponding reference profiles are selected according to a desired performance index. The trajectories are calculated by propagating the energy height along the ground track and propagation stops at the desired energy height. Because the propagation stops at the desired energy height, the propagated trajectory may reach the final energy height at a range that overshoots or undershoots the fixed ALI downrange distance. The amount of overshoot or undershoot determines if a solution is feasible or not.

The energy height is propagated by using a simple Euler integration scheme and the equation for the dissipation of energy with respect to range, equation 5.2. The values that determine this energy rate must be calculated according to a longitudinal strategy. Current values for velocity,

drag coefficient, atmospheric density and flight-path angle are required to compute the energy rate. The atmospheric density is calculated using an exponential model. The other parameters are all based on a reference altitude profile defined by a quadratic polynomial.

A second item in the paper was to obtain optimal trajectories. Optimal trajectories were obtained for both nominal and off-nominal conditions. These trajectories differ from the trajectories that utilize a trajectory geometry derived from the Shuttle. For a bank angle which is limited $\pm$ 20°, the optimal trajectory shows a 'bang-bang' structure. This is a bank reversal in the lateral direction, which means that first a full bank is applied away from the HAC followed by a full bank turn to the proper runway heading. These maneuvers increased the ground track distance. In the vertical plane, the optimal trajectories showed two pull-up maneuvers to modulate the dynamic pressure and to extend the ground range.

5.6.3 Terminal guidance for an unpowered RLV with bank constraints

The guidance algorithm as described in the previous section is adapted in (Kluever, 2007) to an unpowered RLV that has known, limited bank capabilities. These reduced capabilities may be the result of actuator failures. It is assumed that the bank limitations are known before the start of the terminal area.

Although the guidance algorithm as described in (Kluever & Horneman, 2005) is adapted, the general principle of propagating feasible trajectories and selecting the best trajectory is still used. Important differences include the parameters that are used to describe the ground track and the strategy that is used during the propagation.

Based on the optimal trajectories for limited bank capabilities, see (Kluever & Horneman, 2005), the parameters that describe the ground track are changed to the bank reversal switch time and the downtrack location of the HAC. Different combinations of these parameters result in different ground tracks. Similar to the planning algorithm as described above, trajectories are propagated along several ground tracks by numerical integration. Feasible trajectories are stored and the best trajectory is chosen based on the evaluation of the normalized terminal state error. The best trajectory with the accompanying two parameters is used as the reference trajectory. Control laws are used to track this reference trajectory.

The propagation of the energy along the ground trajectory must be done according to strategy. In this paper, a control law is used during the propagation that uses a dynamic pressure tracking scheme. A vertical guidance law is used to track the minimum dynamic pressure, by regulating the lift coefficient.

The minimum dynamic pressure is used for all trajectory planning simulations. Off-nominal conditions are dealt with by only adapting the ground track, while the longitudinal strategy is kept fixed. An improvement might be to both adapt the longitudinal strategy and the ground track.

5.6.4 In-flight TAEM/final approach trajectory generation for RLVs

(Hull, Gandhi, & Schierman, 2005) describes another RLV guidance algorithm that accounted for effector failures. This guidance algorithm is an optimization based only trajectory generation

and reshaping method. This method can adapt the trajectory in case a effector failure occurs during the flight. In case of an effector failure, the rate at which the vehicle dissipates energy might be too large or too small to reach the desired touchdown conditions without changing the trajectory. The solution is an online trajectory reshaping method.

The key elements of the in-flight generation and reshaping algorithm are a parameterized trajectory model to efficiently describe the trajectory, an optimal updating procedure to correct these parameters online in response to changes in the vehicle's aerodynamic characteristics and an efficient method to convert the trajectory parameters to the reference trajectory commands.

Important to note is that the TAEM and approach and landing phase are combined to form a single trajectory generation problem because it is stated that under certain extreme high energy or low energy failure scenarios, the requirement that the vehicle passes through the nominal interface point between the two phases is an overly-limiting constraint that makes it more difficult to find feasible trajectories.

The parameterized trajectory model consists of two model parameters that determine the vehicle trim condition, two longitudinal geometric parameters and two lateral geometric parameters. More information about these parameters, about the transformation of the trajectory parameters to reference trajectory commands and about the online trajectory reshaping algorithm can be found in (Hull et al., 2005). Only the longitudinal parameters are discussed below because it is important for the current study.

The longitudinal trajectory parameters define the shape of the dynamic pressure command profile over altitude. Specifically, the shape of the shallow glide slope and final flare portions of the profiles are controlled by the two longitudinal parameters: the altitude to begin the pull-up maneuver and the desired touchdown dynamic pressure. Above a particular altitude that specifies the boundary between the terminal area and the landing, the shape of the dynamic pressure is predetermined and static. This means that a fixed dynamic pressure is used, as a function of altitude, for every possible off-nominal condition. This reference dynamic pressure is placed in between the vehicle's maximum range and maximum dive capabilities. The planning and reshaping algorithm does not changes the dynamic pressure profile during the terminal area in case of off-nominal conditions. Moreover, it is not investigated if the dynamic pressure profiles for a maximum range and maximum dive changes for different off-nominal conditions.

Other terminal area studies are described in (Camara, 2003), (Chartres, 2007), (Girerd & Barton, 2000) and (Mayanna, Grimm, & Well, 2006). These studies are not discussed in this thesis study and the reader is referred to the documents for further information.

5.7 Summary and study objectives

There are two important classes of terminal area guidance systems. The first class is based on guidance using reference trajectories, while the second class is based on guidance using predicting capabilities. In case reference trajectories are used, the actual flight state is compared to the nominal reference trajectory and control laws generate commands to bring the actual

trajectory to the reference one. The guidance system of the Space Shuttle uses such reference trajectories. An important disadvantage of the Shuttle algorithm is that the flexibility of pre-computed reference profiles to state deviations due to both expected and unexpected situations is limited, because the guidance relies upon pre-mission planning. To solve this problem, several terminal area studies have investigated to adapt the reference trajectories based on the initial state (onboard planning). In these guidance systems, off-nominal conditions are dealt wilt by adapting the lateral ground track, while the longitudinal strategy remains unchanged. The adaption of the ground track is done by trajectory propagation and by iterating on a few parameters that describe the trajectory in the ground plane. The best configuration is selected and is used during the terminal area. The longitudinal strategy, as used during the trajectory propagation, is specified by a fixed reference dynamic pressure and is tracked by a controller. In some cases, even a constant dynamic-pressure profile is used, as a function of altitude. Hence, a single strategy or even a single longitudinal reference profile is used without investigating the influence of off-nominal conditions on this profile. Moreover, it is not investigated if a combination of adapting both the lateral ground track and the longitudinal strategy would yield better results when off-nominal conditions occur.

Another possibility to deal with off-nominal conditions is to use a predicting-capability based guidance algorithm. Saab Space proposed such a guidance algorithm for the HORUS-2B. A guidance system using predicting capabilities does not need any reference trajectory. The commanded control variables are determined by estimating the required energy to reach the runway and comparing this with the vehicle its current energy. This energy estimator is the key feature of the HORUS guidance. In the system designed by Saab Space, this estimator is based on analytical formulas. Large errors in energy estimation can occur using this estimator and hence, an improved energy estimator is required. A suggestion is to solve the equations numerically onboard. Also, in the Saab Space study, a fixed HAC placement is used and HORUS is forced to always execute a left-hand turn around the HAC. The concept of an improved energy estimator in combination with a variable HAC placement yields a high flexibility regarding off-nominal conditions. This energy estimation and automatic HAC selection scheme (HAC planning) are the main topics of this thesis study.

If a guidance system has to be designed which uses predicting capabilities, it is very important to know the correct vertical corridor. This vertical corridor determines the capabilities of the vehicle in terms of the maximum range that it can fly and the maximum dive that it can perform. These boundaries are required during the energy estimation. Moreover, these boundaries are also important for guidance systems using an explicit reference trajectory. In the guidance systems as described above in section 5.6, off-nominal conditions are dealt with by adapting the lateral ground track, but using a fixed longitudinal strategy. A different longitudinal strategy results in a different ground track. The dynamic profile that is used as the longitudinal strategy, is placed in between the maximum range and the maximum dive boundary. Hence, it is necessary to study and analyze the maximum range and maximum dive trajectories.

In the introduction, the calculation of the optimal trajectories is mentioned as one of the study goals. Based on the observations as described above, focus will be on optimal longitudinal strategies and trajectories. This results in the following questions that will be addressed during the optimization:

- What are the optimal strategies to perform a maximum-range and a maximum-dive flight?
- What is the influence of variations in initial altitude and velocity on these strategies?

It is impossible to calculate onboard a complete optimal trajectory, in terms of steering commands. This is computationally too expensive. It is only possible to do an optimization of a small set of parameters that describe the trajectory, as is done for example in (Hull et al., 2005). Also during the optimization of the longitudinal strategies in this thesis study using genetic algorithms, see chapter 7, it will be found that this is computationally to expensive to apply in an onboard system. Hence, fast approximations are required. This will be accomplished by analyzing the obtained optimal results (chapter 8) and by designing guidance laws for the longitudinal motion (chapter 9). This corresponds with another study goal as mentioned in the introduction.

Using the obtained guidance laws, the required energy can be estimated. Questions related to energy estimation that will be studied in chapter 10, include:

- What is the minimum energy required to fly a specific distance?
- What is the maximum energy with which a specific distance can be flown without overshooting the target?
- What is the influence of a change in initial position and velocity on these minimum and maximum energy levels?

Next to the energy estimation issue, also a HAC planning algorithm is required for HORUS. This planning algorithm is based on the obtained maximum range and maximum dive strategies and is described in chapter 11. A similar approach is used as described in (Kluever & Horneman, 2005) and (Kluever, 2007). Chapter 12 describes an analysis of how this planning algorithm is able to cope with off-nominal conditions by calculating an new HAC geometry. This concludes the study goals as mentioned in the introduction.

Chapter 6

Terminal area trajectories based on steady-state approximation

To overcome the problems of computational complexity encountered in optimal control problems, efforts have been made to generate near-optimal solutions based on simplified system models (Visser, 2007). The steady-state approximation is the most basic approximation and is commonly applied in other terminal area studies, especially for the maximum range problem. Hence, the steady-state approximation is a valuable and valid first step in the performance investigation of HORUS and the analysis of terminal area trajectories. In the next two chapters, optimal terminal area trajectories will be studied and compared to the solutions obtained in this chapter using the steady-state approximation. As described earlier, a steady flight is a flight situation in which the forces (and moments) acting on the vehicle do not change with time, neither in magnitude nor in direction.
Section 6.1 describes the maximum range capability of HORUS based on the steady-state approximation, while a diving flight is discussed in section 6.2. The steady-state turning performances is described in section 6.3.

6.1 Maximum range glide in the vertical plane

The capabilities of the vehicle are bounded by the maximum range that it can fly, given an initial state, and the minimum distance that can be obtained by using a maximum dive strategy. These two boundaries limit the capabilities of the vehicle. Any point situated between these two boundaries can be reached by the vehicle. Moreover, to extend the flexibility of selecting a terminal area trajectory to the landing spot in case of off-nominal conditions, it is of interest to know the maximum range that can be reached from both the terminal area entry point and from each state during the TAEM. The maximum range capability is discussed in this section, while section 6.2 describes a diving flight.

6.1.1 Theory of steady state maximum range glide

The fundamental tool used in the steady-state glide theory is the performance curve or the velocity polar. An example of a performance curve is given in figure 6.1. The performance

curve gives an indication of the point performance of the vehicle (Ruijgrok, 1996). This curve tells us the rate of descent of the vehicle at each horizontal velocity. The length of a vector from the origin to a point on the performance curve represents the magnitude of the airspeed along the flight path that corresponds to that path. The angle confined between the horizontal axis and the velocity vector is the flight path angle. The performance curve is only valid for a specific altitude and specific vehicle weight.

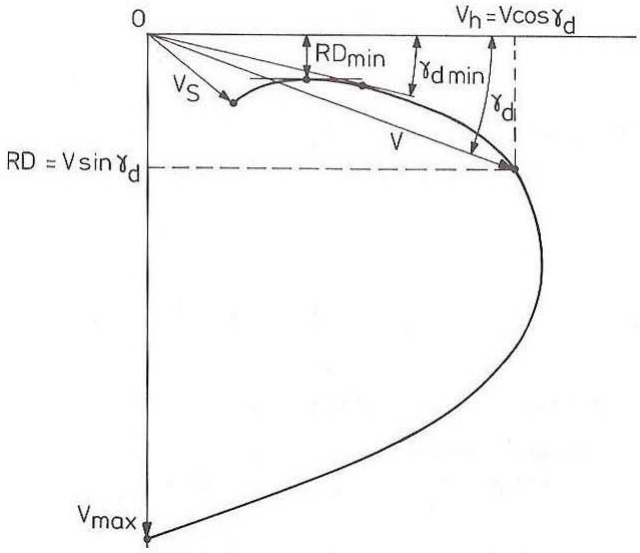

Figure 6.1: Performance curve for a gliding flight. RD = Rate of Descent (Ruijgrok, 1996)

The performance curve is constructed by using the force equations for a stationary glide. Assuming a constant magnitude of the velocity ($\dot{V} = 0$), a constant direction of the velocity ($\dot{\gamma} = 0$) and a zero bank angle, the dynamic equations specified by equations 2.31 and 2.32 are reduced to:

$$-D - mg\,sin\gamma = 0 \tag{6.1}$$

$$L - mg\,cos\gamma = 0 \tag{6.2}$$

These equations represents a force equilibrium both in parallel and normal direction with respect to the flight path, see figure 6.2. The resulting aerodynamic force (vector sum of lift force and drag force) is in equilibrium with the weight. Substituting the expressions for the lift and drag force gives:

$$-C_D\frac{1}{2}\rho V_G^2 S = mg\,sin\gamma \tag{6.3}$$

$$C_L\frac{1}{2}\rho V_G^2 S = mg\,cos\gamma \tag{6.4}$$

The airspeed in a stationary glide is obtained by re-writting equation 6.4:

$$V = \sqrt{\frac{mg}{S}\frac{2}{\rho}\frac{1}{C_L}cos\gamma} \tag{6.5}$$

Dividing equation 6.4 by equation 6.3 gives an expression for the flight path angle:

$$-tan\gamma = \frac{C_D}{C_L} \tag{6.6}$$

The rate of descent is equal to the vertical component of flight velocity. Using the velocity and the flight path angle, the rate of descent is defined as:

$$RD = V sin(\gamma) \tag{6.7}$$

At low subsonic velocities and ignoring the Reynolds number effect, the quantities V_G, γ_G and RD are fully determined by the angle of attack through the lift and drag coefficient (Ruijgrok, 1996).

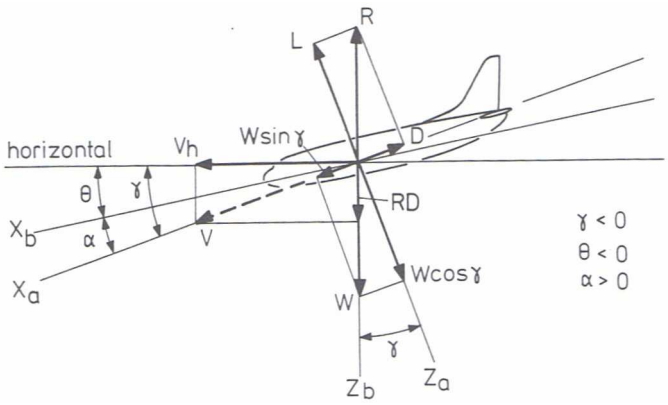

Figure 6.2: Steady glide conditions (Ruijgrok, 1996)

The performance curve for a specific altitude can be calculated by a simple proces:

- take a specific value for the angle of attack
- compute the corresponding values for the lift and drag coefficient
- calculate the flight path angle and velocity
- calculate the rate of descent and the horizontal velocity
- repeat this process for the whole angle of attack interval

Important to note is that the performance curve can only be calculated if it is physically possible to obtain a steady state situation, i.e. if the aerodynamic coefficients and characteristics allow the vehicle to obtain this stationary state.

Two important points can be obtained from the performance curve:

- **Point for maximum endurance**
  The maximum endurance (maximum amount of flight time) occurs when the rate of descent is the smallest and can be found at the point where the performance curve has a horizontal tangent. This corresponds with RD_{min} in figure 6.1.
- **Point for maximum range**
  In a steady glide, the maximum range is flown with a maximal ratio between the horizontal velocity and the negative of the rate of descent (Reichmann, 1976). This maximum ratio can be found by drawing a line in the performance curve from the origin, tangent to the

performance curve, see figure 6.1. The corresponding horizontal velocity and the rate of descent can be found by just reading the values on the horizontal and vertical axis. Note that a maximum range flight is conducted at a higher velocity than for a maximum endurance flight. As can be seen from figure 6.1, the maximum range glide is flown with the minimal flight path angle. Using equation 6.1 and 6.6, this minimum flight path angle requirement for a maximum range flight is transformed to a minimum drag requirement and a maximum lift to drag ratio, $(C_L/C_D)_{max}$, requirement.

Because of this last element, a common interpretation of the steady-state approximation is to construct an angle-of-attack profile for a maximum lift to drag ratio, as a function of velocity or Mach number, and use this profile to calculate the maximum range.

In a steady gliding flight, the rate of dissipation of energy due to the drag, must be equal to the rate of loss of potential energy (Welch, Welch, & Irving, 1970). Normally, the total rate of energy dissipation consists of a two terms, one accounting for the rate of potential energy and another term accounting for the rate of kinetic energy. But because in a steady gliding flight where nor the magnitude nor the direction of the velocity changes and hence the rate of kinetic energy is equal to zero, the total rate of energy dissipation is equal to the rate of potential energy.

The performance curve as given in figure 6.1 indicates that the rate of descent during a maximum range flight is larger than RD_{min}. Hence, it can be concluded that a maximum range flight is conducted at a velocity for which the rate of total energy height dissipation $\frac{dE_h}{dt}$ is larger than the minimum value. The energy height E_h has been defined in section 2.6.

Because of the changing density, altitude has an effect on the performance curve. A performance curve is only valid for a specific altitude and hence, several performance curves can be constructed for different altitudes. The lower the density, the faster the vehicle flies and sinks. But the ratio between the velocity and the sink rate stays the same (Reichmann, 1976). This means that the performance curve shifts downward and to the right along a straight line through the origin when the altitude increases and the density decreases. The performance curves for different altitudes have joint tangent and hence the same minimum flight path angle for maximum range.

The ratio of the steady glide velocity for a maximum range glide at an altitude h_1 and at sea level h_0 is calculated by using equation 6.5, inserting the constant flight path angle and assuming a constant lift coefficient:

$$\frac{V_{h1}}{V_{h0}} = \sqrt{\frac{\rho_0}{\rho_1}} \tag{6.8}$$

This equation shows that a maximum range flight requires that the vehicle is controlled such the dynamic pressure or equivalent airspeed is kept constant throughout the glide. So the gliding vehicle actually executes a quasi-steady flight where the equivalent airspeed is kept constant, but the true airspeed decreases when the altitude decreases. Hence, another improved solution to the maximum range problem based on a steady-state approximation, is to keep the dynamic pressure or equivalent airspeed to the required constant value. This constant equivalent airspeed interpretation of the maximum range problem is used in (Helmersson, 1988b).

It can be concluded that by making a quasi-steady assumption, the maximum range problem has moved from dynamic optimization problem to a static optimization problem. The global path optimization problem has been reduced to solving a sequence of local point performance

problems. By optimizing the point performance problem for a range of altitudes, an estimation of the overall quasi-steady path performance can be obtained.

When speeds are relatively low, it is quite acceptable to use a quasi-steady approximation (Visser, 2007). Hence, the performance curves of HORUS are calculated only for subsonic velocities.

6.1.2 Performance curves of HORUS

Constructing the performance curve for HORUS is somewhat more difficult than for a simple subsonic glider, because the aerodynamic data of HORUS cannot be specified by one lift and drag curve, due to the effects of compressibility at high velocities. Several lift and drag curves exist for different Mach numbers, see appendix A. The lift and drag coefficient are not only dependent on the angle of attack but also on the Mach number. Changing the velocity means a change in Mach number and hence, a different lift and drag curve has to be used in order to find the corresponding lift and drag coefficient.

Due to this effect, the calculation of the performance curves becomes more complicated and an iterative process is required to find a single point on the performance curve for a specific altitude. The steps required to find a single point on the performance curve, i.e. the horizontal velocity and the rate of descent, corresponding to a specific velocity V_{req} between the stall speed and maximum velocity, are:

- 1. calculate corresponding Mach number for V_{req} at the required altitude
- 2. use an initial guess of the angle of attack
- 3. calculate lift and drag coefficients
- 4. calculate flight path angle; equation 6.6
- 5. calculate velocity V; equation 6.5
- 6. compare V with V_{req}
- 7. update the guess for angle of attack and repeat steps 3, 4, 5 and 6 until the difference between V and V_{req} is small enough
- 8. When the difference is small enough, one has found the angle-of-attack and flight path angle corresponding to V_{req}. The horizontal component of the velocity and the rate of descent can now be calculated.

Finding the required angle-of-attack and flight path angle required for a specific velocity is an iterative process. Repeating the process as described above for several velocities between the stall speed and the maximum velocity yields the complete performance curve for a specific altitude.

Figure 6.3 shows the calculated performance curves for HORUS at altitudes between sea level and 12 km, while the characteristics of the stationary maximum range points are give in table 6.1. Note that only a part of the performance curves can be used because of the maximum velocity boundary. All the stationary maximum range points have Mach numbers below 0.8.

The table indicates that in a subsonic glide, the equivalent airspeed has approximately a constant value of 116 m/s while the true velocity varies. This is consistent with the definition of a quasi-steady flight. The corresponding angle-of-attack for a maximum range glide is also approximately constant and is equal to 7.5°.

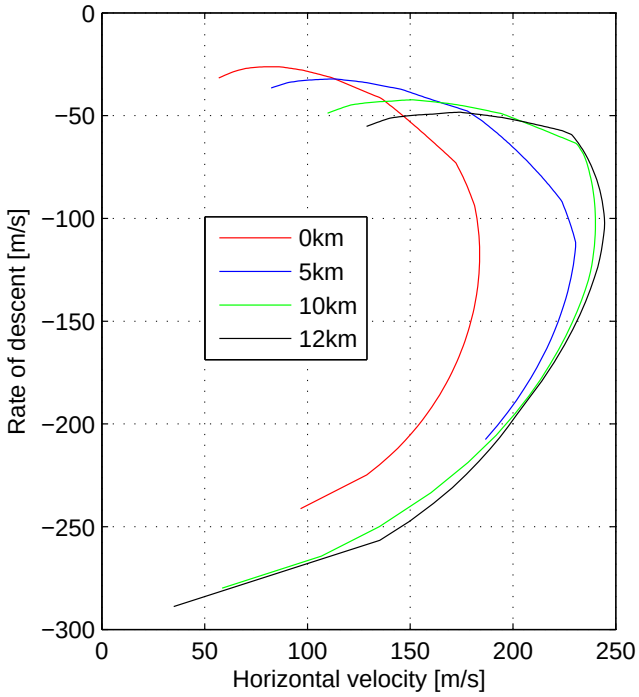

Figure 6.3: Performance curves for 0-12 km altitude

Table 6.1: Stationary maximum range points for 0-12 km altitude

Altitude	**0km**	**5km**	**10km**	**12km**
Ground velocity [m/s]	116.09	150.10	200.10	231.09
Horizontal velocity [m/s]	111.75	145.43	194.02	223.88
Rate of descent [m/s]	31.47	37.14	48.96	57.28
Angle of attack [deg]	7.52	7.54	7.60	7.50
Flight path angle [deg]	-15.73	-14.33	-14.16	-14.35
Equivalent airspeed [m/s]	116.09	116.35	114.93	116.63
Mach	0.34	0.47	0.67	0.78

6.1.3 Steady state maximum range flight of HORUS

In several terminal area studies, the angle-of-attack profile for maximum lift to drag ratio interpretation is used to solve the maximum range problem, see (Camara, 2003) and (Buechner, 2003), where this interpretation is even extended to the supersonic speed regime. The angle-of-attack profile for maximum lift-to-drag ratio, as a function of velocity, is calculated over the complete velocity regime. Hence, a good starting point for calculating the maximum range

performance of HORUS is to perform simulations using the angle-of-attack profile for maximum lift-to-drag ratio. In addition, these simulations serve as a benchmark for the the optimised maximum range trajectories, which are calculated in section 7.3. The simulations are performed using the full nonlinear equations of motions.

The maximum lift-to-drag ratio angle-of-attack profile for HORUS is shown in figure 6.4. This profile is obtained by studying the aerodynamic data as given in appendix A, where for each Mach number, the maximum lift to drag ratio value and the corresponding angle-of-attack can be obtained from the graphs. The obtained data is given in table 6.2.

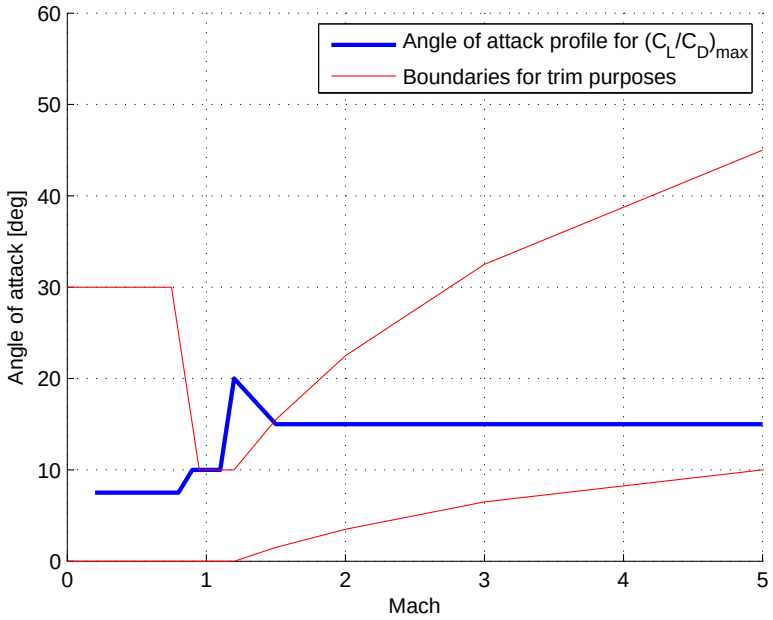

Figure 6.4: Angle-of-attack profile for maximum lift-to-drag ratio as a function of Mach number

Table 6.2: Angle-of-attack and maximum lift-to-drag ratio as a function of Mach number

Mach	0.20	0.60	0.80	0.90	0.95	1.05	1.10	1.20	1.50	2.00	3.00	5.00
α **[deg]**	7.5	7.5	7.5	10.0	10.0	10.0	10.0	20.0	15.0	15.0	15.0	15.0
L/D_{max}	3.75	4.00	3.90	2.73	1.82	1.76	1.74	2.0	2.20	2.27	2.27	2.13

Subsonic maximum range glide

In the subsonic flight regime, maximum range simulations were performed for three initial points, all with an identical energy height of 10 km but with a different distribution of this total energy in kinetic and potential energy. The sum of the potential and kinetic energy for the three initial points is identical, but the ratio of potential and kinetic energy is different for the three initial points.

Table 6.3 shows the initial conditions for the three different starting points, together with

the attained maximum range. The initial flight path angle used in the simulations, was the calculated flight path angle required for an initial equilibrium flight situation. Figure 6.5 shows the altitude, velocity, flight path angle and energy height as a function of range for the three maximum range simulations. These figures indicate that the fluctuations in the parameters are larger for starting points 1 and 3 with respect to starting point 2.

It is common to use one specific value for the minimum energy height which is needed to reach a specific target range. If the energy state of the vehicle falls below this value, the target range cannot be reached. However, figure 6.5 and table 6.3 indicate that although the initial energy height is equal for all three simulation cases, the obtained maximum range is different for the three trajectories. It seems that the distribution of the total energy in kinetic and potential energy is important in determining the maximum range. It looks like there is an optimal value for the distribution of the total energy. This will be further discussed in section 8.2.2. Hence, it is not possible to only specify the minimum required energy height for a specific target range, but it is also necessary to specify for which combination of altitude and velocity this is valid. This is an important conclusion for studying the maximum range and required energy during off-nominal conditions. This will be further discussed in chapter 10.

Table 6.3: Initial conditions and maximum range using angle of attack for maximum lift to drag ratio for three different starting points with initial energy height of 10 km

	V_G **[m/s]**	**h [km]**	γ_G **[deg]**	**Range** $\alpha_{(L/D)max}$ **[km]**
Startpoint 1	108.50	9.40	-29.24	32.78
Startpoint 2	171.60	8.50	-14.55	34.88
Startpoint 3	228.00	7.35	-17.65	33.76

Supersonic maximum range glide

Starting in the supersonic speed regime, maximum range simulations were performed for three initial points, all with an identical energy height of 52.513 km but with a different distribution of this total energy in kinetic and potential energy.

Table 6.4 shows the initial conditions for the three supersonic starting points and the attained range using the angle of attack profile for the maximum lift to drag ratio. In (Mooij, 1998), simulations were performed for the atmospheric re-entry phase of the Horus. The final flight path angle at the TAEM interface was -10°, hence the initial flight path angle in this terminal area study is set to -10°. All supersonic simulations were performed with this initial flight path angle. The initial position and velocity of starting point 6 are the nominal conditions used in the TAEM study of the Horus as described in (Jarmark, 1988) and (Helmersson, 1988b).
Figure 6.6 shows the variation of altitude, velocity, flight path angle and energy height as a function of range. Similar to the subsonic maximum glide range, depending on the distribution of the total energy in potential and kinetic energy the maximum attained range differs. The figure also indicates fluctuations in altitude, velocity and flight path angle.

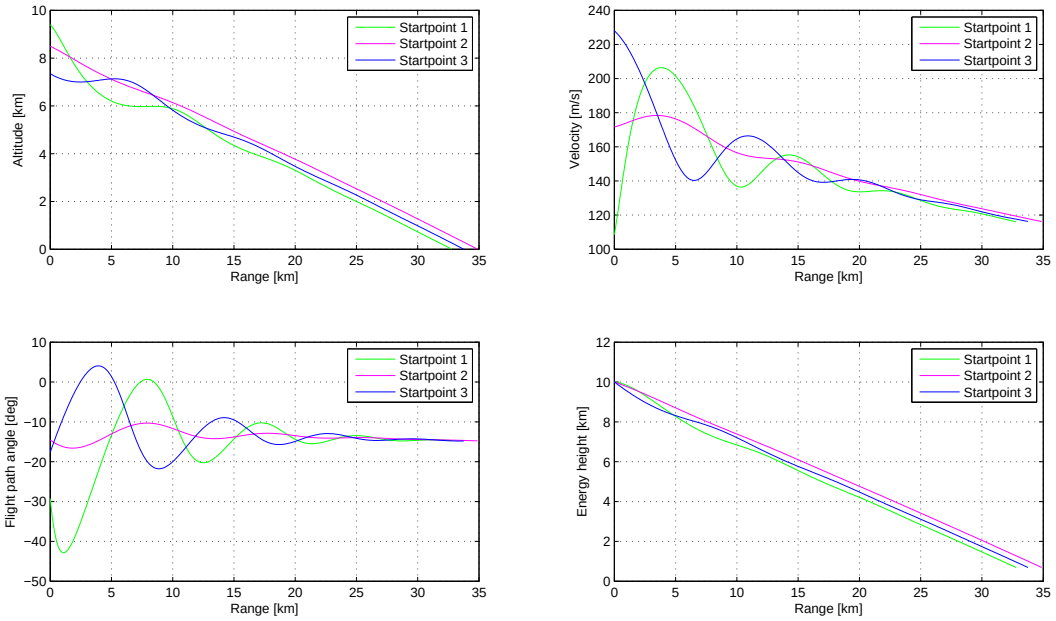

Figure 6.5: Nonlinear simulation results for three subsonic initial states with the same energy height of 10 km. Speedbrakes fully retracted; straight flight; using angle-of-attack profile for maximum lift-to-drag ratio.

Table 6.4: Initial conditions and maximum range for three different starting points with initial energy height of 52.513 km and initial flight path angle of -10 degrees

	V_G [m/s]	h [km]	Range $\alpha_{(L/D)max}$ [km]
Startpoint 4	583.10	35.00	134.63
Startpoint 5	661.64	30.00	136.35
Startpoint 6	732.00	25.00	130.79

6.1.4 Limitations of steady-state approximation

An important fact that can be concluded from the discussion on a subsonic and supersonic maximum range flight of HORUS, is that both the velocity and flight path angle, using the angle of attack profile for a maximum lift to drag ratio, are not constant. This is in violation with the original steady-state assumption.
Furthermore, it was already stated that for relatively low velocities, it is acceptable to use a steady-state approximation. But during the simulations, the use of an angle-of-attack profile for maximum lift-to-drag ratio was extended from subsonic to supersonic velocities without any proof that this really results in a maximum range flight.
A winged re-entry vehicle enters the TAEM phase at about Mach 2.5 and needs to dissipate the kinetic energy excess in order to meet with the required final TAEM conditions at about Mach 0.5. So the vehicle performs a decelerating gliding flight and hence, it is a dynamic process. Due to the presence of this dynamic term, it is not always possible to solve the maximum range flight as a sequence of static problems, and one is forced to resort to dynamic optimization techniques.

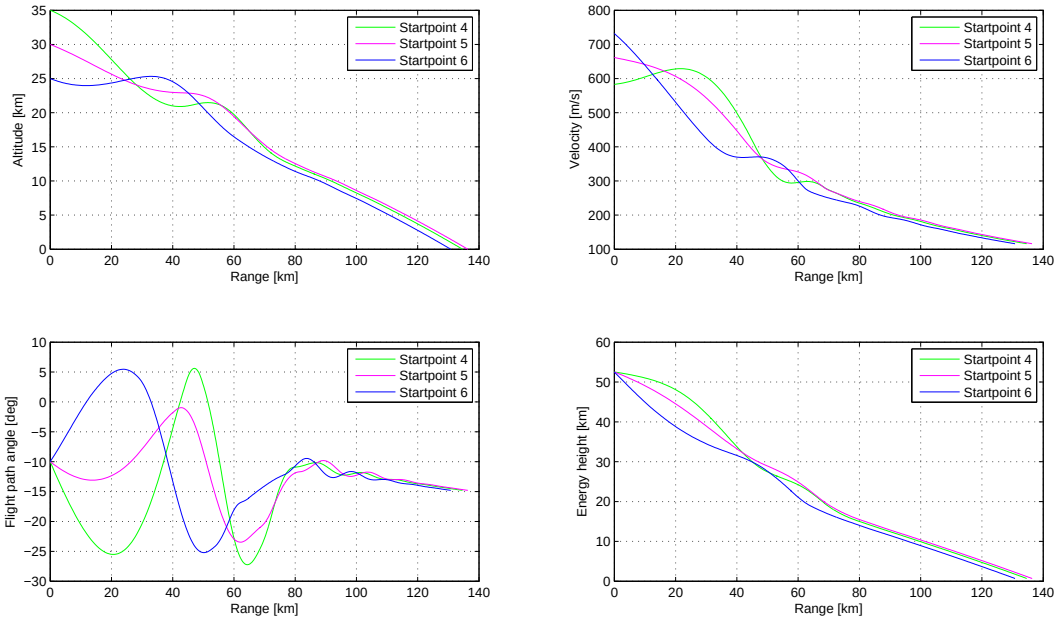

Figure 6.6: Nonlinear simulation results for three supersonic initial states with the same energy height of 52.513 km. Speedbrakes fully retracted; straight flight; using angle-of-attack profile for maximum lift-to-drag ratio

Based on these conclusions, some questions can be raised:

- Is this strategy of following the angle-of-attack profile for a maximum lift-to-drag ratio the correct strategy, which results in the maximum range?
- Is there another strategy, which will allow HORUS to fly a larger distance than the one obtained using the angle-of-attack profile for maximum lift-to-drag ratio?

To address these questions in section 7.3, a GA will be used to calculate the maximum range of HORUS for the same six starting points as used in this section. The GA will calculate the optimal control vector, in terms of angle of attack, that yield the maximum range.

6.2 Diving flight in the vertical plane

Besides the maximum range, the capabilities of the vehicle are also limited by the minimum attainable distance. The minimum range capability corresponds to a maximum dive.

In section 6.1.1, it was stated that the maximum range is obtained by flying at the smallest flight path angle and with the lowest amount of drag. Hence, it is logical that a diving flight is executed at a larger flight path angle and drag level. Looking at figure 6.1, it can be seen that a larger flight path angle can be obtained by flying either at a lower velocity or at a higher velocity, with respect to the velocity required for a maximum range flight. Of course, the most natural instinct in a diving flight is to lower the nose and hence to dive towards the ground with a larger velocity. In (Buechner, 2003), this diving strategy was used and the maximum dive

path was calculated using a diving flight at maximum dynamic pressure or maximum velocity.

In order to dive more rapidly, speedbrakes can be used. A speedbrake deflection is modeled as an increase of the drag coefficient. Using equation 6.6, this increase in drag results in a steeper trajectory. Table 6.5 shows the flight path angle, the drag level and the required angle-of-attack for two speedbrake settings at a stationary point at an altitude of 5.0 km with a velocity of 150 m/s. After an increase of the speebrake deflection, a larger flight path angle is required to have force equilibrium at the same velocity. The required angle-of-attack is slightly decreased. An increase in speed brake deflection directly increases the orbiter drag and steepness of the trajectory, both of which increase the dissipation of energy with respect to range.

Table 6.5: Flight-path angle, drag and angle of attack for a stationary point with an altitude of 5 km and a velocity of 150 m/s, as a function of speedbrake deflection

speedbrake deflection [deg]	γ **[deg]**	**drag [N]**	α **[deg]**
0.0	-14.81	65298.3	7.52
40.0	-20.05	87575.8	7.30

In section 7.4, a complete diving flight both with and without speebrakes is presented to indicate the difference in obtained range.

6.3 Turning performance

The basic maneuver to change the flight path heading is a coordinated turn without sideslip. Therefore, the focus in this section is on a steady curvilinear flight with wings banked and without sideslip. A complete turning flight is not discussed in this section. The goal is to indicate the influence of a turn on the capabilities of a vehicle based on steady-state assumption.

6.3.1 Theory of steady coordinated turn

Figure 6.7 shows a vehicle in a steady level coordinated banked turn. A coordinated turn is a turn where the inward centripetal force[1] required to pull the airplane toward the center of the turn is accomplished by the horizontal component of the lift and, where both the resultant aerodynamic force and the vector sum of the weight and the outward centrifugal force [2] are in the plane of symmetry of the vehicle (Ruijgrok, 1996). Due to the absence of sideslip in a coordinated turn, the side force is zero. In a banked flight situation, the direction of the lift vector is changed and is no longer parallel to the weight vector. In order to have an equilibrium between the vertical component of the resulting aerodynamic force vector and the weight vector, the magnitude of the lift must be larger than in a wings-level situation. If the velocity remains unchanged, this additional component is obtained by increasing the angle-of-attack.

In general, a gliding re-entry vehicle makes a descending turn. The equilibrium equations for the instantaneous conditions on the descending spiral flight path are obtained by assuming

[1] The centripetal force is the external force required to make a body follow a curved path
[2] The centrifugal force is an outward force associated with rotation

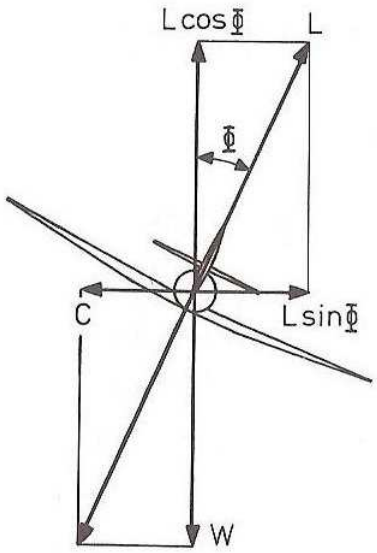

Figure 6.7: Vehicle in a steady level banked situation (Ruijgrok, 1996). Φ = bank angle σ

that the velocity does not change, nor in magnitude nor in direction ($\dot{V} = \dot{\gamma} = 0$). Using these assumptions, the dynamic equations as given by equations 2.31, 2.32 and 2.33, reduce to:

$$-D - mg\,sin\gamma = 0 \tag{6.9}$$

$$L\,cos\sigma - mg\,cos\gamma = 0 \tag{6.10}$$

$$\frac{L\,sin\sigma}{m\,cos\gamma} = V\,\dot{\chi} \tag{6.11}$$

The rate of turn is defined as the degrees/s the airplane changes heading and is represented by the term $\dot{\chi}$. For a gliding vehicle, the rate of turn is equal to:

$$\dot{\chi} = \frac{V\,cos\gamma}{R} \tag{6.12}$$

Inserting this in equation 6.11 and rearranging the terms gives:

$$\frac{V_G^2}{R}\,m\,cos^2\gamma = L\,sin\sigma \tag{6.13}$$

where the term on the left is the definition of the horizontal centrifugal force and the term on the right represents the horizontal component of the lift. So equations 6.11 and 6.13 state that in a coordinated turn, the centrifugal force is equal to the centripetal force. Hence, the vehicle has no tendency to move either inward or outward and travels long a circular path. The vehicle experiences only an additional force in a direction perpendicular to the plane of the wings and there will be no tendency of sliding in a lateral direction (no sideslip).

The additional force in a direction perpendicular to the plane of the wings is expressed by the load factor. The load factor is a parameter which describes the ratio of the lift force to the weight of the vehicle. Using equation 6.10, the load factor during a gliding turning flight is expressed by equation 6.14. The larger the bank angle, the larger the required additional lift force and hence, the larger the load factor.

$$n = \frac{L}{mg} = \frac{cos\,\gamma}{cos\,\sigma} \tag{6.14}$$

The airspeed in a gliding turn is obtained by inserting the expression for the lift force in equation 6.10 and rearranging the terms:

$$V = \sqrt{\frac{mg}{S}\frac{2}{\rho}\frac{1}{C_L}\frac{cos\gamma}{cos\sigma}} \tag{6.15}$$

Dividing equation 6.9 by equation 6.10 gives an expression of the flight path angle:

$$-tan\gamma = \frac{C_D}{C_L}\frac{1}{cos\sigma} \tag{6.16}$$

A relation for the radius of turn can be obtained by inserting the expression for the lift force in equation 6.13, using equation 6.15 and rearranging the terms:

$$R = \frac{V^2 cos\gamma}{g\, tan\sigma} \tag{6.17}$$

This equation indicates that the larger the bank angle and the lower the airspeed in a turn, the smaller the radius of turn will be.

6.3.2 Calculation of turning capabilities of Horus

Using the theory as stated in the previous, it is possible to calculate the subsonic turning performance of HORUS. This is only a point performance analysis, because the performance is expressed in terms of instantaneous quantities along a turning path.

To calculate the performance curves of HORUS during a steady turning flight, the same procedure is used as described in section 6.1.2. But now, each curve is calculated for a specific altitude and bank angle. The flight-path angle and the velocity during a turn are calculated using equation 6.16 and equation 6.15, respectively. The obtained performance curves for different bank angles at sea level are shown in figure 6.8. As a reference, also the performance curve for a level flight is given. The used velocity interval is limited by the stall speed and the maximum dynamic pressure. Figure 6.8 indicates that a larger bank angle induces a larger rate of descent. Several points with an equal value for the lift coefficient are also shown.

The corresponding required angle-of-attack for an equilibrium banked flight situation is indicated in the top left part of figure 6.9. Note that in figure 6.8, the values on the x-axis corresponds to the horizontal component of the velocity, while in figure 6.9, the x-axis indicates the magnitude of the real magnitude vector. In a banked flight situation, the required angle of attack for an equilibrium flight situation is larger than in a straight flight. This larger angle of attack is needed such that in a banked flight situation, an equilibrium exists between the vertical component of the resulting aerodynamic force vector and the weight vector, for the same velocity as in the level flight situation. The larger the bank angle, the larger the required angle of attack.

The radius of turn at each combination of bank angle and velocity for an equilibrium flight situation can be calculated using equation 6.17. The top right part of figure 6.9 shows the evolution of the turn radius as a function of velocity for different bank angles. This figure clearly indicates that the turn radius is smaller at lower velocities and higher bank angles.

The turning rates for the steady banked flight situations are calculated with equation 6.12 and the results are shown in the bottom left part of figure 6.9. The lower the airspeed and the

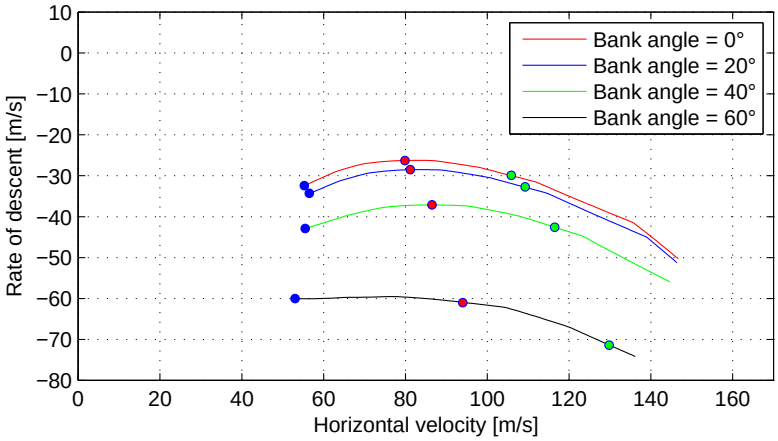

Figure 6.8: Performance curves for a steady-state banked flight situation using different bank angles in a subsonic velocity interval; Altitude = 0 m. The dots indicate points with an equal value for the lift coefficient; blue: $C_L = 0.79$; red: $C_L = 0.51$; green: $C_L = 0.30$

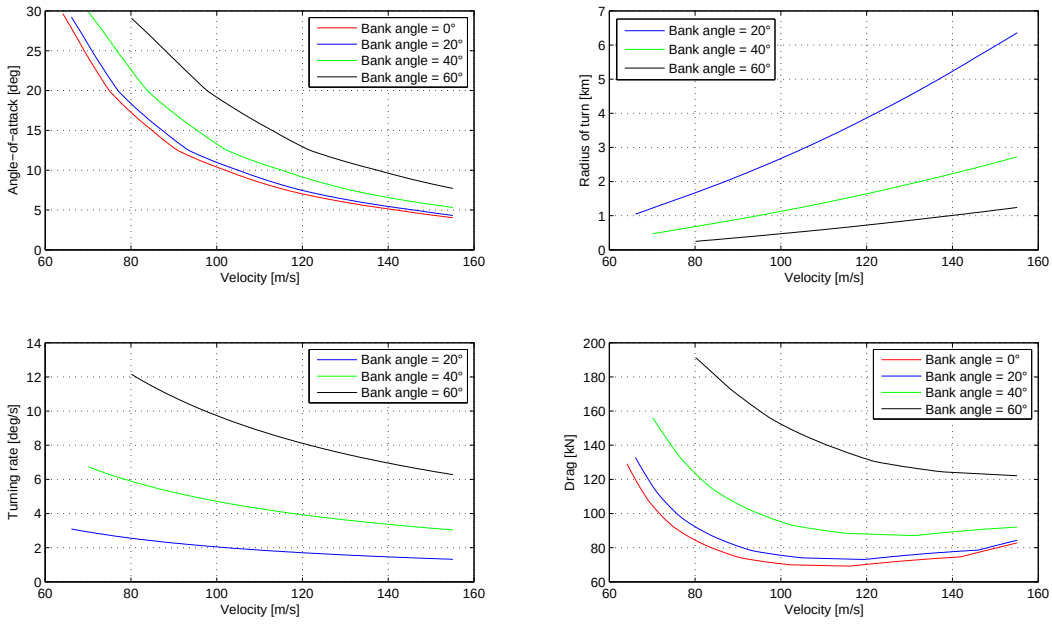

Figure 6.9: Required angle of attack, radius of turn, turning rate and drag for a steady state banked flight situation using different bank angles in a subsonic velocity interval. The real velocity is used rather than the horizontal component. Altitude = 0 m

larger the bank angle, the larger the turning rate of the vehicle.

In a gliding flight, energy is dissipated due to the drag of the vehicle. Hence, it is important to investigate the influence of banking and turning on the drag level. The lower right part of figure 6.9 shows that for a constant velocity, banking always increases the drag. This is due to the larger required angle-of-attack in a banked situation to fly at the same velocity as during a wings-level situation. But for a specific bank angle, there is one velocity and corresponding angle-of-attack for which the drag is minimal. If the desired turn radius is know, the required bank angle at different velocities can be calculated using equation 6.17. Analyzing the drag levels at different velocities will indicate a velocity for which the drag is minimal for the particular turn radius. This will be further discussed in section 8.4.

Till now, only banking maneuvers at sea level were considered. In order to investigate the influence of changing altitude on the banking performance of HORUS, a fixed bank angle of 40°is used. The performance curves are calculated for three different altitudes (0, 5 and 10 km), see figure 6.10. Increasing the altitude shifts the performance curve to the lower right. The characteristics of the points corresponding to a minimal flight path angle are summarized in table 6.6. These points have approximately the same equivalent airspeed. Equations 6.17 and 6.12 indicate that the turn radius and the turning rate are unaffected by the altitude, as long as the velocity and the bank angle are kept constant.

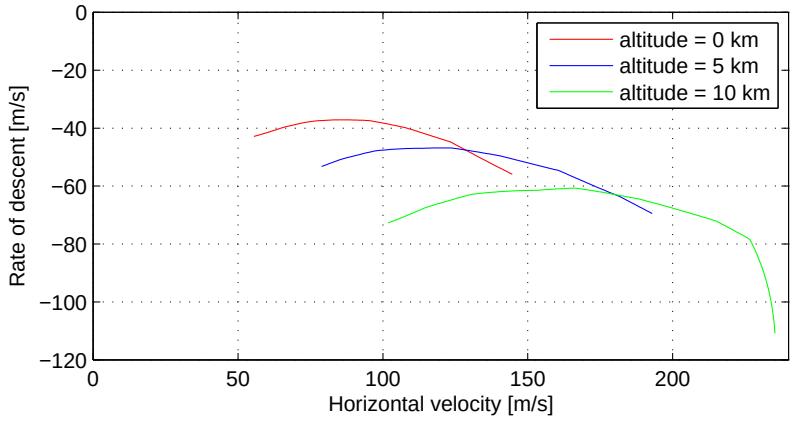

Figure 6.10: Influence of altitude on the rate of descent for a steady state banked flight situation with a fixed bank angle of 40 degrees

It is important to note that the performance analysis as given above, is only a point performance analysis and not an integral analysis of a complete turning flight. Consider again figure 6.9 and assume a constant velocity. Energy is dissipated through drag. So a lower drag results in a lower energy dissipation. The lower right part of figure 6.9 suggests that flying at a higher bank angle is not beneficial in terms of drag encountered during a specific instantaneous point during the turn. But the top right part, which shows the radius of turn, indicates that the radius of turn is smaller at higher bank angles. A smaller radius of turn means that the

Table 6.6: Stationary points with minimum flight path angle for a 40° banked turn at different altitudes

Altitude	**0km**	**5km**	**10km**
Flight path angle [deg]	-19.9	-18.8	-18.5
Horizontal velocity [m/s]	123.2	160.1	211.5
Velocity [m/s]	131.1	170.9	226.1
Equivalent airspeed [m/s]	131.1	132.4	131.4

distance around the turn is smaller and hence, a lower integrated drag and energy dissipation. This indicates that there is one optimal turn radius for which the integrated drag or integrated energy dissipation is minimum. This is further discussed in section 11.3.

Chapter 7

Optimization of Terminal Area trajectories

During the steady-state analysis of both the straight-level flight and the turning flight, it was indicated that this analysis has a limited applicability to the terminal area problem. Several limitations apply to the steady-state approximation. In this chapter, the real, optimal solutions for a straight-level flight and a turning flight will be investigated. The focus is on the optimal longitudinal control variable, i.e., the angle of attack, also during a turning flight. The obtained optimal solutions will be compared to the steady-state approximation to investigate the magnitude of the error introduced using the steady-state approximation. The main question during this chapter is: what are optimal longitudinal strategies, both in a straight flight and in a turning flight? All the optimal results are calculated using OPTIDUS.
Section 7.1 describes the possibilities for the control vector representation. The tuning of the GA for terminal area trajectory optimization is done in section 7.2. The optimal maximum range and maximum dive trajectories are calculated in section 7.3 and 7.4, respectively. Section 7.5 describes the optimal turning problem around a HAC.

7.1 Control vector representation

The genetic algorithm will optimize a control history of a specific control variable. Three representations are investigated: fixed grid points, variable grid points and a polynomial representation. But before discussing these representations in more detail, it is necessary to select an independent variable. The control variables will be expressed as a function of this independent variable.

7.1.1 Energy height as the independent variable

Energy is chosen as the independent variable instead of time, because the energy values are known, both at the beginning and at the end of the terminal area. This enables one to use a fixed interval of the independent variable, for which the optimal control variables will be calculated. The boundaries of the independent variable are known before the optimization

run. The final time at the end of the terminal area is not known and hence in that situation, the boundaries of the interval are not known beforehand. Since the energy of the vehicle is monotonically decreasing during a terminal area flight, energy was preferred above altitude or velocity as the independent variable, as both altitude and velocity can temporarily increase during the flight.Therefore, the output of the genetic algorithm will be the control history of a control variable as a function of energy.

7.1.2 N-vector formulation with fixed grid points

The most basic control-vector representation is a representation that uses fixed grid points of the independent variable. These grid points are specified by the user and do not change during a simulation or optimization. Figure 7.1 shows an example of a grid of energy points, with two known boundary values (E_{begin} and E_{end}) and two intermediate values (E1 and E2) that can be specified by the user. The optimizer calculates the optimal values of the control variable (alpha) at the grid points of the independent variable. The user can specify the values of the grid points such that the spacing between two successive grid points is constant for the complete interval, but different step sizes can also be used.

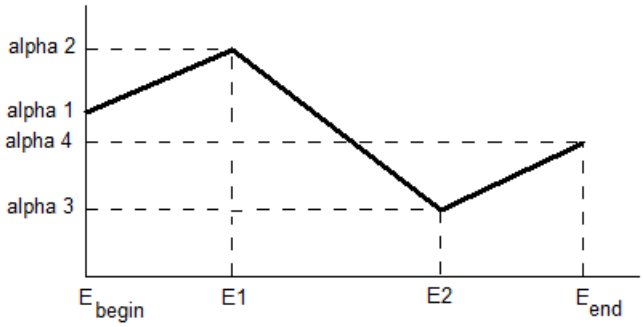

Figure 7.1: Illustration of energy grid with two intermediate grid points. When fixed grid points are used, the values of E1 and E2 are specified by the user and are fixed during the optimization. In case of variable grid points are used, the calculation of the intermediate grid points E1 and E2 is part of the optimization process.

Using an N-vector formulation with fixed grid points, the control variables are described and optimized at discrete points. The values of the control variables in between these data points are obtained through interpolation. During this thesis study, a linear interpolation is preferred above a cubic spline interpolation. In (Yokoyama & Suzuki, 2003), a cubic spline interpolation is used and the obtained results are shown in figure 4.2(b). A cubic spline guarantees a smooth transition at a nodal point and an interpolation function that is continuous through the second derivative. As can be observed in figure 4.2(b), near the end of the flight around 3000 seconds, this might result in oscillations between successive data points. Hence, a simple linear interpolation is selected for this study.

7.1.3 N-vector formulation with variable grid points

The disadvantage of the fixed grid points is that the step size or spacing between two grid points is fixed by the user before the simulation or optimization run. It is not possible to adapt this spacing to the flight situation. When transient flight situations occur, a smaller grid might

give a more accurate solution while on the other hand, a larger grid can be used in steady flight situations in order to safe computational time. This results in large steps in the grid of the independent variable, when the change in required maneuvers is small and the controls are almost constant, and small steps when maneuvers are required.

A solution would be to manually specify a finer grid in the region were maneuvers are required and a larger grid in steady situations. The grid would be again a fixed grid, which is specified before the optimization, and is kept the same during the optimization. This corresponds with grid points that are not equally spaced. This was already mentioned in the previous section. The problem is that case specific information about the flight is needed to determine the specific regions. Often, this information is not available before the simulation. The transient maneuvers and their time of occurrence are the outcome of the optimization. Moreover, a designed fixed grid is problem dependent and hence, for each specific optimization problem, a new fixed grid needs to be defined.

By making the size of the interval between two successive grid points a variable which can be optimized, the optimizer also searches for the optimal grid spacings. The number of grid points is still fixed, only the spacing between the grid points is variable. Consider again figure 7.1. Using variable grid points, the position of the two intermediate grid points are now calculated by the optimizer:

$$E_2 = \delta_2 \, E_{end} \tag{7.1}$$

$$E_1 = \delta_1 \, E_2 \tag{7.2}$$

The two parameters δ_1 and δ_2 determine the grid point or the value of the independent variable. These two parameters must always have a value between 0 and 1. Using this energy grid with two intermediate grid points, the GA has to optimize four control variable values and the two parameters δ_1 and δ_2, which makes a total of six parameters. This is only a simple example. In section 7.2.2, a grid with 10 intermediate grid points will be used, which results in a total of 22 parameters which have to be optimized by the GA.

7.1.4 Polynomial representation

Instead of describing the control vector by discrete points, it can also be represented by a polynomial approximation. A Chebyshev approximation will be used as a polynomial representation because they are considered well suited for the approximation of functions due to their behavior within the interval [-1,1], and more specific due to the easily determination of the contribution of each individual term to the total polynomial representation in this interval. The discussion in this section on Chebyshev polynomials is based on (Press, Teukolsky, Vetterling, & Flannery, 2007).

A Chebyshev polynomial of degree n is denoted by $T_n(x)$ and is given by the explicit formula:

$$T_n(x) = cos(n \; arcos(x)) \tag{7.3}$$

The different terms $T_i(x)$ can also be expressed as simple powers of x:

$$T_0(x) = 1 \tag{7.4}$$

$$T_1(x) = x \tag{7.5}$$

$$T_2(x) = 2x^2 - 1 \tag{7.6}$$
$$T_3(x) = 4x^3 - 3x \tag{7.7}$$
$$T_4(x) = 8x^4 - 8x^2 + 1 \tag{7.8}$$

These polynomial are plotted in figure 7.2. In this thesis, a fourth order Chebyshev polynomial is used, because this type was already used in several other thesis works, see for example (Demeyer, 2007). Moreover, higher-order Chebyshev polynomials have more fluctuations, see figure 7.2. Severe fluctuations are not desirable in the control vector profile and hence it was decided to only use a fourth-order Chebyshev polynomial in order to limit these.

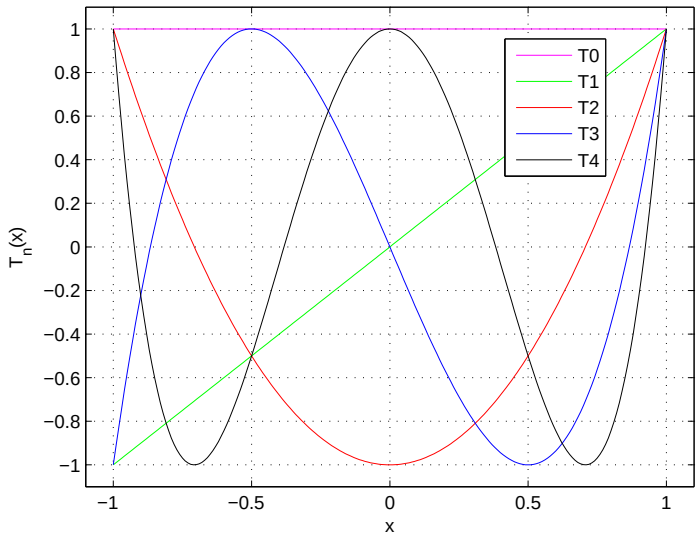

Figure 7.2: Chebyshev polynomials $T_0(x)$ through $T_4(x)$

An arbitrary function f(x) in the interval $[-1, 1]$ can be approximated by a combination of Chebyshev polynomials:

$$f(x) \approx \left[\sum_{k=0}^{N} c_k T_k(x)\right] - \frac{1}{2}c_0 \tag{7.9}$$

where c_k are the coefficients, which determine the strength of the corresponding Chebyshev polynomial. If this representation is used in an optimization problem, finding the optimal control vector corresponds with finding the optimal coefficients c_k.

Normally, a function represented by equation 7.9 is situated in the interval $[-1, 1]$ but a function situated in an arbitrary interval $[a, b]$ can also be represented by this equation if the variable is transformed:

$$x = \frac{y - \frac{1}{2}(b + a)}{\frac{1}{2}(b - a)} \tag{7.10}$$

where y lies in the desired interval $[a, b]$ and x is located between $[-1, 1]$.

7.2 Tuning of the GA

A genetic algorithm is not a unique algorithm or program, but several variations can occur depending on the application. For example, an optimal trajectory from Earth to Mars may require a different version or setting of a genetic algorithm than one for the calculation of optimal trajectories of a winged re-entry vehicle during the terminal area. A different problem may require a different tuning of a genetic algorithm to find the best optimum. In order to assure that the genetic algorithm calculates the correct optimal solution for the type of problems addressed in this thesis, a tuning analysis needs to be performed.

Tuning the genetic algorithm comprises of two items:

- **Control vector model**
  As described in the previous section, several methods exist to parameterize the control vector. One model may lead to better results than the other. The different control-vector models will be investigated and compared.
- **GA parameters**
  A genetic algorithm contains some parameters that need to be defined by the user. The influence of the value these parameters on the performance of the GA will be investigated and a selection of the best values will be made. The parameters that will be investigated are:
  - crossover percentage
  - chance of mutation
  - immigration percentage
  - population size

The goal of the tuning analysis is to come up with a generic genetic algorithm that can be used for several optimization problems related to optimal terminal area trajectories of a winged re-entry vehicle. After the analysis, the same genetic algorithm will be used for all the subsequent optimization problems related to this terminal area. So, the same algorithm will be used for an optimal wings-level flight and for a turning flight. Note that a tuning analysis might be performed for each specific problem within the general application of optimal terminal area trajectories, but due to time limitations, this is not feasible. It is assumed that only a marginal gain in the optimal solution might be possible using a tuning analysis for each specific subproblem.

The entire tuning analysis of the GA is based on a subsonic maximum range glide, starting at an initial altitude of 9.40 km and at a velocity of 108.50 m/s (E_h = 10 km). This corresponds to starting point 1, as used in section 6.1.3. The performance of the optimized maximum range trajectory starting at point 1 will be compared with respect to the reference steady state flight, which had a maximum range of 32.78 km. It must be noted that the best result not only refers to the obtained maximum range, but also to the computational effort required. The analysis below will therefore also show the run time to draw conclusions.

The tuning analysis as presented below, is only a limited tuning analysis. Focus during the tuning is on the selection of the best control vector representation. Also, the seed value used for the random generator is kept constant for all the simulations. An arbitrary value of 8 was

chosen. The influence of changing this value on the optimization result, was not investigated. As already explained in chapter 4, the values for the convergence criteria, minimum lifetime and maximum lifetime are not changed during the optimizations. The maximum number of generations and evaluations are not considered as critical and are adapted such that the main criteria to stop an optimization is the convergence criterion.

Next to the control-vector model and the GA parameters, changing the operators as used in OPTIDUS will also have an influence on the optimal result. This was not part of this study, but is left as a future work. The focus during this study was on the analysis of optimal terminal trajectories and not on the analysis of the optimizer itself. Hence, the optimizer is seen as a black box used to calculate several optimal trajectories and to analyze different trajectories for different flight conditions. If only one optimization problem would be considered, a more extensive investigation to the most optimal genetic algorithm could be done. But in this study, several optimization problems need to be solved and hence, due to time considerations, it was unfeasible to do an extensive tuning analysis.

7.2.1 Trajectory and control variable constraints

Optimal terminal area trajectory problems are subjected to several control-variable and path constraints:

- angle-of-attack, α
- time rate of change of the angle-of-attack, $\dot{\alpha}$
- stall speed, V_{ST}, or minimum dynamic pressure, $q_{dyn,min}$
- maximum dynamic pressure, $q_{dyn,max}$
- maximum load factor, n_{max}

These boundaries were already mentioned in chapter 3, except for the $\dot{\alpha}$ constraint. This extra constraint is added to assure that the angle-of-attack profiles are smooth and without sharp discontinuities, such that the obtained profile can be followed by the controller and is flyable by HORUS.

The boundaries in which the angle of attack must be situated, are indicated in figure 6.4. The time rate of change of the angle of attack is constraint to ± 3 deg/s. These are the only two boundaries that are used during the tuning analysis using a subsonic initial state. The other three boundaries were not used, because the maximum range problem in itself requires that these boundaries are met. A solution that violates the minimum or maximum dynamic pressure boundary yields a trajectory with a non-optimal maximum range, so these solutions are eventually eliminated anyway, based on the results of the optimization criteria or cost function. Including these boundaries, the computational time increased dramatically because individuals are calculated that violated those boundaries and hence, new individuals have to be calculated to fill the population. After an optimization run, the solution was checked for constraint violations, but none occurred.

In other optimization problems described in this chapter, extra constraints will be included, see, for example, the maximum dive problem.

7.2.2 Analysis of influence of GA parameters and control vector representation

Each control-vector representation is investigated and within each representation, several values for the parameters are used to study there effect on the optimal solution. The values for the parameters have been selected based on other thesis works and using common sense.

Fixed-segment N-vector formulation

The first GA optimizations are performed using the simplest control vector representation, the fixed grid-point representation with equally spaced grid points. A vector of 12 grid points is used, with boundary values for the minimum and maximum energy height equal to 0 km and 11 km, respectively. The other 10 grid points are located in this interval with equal spacings of 1km energy height:

$$E_{grid} = [0.0,\ 1.0,\ 2.0,\ 3.0,\ 4.0,\ 5.0,\ 6.0,\ 7.0,\ 8.0,\ 9.0,\ 10.0,\ 11.0] \tag{7.11}$$

Using this representation, four optimization runs are performed with different values for the GA parameters. These values, as well as the results, are given in table 7.1.
For the first run, a low value for the number of crossover and the population size was chosen because this results in a low computational time. The computational times as specified throughout this thesis study are obtained on a *Dell Insiron 1525* laptop with an Intel(R) Core(TM)2 Duo CPU T8100 with a frequency of 2.10GHz. A low computational time is very important if optimization schemes are used in on-board trajectory generation algorithms and guidance algorithms. But even for these low values of initial population and number of crossovers, the computational time is 1 minute and 18 seconds, which already indicates the difficulty of implementing a genetic algorithm in an on-board guidance system. The obtained maximum range was increased by almost 1.5 km with respect to the steady state solution.
In the second run, the initial population size was increased from 40 to 100. A better optimal was found with an increased maximum range value of almost 500 m. This comes at the cost of computational time, which is increased by more than 4 minutes. The second run was ended, because the maximum number of generations of 500 was reached. This means that the obtained solution had not yet converged.
To solve this problem, the maximum number of generations was increased from 500 to 1000 in run 3. The maximum range was only slightly increased.
Run 4 was used to study the effect of increasing the number of crossovers. The value was increased to 0.2, which resulted in a maximum range 34.87 km and computational time of more than 12 minutes. This means an increase of 6.4 percent with respect to the maximum range obtained using the angle-of-attack profile for a maximum lift-to-drag ratio.

Figure 7.3 shows the obtained optimized angle-of-attack profiles for the four different optimization runs. Also the angle of attack for maximum lift-to-drag ratio is shown in this figure. Two important conclusions can be made from figure 7.3. Comparing the optimization result of run 4 and the angle of attack profile for maximum lift to drag ratio, one can see that for the largest part the two angle-of-attack profiles are almost the same. The second conclusion is that all four optimization runs indicate a large deviation of the angle-of-attack profile for a maximum lift-to-drag ratio in the beginning and near the end of the energy interval. In the beginning and near the end of the flight, some transient maneuvers seem to yield the optimal subsonic maximum range. Because this general trend is already clearly visible, it was decided

not to do any more optimization runs to investigate the influence of changing the other GA parameters.

Table 7.1: GA parameters and optimization results for four different runs of the subsonic maximum range problem using a fixed segment N vector formulation of the control vector; starting point 1

	Run 1	**Run 2**	**Run 3**	**Run 4**
Population size	40	100	100	100
Number of crossover	0.08	0.08	0.08	0.20
Chance of mutation	0.01	0.01	0.01	0.01
Number of immigration	0.05	0.05	0.05	0.05
Maximum number of generations	500	500	1000	1000
Range $[m]$	34225.45	34718.77	34769.41	34870.29
Computational time $[s]$	78.4	329.4	477.1	736.8

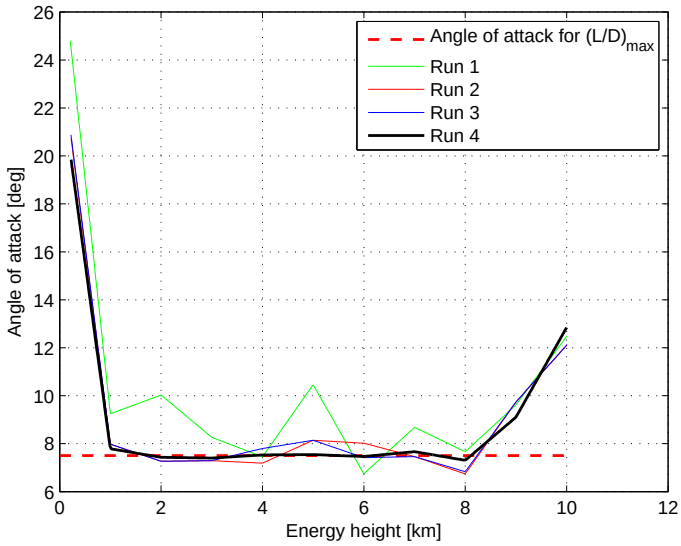

Figure 7.3: Optimized subsonic maximum range angle of attack profiles as a function of energy height for four different optimization runs using a fixed N vector formulation of the control vector; starting point 1

Some improvements might be obtained by looking into these initial and final transient maneuvers in more detail. This can be done by making the grid of the control vector smaller in the initial and final interval of the energy grid of the control vector. Inspecting figure 7.3, it can be seen that the initial transient maneuver takes places between an energy height of 10.0 and 8.0 km and that the final transient maneuver occurs below an energy height of 1.0 km. Using these two intervals, two smaller grid are defined as:

$$E_{initial} = [8.0,\ 8.2,\ 8.4,\ 8.6,\ 8.8,\ 9.0,\ 9.2,\ 9.4,\ 9.6,\ 9.8,\ 10.0,\ 11.0] \quad (7.12)$$

$$E_{end} = [0.0,\ 0.2,\ 0.4,\ 0.6,\ 0.8,\ 1.0] \quad (7.13)$$

Between an energy height of 1.0 km and 8.0 km, the same grid is used, as specified in equation 7.11. This gives a complete energy grid of 24 grid points, where the grid points are not equally

spaced.
During run 5, this enlarged energy grid was used together with the same GA parameters as used during run 4, but no better results were obtained. The optimization was manually terminated after 35 minutes because the GA was still calculating an initial feasible population. Filling the initial population with feasible solutions took a lot of time because of the stringent constraint on the time rate of the angle of attack, in combination with the finer grid. Using a fine grid, the energy height difference between two consecutive grid points is smaller and in combination with the possible angle of attack values between 0 and 30, the possibility that a combination is randomly chosen for which the constraint on the time rate of the angle of attack is violated, is quite large. Two possibilities were investigated to solve this problem. The first solution is to relax the constraint on the time rate of the angle of attack. The second solution is to take larger spacings between the energy grid points, but not as large as in equation 7.11. Both solutions are discussed below.

Table 7.2: Optimization results for two runs of the subsonic maximum range problem using a fixed grid points of the independent variable of the control vector, with a finer grid during the initial and final transient maneuvers; GA parameters as in run 4; starting point 1

	Run 6	**Run 7**
Energy grid spacing during transient maneuvers [km]	0.2	0.5
Constraint on rate of angle of attack [deg/s]	10.0	3.0
Range $[m]$	34428.22	34673.21
Computational time $[s]$	969.7	897.3

During run 6, the constraint on the time rate of the angle of attack was relaxed from 3°/s to 10°/s. Using this new constraint value, it was possible to find a feasible initial population in a reasonable amount of time. The optimization result of this run is shown in table 7.2. The obtained maximum range is 400m smaller than found in run 4, while the computation time is increased by more than 200 seconds. Important to note is that although the constraint on the rate of angle of attack was relaxed to 10°/s to find a feasible initial population, the time rate of the angle of attack of the final optimal solution was never larger than 3°/s. It seems that it is not optimal to execute maneuvers for which the time rate of the angle of attack is too large. The optimization results of run 7 are also shown in table 7.2. In this run, the constraint on the rate of the angle of attack is set again to the original value of 3°/s and instead, the spacing between the grid points during the transients are made a little larger. This results in the new energy height grid of the control vector for the angle of attack:

$$E_{grid} = [0.0,\ 0.5,\ 1,\ 2,\ 3,\ 4,\ 5,\ 6,\ 7,\ 8.0,\ 8.5,\ 9.0,\ 9.5,\ 10.0,\ 11.0] \tag{7.14}$$

As can be seen in table 7.2, also this energy grid does not give any improvement in terms of maximum range but the result is somewhat better than the results of run 6.

Both run 6 and 7 were performed using the GA parameters as used during run 4. So perhaps a better result can be obtained by changing these parameters, see table 7.3. This is done using run 8 till 12, using the same grid as during run 7. The best result is obtained in run 8, where the population size was changed from 100 to 150. But still, the maximum range is not better than the one obtained in run 4, while the computational time is increased by a factor of 3.3. Changing the chance of mutation or the number of crossovers does not yield better results. The optimal angle-of-attack profile from run 8 can be seen in figure 7.4. This figure indicates

that by using a finer grid in the initial transient maneuver, some fluctuations are introduced because of the smaller grid.

Table 7.3: GA parameters and optimization results for five different runs of the subsonic maximum range problem using a fixed segment N vector formulation of the control vector with a finer grid during transient maneuvers; grid as in run 7; starting point 1

	Run 8	**Run 9**	**Run 10**	**Run 11**	**Run 12**
Population size	150	150	200	150	200
Number of crossover	0.20	0.25	0.20	0.20	0.20
Chance of mutation	0.01	0.01	0.01	0.02	0.02
Number of immigration	0.05	0.05	0.05	0.05	0.05
Range $[m]$	34849.64	34674.75	34770.10	34653.21	34751.35
Computational time $[s]$	2460.0	2239.0	2666.3	1623.0	3832.8

At this point, it can be concluded that using an N-vector formulation of the control vector, with fixed grid points and a finer grid during transient maneuvers, does not yield better results, nor in terms of maximum range nor in terms of computational time. The spacing between two successive grid points in the finer grid is too small. Due to this smaller spacing in combination with the possible large difference between two successive angles of attack, more fluctuations in the angle of attack profile during the initial transient maneuver are observed.

Chebyshev representation of control vector during transient maneuvers

Another possibility is to use a Chebyshev representation of the control vector during the transient maneuvers. An optimization run was performed using a combination of the N-vector representation with fixed grid points (equally spaced) and a Chebyshev representation. During the initial transient maneuver, which occurs between an energy height of 8 and 10 km, the angle-of-attack profile is approximated by a Chebyshev polynomial and during the rest of the gliding flight, an N-vector is used as given in equation 7.11 (up to and including an energy height of 8 km).

The parameters which are optimized by the genetic algorithm are now the 5 coefficients of the Chebyshev polynomials and the 9 grid points of the N vector. This gives a total of 14 parameters. The c_0 coefficient must be located in the interval $[0, 40]$ while the other coefficients are constrained to the interval $[-4.0, 4.0]$. The choice of these intervals is explained at the end of this section.

The optimization run (run 13) was performed using a smaller number for both the percentage of crossover and the initial population. The parameters were respectively set to 0.08 and 20. The other GA parameters were the same as in run 4. Even for the small number of crossovers and initial population, the GA needed about 8 minutes to calculate an optimal angle-of-attack profile. This profile is given in figure 7.4 and gives a maximum range of 34.32 km, which is lower than obtained in run 4. The irregular shape of the obtained angle of attack profile can be compared with the profile from run 1 indicated in figure 7.3.

A suggestion to improve the performance of the GA is to increase the population size and the number of crossovers, which is similar to the analysis as shown in table 7.1. The problem

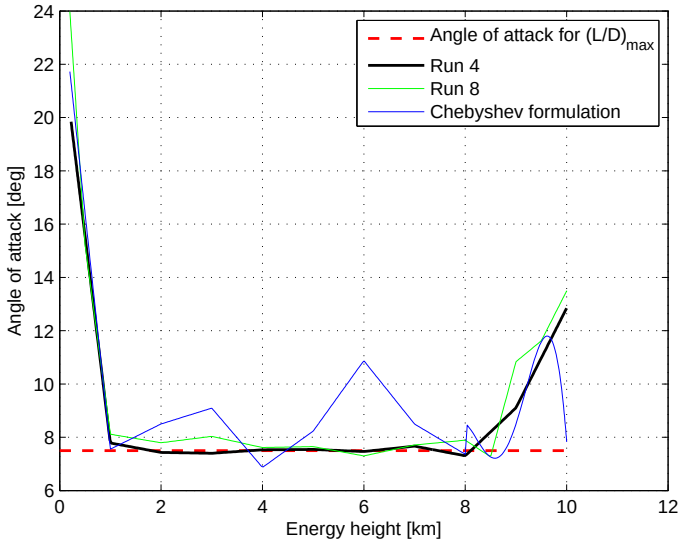

Figure 7.4: Comparison of optimized angle of attack profiles from run 4 and using a finer grid or Chebyshev polynomial during the initial transient maneuver; starting point 1

is that the computational time will increase dramatically, while the computational time for the low values of crossover and population time is already about 8 minutes. Clearly, using a Chebyshev polynomial representation of the control vector during the initial transient maneuver is not a good way to quickly compute a good optimal solution. Hence, it was decided not to perform any further analysis. Instead, a third possibility to represent the control vector was investigated. This is discussed in the next section.

Before investigating this new representation, it is still important to explain why the optimization run using the Chebyshev polynomial representation needs such a large computational time. Most op the computational time was spend on finding a feasible initial population. The time required to find a feasible initial population can be reduced by performing several simulations (e.g., a Monte Carlo) before the GA is applied, to select a good interval in which the variables need to be defined. This strategy is somewhat difficult for the Chebyshev approximation because of the constraint on the time rate of the angle of attack. One can take the derivative of the Chebyshev polynomial, but only with respect to energy due to the choice of energy as the independent variable. To convert this to a derivative with respect to time, the derivative of energy with respect to time needs to be known:

$$\frac{d\alpha}{dt} = \frac{d\alpha}{dE}\frac{dE}{dt} \tag{7.15}$$

The problem is that this is not a constant value but depends on the control history during the simulation and hence on the angle of attack profile itself. During a simulation, this value changes with time. So it is impossible to guess the derivative of energy with respect to time. This makes it difficult to make a reasonable assumption on the interval boundaries of the optimization variables. After the boundary analysis before applying the GA, the intervals, as indicated before, were used, but still many individuals are killed in finding feasible initial population, because of exceeding the boundaries on the time rate of change of the angle of attack.
Another problem is that using the Chebyshev polynomial representation, the angle of attack

value may be lower than zero. This violated the allowable angle of attack corridor indicated in figure 6.4. An individual in which the angle of attack goes below zero is infeasible and is removed from the initial population.
Summarized, the fact that it is not possible to predict the required intervals on the variables and the accompanying large computational time is the main reason why the Chebyshev polynomial representation is not a feasible solution in quickly finding an optimal angle-of-attack profile.

Variable-segment N-vector formulation

The last option which was investigated, is the use of an N-vector formulation of the control vector with variable grid points. Now, the GA does not only has to optimize the values of the angle of attack at the discrete grid points but also the energy spacing between the grid points.

Three optimization runs were performed. The obtained angle-of-attack profiles are shown in figure 7.5 while the optimization results are given in table 7.4. The boundaries for the variable grid are $E_{begin} = 0.0\ km$ and $E_{end} = 10.0\ km$. Ten intermediate grid points (E_1 till E_{10}) were used which gives a total of 22 parameters (α_i, i = 1...12 and E_j, j = 1...10) which have to be optimized by the GA.

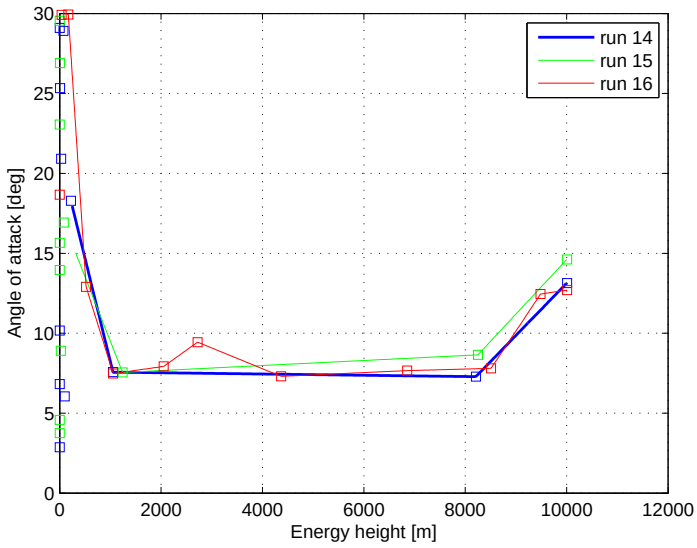

Figure 7.5: Optimized subsonic maximum range angle of attack profiles as a function of energy height for four different optimization runs using a fixed N-vector formulation of the control vector; starting point 1. The symbols indicate the grid positions as calculated during the GA optimization

During the first run, the same GA parameters were used as during run 4. The interval in which the GA searched for the optimal value of the parameters δ_i was between 0 and 1. The obtained maximum range is only 30 meters less than the maximum range obtained in run 4, while the computational time is decreased with 38 percent. This is a large improvement of the performance of the GA in terms of computational time. Figure 7.5 indicates that the optimal solution obtained in run 14 actually uses only four grid points. The other grid points were placed close to zero by the GA, which resulted from the calculated values of the parameters δ_i.

Perhaps not enough solutions from the initial population had more grid points at higher values of the energy height. Hence a second run (run 15) was done with an initial population size of 400. Statistically, this larger initial population would result in an a better spread of the grid points and in more individuals with more grid points at higher energy heights. Table 7.4 indicates that the computational time slightly increased, while no better result was found. Figure 7.5 again indicates that the optimal solution only uses four grid points.
The problem is that for the same value of δ, the step between two grid points at higher energy heights is larger than at lower energy heights. Take for example a value of 0.5 for δ. When the energy height E_n is equal to 10 km, the value of E_{n-1} is equal to 5 km. For E_n equal to 2 km, E_{n-1} is only 1 km. Hence, the difference between two successive grid points is larger at higher values of the energy height. Using the same interval for the value of δ during the compete energy grid results in a larger concentration of grid points at lower values for the energy height. During the third run (run 16), the δ interval was varied as a function of the value of the energy height, see table 7.5. This choice of intervals forces the GA to use more grid points at higher energy height values. Figure 7.5 indicates that in run 16, only one of the intermediate grid points is not used. Although more grid points are used at higher energy height values, no better result in terms of maximal range or computational time was found, see table 7.4.

Table 7.4: GA parameters and optimization results for three different runs of the subsonic maximum range problem using a variable segment N vector formulation of the control vector; starting point 1

	Run 14	**Run 15**	**Run 16**
Population size	100	400	100
Number of crossover	0.20	0.20	0.20
Chance of mutation	0.01	0.01	0.01
Number of immigration	0.05	0.05	0.05
Range $[m]$	34840.23	34522.42	34837.80
Computational time $[s]$	476.5	456.9	582.3

Table 7.5: Interval boundaries for the δ parameter of each variable grid points as a function of energy height

Variable grid point	**Lower limit δ**	**Upper limit δ**
E_1	0.2	0.5
E_2	0.2	0.5
E_3	0.2	0.5
E_4	0.5	0.8
E_5	0.5	0.8
E_6	0.5	0.8
E_7	0.5	0.8
E_8	0.8	0.98
E_9	0.8	0.98
E_{10}	0.8	0.98

7.2.3 Conclusions from tuning analysis

From the tuning analysis, it can be concluded that the best result in terms of maximum range is obtained by using a control vector representation with fixed grid points. But the range obtained by using a variable segment control vector representation is only 30 meters less, while the computational time is decreased with 38 percent. The Chebyshev formulation was not suitable to describe the initial and final transients and hence this option will not be used during subsequent optimizations.
Figure 7.6 shows the optimal angle of attack profiles from run 4 and 14. Both indicate the same trends. In the beginning and final part, a deviation of the steady state solution occurs, while the steady state solution is followed for the largest part of the profile.
The control vector representation with variable segments looks promising because it is able to generate a solution almost identical to the one using fixed segments, but using a lower computational time. To be able to make a well-founded conclusion, both the fixed and variable segments will be used in the optimization runs for the subsonic maximum range problems. After these optimization runs, a conclusion will be drawn about the performance of both control-vector representations.

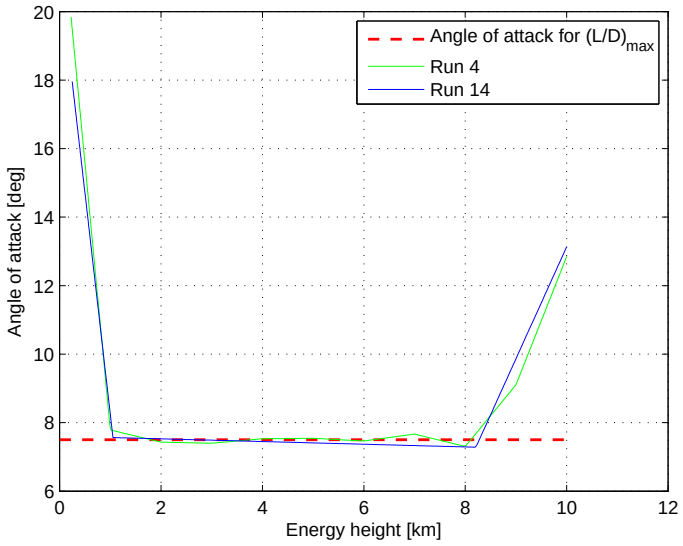

Figure 7.6: Optimal angle of attack profile using a fixed segment (run 4) and a variable segment (run 14) control vector representation

7.3 Maximum range trajectory in the vertical plane

In this section, the optimization results are shown for the maximum range problem in the vertical plane. Both subsonic and supersonic initial flight conditions are considered. The optimal GA parameters obtained from the tuning analysis are used. During all the maximum range optimizations, only the boundaries on the angle-of-attack and the time rate of change of the angle-of-attack are used.

7.3.1 Subsonic maximum range of HORUS

This section describes the obtained maximum range trajectories in terms of the required control variable and the path variables for three subsonic initial states. These states are equal to the ones used in the steady-state analysis and comparison is made between the optimal GA results and the steady state analysis results. But first, both an energy grid with fixed and variable grid points are considered and a conclusion is made about which method is the most suitable for the subsequent optimization problems.

Difference between fixed and variable grid point representation of the control variable

Table 7.6 shows the obtained maximum ranges and the required computational times for three subsonic initial states and for both a fixed and variable energy grid.

Table 7.6: Optimization results for the subsonic maximum range problem

	fixed grid range [km]	**fixed grid time [s]**	**variable grid range [km]**	**variable grid time [s]**
Startpoint 1	34.87	736.9	34.84	476.5
Startpoint 2	35.97	536.9	35.92	191.0
Startpoint 3	35.18	882.6	34.92	297.8

The best results in terms of maximum range are obtained by using an energy grid with fixed grid points. But for initial states 1 and 2, the maximum range obtained by using a variable grid is only slightly smaller, while the computational time is decreased significantly. For initial state 3, the computational time is still decreased, but the difference between the maximum range using the fixed and variable grid points is larger. Figure 7.7 shows the obtained angle-of-attack profile using both the fixed and variable grid point representation of the control variable for initial state 3. The result of the variable grid point representation is marked as 'variable grid points 1'. The fixed grid point representation in this figure indicates that there are some fluctuations in the beginning of the profile. The variable grid representation is not able to cope with these fluctuations. It is not able to calculate the fluctuations because of the phenomena which was already discussed in section 7.2.2. Statistically, it is very difficult to get a lot of grid points at high energy height values, if the same δ interval is used for the complete energy grid. An attempt was made to use a different δ interval throughout the energy grid, such that a only a small interval can be used at large values for the energy height to assure enough grid points in this region. The result is also shown in figure 7.7 as 'variable grid points 2'. The obtained maximum range is now equal to 35.07 km. This is still smaller than the optimum obtained using the fixed grid representation, while the computation time is increased to 2795.96 seconds. The large numbers of grid points at large energy heights means that the selected δ intervals were too small at these energy values.

Based on these results, it was decided to stop the research of using a variable grid point representation of the control variable and to continue only with the fixed grid representation, which always gave the best result in terms of optimal range. But clearly, a variable grid point representation has good potential, although further research is needed to solve the optimal grid

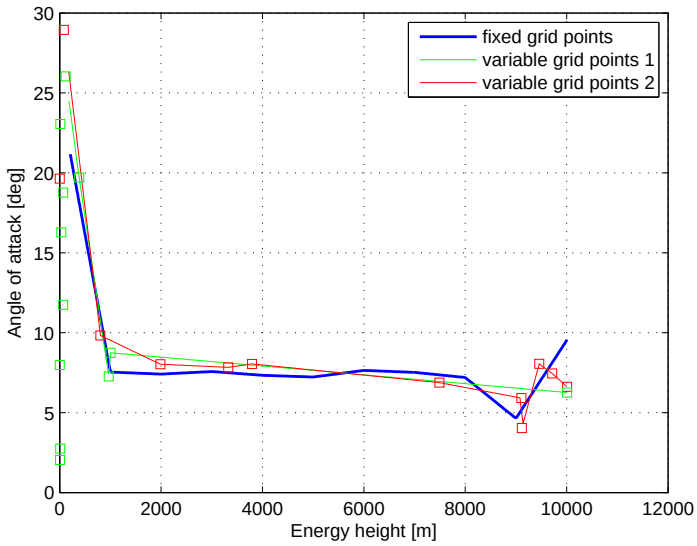

Figure 7.7: Angle-of-attack profiles for a fixed grid point representation and a variable grid point representation of the control variable for initial state 3

spacing problem. If too many grid points are used (too small δ interval), the computational time becomes too large and the advantage of the lower computational time is lost. On the other hand, if not enough grid points are used in a region where there are more fluctuations in the profile, the obtained result is not optimal. The biggest problem remains the choice of the δ interval which determines the grid point spacing. Further research is needed to come up with a general rule to select the required interval as a function of energy height for an optimal solution. A suggestion is to not only make the spacing between the grid points a variable that has to be optimized by the genetic algorithm, but also the number of grid points used.

Subsonic maximum range results

Figure 7.8 shows the obtained angle-of-attack profiles for the subsonic maximum range problems, starting at three different initial states. The initial conditions correspond to the subsonic initial states as used in the steady-state analysis from chapter 6. The angle-of-attack profile of the steady state analysis is also indicated as a reference. These results indicate that the largest part of an optimal maximum range glide is effected at angle-of-attack values near the required value for maximum lift-to-drag ratio, except for the initial and the final phases of the flight. At the end of the flight (at low energy values), the angle-of-attack is increased. This trend can be seen in the profiles for all three initial states. In the beginning of the flight (at high energy values), the three profiles do not follow the same trend, but they all differ from the steady state solution.

Figure 7.9 shows the state variables for the obtained optimal maximum range results, while figure 7.10 indicates both the steady-state solution and the optimal solution for initial state 1. For the optimal result, the amplitude of the variations in the flight-path angle are much smaller with respect to the steady-state solution. A similar trend can be seen for initial state 2 and 3, see figures 6.5 and 7.9. Studying the values of the flight-path angle in more detail, it was found that it steadily increases at a very slow rate, except for the initial and final phase. Also the

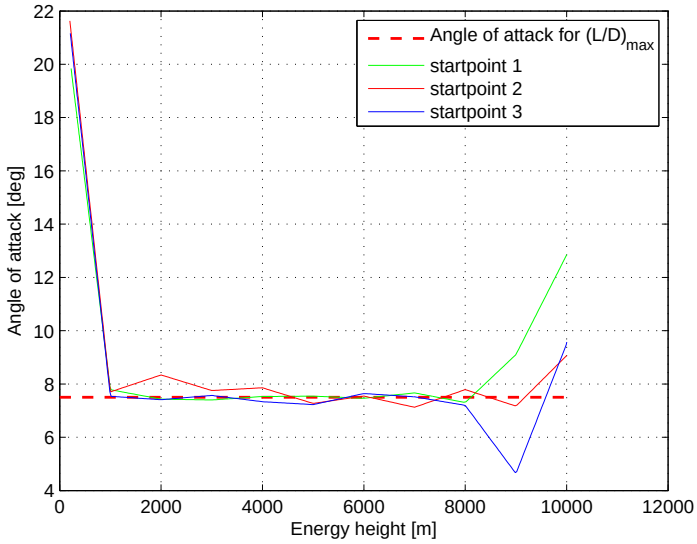

Figure 7.8: Optimal angle-of-attack profiles for three subsonic initial states

magnitude of the variations in altitude and velocity is smaller for the optimal solutions. The altitude and velocity profiles show that the increase in the angle-of-attack at the end of the flight corresponds with a pull-up maneuver to convert the kinetic energy into potential energy and hence, enlarges the range.

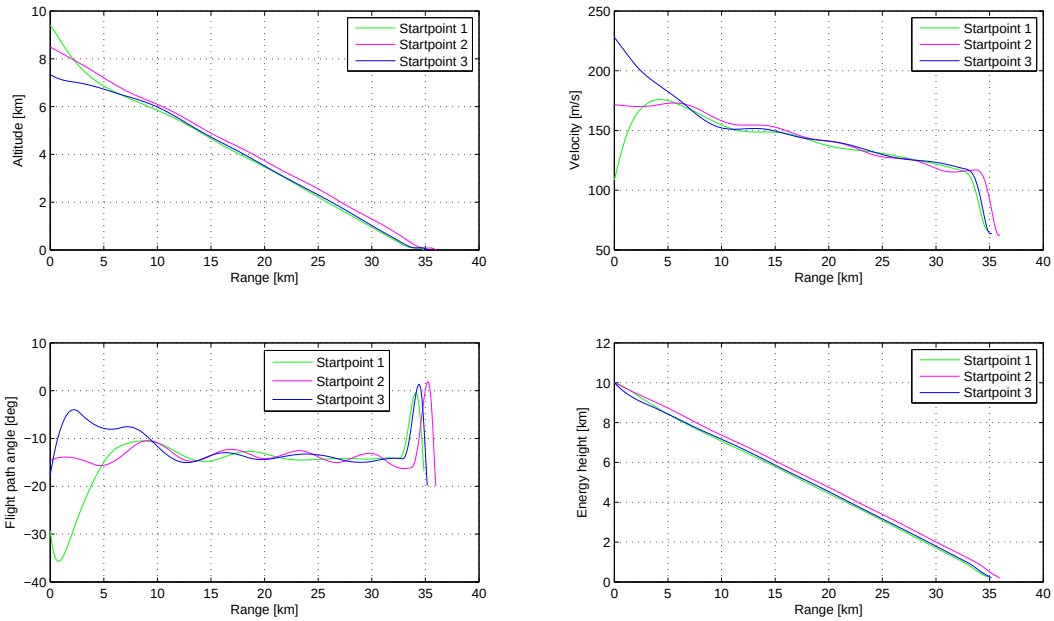

Figure 7.9: Optimization results of the maximum range problem for three subsonic initial states with the same initial energy height. Speebrakes fully retracted and straight flight

The obtained maximum ranges for both the steady-state solution and the optimal GA solu-

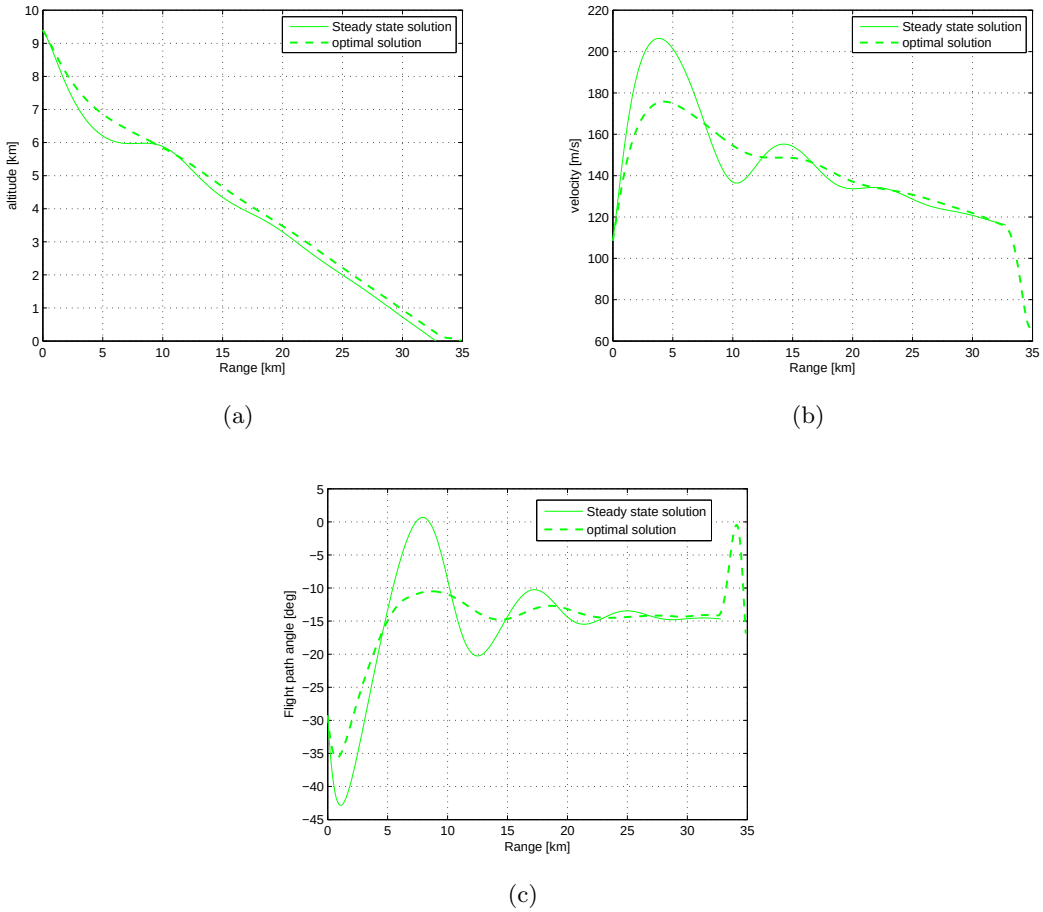

Figure 7.10: Subsonic steady-state solution and optimal solution for initial state 1 (a) altitude (b) velocity (c) flight path angle

tion are given in table 7.3.2. The increase in maximum range for initial state 1, 2 and 3 is respectively 6.4, 3.1 and 4.2 percent. Important to note is that, although the three initial states have the same initial energy height, the obtained maximum ranges are different. This will be further discussed in chapter 10.

7.3.2 Supersonic maximum range of HORUS

In this section, the required control variable and the resulting path variables are shown for the maximum range trajectories for three supersonic initial states. The same supersonic initial states are used as during the steady-state analysis.

During the supersonic optimization problems, only the boundaries on the angle-of-attack and the time rate of change of the angle-of-attack were taken into account. No dynamic pressure boundaries were considered, because the obtained optimal solutions do not violate these boundaries. Table 7.8 indicates the grid points of the independent variables that are used during the optimization.

Figure 6.4 indicates that in the subsonic speed regime, the angle-of-attack is limited between 0°

Table 7.7: Initial conditions and obtained maximum range of HORUS using steady-state solution and optimal solution

	V_G [m/s]	h [km]	Range $\alpha_{(L/D)max}$ [km]	Range $\alpha_{optimal}$ [km]	computation time [s]
Startpoint 1	108.50	9.40	32.78	34.87	736.9
Startpoint 2	171.60	8.50	34.88	35.97	536.9
Startpoint 3	228.00	7.35	33.76	35.18	882.6
Startpoint 4	583.10	35.00	134.63	138.93	3685.0
Startpoint 5	661.64	30.00	136.35	138.80	2565.9
Startpoint 6	732.00	25.00	130.79	132.95	1500.9

Table 7.8: Energy grid points and angle-of-attack interval boundaries as used during the genetic algorithm for the supersonic maximum range problem

Energy height [km]	Initial state 4 α boundary [deg]	Initial state 5 α boundary [deg]	Initial state 6 α boundary [deg]
0	[5 30]	[5 30]	[5 30]
1	[5 30]	[5 30]	[5 30]
10	[5 15]	[5 15]	[5 15]
15	[5 15]	[5 15]	[5 15]
20	[5 15]	[5 15]	[5 15]
25	[5 15]	[5 15]	[5 15]
30	[10 20]	[10 15]	[5 15]
35	[10 20]	[10 15]	[5 15]
40	[10 20]	[10 20]	[5 15]
45	[10 20]	[10 20]	[10 20]
50	[10 20]	[10 20]	[10 20]
55	[10 20]	[10 20]	[10 20]

and 30 ° and hence, these boundaries also determine the interval in which the GA searched for the optimal angle-of-attack. At each energy grid point in the subsonic problem, the interval was equal to [0°, 30°]. During the complete terminal area, the velocity moves from the supersonic to the subsonic speed regime during which the allowable angle-of-attack boundaries change. The same constant α interval may still be used at each energy grid point, but a lot of individuals will be unfeasible because they will violate the angle-of-attack boundaries from figure 6.4, especially at the bottle neck around Mach 1 and the supersonic speed regime. Simulations showed that due to this large number of unfeasible individuals, the optimization process became very slow. To speed op the optimization process and to reduce the computation time, different smaller α intervals were used at different energy grid points. The problem is now to determine of these intervals, because the boundaries in figure 6.4 are given as a function of the Mach number while the intervals need to be defined as function of the energy. The Mach number corresponding to a specific energy grid point is not constant. It depends on the simulation itself and hence, different intervals for the same energy grid point can be chosen for different simulations with different initial states. Table 7.8 indicates the α intervals that gave satisfying results for the three initial supersonic states, for each corresponding energy grid point. These values were selected based on the optimization results for a subsonic initial state and on trial and error.

After an optimization run, the obtained angle-of-attack profile was analyzed to see if an α value was close to the boundary value. If this was the case, the boundary value was slightly adapted to assure that the selected boundary did not prohibit the GA to find the optimal solution. The values as used in table 7.8 give the best optimal results in terms of maximum range.

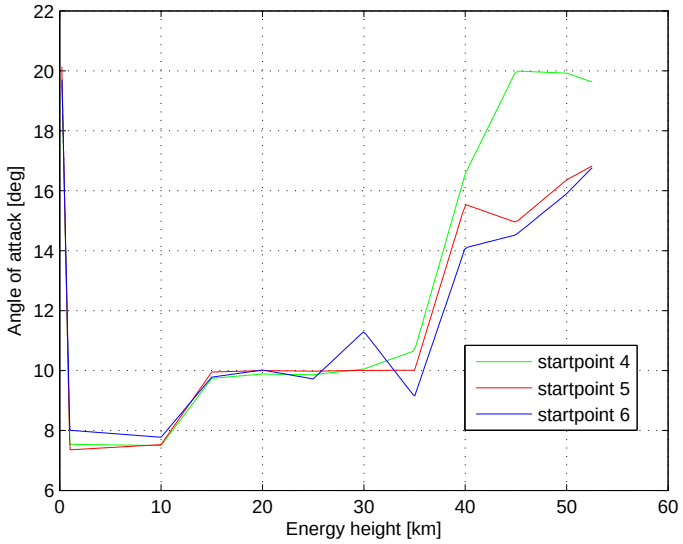

Figure 7.11: Optimal angle-of-attack profiles for three supersonic initial states

Table 7.3.2 indicates the obtained maximum ranges using the GA and the required computation time. The maximum range for initial state 4, 5 and 6 is increased with respectively 3.2, 1.8 and 1.7 percent. Hence, in terms of the range, a glide at maximum lift-to-drag ratio provides a relative good initial guess, especially for moderate initial altitudes (20 km and 25 km). The improvement is less than for the subsonic maximum range problem, while the computational time is increased dramatically. Taking into account the long computational times indicated in table and knowing that the Terminal Area phase only last for 7-8 minutes, it is obvious that a GA in the current configuration cannot be implemented in an on-board guidance system.

Figure 7.11 shows the obtained maximum range angle-of-attack profiles for the three supersonic initial states. At large energy values, the three profiles are different from each other, while between an energy height of 0 km and 25 km, the profiles indicate the same trend and are almost identical. At the end of the flight (low energy values), a pull-up maneuver is performed, which is similar to the results obtained for the subsonic maximum-range problem.

Figure 7.12 presents the variation of the flight path angle for the three optimal solutions. The steady-state solution is also plotted for comparison. For the first cycle in the oscillation of the flight path angle, the trajectories are close to each other because at high altitudes where the atmospheric density is small, the influence of the lift coefficient (and hence the angle-of-attack) on the lift force is small (Vinh, 1981). During the rest of the flight, in the denser layers of the atmosphere, a glide following the steady-state solution produces stronger variations in the flight-path angle as compared to the optimal glide. Near the end of the flight and before the final flare, the flight-path angle steadily increases at a slow rate.
The variations of the altitude and the flight path angle are given in respectively figure 7.13

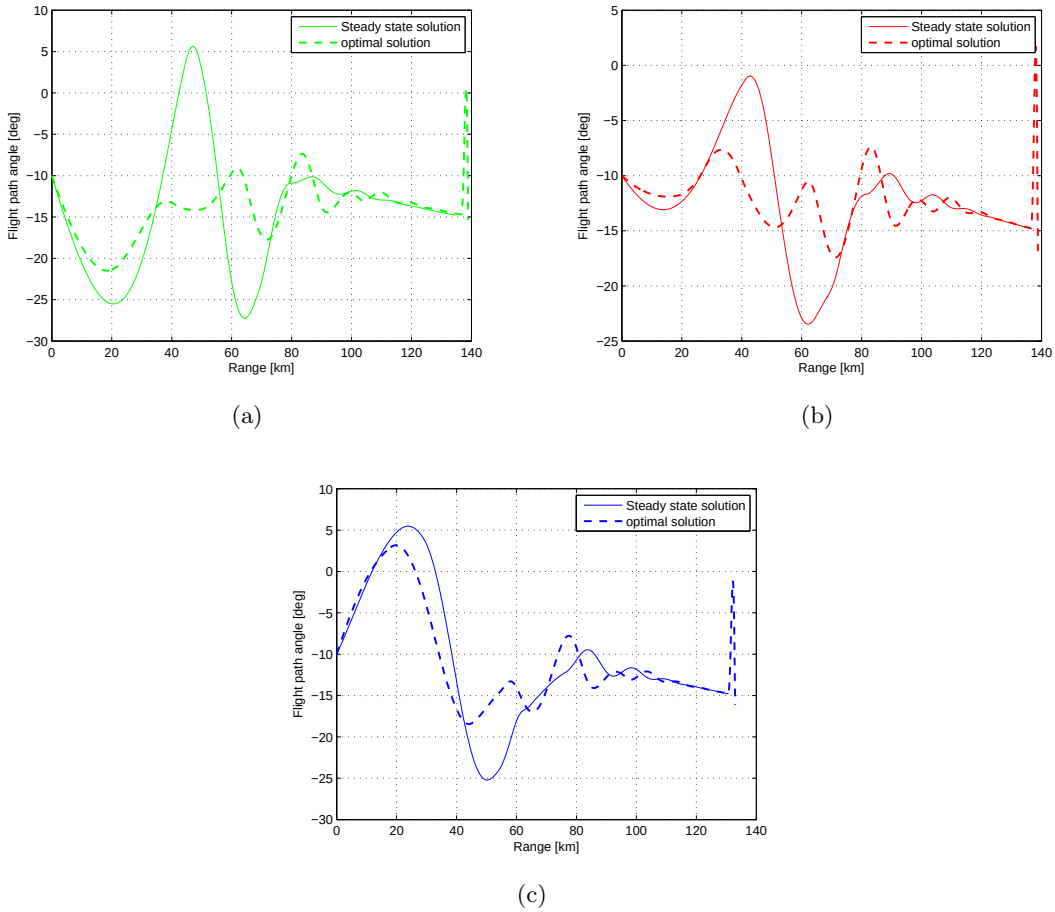

Figure 7.12: Flight path angle variations for steady-state solution and optimal solution (a) initial state 4 (b) initial state 5 (c) initial state 6

and figure 7.14. For the steady-state solutions, the amplitude of the oscillations in the altitude is larger as compared to the optimal solutions. Since in this case there exists an exchange between the potential energy and the kinetic energy, the variation in the velocity also shows some oscillation (Vinh, 1981). The maximum range increases for smaller oscillations.

Note that it might be possible to get a better optimum if different GA settings are used or if the obtained results are substituted in in a local optimizer as an initial guess. The GA, although a global optimizer, does not find the real optimal solution, but a solution that is close to the optimum. Although it cannot be guaranteed that the obtained solutions are the real optimum, they do indicate an optimal 'region' in which the actual optimum is situated.

7.4 Maximum dive trajectory in the vertical plane

This section describes the optimization results for the minimum range or maximum-dive problem. Only subsonic initial states are considered. The same initial states are used as during the subsonic maximum range problem.

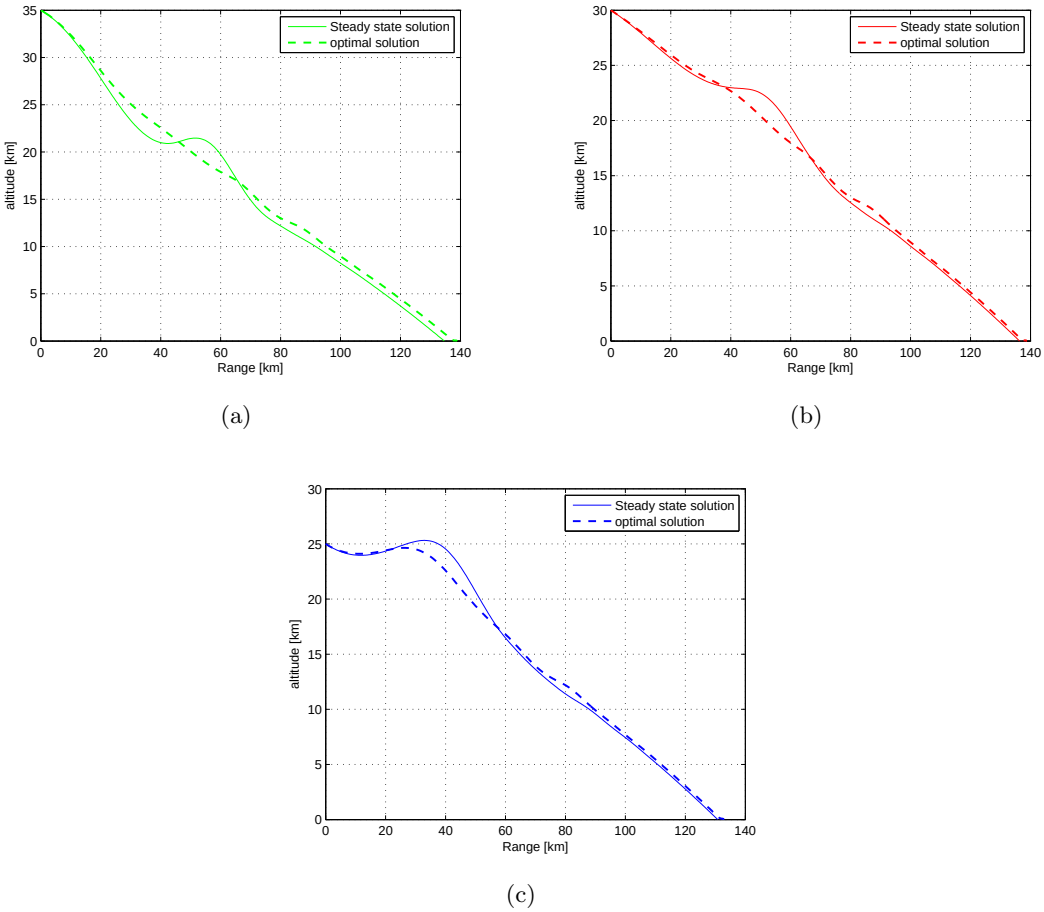

Figure 7.13: Altitude variations for steady-state solution and optimal solution (a) initial state 4 (b) initial state 5 (c) initial state 6

Next to constraints on the angle of attack and the time rate of change of the angle of attack, constraints on the minimum and maximum dynamic pressure are also implemented to assure that the GA calculates a trajectory, which is feasible in terms of path constraints. It is not allowed to cross the maximum dynamic-pressure boundary or to fly at velocities lower than the steady-state stall speed. In theory, transient maneuvers might be performed such that the stall speed boundary can be crossed, but it is not likely that such maneuvers will be performed during an actual flight with a winged re-entry vehicle. Hence, the stall speed boundary is incorporated.
The same grid points are used as during the subsonic maximum range problem, see equation 7.11. The interval in which the GA searches for the optimal α value is again equal to [0°,30°].

Table 7.9 indicates the obtained optimal results in terms of range and the required computation time. The optimization is done both for the case without the use of speedbrakes and with full speedbrake deflection. Below, the results are discussed separately for both cases.

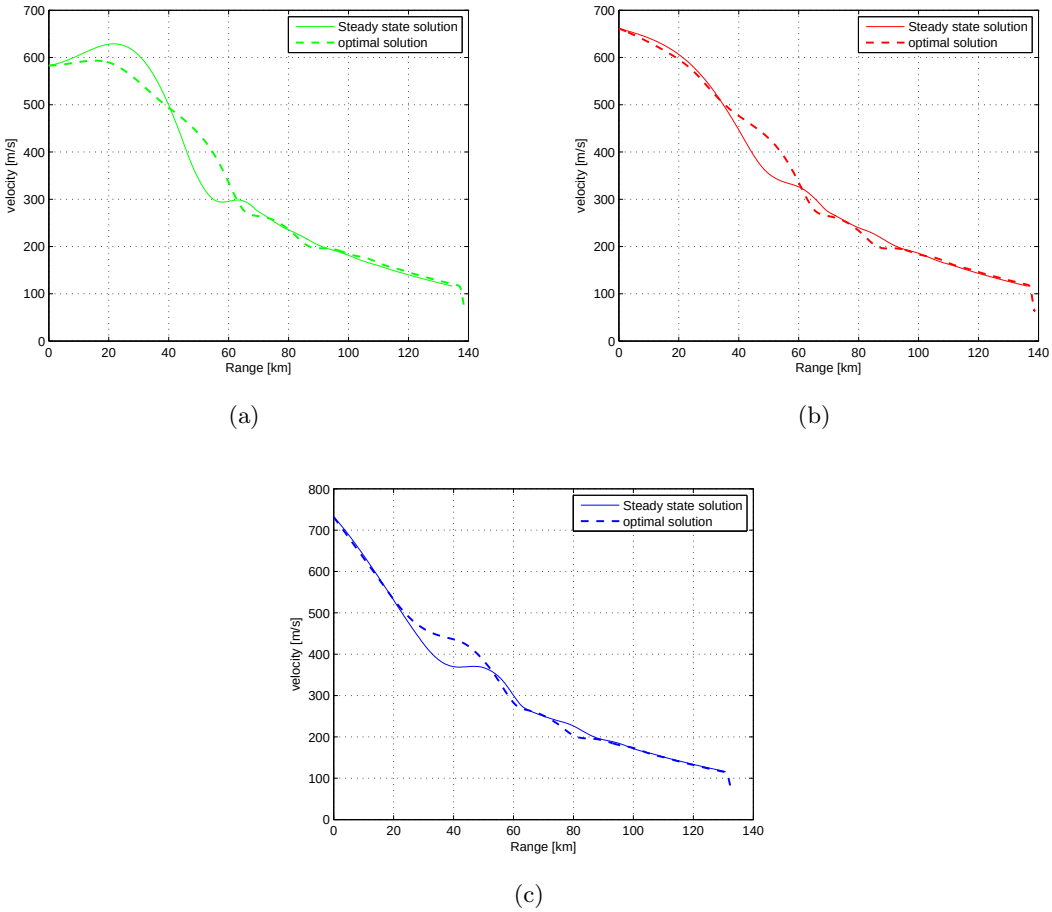

Figure 7.14: Velocity variations for steady-state solution and optimal solution (a) initial state 4 (b) initial state 5 (c) initial state 6

7.4.1 Subsonic maximum dive of HORUS without the use of speed brakes

The obtained angle-of-attack profiles and the state variables for the three subsonic initial states are shown in figure 7.15 and 7.16, respectively.

Consider the maximum dive for initial state 1. The angle-of-attack is nearly 30° for the largest part of the flight. During this part of the flight, HORUS flies at the lowest possible velocity without stalling. The flight path angle profile shows that the flight path angle during a maximum dive flight is indeed larger than during the maximum range flight. Near the end of the flight, the angle-of-attack is lowered and the velocity is increased. This is opposite to the maximum range problem where at the end a pull-up or flare maneuver is performed. The maneuver at the end of the maximum diving flight transforms potential energy into kinetic energy. During this maneuver, the flight-path angle first slightly decreases after which it is increased to -40°.
Although some fluctuations are present, the same trends can be seen in the resulting state variables for the maximum dive trajectory starting at initial state 2. At the beginning of the flight, the velocity is decreased after which HORUS flies with a velocity close to the stall speed. At the end, the velocity is again increased. The profiles for both the velocity and the flight-

Table 7.9: Initial conditions and obtained range in a maximal diving flight, without and with use of speedbrakes. n.a. = not applicable

	no speedbrakes range [km]	**no speedbrakes comp. time [s]**	**full speedbrakes range [km]**	**full speedbrakes comp. time [s]**
fixed grid				
Startpoint 1	16.56	3983.7	14.92	2525.5
Startpoint 2	18.97	3661.3	16.40	3085.2
Startpoint 3	21.10	12842.3	n.a.	n.a.
variable grid				
Startpoint 3	19.96	1953.0	n.a.	n.a.

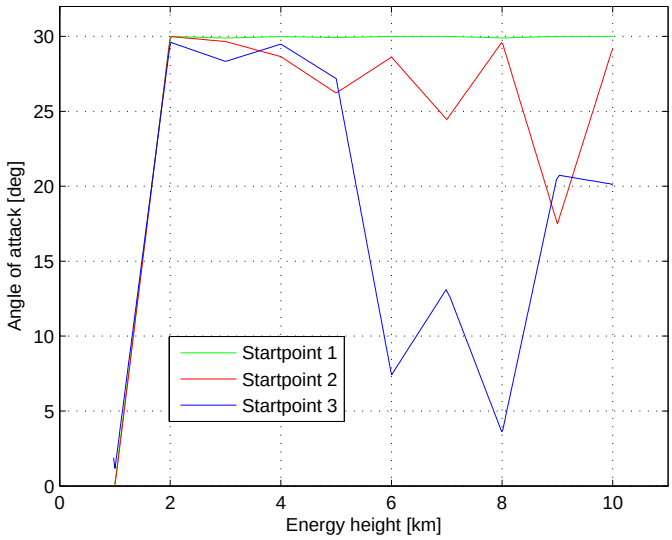

Figure 7.15: Optimal angle-of-attack profiles for three supersonic initial states

path angle show that fluctuations are present in these variables. These fluctuations can also be seen in the obtained optimal angle-of-attack profile. A better optimum might still be found by changing the settings of the GA or by performing a local optimization with the GA results as an initial guess. No further simulations were performed because a computational time of an hour is already required to compute the optimal trajectory. However, the current solution already indicates a general region or trend for a maximum dive. In contrast to a maximum dive strategy used in (Buechner, 2003), where a dive at maximum dynamic pressure is performed, the GA indicates that a maximum dive for HORUS is performed at minimum dynamic pressure.

The optimal result for initial state 3 somewhat deviates from the previous results. Initially, the velocity is also reduced but than, the velocity steeply increases after which it reduces again to a minimum velocity. After a range of 12 km, the result follows the same trends as discussed above. Note that the required computational time increased to more than three hours. To investigate if this is really the optimal solution or the GA is just not capable of finding the optimum, an extra optimization run was performed. As a one-time exception, an energy grid with variable grid points was used again. The results in terms of angle-of-attack and veloc-

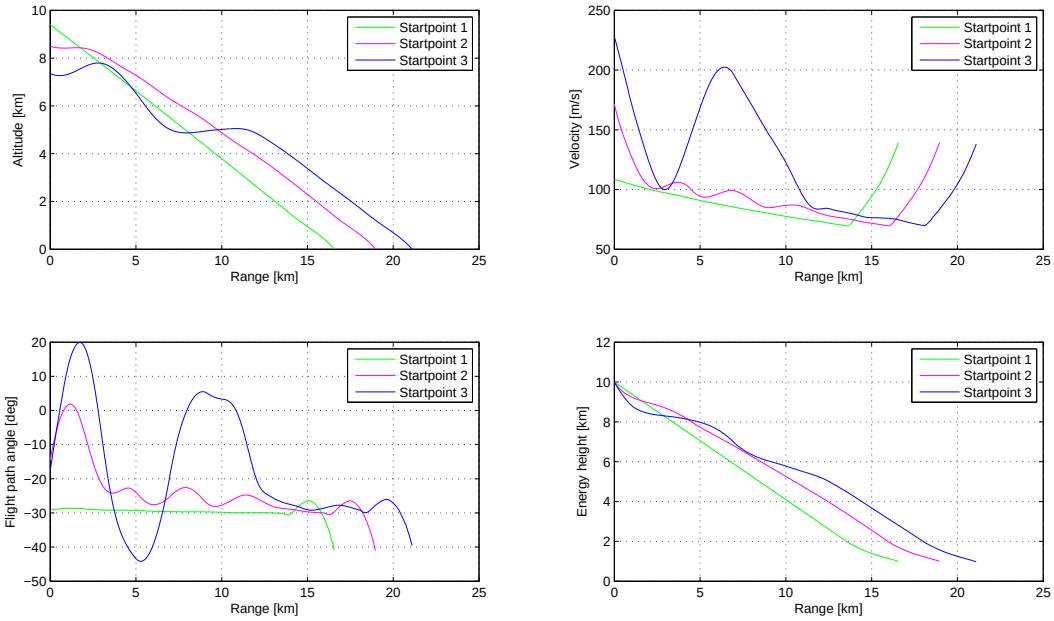

Figure 7.16: Optimization results of the minimum range problem for three subsonic initial states with the same initial energy height. Speebrakes fully retracted and straight flight

ity are shown in respectively figure 7.17(a) and 7.17(b). The range is now 19.96 km and the computation time is equal to 1953.0 seconds. This is the first time that using variable grid point representation gives a better result, both in terms of range and computation time. The velocity profile indicates that the jump from minimal velocity to an increased velocity is much smaller and hence, the trends as seen for initial state 1 and 2 are followed more closely. This indicates that these trends are the optimal trends for a maximum dive, but that the GA is not always capable of finding the correct trajectory. No more simulations were done because the trends are already clear. But further research on adapting the GA or using another optimizer is recommended to eliminate the fluctuation for initial state 2 and to get a better trajectory for initial state 3.

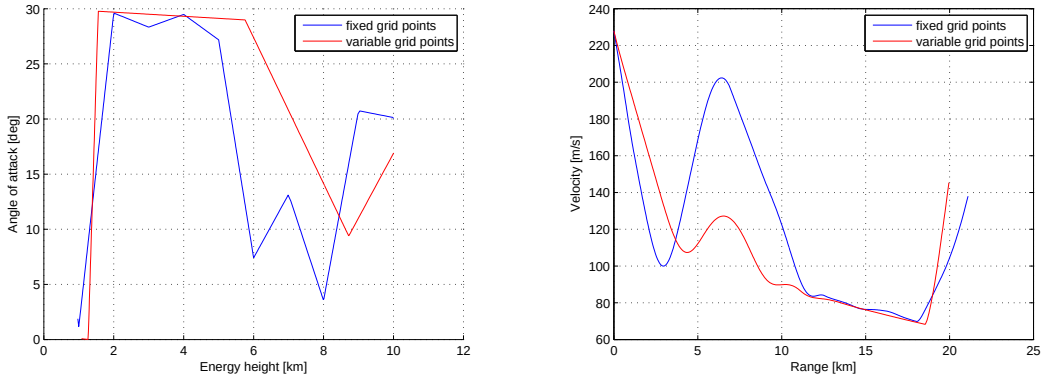

(a) (b)

Figure 7.17: Maximum dive initial state 3(a) angle-of-attack profiles (b) resulting velocity profiles

7.4.2 Subsonic maximum dive of HORUS using speed brakes

This section describes the influence of a full speed brake deflection on the maximum dive of HORUS. Optimal dive trajectories with speed brakes are only calculated for initial states 1 and 2, because the previous section indicated some problems with finding an optimal dive for this state, while the general optimal dive trend was already indicated by states 1 and 2.

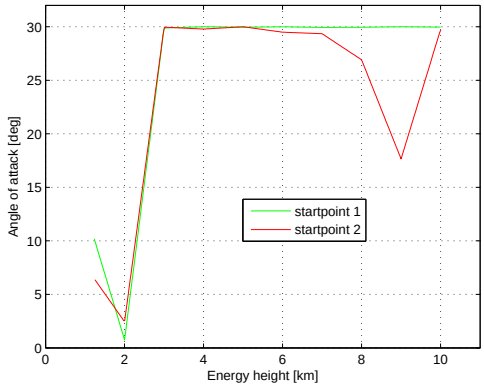

Figure 7.18: Optimal angle-of-attack profiles for maximum dive with full speedbrake deflection; straight flight

Table 7.9 presents the maximum dive results in terms of obtained range and computation time. Using a full speed brake deflection, the range is shortened by 11 and 16 percent for initial state 1 and 2, respectively. Figure 7.18 indicates the obtained maximum dive angle-of-attack profiles, while figure 7.19 presents the resulting flight path angle and velocity profiles. The same trends can be seen as for a dive without the use of speed brakes. The maximum dive is obtained by flying at high angles of attack and at low velocities without stalling. Near the end of the flight, α is lowered and the velocity increases. This is again opposite to a diving flight at maximum dynamic pressure as stated in (Buechner, 2003). Some fluctuations are still present in the flight path and velocity profile for initial state 2. A better optimizer might solve this.

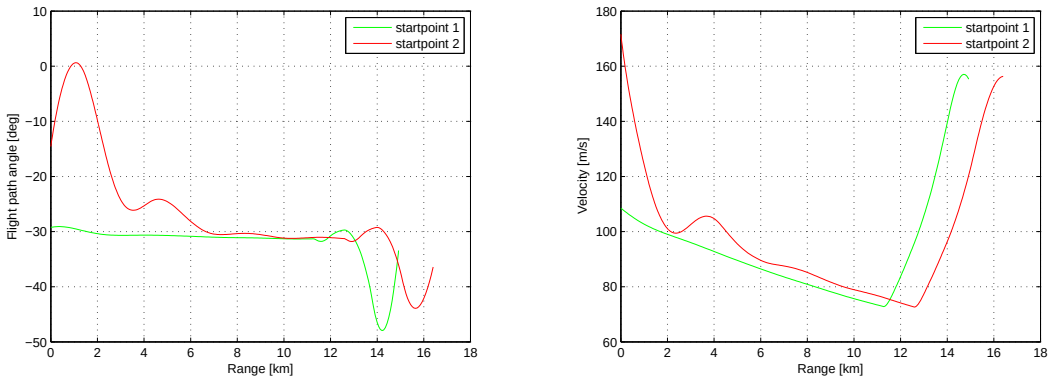

(a) (b)

Figure 7.19: Maximum dive with full speedbrake deflection (a) flight path angle profiles (b) velocity profiles

7.5 Influence of turning on optimal trajectories

7.5.1 Definition of optimal turning problem for the Terminal Area

Several optimal turning problems are described in (Vinh, 1981). These include an optimal turn to a heading, to a line and to a point. The optimization criteria can be a minimum fuel or a minimum time turn. Another performance index that is studied is a minimum radius turn. None of these optimal turning problems is applicable to the terminal-area study in this thesis. During the terminal area, the vehicle makes a turn around the Heading Alignment Cylinder. During this study, an optimal HAC configuration will be calculated. As will be explained in section 11.1.1, the HAC configuration used in this study consists of a single cylindrical HAC (constant radius). Hence, an optimal turning problem in this study can be formulated as:

Given a HAC with a specific radius, what is the optimal longitudinal strategy such that minimal energy is dissipated during the turn around that specific HAC?

The HAC geometry and the corresponding ground track during the turn are known and hence, the bank angle is not an optimization variable, but is simply equal to the required value to track the HAC. The lateral strategy that calculates the bank angle consists of a simple tracking algorithm that tracks the surface of the HAC. The only parameter that is optimized by the GA is the angle-of-attack.

Note that the solutions as found below only indicate an optimal turn around the HAC. For example, if a turn of 180°is required, the solution will be optimal for a specific HAC and corresponding radius. A different HAC will result in a different optimal solution. The goal is not to find both the HAC radius and the α for the lowest possible energy dissipation, but only an optimal solution in terms of α for a specific HAC radius. For a 180°turn, the best solution is obtained by a maneuver called a wing-over, but this is not used in this thesis.

7.5.2 Minimum energy dissipation during HAC turn

This section presents the results of the analysis of the optimal longitudinal strategy during a turn around a HAC with a radius of 5 km. All the used initial points start in point 1, see figure 7.20, with a heading of 90°. After turning 270°around the HAC, a straight flight is executed. The straight flight starts at point 7. During this straight flight, the maximum range strategy is followed. The commanded angle of attack after the turn is not determined by the optimizer but by using a maximum range control law, see section 9.3. The GA only optimizes the angle-of-attack during the turn. Afterward, the bank angle is set to zero and a switch is made to the maximum range control law.

Cost function for optimal turn

Executing a turning flight with minimal energy dissipation means that after the turn, a maximum amount of energy is still available after the turn. If after the turn, a straight wings-level flight is executed and a maximum range strategy is applied, the minimum energy dissipation criteria during the turn is transformed into a maximum range criteria after the turn. Hence, the cost function during the optimization is the y-coordinate of the final state of HORUS when it touches the ground (altitude = 0 m), which corresponds with the distance flown after the turn.

Constraints during optimization of turn

During the optimization of the turning flight around the HAC, constraints on angle-of-attack and the rate of change of the angle-of-attack were taken into account. Since only subsonic turns are studied, the angle-of-attack must be situated between 0°and 30°. The rate of change of the angle-of-attack is constraint to 3°/s. This constraint only applies to the turning part of the flight and was not applied to the switch between the turning part and the straight wings-level part. At this point a switch is made to the maximum range guidance law and the rate of the angle-of-attack can be momentarily larger than 3°/s. Further on in this thesis where complete TAEM trajectories are calculated, a filter is used such that the rate of change of the angle of attack never violates the constraint.

During a subsonic turn, the bank angle of HORUS is limited to 60°. This constraint was not implemented in the optimization process because the obtained optimal solution never dictated a bank angle calculated by the lateral guidance law that was larger than 60°. Also the load factor limit, stall speed or maximum dynamic pressure were not violated by the obtained optimal solution and hence, although they are implemented, they are not active.

Heading as independent variable

Although the initial energy at the start of the turn is known beforehand, it is impossible to know the final energy value at the end of the turn. Hence, the energy cannot be used as the independent variable during the optimal turn problem. Instead, the heading is now used as the independent variable to express the control profile. Both the initial and final heading are known and are equal to respectively 90°and 360°. Five intermediate grid points are used, with a fixed heading value. Hence a fixed grid point representation of the control vector is used with the heading as the independent variable. Figure 7.20 shows a sketch of the position of the grid points in the HAC. The arrows represent the heading angles and give the tangential direction to the HAC circle in each grid point. Table 7.10 summarizes the grid points and the corresponding heading values. The obtained optimal angle-of-attack values are specified as a function of the heading.

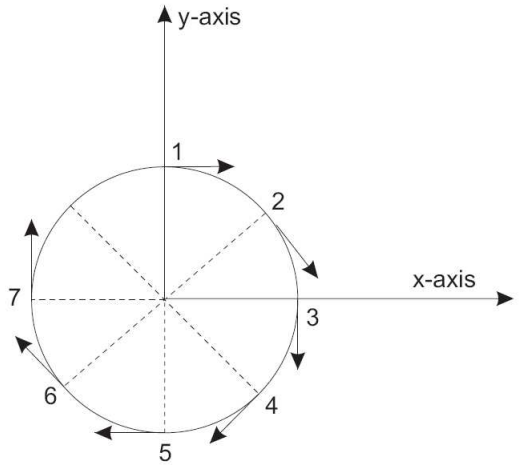

Figure 7.20: Sketch of the used grid points during the optimal HAC turn problem

Table 7.10: Grid points used during optimal turn problem and the corresponding heading values

Grid point	Heading [deg]
1	90.0
2	135.0
3	180.0
4	225.0
5	270.0
6	315.0
7	360.0

Results for optimal turn

The optimal turn around a HAC with a radius of 5 km is calculated for three initial states, see table 7.11. The three initial states all have an initial flight path angle of -10 degrees. Figure 7.21 shows an example of an optimal turn around the 5 km radius HAC and the straight flight afterward.

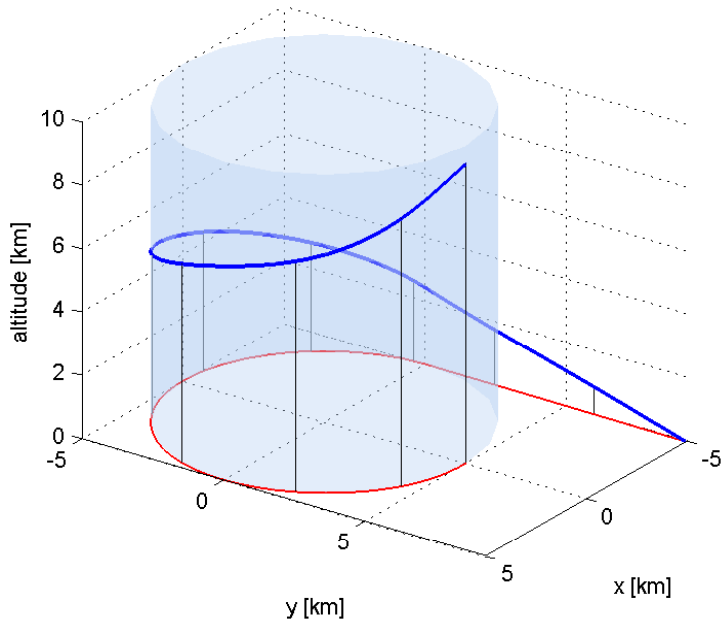

Figure 7.21: 3D view of an optimal turn around a HAC with radius 5 km for start point 1

The obtained optimal angle-of-attack profiles are shown in figure 7.22(a). The fluctuations in these profiles indicate that improvements can still be made. But although a better optimum can be found by adapting the GA or by using a local optimizer, the obtained profiles already indicate the optimal strategy for a turn around the HAC. Initially, the three profiles present very different values for the angle of attack, but from an heading equal to 180°, the three profiles indicate the same angle-of-attack region. This is similar to the trends obtained in the subsonic maximum range problem during a straight flight. In contrast to a maximum-range flight in a straight line the obtained angle-of-attack profiles do not reach a constant value but are always

decreasing. The optimal angle-of-attack values are larger than during a straight flight. During the straight flight after the turn, the heading stays approximately 360°and the angle-of-attack reduces to 7.5°.

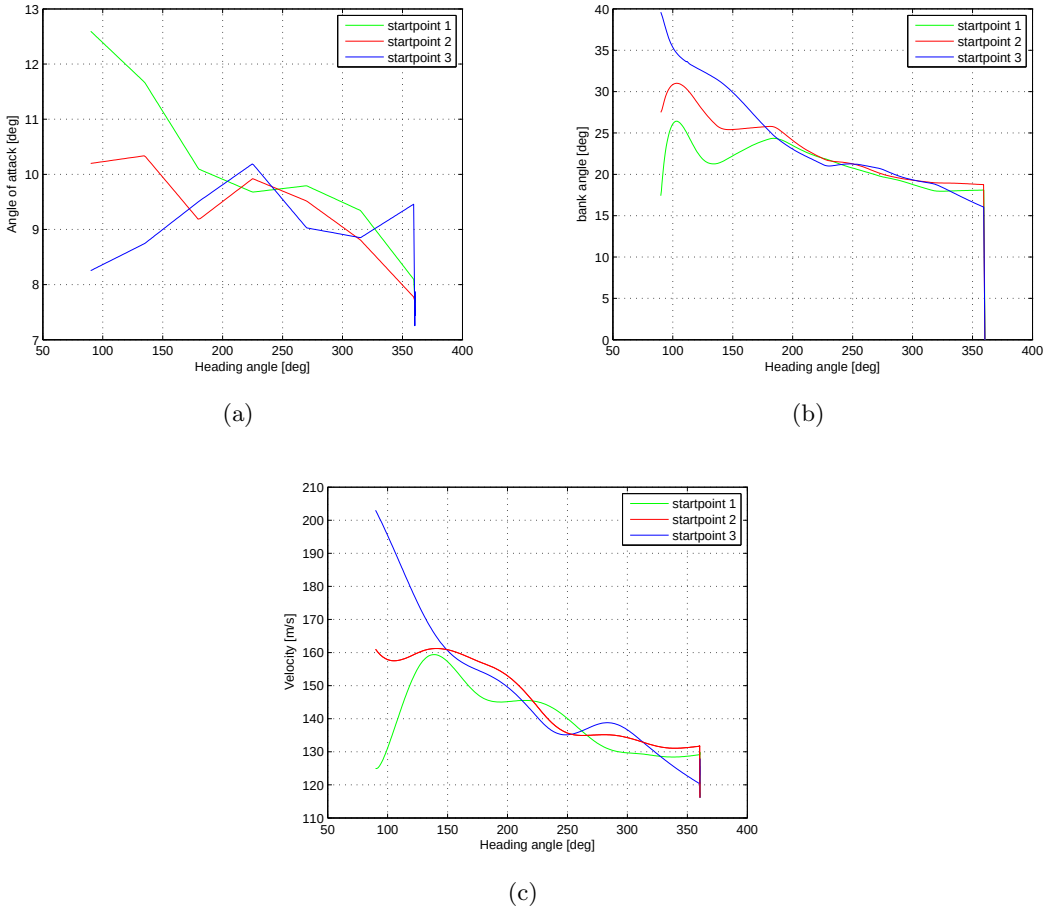

Figure 7.22: HAC radius of 5 km (a) obtained angle-of-attack profiles for optimal turn (b) required bank angle profiles to track the HAC (c) resulting velocity profiles for optimal turn

The resulting velocity, as a function of the heading angle, is shown in figure 7.22(c). This figure indicates that indeed initial maneuvers are performed to intercept an optimal velocity region. A better optimizer would reduce the fluctuations in the angle-of-attack profile and in the resulting velocity profiles. But it is already clear that there is an optimal velocity profile for a turning flight around the HAC. This will be further discussed in section 8.4.

The bank angles required to track the HAC are presented in figure 7.22(b). Due to the decreasing velocity and the constant HAC radius, the bank angle is decreased as the heading angle is increased. During the straight flight (at $\chi = 360°$), the bank angle is decreased to 0°.

7.5.3 Influence of changing HAC radius on optimal trajectory

The HAC planning algorithm will adapt the HAC configuration based on the initial state. Hence, it is necessary to know what the influence is of a different HAC radius on the optimal

Table 7.11: Initial states and obtained range after turn of 270°around the HAC with $R_{HAC} = 5$ km. Initial flight-path angle is equal to -10°.

	altitude [km]	velocity [m/s]	y-distance [km]	computation time [s]
Startpoint 1	9.4	125.0	9.27	614.55
Startpoint 2	8.8	161.0	9.28	485.99
Startpoint 3	8.0	203.0	8.99	544.33

turning trajectory. Therefore, optimal trajectories are calculated for a HAC with R_{HAC} equal to 3 km and 7 km. The same three initial states are used as for $R_{HAC} = 5$ km. The simulations concerning a 3 km radius HAC also start in point 1 (see figure 7.20) but for the 7 km radius HAC, simulations start at point 3. If they would start at point 1, the ground is reached before ending the turn due to the increased distance around the HAC.

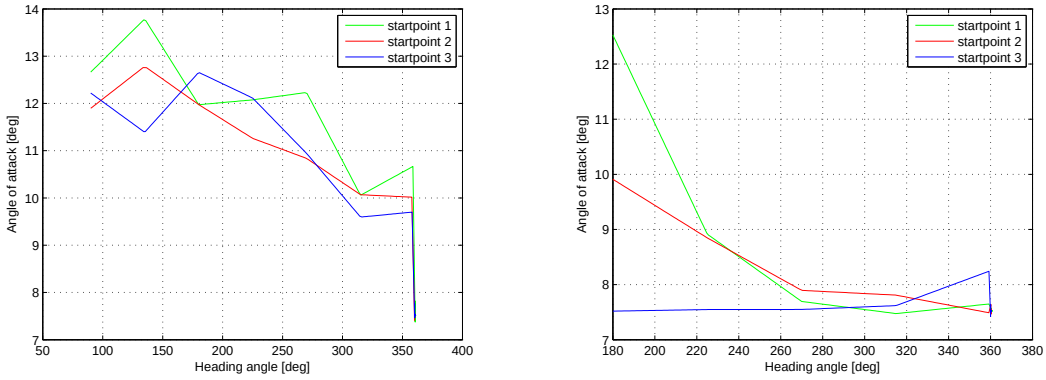

(a) (b)

Figure 7.23: obtained angle-of-attack profiles for optimal turn (a) HAC with 3 km radius (b) HAC with 7 km radius

Figure 7.23(a) and 7.23(b) present the obtained optimal angle-of-attack profiles for a HAC radius of 3 km and 7 km, respectively. The fluctuations again indicated that a better optimum can be found if a better optimizer is used. Comparing these profiles with figure 7.22(a), it can be seen that a smaller turn radius requires a higher angle-of-attack. When the HAC radius decreases, the angle-of-attack profile is shifted to higher values.
The resulting velocity profiles are indicated in figure 7.24. A smaller HAC radius results in a lower optimal turning velocity. This will be further discussed in section 8.4, where this shift in optimal velocity will be further discussed.

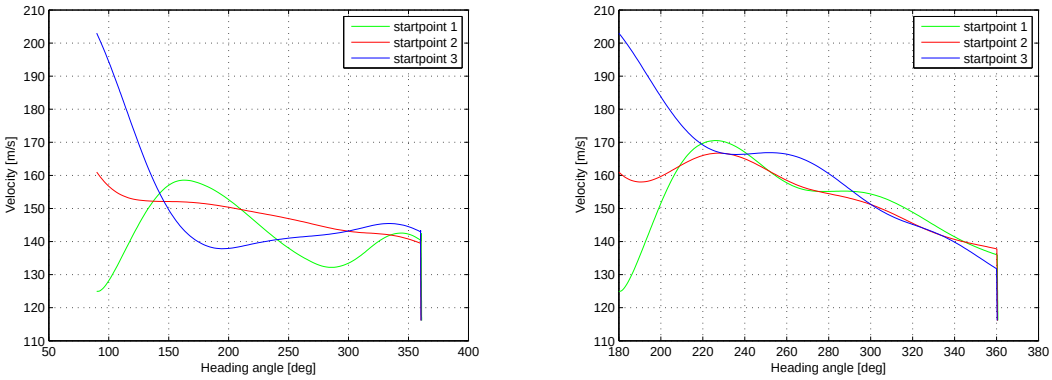

(a) (b)

Figure 7.24: resulting velocity profiles for optimal turn (a) HAC with 3 km radius (b) HAC with 7 km radius

Chapter 8

Characterization of optimal trajectories in the energy space

In the previous chapter, several optimal trajectories were calculated. The computational time required to find these optimal solutions is too large and hence, the GA cannot be used in an on-board system. It is also not possible to use a fixed angle-of-attack profile since these profiles differ for different initial states and hence also for off-nominal conditions. In this chapter, the optimal solutions will be analyzed and studied in the energy space to come up with a strategy, which approximates the optimal solution. In the next chapter, this strategy will be used to design a controller that calculates an optimal trajectory for different initial states. Such a controller can then be used in an on-board system. A fast controller allows us to calculate and analyze optimal trajectories in a short period of time. The goal of this chapter is to study the optimal solutions and to understand why they are optimal.
In section 8.1, the energy-state approximation is introduced. This energy-state approximation is used in section 8.2 and 8.3 to characterize the optimal maximum range and maximum dive solutions, respectively. In section 8.4, the use of the energy-state approximation is extended to the optimal HAC turn problem.

8.1 Energy-state approximation

In the energy-state approximation, it is assumed that kinetic and potential energy can be exchanged in zero time without loss of total energy (Bryson et al., 1968). The total energy is now considered as the state variable of the system and is continuously decreasing for a gliding vehicle. The total energy per unit of weight, or energy height E_h, was already defined in section 2.6 and is given as:

$$E_h = h + \frac{1}{2g}V^2 \tag{8.1}$$

The time derivative of the energy height is expressed as:

$$\frac{dE_h}{dt} = \dot{h} + \frac{V\dot{V}}{g} \tag{8.2}$$

Inserting equations 2.28 and 2.31 gives an expression for the time rate of change of the energy height:

$$\frac{dE_h}{dt} = \frac{-VD}{mg} \tag{8.3}$$

The most important derivative used in the energy-state approximation is the rate of energy dissipation with respect to glide range:

$$\frac{dE_h}{dR} = \frac{dE_h}{dt}\frac{dt}{dR} \tag{8.4}$$

with $\frac{dE_h}{dt}$ given by equation 8.2. $\frac{dR}{dt}$ is equal to the time rate of change of the range, or the horizontal component of the velocity. Inserting expressions for both terms results in:

$$\frac{dE_h}{dR} = (\frac{\dot{h}}{V} + \frac{\dot{V}}{g})\frac{1}{cos\gamma} \tag{8.5}$$

A new form can be found for the first term on the right side by using equation 2.31 and substituting equation 2.28:

$$\frac{D}{mg} = -sin\gamma - \frac{\dot{V}}{g} = -(\frac{\dot{h}}{V} + \frac{\dot{V}}{g}) \tag{8.6}$$

Substituting equation 8.6 in equation 8.5 gives the final expression for the rate of energy dissipation with respect to glide range:

$$\frac{dE_h}{dR} = -\frac{D}{mg}\frac{1}{cos\gamma} \tag{8.7}$$

The energy of a vehicle consists of an altitude component and a velocity component. Plotting a trajectory in terms of the altitude as a function of the velocity results in a trajectory in the energy space or the (V,h) space.

8.1.1 Maximum range glide

Within the energy-state approximation, where the total energy is considered as a state variable, the maximum range is obtained by minimizing the magnitude of dE_h/dR (Bryson et al., 1968). This means that, assuming a small influence of the cosine of the flight-path angle, the drag has to be constantly minimized for a specific energy height to maximize the range.

The drag level depends on the angle-of-attack (drag coefficient), the altitude (density) and the velocity, see equation 2.5 . Hence, to be able to plot the drag level in the (V,h) space or energy space, a specific value for the angle-of-attack needs to be defined such that the drag becomes only a function of altitude and velocity. In (Bryson et al., 1968), the angle-of-attack required for an equilibrium between the lift and the weight is used.
Using this strategy to calculate α, the drag level can be calculated for each combination of altitude and velocity. For a specific energy level, there is one combination of altitude and velocity for which the drag encountered by the vehicle is minimum. Hence, a trajectory in the energy space can be defined for which the drag is minimum at each energy level. If the initial conditions are not on this minimum drag or maximum range glide path, the vehicle should either zoom-climb or zoom-dive with constant energy to join the curve (Bryson et al., 1968), (Vinh, 1981). Near the end of the flight, an improvement in range can be obtained by performing a

final flare during which kinetic energy is converted into potential energy until the stall speed is reached. Figure 8.1 shows a sketch of a typical maximum range glide path in the energy space. In reality, the zoom-climb or zoom-dive without loss of energy is of course not possible for a gliding vehicle. These discontinuities in altitude and velocity are unrealistic. The total energy of a gliding vehicle always decreases and because of this loss of energy, the trajectory is curved.

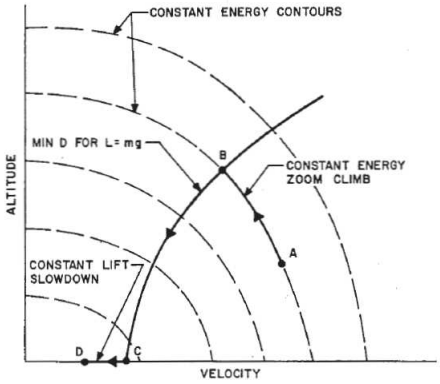

Figure 8.1: Sketch of a typical maximum range glide (Bryson et al., 1968)

Before the energy-state approximation is applied to HORUS, the energy-state approximation is applied to a supersonic aircraft as used in (Bryson et al., 1968) to validate the method. The energy-state approximation is also applied to a modified version of the supersonic aircraft to validate the method for a supersonic aircraft with poor gliding capabilities. Such a vehicle resembles a winged re-entry vehicle more closely.

8.1.2 Supersonic aircraft

In (Bryson et al., 1968), the energy-state approximation was used to calculate the maximum glide path for a supersonic aircraft. The aerodynamic characteristics of the used supersonic aircraft are given in appendix C. The supersonic aircraft has relative good gliding capabilities with a maximum lift-to-drag ratio of 10.3 and 7.6 in the subsonic and supersonic speed regime, respectively.

Contours of constant drag

Figure 8.2(a) shows the contours of constant drag in the energy space as given in (Bryson et al., 1968) for this supersonic aircraft. The contours of constant drag are calculated for an equilibrium situation, where the lift equals the weight of 34200 lb (15512.86 kg).

The first goal in this section is to calculate the same contours of constant drag and to confirm the values and shape as indicated in figure 8.2(a). Using the aerodynamic data as presented in appendix C and the lift-equal-to-weight assumption, the drag was calculated throughout the (V,h) space. Figure 8.2(b) shows the calculated contours of constant drag for the supersonic aircraft. In figure 8.3, a 3D-view of the drag levels is given. The drag valley in which the maximum range path is situated, is clearly visible. The calculated drag levels and the shape of the drag valley correspond with figure 8.2(a).

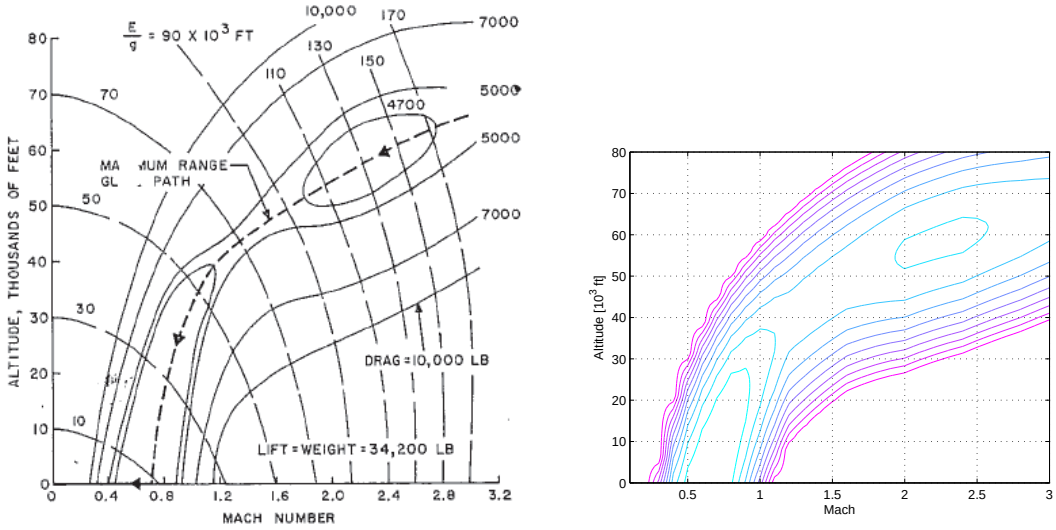

(a) (b)

Figure 8.2: (a) Maximum range glide path for a supersonic aircraft and contours of constant drag for L=W (Bryson et al., 1968) (b) Contours of constant drag for supersonic aircraft

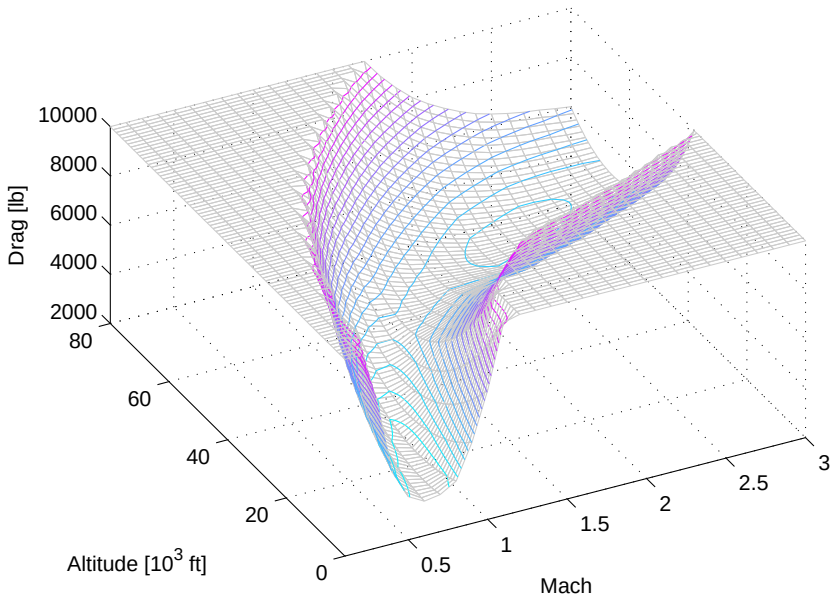

Figure 8.3: 3D-view of the contours of constant drag for a supersonic aircraft

The lift-equal-to-weight assumption is actually not correct, because a gliding vehicle does not perform a level flight in a steady situation, but a descending flight. So the real equilibrium in a zero bank situation is described by:

$$L = W cos\gamma \tag{8.8}$$

Due to the introduction of the flight-path angle, the calculation of the required angle of attack becomes an iterative process similar to the one described in section 6.1.2. Once the angle of

attack is found, the corresponding drag level can be calculated at the specific altitude and velocity. Results indicated that the introduction of the flight-path angle did not have any influence on the shape of the drag valley. Only minor changes were found in the drag levels. This is because of the low values of the flight-path angle and hence, the near unity value of the cosine of the flight path angle. When the flight-path angles are larger, as is the case, for example, for a winged re-entry vehicle, the influence of the flight-path angle must be taken into account.

Figures 8.2(b) and 8.3 were calculated in the foot-pound-second system to be able to compare the calculated results with (Bryson et al., 1968). However, in this thesis study, all the formulas and programs used for simulating the motion of a winged re-entry vehicle are expressed in SI units. To compare the optimal trajectories for the supersonic aircraft calculated with the GA, the figures are converted to SI units. The contours of constant drag will therefore be plotted using SI units from now on.

Optimal trajectories

In (Bryson et al., 1968), only a sketch of the maximum-range glide path for the supersonic aircraft was given, see figure 8.2(a). No actual calculated optimal trajectories were presented. Hence, the second goal of this section is to calculate optimal maximum range trajectories for the supersonic aircraft and investigate if these trajectories actually follow the theoretical maximum range glide path. Hence, this section is used for validation and verification purposes.

Table 8.1: Initial conditions and obtained range for a supersonic aircraft. Results are indicated for both a Genetic Algorithm and a Monte Carlo after the GA. A Monte Carlo is used for the first time in this study to reduce fluctuations in α. Initial flight path angle is equal to -7deg (n.a. = not applicable)

	altitude [km]	**velocity** [m/s]	**GA range** [km]	**MC after GA range** [km]
Startpoint 1	22.86	653.40	342.32	n.a.
Startpoint 2	18.50	715.00	341.09	341.65
Startpoint 3	14.00	770.00	332.70	333.22

Optimal maximum range trajectories are calculated for the supersonic aircraft using a GA with the same parameter settings as used in chapter 7. The control vector is represented by 10 fixed grid points with energy as the independent variable. The GA searches an optimal value for the angle-of-attack at each grid point in an interval of [0°, 10°] degrees. The grid points are specified by the following energy values:

$$E_{grid} = [0.0,\ 2.5,\ 10.0,\ 15.0,\ 20.0,\ 25.0,\ 30.0,\ 35.0,\ 40.0,\ 45.0] \tag{8.9}$$

Table 8.1 indicates the initial conditions of three different starting points for which an optimal maximum range trajectory was calculated. Also the obtained maximum range results are indicated in this table for a GA optimization. Figure 8.4(a) indicates the optimal maximum range trajectories in the (V,h) space or energy space. It is clear that the optimal trajectories all go to the drag valley, but some fluctuations are present during the path through the drag valley. Due to the relative large L/D, the trajectory is sensitive to small changes in the angle of attack

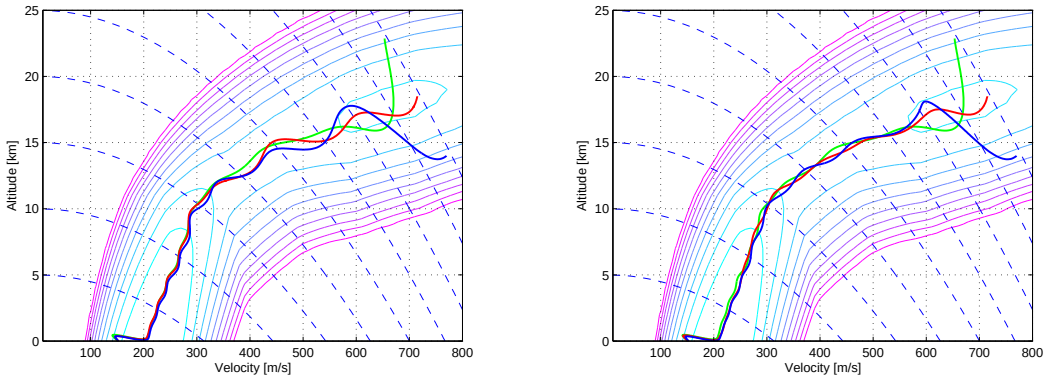

(a) (b)

Figure 8.4: Maximum range trajectories for the supersonic aircraft using (a) only a Genetic Algorithm and (b) a Monte Carlo after the GA. Three trajectories are indicated, corresponding to the three initial starting points.

and hence, fluctuations in the trajectory exist.

These fluctuations are present because the GA is a global optimizer that only gives a solution close to the optimum, but not exactly the optimum. In an attempt to diminish these fluctuations, a local Monte Carlo analysis was performed on the angle-of-attack profile resulting from the GA. Since the fluctuation are the largest for initial state 2 and 3, a Monte Carlo was performed on those α-profiles but none was performed on the GA result for initial state 1.

During a Monte Carlo analysis, 1000 new angle-of-attack profiles were randomly calculated and the profile that gives the maximum range has been selected. A new profile is obtained by taking a number of angle-of-attack values from the profile obtained using the GA and for each value, an α variation is calculated which is added to the original value. So to obtain a new profile, all the α values at the grid points are changed at once, but all with a different random value. The random value is bounded by a maximum and a minimum value. For example, a $\Delta\alpha$ value of 0.05° means that the α value at a particular grid point obtained from the GA can only be changed by a maximum of 0.05° (added or subtracted). For the Monte Carlo analysis, more grid points are used than during the GA. The grid points as given in expression 8.9 are still used, but additional grid points have been selected in between. The angle-of-attack profiles resulting from the GA and the new profiles obtained after the Monte Carlo are shown in figure 8.5, both for initial states 2 and 3.

The profiles after the MC analysis as shown in this figure are actually a combination of two MC runs with different $\Delta\alpha$ boundaries. For initial state 2, the profile after the MC which gave the least fluctuations of the complete optimal trajectory in the energy space, is obtained using a $\Delta\alpha$ value of 0.2° for energy heights between 0 km and 22.5 km, and a $\Delta\alpha$ value of 0.5° for energy heights between 25 km and 45 km. For initial state 3, the best result is obtained by combining a $\Delta\alpha$ value of 0.1° for energy heights between 0 km and 20 km, and a $\Delta\alpha$ value of 0.5° for energy heights between 22.5 km and 45 km.
The new optimal maximum range trajectories in the energy space are shown in figure 8.4(b). This figure indicates a reduction in fluctuations, while table 8.1 shows that the maximum ranges are slightly increased with respect to the results after the GA.

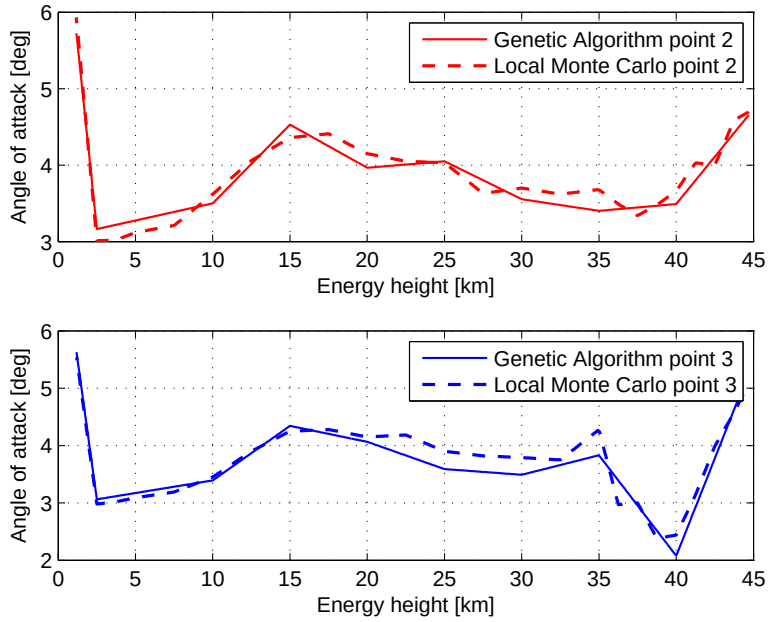

Figure 8.5: Angle-of-attack profiles for initial states 2 and 3 of the supersonic aircraft using a Genetic Algorithm and a GA + Monte Carlo

The optimal maximum-range results confirm the energy-state approximation theory of a maximum-range glide. The three trajectories follow the minimum-drag or maximum-range glide path. If the initial state is not situated on this maximum-range glide path, a dive or zoom maneuver is performed to join this path. At the end of the flight, a flare maneuver is performed to gain some extra range.

As a final note, consider the initial transient maneuvers as indicated in figure 8.4(b). Both for situations that require a dive or a zoom maneuver, the optimal solution indicates a small overshoot of the drag valley before entering this valley. For a supersonic aircraft with relative good gliding capabilities, this overshoot is only marginal and can be ignored. But for an aircraft with poor gliding capabilities and hence, for HORUS, this may be a problem.

8.1.3 Adapted supersonic aircraft with poor gliding capabilities

A gliding re-entry vehicle has poor gliding capabilities in comparison to the supersonic aircraft as used in (Bryson et al., 1968). Therefore, the aerodynamic data of the supersonic aircraft are adapted such that the maximum lift-to-drag ratio is lowered to a value of 4.3 and 3.2 in the subsonic and supersonic velocity regime, respectively. The aerodynamic data of the adapted supersonic aircraft are given given in appendix C. The goal of this section is to extend the maximum-range theory of the energy-state approximation to supersonic vehicles with poor gliding capabilities.

The new contours of constant drag for this adapted supersonic aircraft are given in figure 8.6(a). The optimal maximum range trajectories are obtained using a genetic algorithm with the same GA parameters as specified in chapter 7. The control vector is represented by 11 fixed

grid points with energy as the independent variable. The angle-of-attack interval in which the GA searches for the the optimal α value is different for each grid point. The energy values at the grid points and the corresponding α interval boundaries are specified as:

$$E_{grid} = [0.0,\ 4.8,\ 6.0,\ 10.0,\ 15.0,\ 20.0,\ 25.0,\ 30.0,\ 35.0,\ 40.0,\ 45.0] \quad (8.10)$$

$$\alpha_{min} = [8.0,\ 5.0,\ 5.0,\ 5.0,\ 0.0,\ 0.0,\ 8.0,\ 8.0,\ 8.0,\ 8.0,\ 8.0]^\circ \quad (8.11)$$

$$\alpha_{max} = [20.0,\ 12.0,\ 12.0,\ 10.0,\ 10.0,\ 10.0,\ 20.0,\ 20.0,\ 20.0,\ 20.0,\ 20.0]^\circ \quad (8.12)$$

The α boundary values were obtained by trial and error. They were chosen such that the GA gave relatively quickly (288 seconds) an optimal solution without being close to the chosen α boundaries. The angle-of-attack values of the obtained optimal profile never came close to the boundaries and hence, these boundaries do not prohibit the GA to find the optimum.

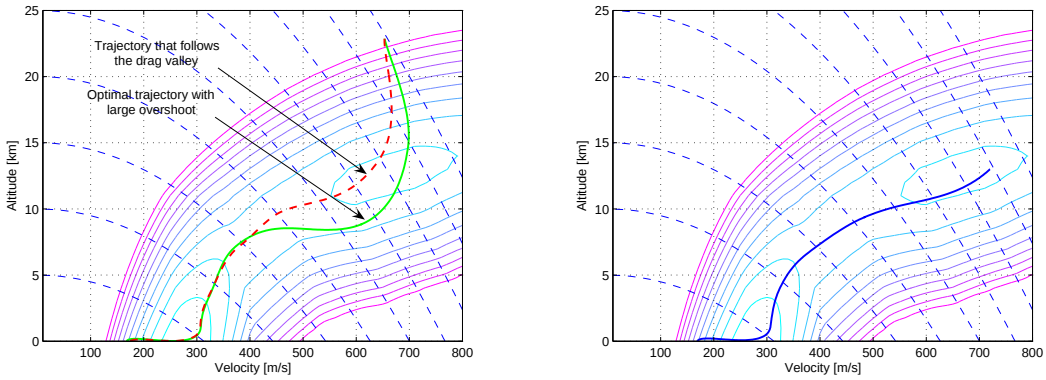

(a) (b)

Figure 8.6: Contours of constant drag for adapted supersonic aircraft with poor gliding capabilities and corresponding maximum range glide trajectories

In figure 8.6(a), the obtained optimal maximum range trajectory is presented in the energy space for the same initial state of starting point 1, see table 8.1. The obtained maximum range is equal to 132.76 km. The optimal trajectory indicates a large overshoot of the drag valley before entering it. To check if this really is the optimal solution, a trajectory was manually calculated that does follow the drag valley without any overshoot. This trajectory is also indicated in figure. The obtained range of this trajectory is 129.58 km and hence, the optimal solution indeed contains an overshoot of the drag valley. Figure 8.6(b) shows an optimal maximum range trajectory for an initial state which is already situated in the drag valley. In this case, the optimal trajectory does follow the drag valley, except for a small deviation in the beginning. Note that the trajectories as given in both figures 8.6(a) and 8.6(b) do not fluctuate. Due to the low L/D, the trajectory is less sensitive to small changes in α.

It can be concluded that for a supersonic vehicle with good gliding capabilities, the maximum glide path is followed. The small overshoot during the transient maneuvers required to join this maximum range path can be neglected. But for a supersonic aircraft with poor gliding capabilities, these maneuvers must be taken into account and have a great influence on the optimal maximum range trajectory. When such a vehicle starts at an initial state above the maximum range glide path, the vehicle first has to dive and then a pull-up maneuver is required to join the maximum range glide path. Hence, the lift force has to be increased by using

a higher angle-of-attack. An increase in lift also means an increase in drag force. For a vehicle with a lower lift-to-drag ratio, the drag will increase more rapidly for a specific increment in lift (specific angle-of-attack increase) than for a gliding vehicle with a higher lift-to-drag ratio (better gliding capabilities). Due to the combination of the supersonic velocity and the lower lift-to-drag ratio, the optimal dive and pull-up maneuver that requires the least amount of integrated drag, is obtained at a lower angle-of-attack than the one required to not overshoot the drag valley. The result is an overshoot of the maximum range glide path. The principle of flying a trajectory with minimum integrated drag is still valid, but this trajectory does not follow the minimum drag path that was obtained using an equilibrium situation. At supersonic velocities and poor gliding capabilities, the maximum range path can no longer be visualized in the energy space by computing the drag for an equilibrium situation. This will be further discussed in the next section.

8.2 Maximum range flight of HORUS

The goal of this section is to investigate if the energy-state approximation is a valid approximation to the optimal maximum range results as obtained in chapter 7 by the GA.

8.2.1 Contours of constant drag of HORUS

The contours of constant drag are obtained by calculating the drag level at each combination of altitude and velocity throughout the (V,h)-space. It was already stated that next to the altitude and velocity, the drag also depends on the angle-of-attack. Similar to the strategy used in (Bryson et al., 1968), the angle of attack required for an equilibrium or stationary-flight situation will be used. Because the aerodynamic data of HORUS consists of several lift and drag curves for different Mach numbers, the calculation of the required angle-of-attack and resulting drag level is an iterative process. The same steps as given in section 6.1.2 are used to determine the angle of attack (steps 1-7). Once α is found, the drag is simply calculated by using equation 2.5.

Figure 8.7 presents the obtained drag contours between the minimum and the maximum dynamic pressure boundaries, and for subsonic velocities (Mach < 0.8). Figure 8.8 gives a 3D-view of the drag contours. The drag valley is clearly visible in both plots. The drag levels at low velocities near the minimum dynamic pressure boundaries are larger than at the maximum dynamic pressure boundary.

Figure 8.9 shows a 3D-view of the drag levels in the supersonic region using the trim boundaries on the angle of attack as indicated in figure 6.4. In contrast to the subsonic region, no clear drag valley is visible. Going from low altitudes and high velocities to high altitudes and low velocities, one can see that in the beginning the drag level descends and even reaches a steady level or slightly increases, which indicates a hint of a drag valley, but then descends again. This is due to the angle-of-attack boundaries for trim considerations. Flying in a steady state at lower velocities requires an increased angle of attack to raise the lift coefficient. This is necessary to keep the vertical component of the lift equal to the weight, at lower velocities. At a certain point, when the velocity is decreased further, the required angle of attack for a steady-state glide is larger than the angle of attack which is possible using the α filter due to trim considerations. The angle of attack is not large enough to have a steady-state and HORUS

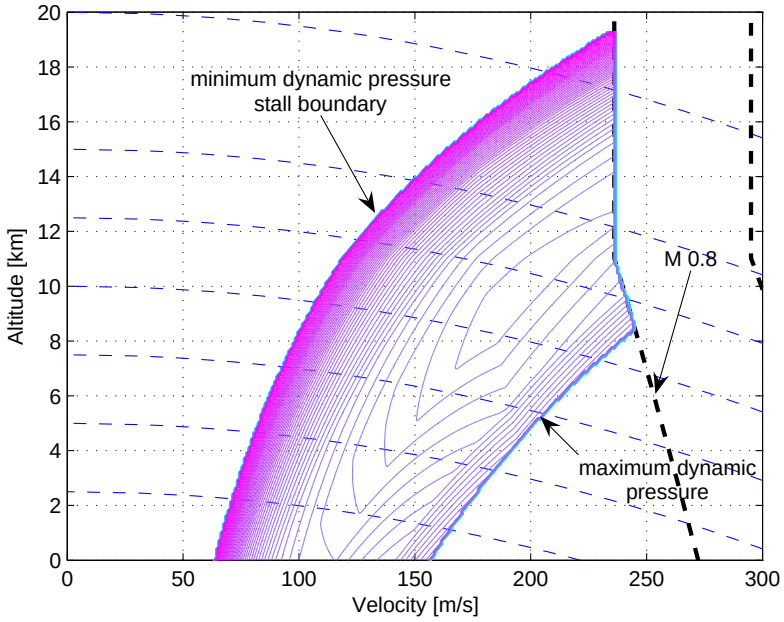

Figure 8.7: Contours of constant drag for HORUS in the subsonic velocity regime

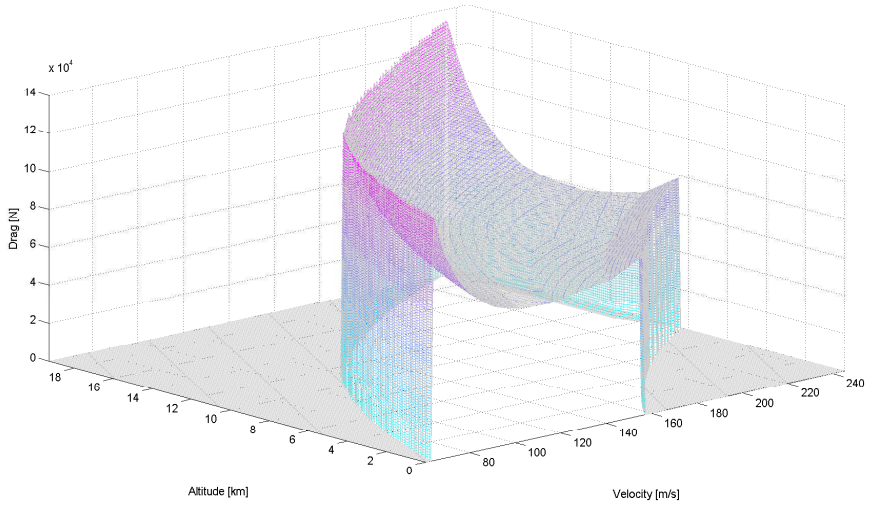

Figure 8.8: 3D-view of the contours of constant drag for HORUS in the subsonic velocity regime

executes a falling motion. The drag level in that flight situation is lower than the drag level at a steady-state glide. Turning off the α filter due to trim considerations results in the drag levels as indicated in figure 8.10. The drag valley is now clearly visible. Comparing figure 8.9 and 8.10 indicates the velocity profile at which the α filter limits the used angle-of-attack value. To be able to investigate the complete maximum range capabilities of HORUS during the thesis work and to be able to study the governing general physical principles of a supersonic maximum range glide for a winged re-entry vehicle, the upper α boundary in the supersonic region due to trim considerations will not be taken into account. Since HORUS needs to be able to

fly in the drag valley, the trim law should be adapted. If the required trim deflections of the wing flaps (elevons) becomes too large such that there is not enough margin left for control and maneuvering purposes, the design of HORUS should be changed such that alternative trim strategies can be used. Two possibilities might be considered: the use of reaction-control jets and adding a canard. This is outside the scope of this thesis work. Instead it is just assumed that it is possible to use a new trim strategy that allows HORUS to fly in a trimmed supersonic steady-state within the complete flight envelope. Hence the drag levels as shown in figure 8.10 will be used. Note that in the subsonic region, HORUS is capable of flying in the drag valley using the original trim law.

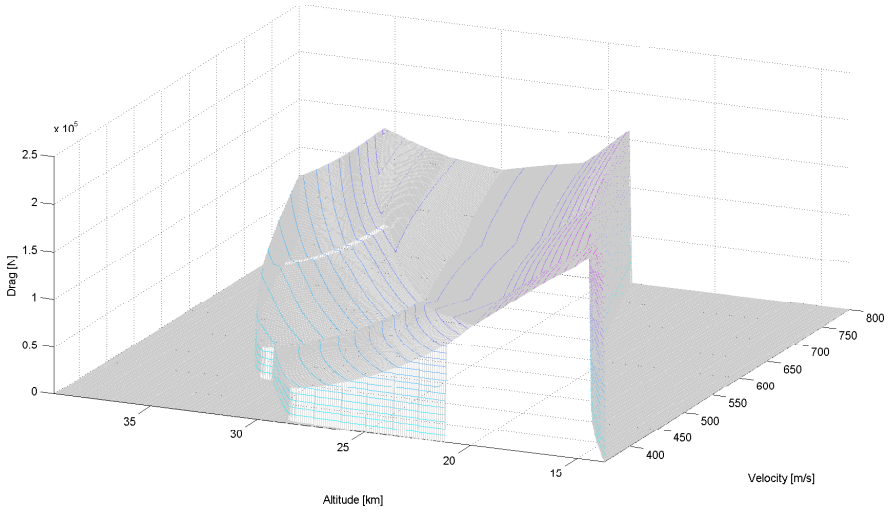

Figure 8.9: Contours of constant drag for HORUS in the supersonic velocity regime using the α filter due to trim considerations

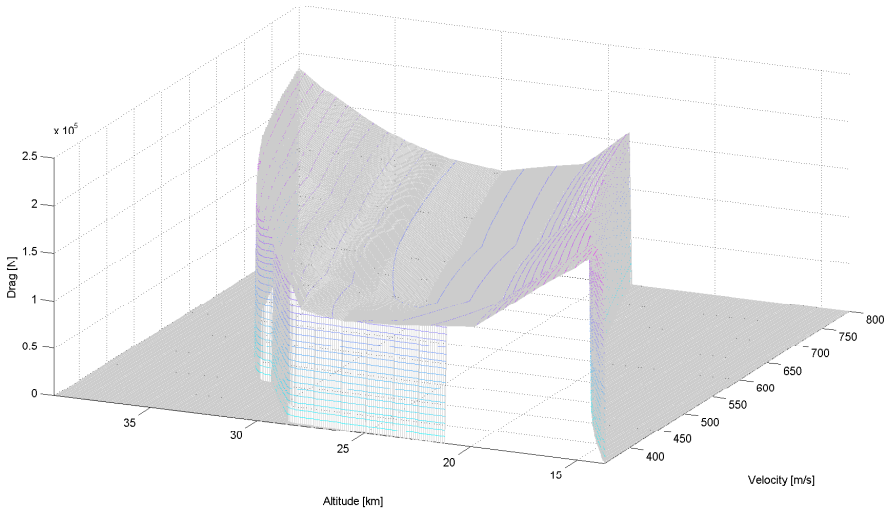

Figure 8.10: Contours of constant drag for HORUS in the supersonic velocity regime using no α filter

The contours of constant drag in the energy space for the complete velocity interval (subsonic and supersonic) can, for example, be seen in figure 8.12(a). No contours of constant drag are shown in the transonic speed regime, because the vehicle capabilities in this region are insufficient to have an equilibrium flight situation. A falling motion is performed in the transonic region, see (Helmersson, 1988b). Also note that the drag valley in the supersonic regime is situated at a different dynamic pressure than for the subsonic regime.

8.2.2 Optimal maximum range trajectories

Figure 8.11(a) presents the steady-state subsonic maximum range trajectories in the (V,h) space, while the optimal trajectories are indicated in figure 8.11(b). The steady-state solutions fluctuate around the drag valley and are damped out near the end of the flight. These fluctuations correspond to the fluctuations in altitude and velocity as already described in chapter 4. The optimal solutions are obtained by flying in the drag valley for the largest part of the flight. Initial maneuvers are performed to go to the drag valley and a final flare maneuver is performed to convert kinetic energy into potential energy. The optimal solutions do not show the large fluctuations around the drag valley. However, some small fluctuations are still present because the GA is a global optimizer, which can only give a solution that is close to the optimal one. Performing a local optimization that uses the result of the GA as an initial guess would help to eliminate the fluctuations. Despite these small fluctuations, the GA is able to find a solution that is very close to the optimal solution and the obtained results confirm the theory as stated in (Bryson et al., 1968) for a supersonic aircraft. The energy-state approximation can be applied to a winged re-entry vehicle with poor gliding capabilities in a subsonic glide.

The largest range is obtained for initial state 2, see table 7.3.2. Figure 8.11(b) indicates that this point is already situated in the drag valley. Hence, the maximum range will be larger for initial states that are already situated in the drag valley than for initial states that require transient maneuvers to intercept the drag valley. The drag valley can be compared with a highway. Following this highway will result in the largest distance for a specific amount of fuel (energy). If a car does not begin on the highway, an additional route is required to first get to the highway. This will cost some energy and hence, less energy is available on the highway, resulting in a smaller maximum distance.

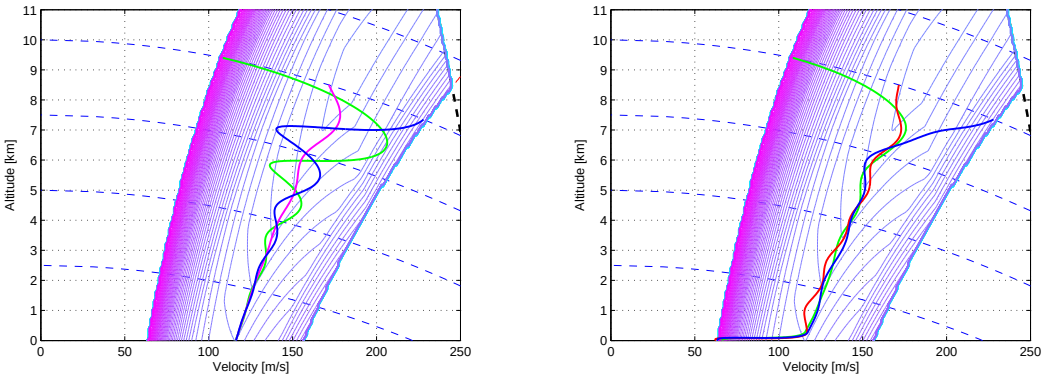

(a) (b)

Figure 8.11: (a) Steady-state solutions to the subsonic maximum range problem in the energy space (b) Optimal subsonic maximum range trajectories in the energy space

Figure 8.12(a) presents the steady-state maximum range trajectories in the energy space for supersonic initial states. In the supersonic region, the fluctuations are less severe but the obtained solutions are relatively far away from the drag valley. When entering the subsonic velocity regime, no fluctuations are present any more. As shown in figure 8.12(b), the obtained optimal solutions for initial supersonic conditions do not follow the drag valley. There are two reasons for this behavior. The first reason was already described for the adapted supersonic aircraft with poor gliding capabilities. Due to the combination of high velocities and the poor gliding characteristics, the drag encountered during the maneuver to reach the drag valley is not optimal. A second reason for not following the drag valley, is the optimal trajectory in the transonic region. Figure 8.12(b) indicates that the three optimal trajectories all start the transonic phase of the flight with the same entry conditions in terms of altitude and velocity. The followed trajectories from these entry conditions until the end of the flight are almost identical to each other. The trajectories in the supersonic part are shaped such that the transonic entry point is reached with the optimal conditions.

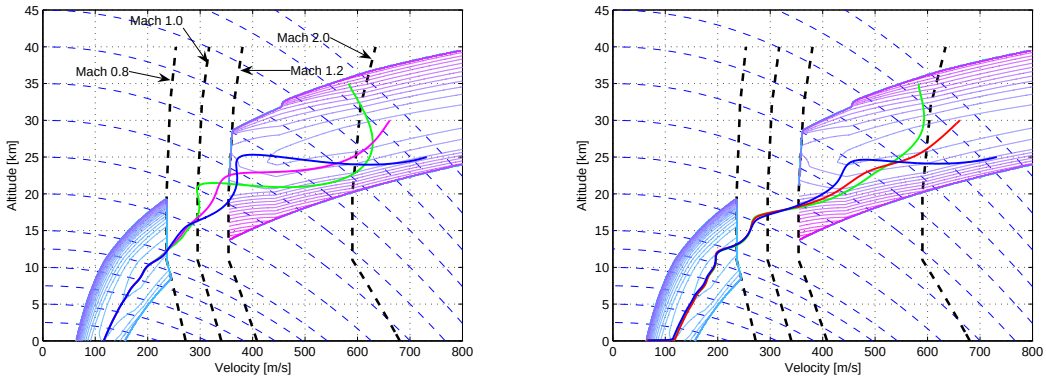

(a) (b)

Figure 8.12: (a) Steady-state solutions to the supersonic maximum range problem in the energy space (b) Optimal supersonic maximum range trajectories in the energy space

In the energy-state approximation, the value of the drag is calculated using the required angle of attack for a steady-state. Hence, one could wonder what the difference is between the steady-state approximation and the energy-state approximation. Figure 8.13 indicates the the stationary maximum range points from the steady-state analysis, see table 6.1, in the energy space. The points are all situated on a curve of constant equivalent airspeed (116.0 m/s), which coincides with the drag valley. At each stationary point, the lift-to-drag ratio is maximal and hence, the first interpretation is to fly at maximum lift-to-drag ratio. But actually, this is only valid for those points as indicated in figure 8.13 with specific combinations of velocity and altitude. An improved and second interpretation is to fly at a constant equivalent airspeed. The result of this interpretation of the steady-state solution is identical to the energy-state approximation. Hence, the difference between the steady-state interpretation which uses the angle-of-attack profile for maximum lift-to-drag ratio as a function of velocity, and the energy-state approximation is the interpretation of the theory and the used independent variables. The α-profile for maximum lift-to-drag ratio uses only the velocity as the independent variable, while the energy-state approximation uses energy, which is a function of both velocity and altitude. The α value obtained from the stationary maximum range points at the optimal velocity are

only correct if used at the altitude for which the performance curve is calculated. So instead of flying at a maximum lift-to-drag ratio at each velocity, a better approximation is to fly with a different α until the required equivalent airspeed or dynamic pressure is reached and then, a maximum lift-to-drag ratio can be used.

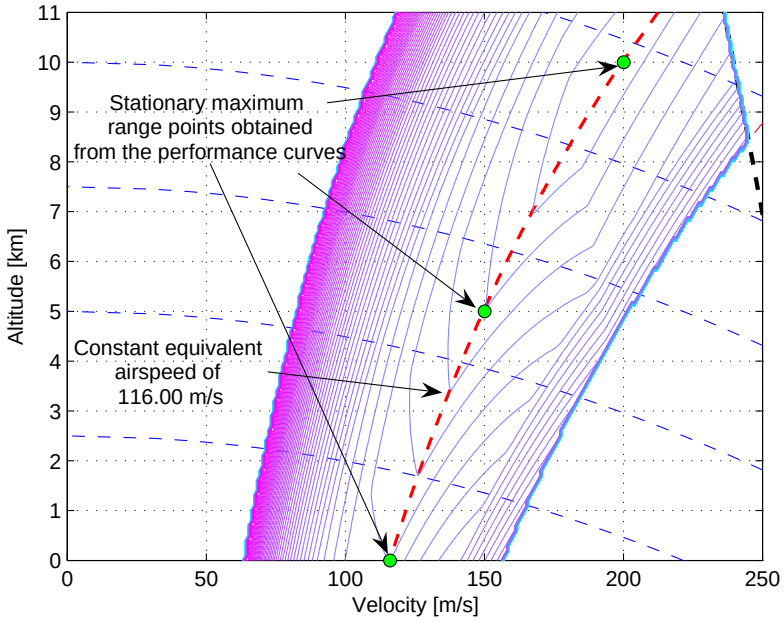

Figure 8.13: Stationary maximum range points in the energy space

It can be concluded that the energy-state approximation is a valid approximation to the maximum range problem of a winged re-entry vehicle at subsonic velocities. For a supersonic glide, the principles of dissipating the least amount of energy with respect to flown range and flying at minimum drag are still valid, but the angle of attack for an equilibrium stationary situation can no longer be used to visualize the drag valley in the energy space.

8.3 Maximum dive of HORUS

The maximum dive or minimum range trajectories for HORUS in the vertical plane were calculated using a GA in the previous chapter. This section describes how these results relate to the contours of constant drag in the energy space.

Figure 8.14 shows the maximum dive trajectories for initial states 1 and 2, without the use of speedbrakes. This figure clearly indicates that the maximum dive is obtained by flying at a minimum dynamic pressure and accelerating (by lowering the nose) at the end of the flight. At the minimum dynamic pressure boundary, the encountered drag is much higher than when flying at maximum dynamic pressure. In order to perform the maximum dive, the nose of the vehicle must be raised to fly at the minimum dynamic pressure boundary, which is opposite to the natural instinct of lowering the nose of the vehicle to dive as fast as possible.

Figure 8.15(a) shows the maximum diving flight for initial state 3. As explained in section

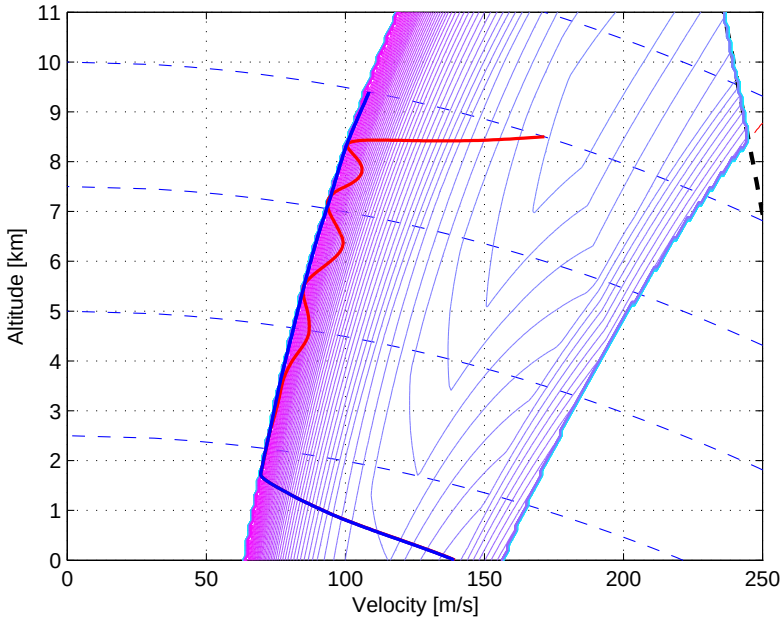

Figure 8.14: Maximum dive for subsonic conditions; without the use of speedbrakes. Two trajectories are indicated, corresponding with initial states 1 and 2.

7.4, the trajectory obtained by using fixed grid points deviates from the trends as seen in the dive trajectories for initial states 1 and 2. A new optimization using variable grid points indicates a trajectory which follows the trend from the trajectories for initial states 1 and 2 more closely. Since the range for initial state 3 is shorter using the variable grid points, it can be concluded that flying at minimum dynamic pressure is indeed the optimal dive strategy, but the GA is not capable of exactly finding this optimum.

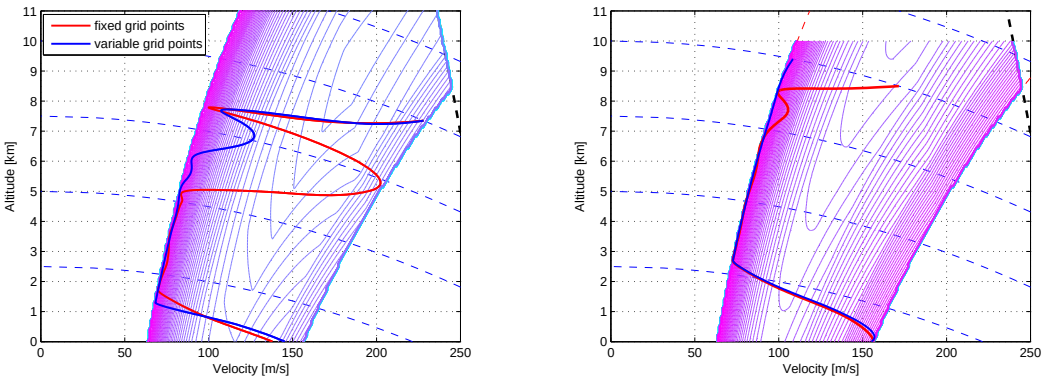

(a) (b)

Figure 8.15: (a) maximum dive without speedbrakes for initial state 3 (b) maximum dive trajectories for two subsonic initial states using a full speedbrake deflection

An increase in speedbrake deflection directly increases the orbiter drag and the steepness of the trajectory, both of which increase the dissipation of energy with respect to range (Kraemer & Ehlers,

1975). The obtained optimal maximum dive trajectories with full speedbrake deflection are shown in figure 8.15(b), for initial states 1 and 2. New contours of constant drag were calculated because a speedbrake deflection has an influence on the obtained steady-state, the required angle-of-attack and the corresponding drag level. The minimum drag valley is shifted to lower velocities and the overall drag level has increased.
The results indicate that also when the speedbrakes are used, the maximum diving flight is obtained by flying at a minimum dynamic pressure and by accelerating near the end of the flight. Some fluctuations are present in the optimal diving trajectories for initial point 2. This is again due to the fact that the GA is a global optimizer which only gives a solution close to the real optimum.

These results are opposite to the maximum dive strategy as used in (Buechner, 2003), where a maximum dive is executed at a *maximum* dynamic pressure. This maximum dynamic pressure strategy will also be used in the rest of this thesis as the maximum dive strategy, because it is the natural instinct to lower the nose of the vehicle and to perform a dive at larger velocities. Also, this strategy enables astronauts to always have a clear view on the ground and runway as a reference. Moreover, the disadvantage of flying at a low dynamic pressure is the inherent reduction in control authority (Hull et al., 2005). By flying at a maximum dynamic pressure, the diving capabilities of HORUS are reduced. The optimal maximum dive solution for HORUS to fly at a minimum dynamic pressure might still be used as a back-up in case the diving capabilities using the maximum dynamic pressure are insufficient.

The optimizations using speedbrakes were done for a full deflection of 40°. In reality, this is not possible because enough margin has to available for control purposes (rudder deflection). Therefore, during the rest of this thesis, a maximum speedbrake deflection of 25° is used.

8.4 Extension to the optimal HAC turn problem

In (Bryson et al., 1968) and (Vinh, 1981), the energy-state approximation is solely used to approximate the maximum range problem in the vertical plane. In this section, the energy-state approximation is extended to the problem on an optimal turn around a circular HAC.

During a turn around a circular HAC with a specific fixed radius, the covered ground track range is constant. Hence, the optimization criterion of minimum energy dissipation during the HAC can be transformed into a requirement of minimum energy dissipation with respect to range around the HAC: $(\frac{dE_h}{dR})_{min}$. This criterion is identical to the maximum-range criterion for the maximum-range problem in a straight wings level flight as used in the energy state approximation, see section 8.1.1. Hence, the same methodology can be used in the problem on an optimal turn around a HAC. Using equation 8.7 and assuming a small influence of the flight-path angle, the drag has to be minimized during a turn around the HAC to dissipate the least amount of energy, which is similar to the maximum range problem in a straight flight.

The contours of constant drag can be recalculated for a specific radius of the HAC. The angle of attack that is used to calculate the drag again equals the value required for an equilibrium stationary flight situation. The bank angle now has an influence on this α value. The same steps as given in section 6.1.2 are used to determine the angle of attack and the drag level. In this iteration scheme, the flight path angle and the velocity are now calculated using equations 6.16 and 6.15, respectively. The bank angle has an influence on the flight-path angle and the

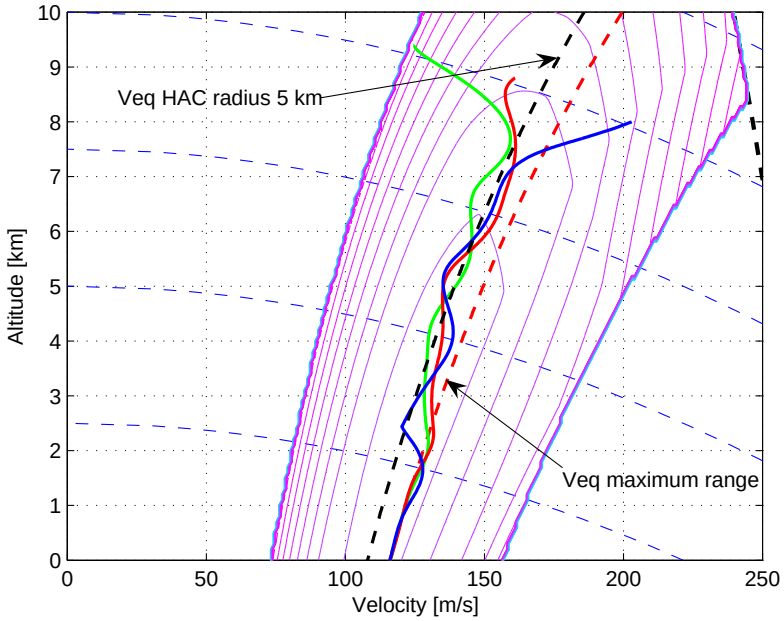

Figure 8.16: Contours of constant drag for a HAC with a radius of 5 km and optimal GA trajectories. Three optimal trajectories are indicated for three different initial states

velocity in a steady banked-flight situation. In section 6.3.2, the influence of the velocity and bank angle on the turn radius was investigated. The higher the velocity, the larger the required bank angle to keep a constant turn radius. The required bank angle changes with velocity and is calculated using equation 6.17. Throughout then energy space, different bank angles are used to have a constant HAC radius.

Figure 8.16 presents the contours of constant drag for a HAC radius of 5 km and the optimal trajectories obtained using the GA as described in the previous chapter. The equivalent airspeed in the drag valley for a maximum range flight in the vertical plane is also indicated. The drag valley for the banked situation is shifted to a lower equivalent airspeed with respect to this maximum range path. The optimal trajectory are situated in the new drag valley for a banked situation with a radius of 5 km and initial transient maneuvers are performed to intercept this new drag valley. Hence, the optimal turn must be performed at a lower velocity with respect to the optimal maximum range velocity. At the end of the turn, a switch is made to a control law that tracks the equivalent airspeed of the maximum range glide path. This is clearly visible in figure 8.16. The obtained optimal trajectories for initial states 1 and 2 already tend toward the equivalent airspeed for the maximum range at the end of the turn, while the trajectory for initial state 3 stays longer at the drag valley for the turning flight. In this case, the switch to the control law for a maximum range flight is more pronounced. The optimal switch from one drag valley to the other is not studied in the current study. In the rest of this thesis, the drag valley for the turn is used throughout the complete HAC turn and a switch is made to the drag valley for the maximum range when the bank angle is set to zero. This resembles the blue trajectory of initial state 3.

Figures 8.17(a) and 8.17(b) indicate the optimal turning trajectories obtained using the GA and the contours of constant drag for a HAC radius of 3 km and 7 km, respectively. These

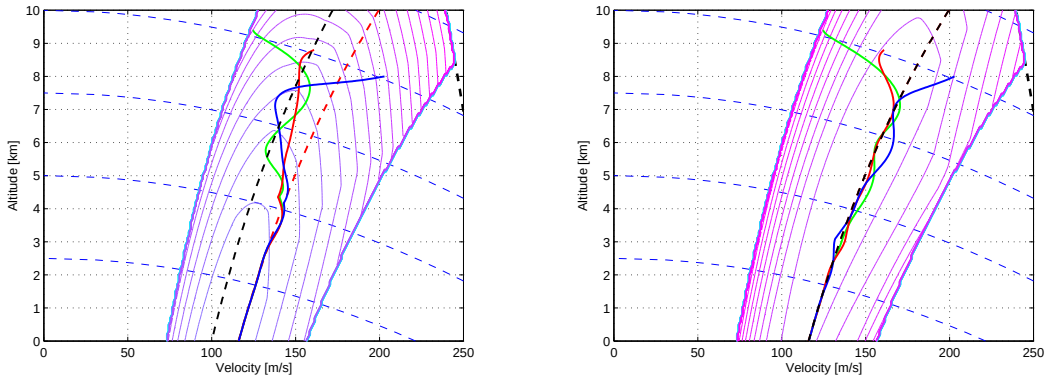

(a) (b)

Figure 8.17: Optimal GA trajectories and contours of constant drag for a HAC with a radius of (a) 3 km and (b) 7 km. Optimal trajectories are indicated for three different initial states.

figures indicate that the smaller the HAC radius, the lower the optimal turn velocity. Consider the HAC radius of 3 km. The optimal trajectory for initial state 1 does follow the drag closely and only at the end of the turning flight, the switch is made to the equivalent airspeed for maximum range. For the other two initial states, the trajectories follow the drag valley in the beginning but then, they deviate from the valley already during the turn in order to start the straight flight closer to the equivalent airspeed for maximum range. In case of a turn radius of 7 km, the drag valley for the turning flight coincides with the maximum range drag valley.

In case of a maximum range flight in the vertical plane, the drag valley corresponds to a unique value for the equivalent airspeed (116.0 m/s). For a turning flight, the drag valleys do not correspond to a constant equivalent airspeed, but changes with altitude. This effect is more pronounced in case of a small turn radius. In case of a greater turn radius, the effect can be observed especially at higher altitudes. This will not be taken into account in the rest of this thesis and a constant equivalent airspeed for the drag valley will be assumed for simplicity. Table 8.2 presents the used values for the equivalent airspeed as a function of the radius of the HAC. In the figures above, this equivalent airspeed is represented by the black line. A better result that represents the drag valley more closely can be used by making this value a function of the altitude, but this comes at the cost of complexity. Since these values will be used in a guidance system, the more simple approximation is used. The most important thing is that the optimal airspeed during the turn changes and is not equal to the optimal airspeed in a straight flight. The smaller the radius, the lower the velocity. This is already an improvement with respect to other studies on the terminal area, see for example (Helmersson, 1988b) or (Buechner, 2003), where the same reference velocity or dynamic pressure is used for both a wings-level and a turning flight. Next to the values for a radius of 3 km, 5 km and 7 km, table 8.2 also indicates the values for a HAC radius of 4 km and 6 km.

Table 8.2: Equivalent airspeed in the drag valley for a turning flight around a HAC with different radii

HAC radius [km]	V_{eq} **[m/s]**
3.0	100.0
4.0	104.0
5.0	108.0
6.0	112.0
7.0	116.0

Chapter 9

Guidance algorithms for vertical motion

The calculation of an optimal trajectory using a genetic algorithm is time consuming and hence, is not feasible to use as an on-board guidance system. In the previous chapter, the optimal trajectories were analyzed in the energy space and it was possible to detect some general trends in the optimal trajectories. This knowledge is used in this chapter to design fast control algorithms to approximate the optimal solutions, and which could serve as a template for the design of the guidance algorithm.
Section 9.1 gives an introduction to control theory. The type of control law as used for the vertical motion is described in section 9.2. The subsonic and supersonic maximum range guidance laws are discussed in sections 9.3 and 9.4, respectively. Section 9.5 presents the maximum dive guidance. In the last section, section 9.6, the guidance law is introduced for the vertical motion during a turning flight.

9.1 Control theory

An open-loop control system is a system in which the output or the state of the plant has no effect on the control action or the input signal to the plant generated by the control system. The output of the system is not fed back to the control system.
A feedback or a closed-loop control system controls the state of a plant (vehicle) by generating a control signal (control variables) as input signal to the plant based on the actuating error signal, see figure 9.1. In this thesis, the plant is the winged re-entry vehicle and is described by the nonlinear differential equations as given in chapter 2. The error signal is the difference between the reference signal and the feedback signal of the plant. The feedback signal may be output signal of the plant or a function of the output signal and its derivatives and/or integrals. Several control algorithms exist that calculate the input signal to the plant based on the error signal e(t):

$$e(t) = x_{ref} - x_{out} \tag{9.1}$$

Below, three simple linear control laws are described which are commonly used.

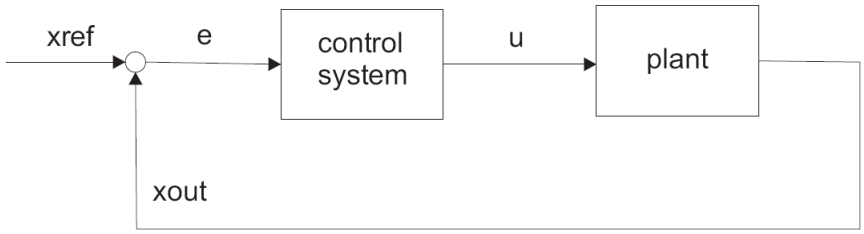

Figure 9.1: Schematic view of feedback control system

9.1.1 Simple controllers

The manner in which a controller produces the control signal is called the control action. Control laws may be classified according to their control actions and three types of controllers are commonly used (Ogata, 2002):

- **Proportional controllers**
  Proportional controllers have a proportional control action and the relation between the output of the controller $u(t)$ (control signal) and the error signal $e(t)$ is given by:

$$u(t) = K_p e(t) \tag{9.2}$$

  where K_p is the proportional gain. This controller is essentially an amplifier (Ogata, 2002).

- **Proportional-plus-Derivative controllers**
  The control action for a Proportional-plus-Derivative (PD) controller is defined by

$$u(t) = K_p e(t) + K_d \frac{de(t)}{dt} \tag{9.3}$$

  where K_d is the derivative gain. The performance of the system is increased by including derivative information.

- **Proportional-plus-Integral-plus-Derivative controllers**
  A Proportional-plus-Integral-plus-Derivative (PID) controller has a combined proportional control action, an integral control action and a derivative control action. The control law for this controller is:

$$u(t) = K_p e(t) + K_i \int_0^t e(t)\, dt + K_d \frac{de(t)}{dt} \tag{9.4}$$

  where K_i is the integral gain.

The gains of the control laws determine the characteristics of the control system. Many possibilities exist to determine the gain values and hence, to design the control system. One possibility is to apply linear control theory in which the non-linear equations of motion describing the motion of the vehicle are linearized around a specific state. These linear equations are then used to design the gains of the control law by using for example the root locus method. In this case, the control law, which is applied to the complete non-linear system (plant), is only valid in the proximity of the state around which the system is linearized. Another possibility is to

use Nonlinear Dynamic Inversion (NDI) or Feedback Linearization (FBL). Using this nonlinear control technique, a single linear control law can be used for several states, because the feedback linearization results in exact cancellation of the nonlinearities rather than a linear approximation.
In this thesis, linear control laws will be used to calculate directly the input to the plant (nonlinear vehicle model). A genetic algorithm will be used to calculate the optimal gain values of these linear control laws for the motion in the vertical plane. The GA will optimize the gain values such that the trajectory flown by the vehicle using the guidance commands resulting from the control law, is as close as possible to the optimal trajectory.

9.1.2 Dynamic behavior of a control system

Although the gains will be optimized using a genetic algorithm, it is important to understand what the influence of these gains is on the dynamic behavior of a controlled system. The total system consists of the controller and the plant. This combined physical system cannot follow the input (reference signal) immediately, but exhibits a transient response before a steady state can be reached. The transient response of a practical system often exhibits damped oscillations before reaching a steady state. If the output of the system at steady state does not exactly agree with the input (reference signal), the system is said to have a steady-state error. This error is indicative of the accuracy of the system (Ogata, 2002). In analyzing a controlled system, it is important to study the transient response behavior and the steady-state behavior.

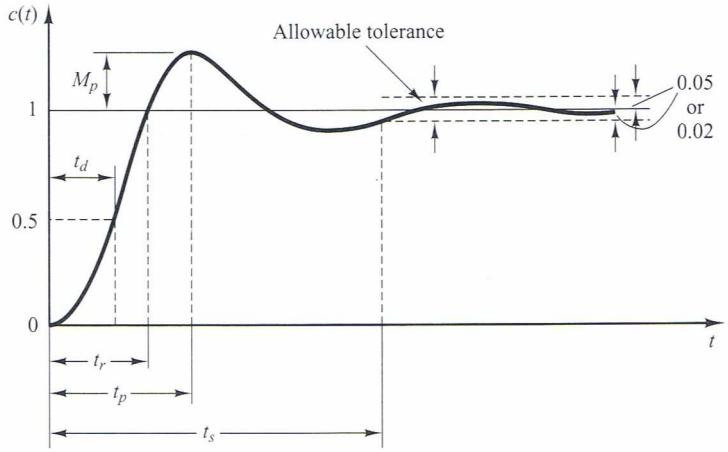

Figure 9.2: Unit step response curve (Ogata, 2002)

Consider a second-order system. The PID control algorithm attempts to make the error signal obey a differential equation of form (Fortescue, Stark, & Swinerd, 2003):

$$\ddot{e} + 2\zeta\omega_n\dot{e} + \omega_n^2 e = 0 \tag{9.5}$$

where ζ defines the damping ratio and ω_n is equal to the undamped natural frequency.

In control theory, transfer functions are commonly used to characterize the input-output relation of a system that can be described by linear time-invariant differential equations. The transfer function is defined as the Laplace transform of the output to the Laplace transform of

the input under the assumption that all initial conditions are zero (Ogata, 2002). The transfer function for a second-order system, in terms of ω_n and ζ, is given as:

$$\frac{C(s)}{R(s)} = \frac{\omega_n^2}{s^2 + 2\zeta\omega_n s + \omega_n^2} \tag{9.6}$$

This is called the standard form of the second-order system, where s is a complex variable, C(s) is the output in the Laplace domain and R(s) is the input (reference signal) in the Laplace domain. The undamped natural frequency ω_n is the frequency at which the system would oscillate if the damping were decreased to zero and governs the speed of the response to a disturbance, while the damping ratio ζ indicates how rapidly the oscillatory response dies away. If a system has damping, ω_n cannot be observed directly. The frequency that may be observed is the damped natural frequency ω_d, which is related to ω_n and ζ as:

$$\omega_d = \omega_n\sqrt{1 - \zeta^2} \tag{9.7}$$

The dynamic behavior of a second-order system can be completely described in terms of the two parameters ω_n and ζ. If $0 < \zeta < 1$, the system is called underdamped and the transient response is oscillatory. If $\zeta = 0$, the transient response does not die out. If $\zeta = 1$, the system is called critically damped. Overdamped systems corresponds to $\zeta > 1$. It is common to specify the performance characteristics of a control system in terms of time-domain quantities and more specific in terms of the transient response to a unit-step input (U(s) = 1). The transient response of a practical control system often has a damped oscillation before reaching steady state. Figure 9.2 shows a characteristic response of such an underdamped system to this input. The transient-response characteristics of a control system can be specified by (Ogata, 2002):

- **Delay time**
  The delay time t_d is the time required for the response to reach half the final value for the first time.

- **Rise time**
  The rise time t_r is the time required for the response to rise from a certain percentage to another percentage. For underdamped systems, the most common is from 0 percent to 100 percent.

- **Peak time**
  The peak time is the time required for the response to reach the first peak of overshoot.

- **Maximum (percent) overshoot**
  The maximum overshoot is the maximum peak value of the response curve measured from unity. The amount of maximum (percent) overshoot directly indicates the relative stability of the system.

- **Settling time**
  The settling time is the time required for the response curve to reach and stay within a range about the final value of size specified by absolute percentage of the final value (2 or 5 percent).

These characteristics are completely determined by the damping ratio ζ and the undamped natural frequency ω_n. Using the same natural frequency, the settling time for a very lightly damped system is larger than that for a properly damped system. The damping ratio is usually

determined from the requirement of permissible maximum overshoot and the settling time is determined primarily by the undamped natural frequency. The duration of the transient response may be varied, without changing the maximum overshoot, by adjusting the undamped natural frequency. For a rapid response, ω_n must be large. To limit the maximum overshoot and to make the settling time small, the damping ratio should not be too small (Ogata, 2002).

The trends as described above indicate that the control system can be modified until the required values for ω_n and ζ are found and hence, until the transient response is satisfactory. The values of the gains influence the parameters ω_n and ζ and hence the characteristics of the transient response. Below, some general guidelines are presented that indicate the influence of the each gain on the transient response. Note that these correlations may not be exactly accurate because the gains are dependent of each other, but the given correlations can be used as a rough or general reference in designing a PID controller.

- **proportional gain**
  Increasing the proportional gain will have the effect of reducing the rise time and increasing the overshoot. The steady-state error will be reduced, but never eliminated. The settling time is only slightly changed.

- **derivative gain**
  Including a derivative gain or increasing its value will decrease the overshoot and the settling time. Both the rise time and the steady-state error are only slightly changed.

- **integral gain**
  Using a PD controller, a small steady-state error will be present. The use of the extra integral term in the PID controller will eliminate this steady-state error. Increasing the value of the integral gain will decrease the rise time and increases both the overshoot and the settling time.

It can be concluded that in designing a PID controller for a given system, using a proportional control improves the rise time, adding a derivative control improves the overshoot, while an integral control will eliminate the steady-state error. One can adjust the values for K_p, K_d and K_i until the required response is obtained. Note that it is not necessary to implement all three components into a single controller.

9.1.3 Robust design

For the purpose of analyzing the energy management capabilities during off-nominal conditions, the guidance system has to perform adequate, not only under nominal conditions but also when variations in the initial state are present.

A robust guidance system is a system which can cope with off-nominal conditions. But a robust system might not be the same as an optimal system. A specific guidance law that results in the optimal trajectory for a specific nominal conditions may result in a trajectory far from the optimal solution for different conditions. But it might be possible to obtain a suboptimal solution for the nominal condition which has an optimal global performance. The obtained suboptimal solution for the nominal condition results in an acceptable optimal performance for off-nominal conditions.

The purpose of using robust design to design a control law is to find the optimal gains such that the system will perform well under all conditions.

9.2 Longitudinal control law

The control variable that regulates the motion a vertical plane is the angle of attack. In the previous chapter, the obtained optimal trajectories and guidance strategies were expressed using an optimal velocity or dynamic pressure. Hence, a simple guidance law is designed which regulates the angle of attack to follow the an optimal dynamic pressure profile:

$$\alpha = \alpha^* + K_p(q_{ref} - q_{dyn}) + K_d(\dot{q}_{ref} - \dot{q}_{dyn}) \tag{9.8}$$

This vertical guidance law is a PD control law that tracks a nominal or reference trajectory represented by a reference dynamic pressure profile q_{ref} and is similar to the law used in (Buechner, 2003). The resulting angle of attack is determined by both open-loop commands and closed-loop commands. The open-loop angle of attack is given as α^* and represents the value of the nominal trajectory. If the actual trajectory deviates from the nominal trajectory, the proportional and derivative term assures that the state returns to the nominal one. Normally, this control law is only valid for a flight situation close to the reference trajectory. The values of the proportional gain K_p and the derivative gain K_d determine how the system reacts to deviations from this nominal trajectory.

The longitudinal guidance system as used during the simulations in this thesis consists of the control as given by equation 9.8, an angle-of-attack filter and an angle-of-attack rate ($\dot{\alpha}$) filter. These filters assure that the a new angle-of-attack is calculated such that the constraint on α and $\dot{\alpha}$ are not violated. In this thesis study, the guidance system runs at the same frequency as the simulation of the motion of the vehicle (using an integration with variable stepsize). A better simulation of the reality consists of a vehicle simulator and a guidance system that runs at two different frequencies. In reality, the guidance system runs at a fixed frequency. This is not taken into account in this study.

The input of the control law consists of the actual dynamic pressure q_{dyn} and the rate of change of the dynamic pressure, $\dot{q}_{dyn}$. The dynamic pressure rate $\dot{q}_{dyn}$ is calculated numerically, which is also common in real flights. The on-board computer compares two successive values of q_{dyn} and calculates $\dot{q}_{dyn}$. But in real-life guidance systems, also the input to the control law would be filtered. Since the analysis in this thesis is only a preliminary study, these input filters are not taken into account. Including input filters reduces or eliminates spikes in the output and must be therefore used in on-board systems.

9.3 Subsonic maximum range guidance

The optimal strategy for a maximum range flight starting at subsonic initial conditions is to glide toward the drag valley or optimal dynamic pressure and then maintain this dynamic pressure throughout the rest of the gliding flight. Figure 9.3 shows the dynamic pressure profiles as a function of the energy height for the optimal maximum range trajectories with subsonic initial conditions. The three optimal trajectories all have a different dynamic-pressure profile in the initial phase of the flight were transient maneuvers are performed to intercept the maximum

range glide path of constant dynamic pressure. Different initial states yield different optimal dynamic-pressure profiles. Hence, it is not possible to use only one nominal trajectory or reference dynamic-pressure profile for a subsonic maximum range problem, if the maximum range must be calculated for different initial states. The best, but also the most difficult solution, is to use the guidance law as given in equation 9.8, in combination with an on-board planning algorithm that is able to quickly calculate the optimal dynamic pressure profile for a maximum range, based on the current initial state. Due to time concerns, this is beyond the scope of this thesis study.

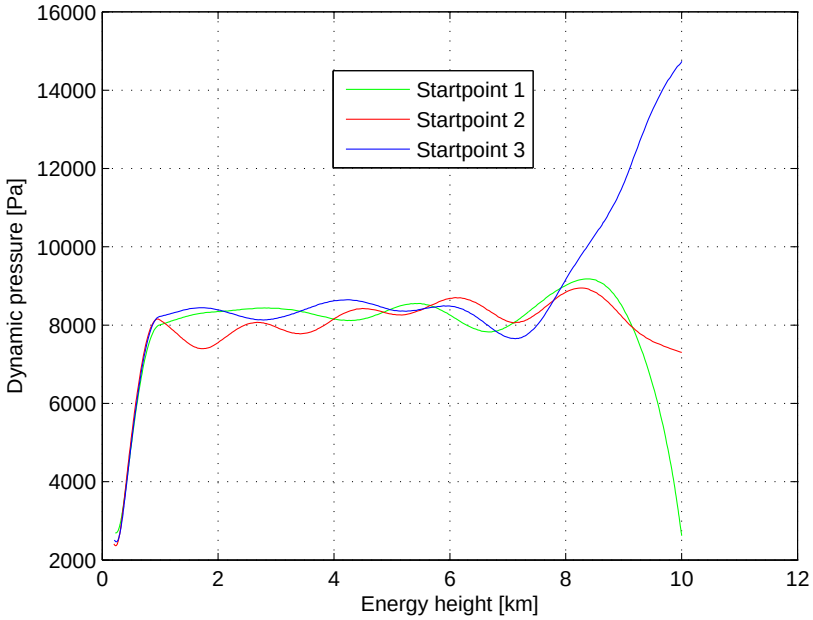

Figure 9.3: Dynamic pressure profiles of subsonic maximum range trajectories

Another solution is to use the constant dynamic pressure value of the maximum range glide path as a reference, since this dynamic pressure value is constant for all subsonic maximum range problems. The optimal transient maneuvers are now hidden in the values of the proportional and the derivate gains. Changing the gain values K_p and K_d results in different trajectories. During initial simulations, it was observed that although the chosen gains resulted in a trajectory that followed the constant dynamic pressure profile, the obtained range was far from optimal. It is not only important to follow the constant optimal dynamic pressure, but also the interception maneuver is important. Hence, optimal gains must be found that resemble the the optimal transient maneuver to the constant dynamic pressure as closely as possible. The calculation of the optimal gains is described in the rest of this section.

In equation 9.8, the reference dynamic pressure q_{ref} is now equal to a constant value of 8242 Pa, which corresponds to an equivalent airspeed of 116.0 m/s. The value of the open loop α is equal to 7.5°, which is the value required for an equilibrium flight situation at the optimal reference dynamic pressure and the current energy height. Since the reference dynamic pressure is constant, the reference dynamic pressure rate is equal to zero and the control law reduces to equation 9.9. Note that the change of sign of the derivative term is contained within the K_d

value.

$$\alpha = \alpha^* + K_p(q_{ref} - q_{dyn}) + K_d\,\dot{q}_{dyn} \tag{9.9}$$

9.3.1 Gain selection for a single initial state

The gain selection in this section is done for an initial state with an altitude of 9400 m, a velocity of 108.5 m/s and a steady state flight-path angle of -29.24°. This corresponds with initial point 1 as used in chapters 6 and 7. The optimal set of gains, which result in an optimal interception and tracking of the constant dynamic pressure, are calculated using a genetic algorithm. Instead of optimizing the angle-of-attack vector directly, the genetic algorithm is now used to optimize the gains of the guidance law given in equation 9.9. The same GA parameters are used as given in chapter 7.

Optimization criterion, constraints and interval of GA search

The goal is to approximate the optimal solution as close as possible. Hence, the optimization criterion or cost function is the obtained maximum range. Because the final flare maneuver will not be taken into account, the gained range during this flare must be subtracted from the total range. Therefore, the obtained range at an energy height of 1.4 km is concerned. The steady state solution gives a range of 30.16 km, while the optimized solution gives a range of 31.03 km. These ranges will be used to evaluate the performance of the guidance law.

Since the the angle of attack is filtered (α and $\dot{\alpha}$) after being calculated with the control law, no constraints on the angle of attack and angle-of-attack rate were taken into account during the optimization with the GA. Because no transient maneuvers are used at the end of the flight, an extra constraint is added on the final velocity. The difference with the maximum range equivalent airspeed (116.0 m/s) cannot be larger than 1 m/s. If this constraint is violated, the individual is unfeasible and is eliminated from the population.

The intervals in which the GA looks for the optimal K_p and K_d values are limited between [-0.02 0.02] and [-0.004 0.004], respectively. These values have been obtained by trial and error. More information on why different limits apply for the two gains, is given at the end of this section.

Table 9.1: Maximum ranges using the guidance law for maximum range in the vertical plane. Range*: obtained range at an energy height of 1.4 km. n.a.: not applicable

	Range	**Range***	GA computation time
Steady state	32.78	30.16	n.a.
Optimal	34.87	31.03	736.86
Run 1	33.28	30.69	166.40
Run 2	33.51	30.83	165.42
Run 3	33.59	31.02	451.75

Gain scheduling

A single set of gains can be used throughout the complete trajectory, or it is possible to use multiple sets of gains, depending on the flight phase. Both options are discussed below. The

Table 9.2: Optimal gains for the maximum range guidance law

	$\Delta q[Pa]$	K_p	K_d
run 1	/	0.000108	0.003999
run 2	> 2000	0.001390	0.002934
	< 2000	0.000047	0.003999
run 3	> 5000	0.000489	0.003902
	[5000 3000]	0.001305	0.000130
	[3000 1500]	0.002290	-0.002519
	[1500 500]	0.003725	-0.000892
	< 500	-0.000468	0.002753

gain scheduling as used in this study, depends on q_{dyn}. The dynamic pressure determines which set of gains is used. If multiple sets are used, it is not possible in real-life system to use a single switch point between the gains, but rather a linear transition is required. Otherwise, jumps or oscillations in the output can be present. However, in the discussion below, a single switch point is used because a $\dot{\alpha}$ filter is included after α is calculated by the control law. This assures that α does not changes more than $\pm$ 3°/s. This can be seen as a linear slope. But for further, more elaborate studies, the switch points as used for gain scheduling (inside the control law and before the filter) should be adapted to a linear transition.

Single set of gains

During a initial optimization run, only one set of gains is used. Table 9.1 indicates the obtained range at an energy height of 1.4 km ($Range^*$), while table9.2 shows the corresponding optimal gains. Both present the results for three runs. Run 1 corresponds to single set of gains as discussed in this part. Run 2 and 3 will be discussed further on and represents the results for two sets and five sets of gains, respectively.

The maximum range for run 1 is already larger with respect to the steady-state solution. Figure 9.4 indicates that the trajectory during the intercepting maneuver still differs from the optimal solution. Hence, some improvements in the maximum range can be obtained by investigating a more optimal transient maneuver. Using only one set of gains is not sufficient to approximate the optimal transient maneuver. Figure 9.5 indicates that a single set of gains is insufficient to produce the same trend in the optimal angle-of-attack profile for the complete transient maneuver and the complete trajectory. In the beginning of the flight, the angle of attack must be considerably larger.

Two sets of gains

The use of multiple gain sets might result in a better trajectory since a single set of gains for the complete trajectory is not able to approximate the optimal trajectory. Therefore, two sets of gains are used with a switch point depending on the dynamic pressure difference between the q_{ref} and q_{dyn}. A switch is made at a Δq of 2000 Pa and table 9.2 presents the obtained optimal gains for both dynamic pressure regions. Figure 9.4 and table 9.1 indicate that improvements in range are made with respect to a single set of gains. The switch in gains can be seen in the resulting angle-of-attack profile as presented in figure 9.5 (run 2). The α-profile resembles the

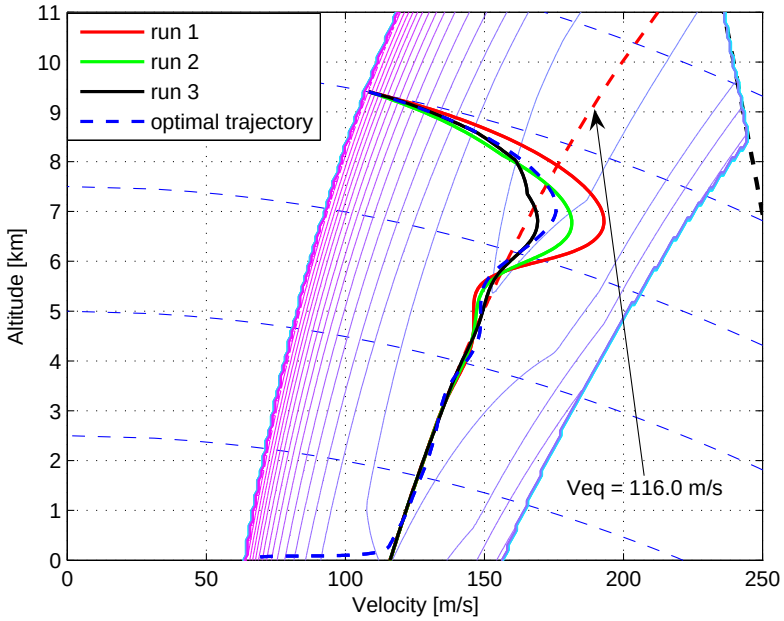

Figure 9.4: Subsonic maximum range trajectories in the energy space using a control law

optimal profile already more closely. A the switch point, the angle-of-attack rate is momentarily larger than $3°/s$, but since the control law will be always used in combination with an angle-of-attack rate filter, this limit will never be violated.

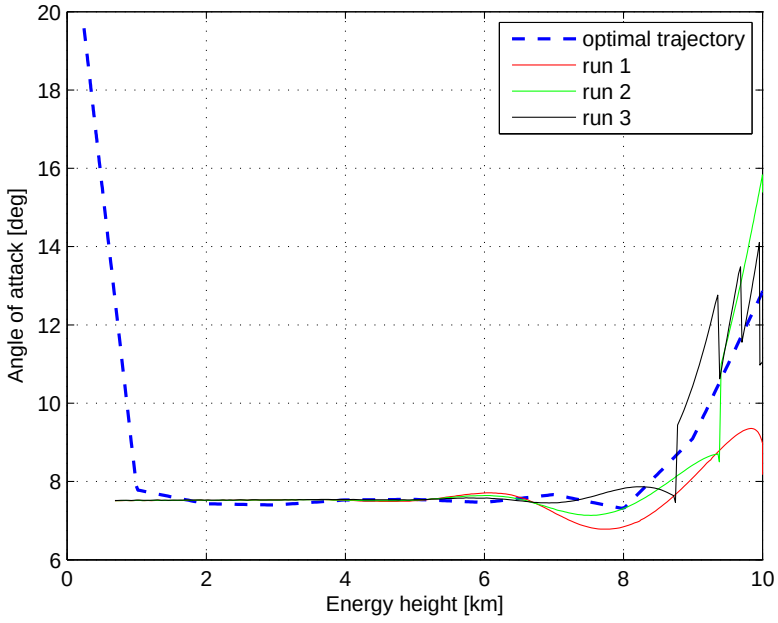

Figure 9.5: Angle-of-attack profiles using control law

Five sets of gains

The results obtained for two sets of gains indicate that some improvement is still possible. Hence, an optimization with five sets of gains was performed. Table 9.2 indicates the used switch points and the obtained optimal values for the gains (run 3). The maximum range is now only 10 m less than the optimal maximum range. The obtained solution has almost no overshoot of the required dynamic pressure, but there is still a difference between the optimal trajectory and the trajectory obtained using the control law, see figure 9.4. But taken into account that the obtained optimal solution with the GA was only an approximation, this result is satisfying an no further gain optimization was performed for this initial state. Figure 9.5 indicates that the angle-of-attack profile resulting from the control law indicates the same trends as the optimal trajectory.

Choice of gain intervals

During the optimization of the gains, the genetic algorithm just looks for an optimal mathematical combination of K_p and K_d and corresponding $\Delta\alpha_1$ and $\Delta\alpha_2$. But the GA has no knowledge about the physical meaning of the obtained values. Figure 9.6 indicates the resulting contributions to the total angle of attack resulting from the optimal values for K_p and K_d, which are obtained using an identical interval in which the GA searches for the optimal solution. The interval is situated between -0.02 and 0.02. The figure indicates that the the derivative term has a large contribution to the total angle-of-attack and sometimes even exceeds the contribution of the proportional term. In reality, the proportional term should be the dominant term and the derivative term is only used to make small corrections. Hence a different interval is used for K_p and K_d, in which the GA searches for the optimal gain values. As a general rule, it can be stated that the contribution of the derivative part must be at maximum 20 percent of the proportional part. This results in two intervals:

- K_p = [-0.02 0.02]
- K_d = [-0.004 0.004]

Figure 9.6 indicates that using these intervals, the dominant contribution to the angle-of-attack in the optimal solution is the proportional part. The contribution of the derivative part is reduced significantly.

9.3.2 Influence of changing the initial state

The goal of this thesis is to investigate the capabilities of a winged re-entry vehicle with respect to energy management during off-nominal conditions. Hence, the maximum range guidance law that will be used during that analysis must be able to calculate the correct maximum range trajectory for different initial states.

Figure 9.7 indicates the resulting trajectory (blue trajectory) in the energy space if the maximum range strategy is applied using the five sets of gains as calculated in the previous section for initial state 1, see table 9.2. The used initial state corresponds to initial state 2 as presented in table 9.3. The initial energy height is identical to point 1. The obtained trajectory does not follow the drag valley and the corresponding required equivalent airspeed. The trajectory does

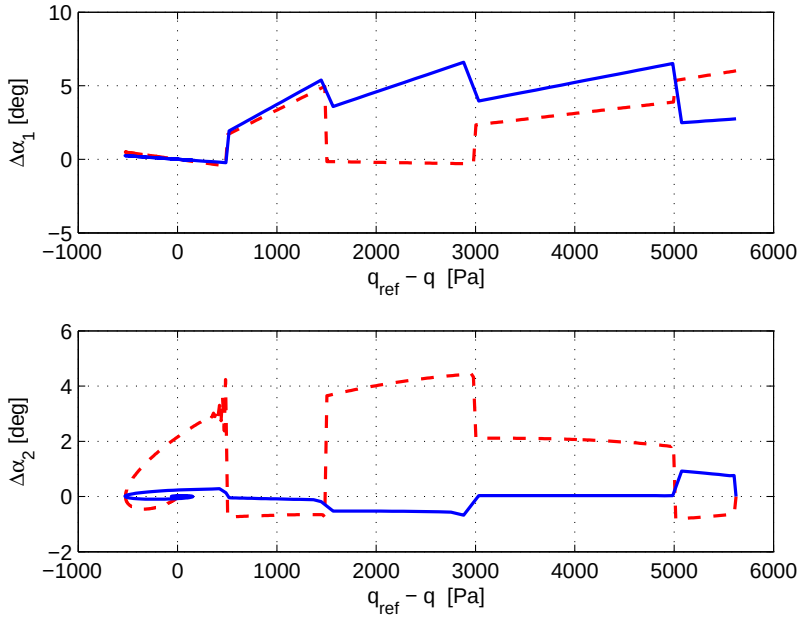

Figure 9.6: Contribution of proportional ($\Delta\alpha_1$) and derivative ($\Delta\alpha_2$) term to the angle-of-attack. Two intervals are considered in which the GA searches for optimal gain values. RED DASHED: equal interval for both K_p and K_d term of [-0.02 0.02]. BLUE: K_p = [-0.02 0.02]; K_d = [-0.004 0.004]

follow a constant dynamic pressure profile, which has a value that is 3000 Pa smaller than the dynamic pressure value in the drag valley. New optimal gains were calculated, using the same five switch from table 9.2, for initial state 2. This trajectory is indicated in figure 9.7 by the blue line. This trajectory does follow the drag valley.

Figure 9.8(a) indicates the resulting α values as a function of the difference in dynamic pressure. The angle-of-attack profile from initial state 1 is also shown as a reference. If the optimal gains for initial state 1 are used to calculate the maximum range trajectory for initial state 2, the angle-of-attack profile indicates the same trends as the α profile from initial state 1. The α profiles are not completely identical, because an equal difference in dynamic pressure is reached with different conditions (altitude, velocity and flight path angle). The newly obtained α profile indicates that the angle of attack should be significantly lower, especially in the beginning of the flight. Using the gains from initial state 1, the flight starts with larger α values. This is the reason why, using the original gains from initial state 1, the drag valley is not reached and why the trajectory appears to follow another reference dynamic pressure. Due to the high α in the beginning of the flight, HORUS performs a pull-up maneuver, see figure 9.7. It crosses the Δq boundary of 3000 Pa. Due to the high α Horus does not continue to the drag valley, but performs a pull-up and hence, crosses the Δq boundary of 3000 Pa for a second time. This results in an oscillatory movement around the 3000 Pa Δq boundary. The value of 3000 Pa is used as a switch point to select the corresponding gains. Figure 9.8(b) presents the angle-of-attack profile as a function of time for the first 70 seconds. The oscillations are clearly visible. Do to a high α, the Δq boundary of 3000 Pa is crossed for a second time. This results in a new choice of gains which yields a lower angle-of-attack that forces HORUS to dive. HORUS crosses again the Δq boundary of 3000 Pa resulting a new selection of the gains yielding a higher

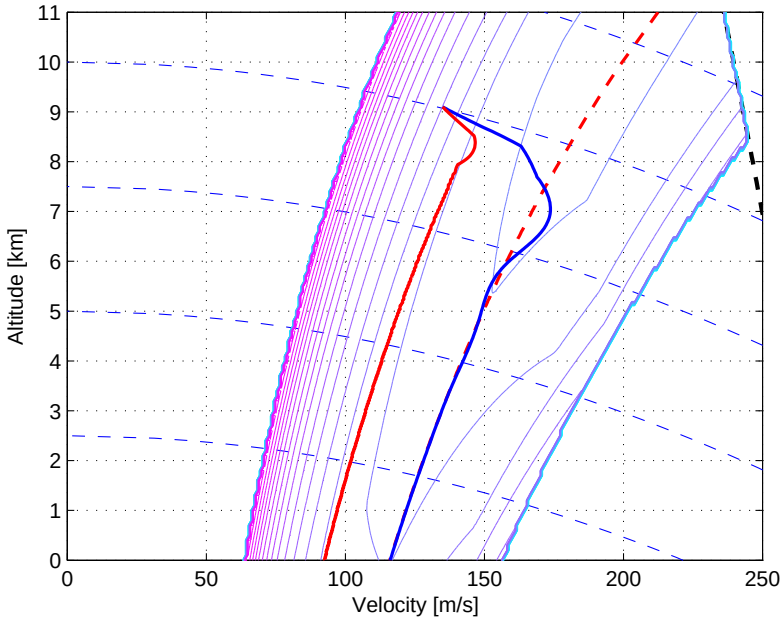

Figure 9.7: Subsonic maximum range trajectories in the energy space for initial state 2. BLUE: trajectory using the original gains of initial state 1. RED: trajectory using new calculated optimal gains for initial state 2

angle-of-attack. Horus climbs and the Δq boundary of 3000 Pa is crossed again. This process continues and HORUS appears to follow another reference dynamic pressure, but actually it performs an oscillatory motion around the Δq boundary of 3000 Pa. This is also an example of the sharp oscillations that can occur, due to the use of switch points. A linear transition in between the gains would reduce the sharp oscillations.

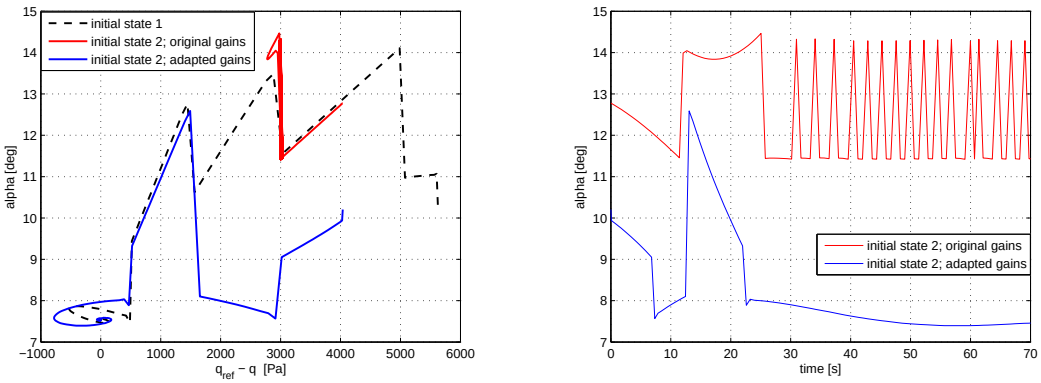

(a) (b)

Figure 9.8: Angle-of-attack profiles using the maximum range control law with different gains

9.3.3 Sub-optimal guidance law using Robust Design

The previous section indicates that different optimal gains are required for different initial states. One could apply the principle of gain scheduling based on the initial state, but this would require a lot of simulations to investigate the influence of the initial state on the optimal gains. A more practical solution is to use robust design. For a further initial analysis of the energy management capabilities of HORUS, it seems wise to have only one simple set of gains which can be used for all subsonic initial states rather than a complex system. The goal is to determine only 1 set of suboptimal gains which is used for several initial conditions.
It was stated before that the optimal transient maneuvers must be contained within the chosen gains. The transient maneuvers required to intercept the drag valley differ for initial states with a lower or higher initial dynamic pressure than the reference dynamic pressure. The required maneuvers are totally different. Hence, the method of robust design is applied separately to these two regions of initial states.

Table 9.3: Initial states used in robust design. All initial flight path angles are equal to γ = -10°

	altitude [m]	**velocity [km]**	Δq **[Pa]**
1a	9400.0	108.5	5622.0
2a	9100.0	135.0	4041.0
3a	8800.0	154.0	2573.0
4a	8500.0	171.0	990.0
5a	8400.0	177.0	378.0
1b	7350.0	228.0	-6478.0
2b	7700.0	212.0	-3980.0
3b	8000.0	198.0	-2052.0
4b	8200.0	189.0	-920.0
5b	8300.0	184.0	-340.0

Initial states with $q_{ini} < q_{ref}$

The obtained gains for the control law will again consist of the same five sets (four corresponding switch points) depending on Δq. The intervals can be found in the top part of table 9.4. Since five Δq intervals or five gain sets are used, five initial states with an initial energy height of 10 km are used. These five initial conditions are given in the top part (a) of table 9.3, together with their initial Δq. Each point is situated in a different Δq interval to ensure that the found gains set are applicable to initial state within a specific Δq region. All initial states have a flight path angle of γ = -10°.

Using robust design, the cost function of the GA must be adapted. For a specific set of gains, the GA calculates the obtained range for the five initial states. These ranges are combined into on single cost function by taking the summation of all the five obtained ranges. The GA tries to maximize the total range for the five initial states.

The optimal total maximum range for the five initial states is equal to 173.74 km, which was found by the GA after 5000 seconds. Table 9.4 presents the obtained gain sets using the GA, while figure 9.9 indicates the resulting trajectories in the energy space. All the trajectories follow the drag valley. The trajectory for initial state 1a shows that a larger overshoot is present

before the reference equivalent airspeed is followed. Using initial state 1a and adapting the initial flight-path angle to the steady-state value of -29.24° gives a maximum range of 33.40 km. This is 200 meters less than the optimal solution using the control law with five sets of gains optimized for a single state (state 1). The obtained range is still more than 600 meters longer than the steady-state solution. This indicates that the solution found by the robust design method is suboptimal for a specific case but has a global optimal performance for several initial states. The most optimal solution does not represent a large overshoot of the drag valley, but the gains resulting from the robust design allow some extra overshoot in order to improve the performance for different initial states.

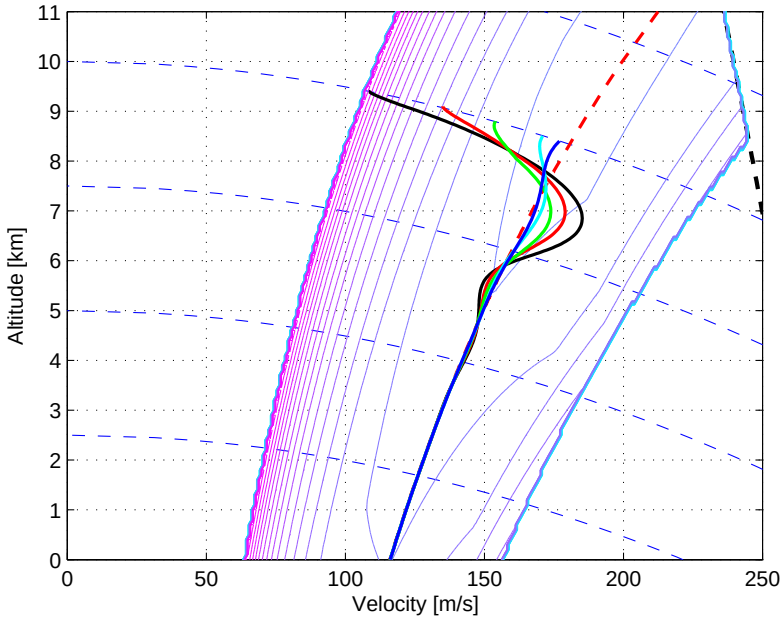

Figure 9.9: Suboptimal trajectories in the energy space for initial states with $q_{ini} < q_{ref}$, using robust design

Initial states with $q_{ini} > q_{ref}$

The same robust design strategy can be applied to initial states with an initial dynamic pressure larger than the reference dynamic pressure. These points require a different type of transient maneuvers to intercept the drag valley. Also in this case, five sets of gains are used depending on Δq, see the lower part of table 9.4. The five initial states used in the robust design are given in table 9.3. Again, all the initial flight-path angles are equal to γ = -10°.

The optimal total range for the five initial state as calculated with the GA is equal to 172.11 km. The HA needed 4291.7 seconds to calculate the optimal gains. Table 9.4 presents the obtained optimal gains using the GA. Figure 9.10 shows the corresponding trajectories in the energy space. All the trajectories intercept the drag valley and follow the reference dynamic pressure. Using the obtained optimal gains, the maximum range for initial state 1b with an equilibrium flightpath angle of -17.65° results in range of 33.92 km. This is only 200 meters larger than the steady-state analysis. The increase in obtained range is smaller than for initial

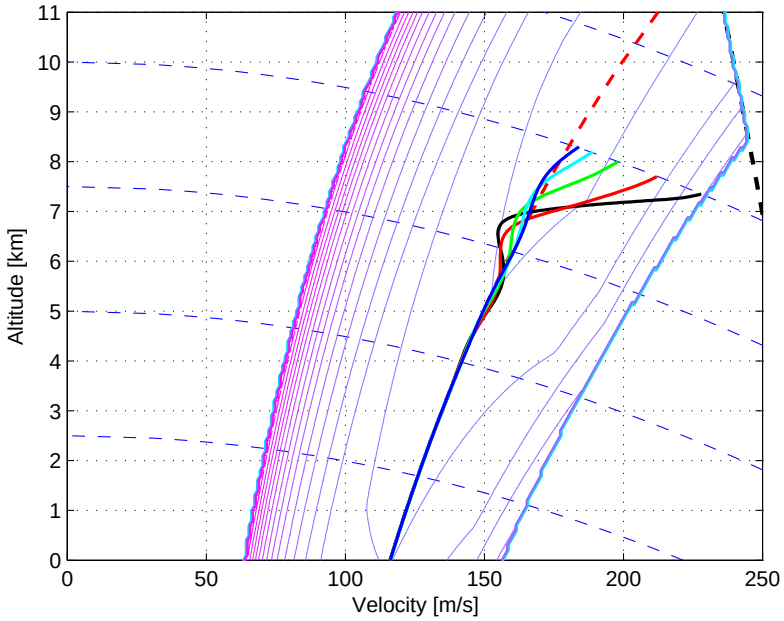

Figure 9.10: Suboptimal trajectories in the energy space for initial states with $q_{ini} > q_{ref}$, using robust design

states with a dynamic pressure lower than the reference dynamic pressure. A better results can be obtained if the gains are optimized for only initial state 1b.

Table 9.4: Optimal gains for subsonic maximum range resulting from robust design. If the initial dynamic pressure is lower than the reference dynamic pressure, set 1 must be used. If the initial dynamic pressure is larger, set 2 must be used.

	Δq [Pa]	K_p	K_d
set 1	$>$ 5000	0.001015	-0.002906
	[5000 3000]	0.000478	0.003800
	[3000 1500]	0.000591	0.002438
	[1500 500]	-0.000171	0.003850
	$<$ 500	-0.000027	0.003862
set 2	$<$ -5000	0.000045	-0.000288
	[-5000 -3000]	0.000368	0.003092
	[-3000 -1500]	0.000385	0.003999
	[-1500 -500]	0.000206	0.003613
	$>$ -500	-0.000188	0.003825

Influence of changing initial energy

The gains obtained by using robust design were calculated for initial states with both a larger and lower dynamic pressure than the reference dynamic pressure, but the initial states all have an initial energy height of 10 km. If this guidance law must be used to calculate the maximum range flight for off-nominal initial states, it must also be valid for initial states with a different

initial energy.

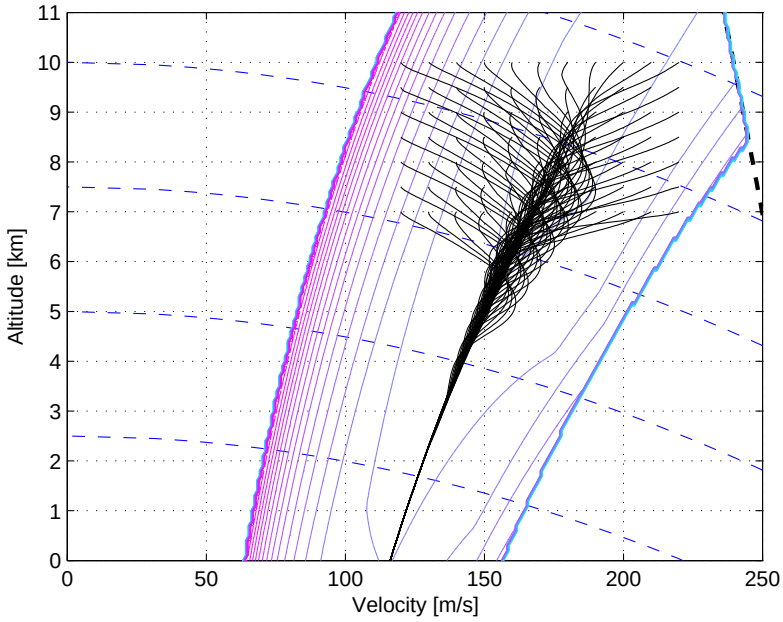

Figure 9.11: Suboptimal trajectories in the energy space for initial states with a different initial energy. Gains obtained from the robust design are used to calculate the trajectories.

Figure 9.11 shows the maximum range trajectories for initial states with an altitude between 7.0 km and 10.0 km and with a velocity between 115.0 m/s and 220.0 m/s. The used gains are those as given in table 9.4, obtained from the robust design. Depending on the initial dynamic pressure, either gain set 1 or 2 is selected. The figure indicates that these gains can also be used for initial states with different initial energy.
It was also observed that changing the initial flight-path angle does not influence the use of the gains, and give a good performance.

9.3.4 Conclusions of subsonic maximum range control law

For a subsonic maximum range flight, it is not only necessary to follow the reference dynamic pressure, also the intercepting maneuvers are important. For a single initial state, it was possible to calculate a set of gains which approximate the real optimal trajectory very well. It is not possible to use the same set of gains for a different initial state. An incorrect trajectory is followed. A different initial state requires a different set of optimal gains. Since the guidance law must be used to calculate the maximum range for several off-nominal initial states, it is not feasible to calculate an optimal set of gains or each initial state. A practical solution is to use the robust design method to calculate a sub-optimal set of gains, which can be used for several initial states. For a subsonic initial state, the control law presented in equation 9.9, in combination with the gains as presented in table 9.4, can be used to calculate a maximum range flight. The obtained range is larger than using the steady-state solution, but smaller than the most optimal solution. Depending on the initial dynamic pressure, either set 1 or set 2 must be selected.
A better solution can be obtained if a different set of gains can be used for each initial state.

It is thought that adaptive guidance might be a good solution. This type of guidance adapts the gains to the state of the vehicle and hence is valuable candidate for further research. More research is required to design a guidance system that uses adaptive guidance, such that for each initial state, the optimal solution can be found and one does not have to resort to sub-optimal solutions. But for the initial analysis performed in this thesis study, the robust sub-optimal solution is sufficient.

9.4 Supersonic maximum range guidance

The optimal maximum range strategy for supersonic initial states does not follow the minimum drag valley in the supersonic speed regime, see chapter 8. But the trajectories all seem to enter the transonic regime at a specific optimal entry point. Figure 9.12 indicates the optimal dynamic pressure profiles for the three supersonic initial states. The maneuvers in the supersonic speed regime are very important in case of a re-entry vehicle with poor gliding capabilities. The three dynamic-pressure profiles are all different in the supersonic speed regime and hence, it is not possible to use only one dynamic pressure-profile to describe the optimal supersonic maximum range trajectory to go the optimal transonic entry point. Again, the best solution would be to use a dynamic-pressure tracking scheme in combination with an on-board planning algorithm that calculates the optimal trajectory based on the current initial conditions. Due to time concerns, this is beyond the scope of this thesis and hence, a more practical solution is investigated and the same approach as for the subsonic maximum range problem is studied. The control law as specified in equation 9.9 will be used for this purpose. A constant dynamic pressure is used as a reference and the maneuvers are captured in the values of the proportional and the derivative gains. The choice of reference dynamic pressure and the optimization of the gains is described below.

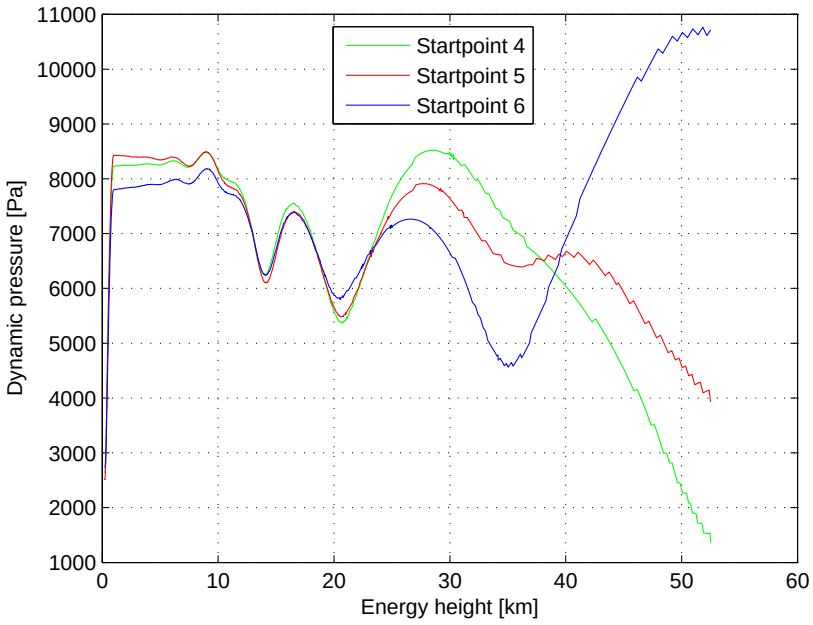

Figure 9.12: Dynamic pressure profiles of supersonic maximum range trajectories

The maximum range guidance for the complete flight consists of a subsonic maximum range guidance law, a transonic part and a supersonic maximum range guidance law. For the subsonic part, the sub-optimal gains were found in the previous section using robust design. For the transonic part, the optimization results of chapter 7 indicated that the optimal angle of attack between M 0.8 and M 1.2 is equal to 10°. Both the subsonic maximum range guidance law and the constant α in the transonic region will be used for a flight with supersonic initial conditions. Hence, this section only considers the maximum range guidance law in the supersonic regime. Once HORUS enters the transonic regime, a switch is made to the transonic guidance and later on to the subsonic guidance.

9.4.1 Reference dynamic pressure

In the subsonic maximum range problem, the choice of reference dynamic pressure was quite simple because all optimal trajectories intercepted and followed the minimum drag path. For supersonic initial states, this is not the case and a different reference must be chosen. The only characteristic that the three optimal supersonic trajectories have in common is that they enter the transonic regime through the same entry gate. Hence, the dynamic pressure at this entry gate is proposed as the reference dynamic pressure and has a value of 7277.0 Pa. This corresponds to an equivalent airspeed of 109.0 m/s. Figure 9.13(a) indicates this reference equivalent airspeed, together with the three optimal trajectories in the supersonic regime.

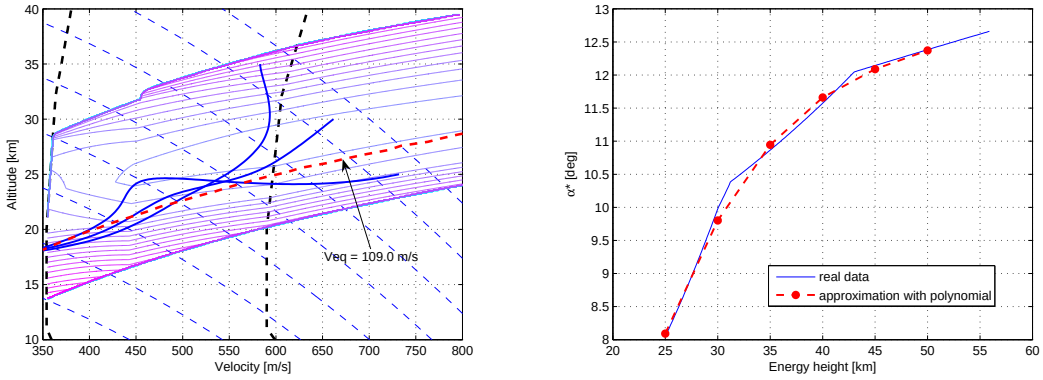

(a) (b)

Figure 9.13: (a) Reference equivalent airspeed in supersonic speed regime (b) α^* corresponding to reference equivalent airspeed

The corresponding open-loop steady-state angle-of-attack α^* at the dynamic pressure reference is shown in figure 9.13(b). This α^* is not a constant, but changes as a function of the energy height. The data were obtained by calculating the steady state angle-of-attack for each combination of altitude and velocity situated at the reference dynamic pressure. To store this α^* data in the guidance system, an approximation is used. A third order polynomial approximation gives an acceptable result, with the energy height as the input:

$$\alpha^* = c_1 E_h^3 + c_2 E_h^2 + c_3 E_h + c_4 \tag{9.10}$$

The coefficients are found using the 'polyfit' function in Matlab:

$$c_1 = 1.8711 \cdot 10^{-13} \tag{9.11}$$

$$
\begin{aligned}
c_2 &= -2.8192 \cdot 10^{-8} \\
c_3 &= 0.001467 \\
c_4 &= -13.8875
\end{aligned}
$$

9.4.2 Optimal gains for different initial states

First, it must be investigated if a control law in combination with the proposed reference dynamic pressure can be used to approximate the optimal trajectories. The goal is to optimize the gains of the supersonic control law such that the obtained trajectory in the supersonic part is as close as possible to the optimal trajectory obtained in chapter 7. The optimization of the gains of the supersonic guidance law is done using the GA and using the obtained maximum range as the cost function. The GA searches for the gains that maximize the obtained range.

Table 9.5: Optimal gains for supersonic maximum range starting at two different initial conditions

	Δq [Pa]	K_p	K_d
point 1	> 5000	0.000967	-0.000415
	[5000 3000]	0.002370	-0.000475
	[3000 1500]	0.002943	-0.000258
	[1500 500]	0.002953	0.000395
	< 500	-0.001785	-0.000536
point 2	> 5000	n.a.	n.a.
	[5000 3000]	0.002576	-0.000543
	[3000 1500]	0.001749	0.000574
	[1500 500]	0.001269	-0.000432
	< 500	-0.001680	-0.000432

No constraints on α and $\dot{\alpha}$ were taken into account during the optimization, since in further simulations, the obtained control law is always used in combination with both an α filter and an $\dot{\alpha}$ filter. The intervals in which the GA looks for the optimal K_p and K_d values are limited between [-0.003 0.003] and [-0.0006 0.0006], respectively. These values differ from the used intervals for the subsonic maximum range guidance law because using these old intervals resulted in too large angles of attack. The new intervals are obtained by trial and error. But the values for K_p are still larger than for K_d to assure that the proportional term has the largest contribution to the obtained angle-of-attack. Since the best results for the subsonic guidance law were obtained by using five different sets for K_p and K_d depending on the value of Δq, the same sets and the according switch points are used for the supersonic case. The Δq depending switch points are again given in table 9.5.

The optimal gains are calculated for two initial conditions. Initial state 1 has an initial altitude of 35.0 km and a velocity of 583.10 m/s, while initial state 2 corresponds with an initial altitude of 30.0 km and a velocity of 661.64 m/s. The initial flight-path angle is in both cases equal to 10.0°. These conditions corresponds to familiar supersonic initial conditions as used in chapters 6 and 7. The obtained optimal gains are summarized in table 9.5. The initial dynamic pressure for initial state 2 is around 3300 Pa and hence, no gains are given for a Δq larger than 5000.0 Pa. The corresponding trajectories in the energy space are presented in figure 9.14 and

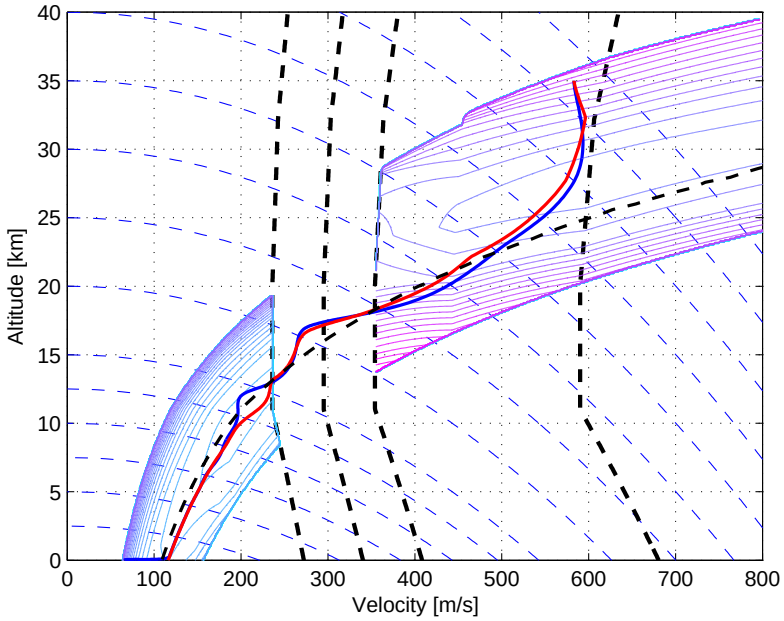

Figure 9.14: Supersonic maximum range trajectories for initial state 1. BLUE: optimal trajectory; RED: optimal control law

9.15, for respectively initial state 1 and 2. Both figures indicate that it is possible to approximate the optimal trajectories in the supersonic regime using the proposed reference dynamic pressure, especially for initial state 1. Table 9.6 presents the obtained maximum ranges. In both cases, an improvement is obtained with respect to the steady-state solutions.

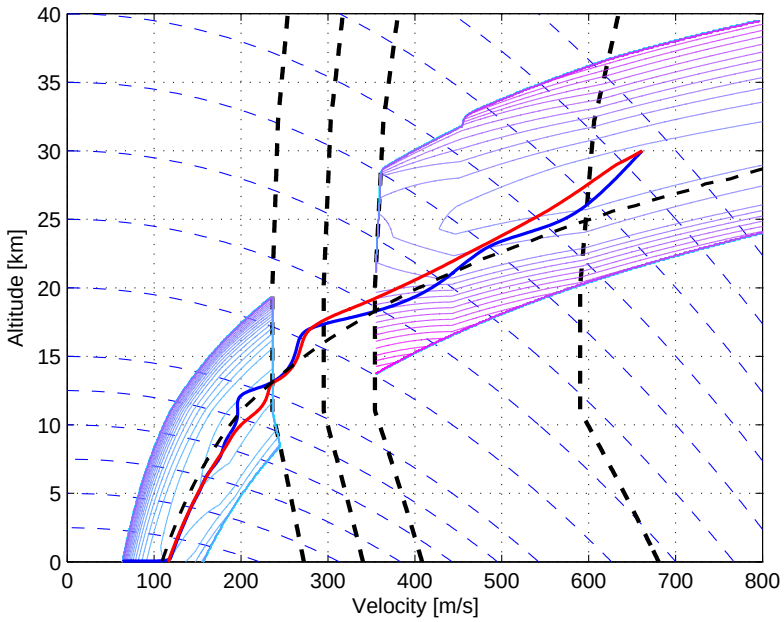

Figure 9.15: Supersonic maximum range trajectories for initial state 2. BLUE: optimal trajectory; RED: optimal control law

Comparing the optimal gains for initial state 1 and 2 as given in table 9.5, it can be seen that large differences occur for both states. Hence, it is not possible to use only one set of optimal gains for all initial states. A different initial state requires a different set of optimal gains, which is impractical to compute all. Again, a more practical solution is studied by using the robust design method to obtain a single set of sub-optimal gains, which gives good results for several initial states.

Table 9.6: Maximum ranges for two initial conditions in the supersonic regime

	Steady-state [km]	**Optimal control law [km]**	**Robust design [km]**
Point 1	134.63	137.69	136.89
Point 2	136.35	137.27	135.68

9.4.3 Robust design of supersonic guidance

Now that it has been shown that it is possible to obtain an optimal set of gains for a specific initial state using the proposed reference dynamic pressure, it must be investigated if a single set of sub-optimal gains can be used for several initial states. The robust design method is used in a attempt to find a single set of gains for initial conditions with $q_{ini} < q_{ref}$. The same Δq switch points are used as before and hence, 5 initial conditions must be used. The used initial conditions are summarized in table 9.7, together with the initial Δq values. To calculate the cost function, the same approach is used as for the subsonic robust design.

Table 9.7: Initial states as used in supersonic robust design. All initial flight path angles are equal to γ = -10°

	altitude [km]	**velocity [km]**	Δq **[Pa]**
1	35.0	583.1	5880.7
2	31.0	630.0	4215.2
3	28.5	672.0	2140.6
4	27.5	686.0	1017.2
5	27.0	695.0	327.1

The obtained combined maximum range for the five initial states is equal to 670.38 km. The GA needed 2205 seconds to calculate the optimal set of gains, which are presented in table 9.8. Figure 9.16 shows the corresponding trajectories in the energy space.

To assess the performance of the obtained set of sub-optimal gains, the maximum range trajectories are calculated for initial points 1 and 2 using these sub-optimal gains. The results are indicated in table 9.6. The obtained range is in both cases smaller than the ones obtained with separate optimal gains sets. For initial state 1, the range is still improved with respect to the steady-state solution but for initial point 2, the obtained range is smaller than for the steady-state solution. Hence, the gains resulting from the robust design method cannot be used because they do not give good overall results. For a good performance, each initial state requires a different set of gains, or the use of an adaptive algorithm should be considered.

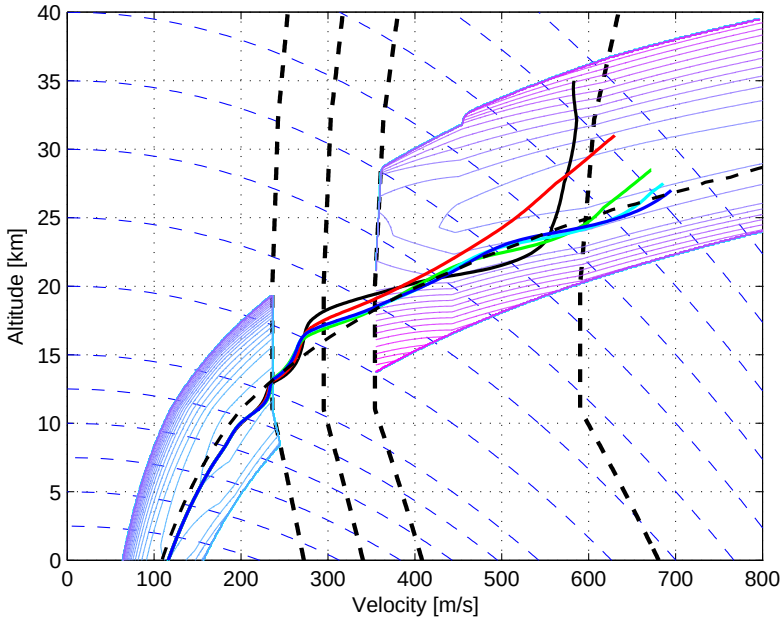

Figure 9.16: Suboptimal trajectories in the energy space for supersonic initial states with $q_{ini} < q_{ref}$, using robust design

Table 9.8: Gains obtained using robust design for supersonic maximum range

Δq [Pa]	K_p	K_d
> 5000	0.001563	-0.000003
[5000 3000]	0.002073	-0.000427
[3000 1500]	0.001565	-0.000455
[1500 500]	0.001406	0.000595
< 500	-0.002955	0.000502

9.4.4 Conclusions of supersonic maximum range control law

For a supersonic maximum range flight, the maneuvers in the supersonic regime are very important and the optimal trajectories all have a different dynamic pressure profile. But all the optimal trajectories enter the transonic regime in an optimal entry point and hence, it was proposed to use the dynamic pressure of this entry point as the reference. Using this fixed reference dynamic pressure, it was possible to find an optimal set of gains for a specific initial state. A different initial state required a different set of optimal gains. The attempt to design a single set of gains for several initial states using the robust design method did not succeed. The resulting range for initial point 2 is even lower than using the simple steady-state solution. Hence, for a supersonic maximum range flight, it is necessary to optimize the gains for each initial state. An even better solution is to use an on-board planning algorithm that calculates the optimal dynamic pressure profiles for a specific initial state, in combination with a tracking algorithm using for example the Model Reference Adaptive Control (MRAC) method to adapt the gains of the guidance law. MRAC is based on matching the response of the system that is to be controlled (HORUS) to that of a reference model (Mooij, 1998). MRAC adapts the gains based on the difference between the actual and the reference state. In the subsonic case, the

single sub-optimal set gave good result and a tracking algorithm together with MRAC could be used to improve the results. But for the supersonic flight, the planner and MRAC are absolutely necessary to get a good approximation of the maximum range flight. This is outside the scope of the thesis. More research is necessary and hence during the rest of the analysis in this thesis, the simple steady-state solution is used for the maximum range flight in the supersonic regime.

9.5 Maximum dive guidance

For the maximum dive guidance, again the control law as specified in equation 9.9 will be used. A maximum dynamic pressure strategy is used to perform a maximum dive in combination with the use of speedbrakes. This section describes the design of the corresponding gains. In contrast to the maximum range guidance, the maneuvers to intercept the reference dynamic pressure do not have to be optimal. Hence, the gains are not obtained by using the GA optimizer, but the general characteristics and trends as described in section 9.1.2 are used. The most important in the maximum dive flight is that the dynamic pressure is increased as fast as possible, but in a smooth and flyable way. First, the gains are obtained for a subsonic and a supersonic dive without the use of speedbrakes. Then, the influence of the speedbrakes is investigated.

9.5.1 Subsonic maximum dive

The maximum dynamic pressure for HORUS is equal to 15000 Pa. For the maximum dive strategy, some margin is taken to assure that the maximum dynamic pressure constraint is respected. A reference equivalent airspeed of 150.0 m/s is used, which corresponds to a reference dynamic pressure q_{ref} of 13800 Pa. The value of the corresponding open loop α for flight without the use of speedbrakes is equal to a constant 4.4°, independent of the energy height. The control law, equation 9.9, is used in combination with a filter on the magnitude of the angle-of-attack and a filter on $\dot{\alpha}$.

Table 9.9: Gains for the subsonic maximum dive guidance law. n.a. = not applicable

	$\Delta q[Pa]$	K_p	K_d
set 1	n.a.	-0.02	0.0002
set 2	n.a.	-0.01	0.03
set 3	n.a.	-0.01	0.02
set 4	$\geq$ 900.0	-0.008	0.016
	$\leq$ 300.0	-0.01	0.008

The calculation of the gains is done for an initial state of h_0 = 9.4 km, V_0 = 108.5 m/s and γ_0 = -10°. Several trials are used to determine the best set of gains. Table 9.9 indicates the gains as used during the several trials.

During the first trial, a complete arbitrary K_p = -0.02 was chosen, together with a K_d = $2{\cdot}10^{-4}$ to assure that the contribution of the proportional term to α is the dominant part. Figure 9.17(a) and 9.18(a) indicate the resulting dynamic pressure profile and the angle-of-attack profile, respectively. These figures indicate that the maximum dynamic pressure overshoots the boundary and that large oscillations are present. Based on the discussion in section 9.1.2, the

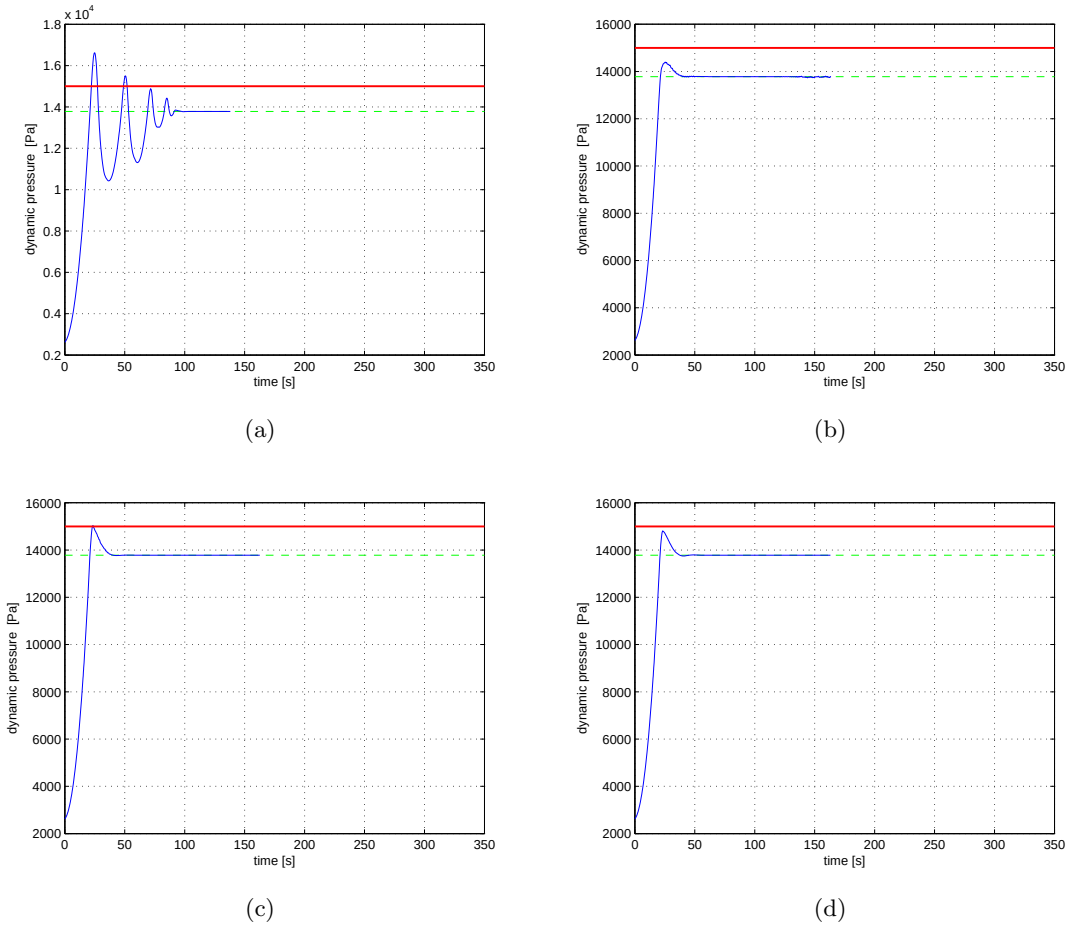

Figure 9.17: Dynamic pressure profiles using maximum dive guidance. RED: maximum dynamic pressure GREEN: reference dynamic pressure BLUE: actual dynamic pressure (a) gain set 1 (b) gain set 2 (c) gain set 3 (d) gain set 4

K_p term is decreased to reduce the overshoot while the K_d is increased to increase the damping and to reduce the oscillations, see set 2. Figure 9.17(b) indicates that the maximum dynamic pressure does not violate the boundary any more and that the fluctuations are removed. But figure 9.18(b) shows that high frequency oscillations are present in the angle-of-attack profiles. This is due to the increased influence of the derivative term. The oscillations that are present in $\dot{q}$ have a large influence and are therefore visible in α. In set 3, K_d is decreased and figure 9.18(c) indicates that the high frequency oscillations are eliminated from α profile when a constant value is reached. Some fluctuations are still present between 20 and 40 seconds. Figure 9.17(c) shows that the overshoot of the reference dynamic pressure is increased. In order to eliminate the high frequency oscillations in the beginning of the flight, K_d must be decreased even further. This will further increase the overshoot and hence, also K_p must be increased. In set 4, these changes are made in combination with three regions for the gain selection based on Δq. For a region close to the reference dynamic pressure, $\Delta q \leq 300.0$ Pa, the same K_p is used as during run 3, but the derivative term is further decreased. In between the Δq values of 300 Pa and 900 Pa, a linear interpolation of the gains is used. The linear section in between is preferred above a single discontinuous switch point. Both figures 9.17(d) and 9.18(d) show that the resulting performance is satisfying. The values of the gains of set 4 as given in table 9.9

are used in the HAC planning algorithm (chapter 11) for the subsonic maximum dive guidance law.

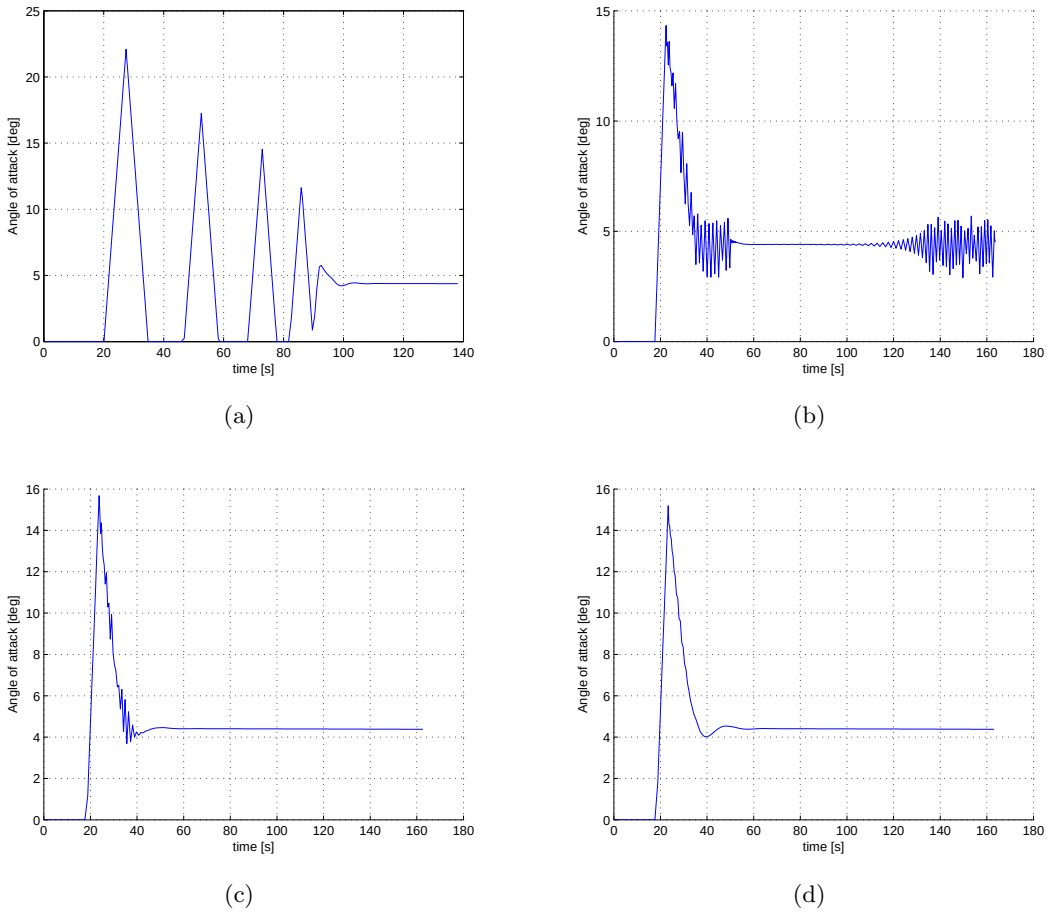

Figure 9.18: Resulting angle-of-attack using the maximum dive guidance law (a) gain set 1 (b) gain set 2 (c) gain set 3 (d) gain set 4

9.5.2 Supersonic maximum dive

The subsonic maximum dive guidance law obtained in the previous chapter can be used up to Mach 0.95. Between M 0.95 and M 1.2, it is not possible to calculate a steady-state angle-of-attack at the reference dynamic pressure. The capabilities of HORUS are insufficient and hence, a falling motion is performed. In this Mach interval, no guidance law is used, but the angle-of-attack is set to a fixed maximum dive value of $\alpha = 2.5°$. For M > 1.2, a guidance law as specified by equation 9.9 is again used. This section concerns the gain selection for this supersonic maximum dive guidance law. In the supersonic regime, no speedbrakes can be used. The obtained guidance law is used in combination with an α- and an $\dot{\alpha}$-filter.

Similar to the subsonic dive, the reference equivalent airspeed is equal to 150.0 m/s. However, the corresponding α^* is no longer constant. Figure 9.19 presents the variation of α^* as function of the energy height. To use this profile in the guidance law, an approximation is made

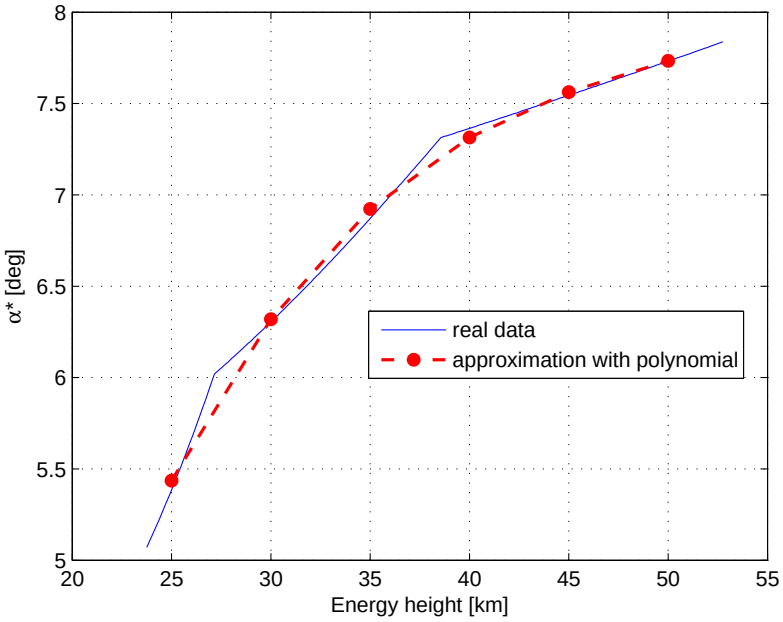

Figure 9.19: Open-loop α^* for the supersonic maximum dive guidance, as a function of energy height.

by using a second order polynomial:

$$\alpha^* = c_1 \, E_h^2 + c_2 \, E_h + c_3 \tag{9.12}$$

where the coefficients are found to be:

$$\begin{aligned} c_1 &= -3.3562 \cdot 10^{-9} \\ c_2 &= 0.0003409 \\ c_3 &= -0.9303 \end{aligned} \tag{9.13}$$

An analysis similar to the one for the subsonic maximum dive is performed. The design of the guidance law is based on a supersonic initial state with $h_0 = 35.0$ km, $V_0 = 583.1$ m/s and $\gamma_0 = 10°$. The same high frequency oscillations were observed in initial trials. After some modifications based on the observations from the subsonic maximum dive analysis, the gains as specified in table 9.10 are obtained. The familiar Δq regions are used in the selection of the gains. Between $\Delta q = 900$ Pa and $\Delta q = 300$ Pa, a linear interpolation is used.

Table 9.10: Gains for the supersonic maximum dive guidance law.

$\Delta q[Pa]$	K_p	K_d
≥ 900.0	-0.008	0.032
≤ 300.0	-0.0012	0.015

Figure 9.20 shows the dynamic pressure profile for the guidance law in combination with the gains from table 9.10. This figure indicates that after an initial overshoot of the reference dynamic pressure in the supersonic regime, q_{ref} is intercepted. The deviation from q_{ref} between

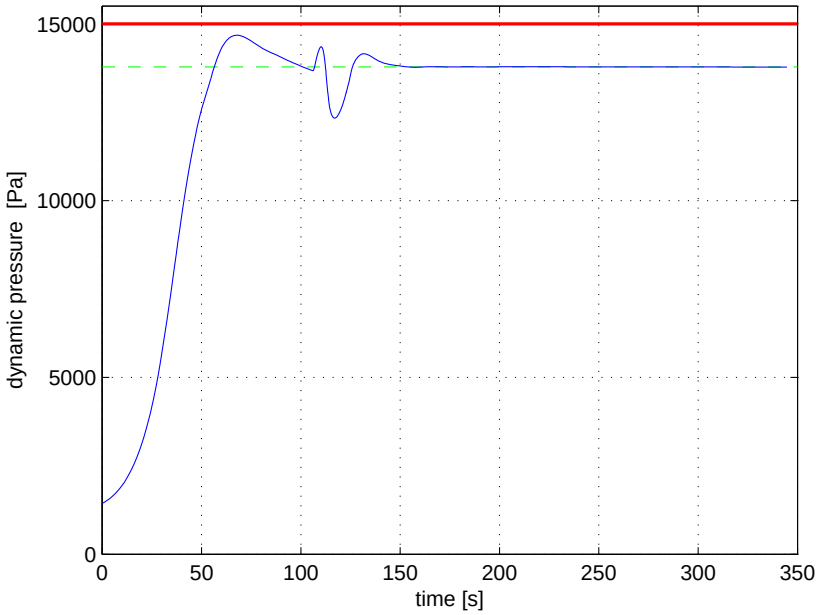

Figure 9.20: Dynamic pressure profile using maximum dive guidance. RED: maximum dynamic pressure GREEN: reference dynamic pressure BLUE: actual dynamic pressure

100 and 150 seconds is due to the constant α of 2.5°. In this interval, no tracking of the reference dynamic pressure occurs. Once HORUS reaches a Mach number lower than 0.95, the subsonic guidance is law used which tracks again q_{ref}. Figure 9.21 presents the resulting angle-of-attack profile. The three phases during the flight are clearly visible. No high frequency oscillations are present. On the switch points between the phases, $\dot{\alpha}$ is never larger than 3°/s due to the use of a rate filter.

9.5.3 Influence of speedbrake deflection

Since the speedbrakes cannot be used in the supersonic speed regime, including a speedbrake deflection in the maximum dive guidance law only influences the subsonic part. A full speedbrake deflection cannot be used, because the combined function of airbrakes and the rudder. Enough control margin must be left for maneuvers, or control actions that require a rudder deflection and hence, a maximum speedbrake deflection of 25° is used for the maximum dive.

Table 9.11: Ranges using the maximum dive guidance, without and with the use of speedbrakes

	subsonic initial state	supersonic initial state
range without speedbrakes [km]	26.06	101.10
range using speedbrakes [km]	20.18	92.38

Once HORUS passes the Mach boundary of M 0.95, the speedbrakes are deflected. Using the same reference equivalent airspeed of 150.0 m/s, the open-loop steady state angle-of-attack is slightly changed and has a constant value of 4.2° in the subsonic regime. It is evident that α^* does not change in the supersonic regime.

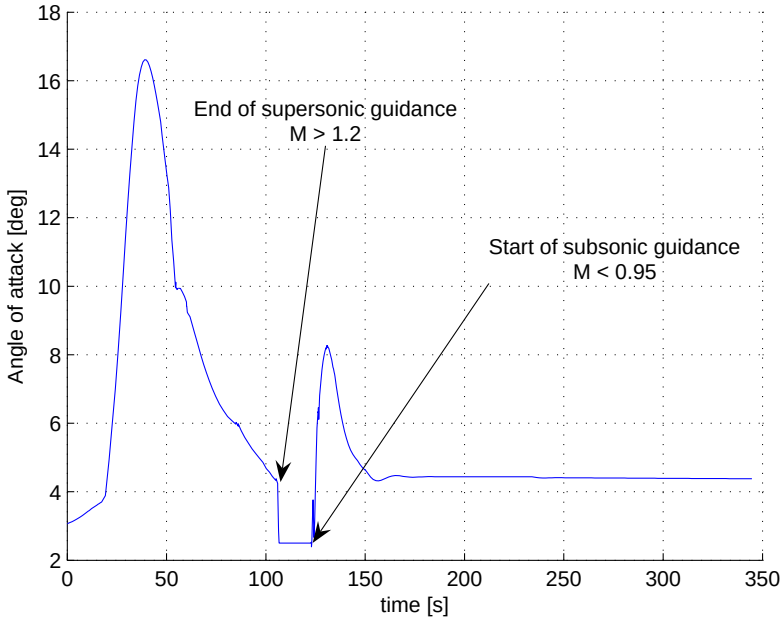

Figure 9.21: Resulting angle-of-attack using the maximum dive guidance law

Using the control law from equation 9.9, in combination with the gains as obtained in the previous sections and the new $\alpha*$, gives the results as indicated in figures 9.22 and 9.23. The same subsonic and supersonic initial states are used as in the previous sections. These results indicate that the use of speedbrakes does not influence the performance using the familiar subsonic gains. The gains as specified in table 9.9 are still valid in case speedbrakes are used. No high frequency oscillations occur in the angle-of-attack profiles. After an initial overshoot of q_{ref}, the reference dynamic pressure is followed and the maximum dynamic pressure boundary is not violated.

To indicate the influence of the speedbrake deflection on the trajectory, the obtained ranges are presented in table 9.11. It is clear that the range is reduced when speedbrakes are used with respect to the case without speedbrakes. In the subsonic case, this means a reduction of 6 km, while for the supersonic initial state, the range is reduced by 9 km.

9.6 Influence of a turn on the longitudinal guidance

In chapter 7, optimal turning flights were calculated with a genetic algorithm. More specific, the optimal longitudinal strategy during a cylindrical HAC turn with a particular radius was studied. A lateral guidance law is used to track the surface of the HAC. This lateral guidance law is described in section 11.2. In chapter 8, the obtained optimal HAC turn results were analyzed and the obtained information is used in this section to design a longitudinal guidance law during a HAC turn. The influence of a HAC turn on the guidance laws as obtained in the previous sections is investigated, both for the maximum range guidance and the maximum dive guidance.

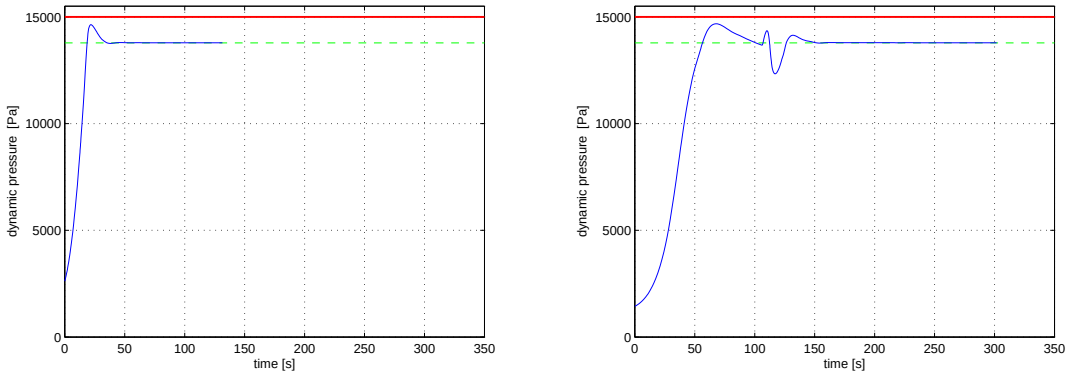

(a) (b)

Figure 9.22: Dynamic pressure profiles using maximum dive guidance, together with a speedbrake deflection of 25 degrees. RED: maximum dynamic pressure GREEN: reference dynamic pressure BLUE: actual dynamic pressure (a) subsonic initial state (b) supersonic initial state

9.6.1 Maximum range guidance

An optimal HAC turn was specified as a turn with the lowest amount of energy dissipation with respect to range, dE/dx. During the turn, the drag must be minimized. In chapter 8, it was observed that the optimal HAC turn trajectories all intercepted the drag valley or minimum drag path corresponding with the particular HAC radius. These minimum-drag paths occur at a constant equivalent airspeed or dynamic pressure, for a specific HAC radius. These values are already given in chapter 8, but are repeated here for convenience in table 9.12. Hence, also for an optimal HAC turn, the longitudinal guidance can be based on reference dynamic pressure or equivalent airspeed tracking, and the control law from equation 9.9 can be used.

Normal banking

First, the turning flight is discussed for the case where HORUS is able to follow the HAC surfaces. The combination of velocity and turn radius is such that HORUS has enough bank capabilities (maximum bank angle) to follow the HAC surface.

Table 9.12: Reference dynamic pressure and α^* for a HAC turn with minimum energy dissipation

HAC radius [km]	V_{eq} **[m/s]**	c_1	c_2	c_3
3.0	100.0	$4.7993{\cdot}10^{-8}$	$-2.2636{\cdot}10^{-4}$	11.3271
4.0	104.0	$2.3197{\cdot}10^{-8}$	$-8.4830{\cdot}10^{-5}$	10.1302
5.0	108.0	$1.4059{\cdot}10^{-8}$	$-2.2545{\cdot}10^{-5}$	9.1268
6.0	112.0	$1.2253{\cdot}10^{-8}$	$-3.2133{\cdot}10^{-5}$	8.3949
7.0	116.0	$9.5515{\cdot}10^{-9}$	$-2.3974{\cdot}10^{-5}$	7.7244

In equation 9.9, α^* is no longer a constant. It changes as a function of both the energy height and turn radius (figure 9.24). The smaller the turn radius, the higher the steady-state angle

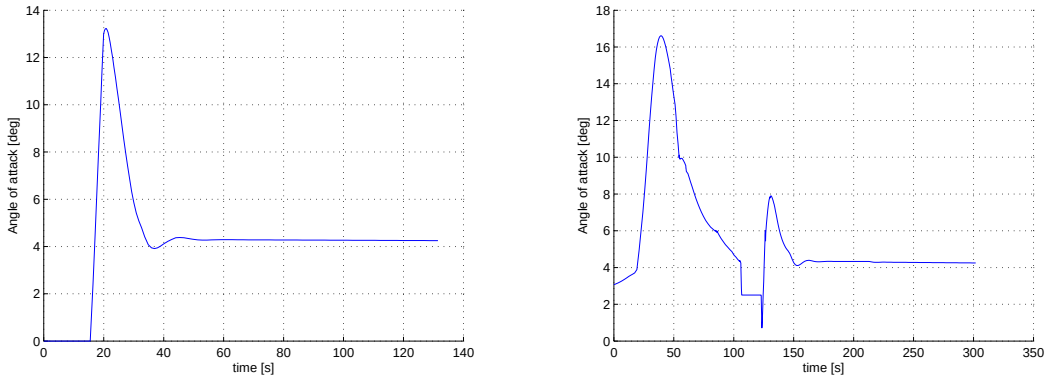

(a) (b)

Figure 9.23: Resulting angle-of-attack using the maximum dive guidance law, together with a speedbrake deflection of 25 degrees (a) subsonic initial state (b) supersonic initial state

of attack. These data are stored in the guidance system by using a second-order polynomial approximation:

$$\alpha^* = c_1 \, E_h^2 + c_2 \, E_h + c_3 \tag{9.14}$$

The coefficients are presented in table 9.12 as a function of the turn radius.

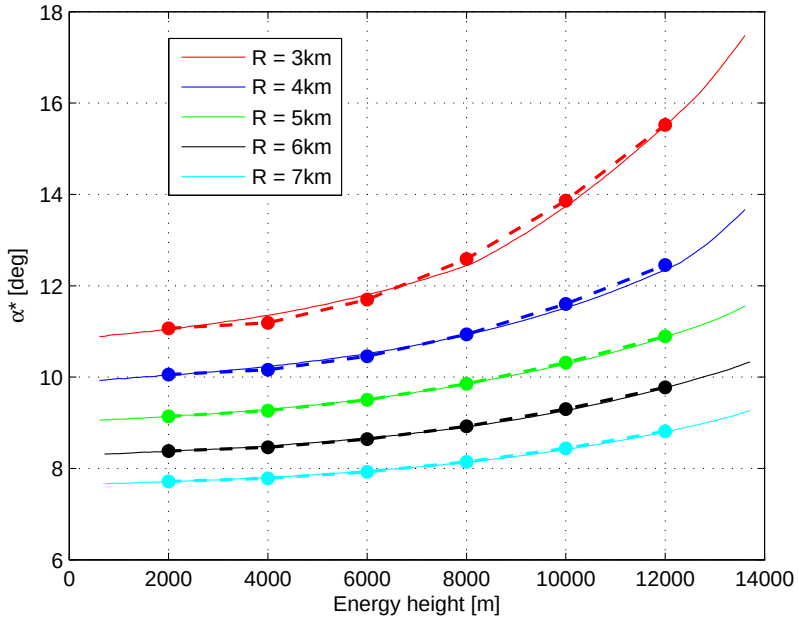

Figure 9.24: Open-loop angle-of-attack α as a function of energy and turn radius for a turn with minimum energy dissipation. The dotted lines and data points corresponds to an approximation using a second order polynomial.

In an optimal turning flight, also the transient maneuvers required to intercept the minimum drag path must be optimal. These maneuvers were taken into account during the optimization

and robust design of the gains for a maximum range flight (section 9.3). Hence, it is investigated if the same gains can still be used for an optimal turning flight. The initial states used in this investigation correspond with the same initial states as specified in chapter 7. The results are shown below for two HAC configurations: a HAC radius of 3 km and 6 km. Figures 9.25(a) and 9.25(a) show the resulting trajectories in the energy space for the three subsonic initial states. Also the reference equivalent airspeed in the turning flight is presented. These figures indicate that the gains obtained from the robust design method in section 9.3 are still able to intercept the reference dynamic pressure in a turn, for different initial states or off-nominal conditions. The initial states are already situated on the HAC surface and after a turn of 270°, the bank angle is reduced to 0° and a straight maximum-range flight is performed. This transition can be seen in both figures.

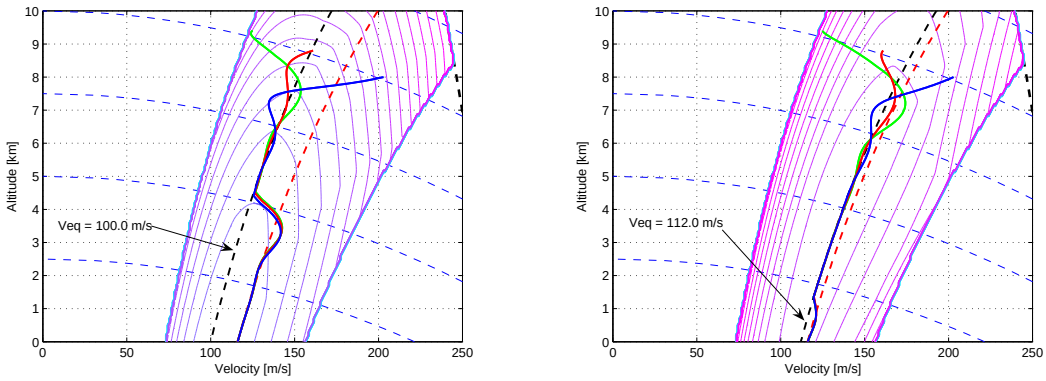

(a) (b)

Figure 9.25: Trajectories in the energy space using a longitudinal guidance law and the optimal gains resulting from the robust design analysis. (a) HAC radius of 3 km (b) HAC radius of 6 km

The same satisfying results were observed for other radii of turn. Hence, the gains obtained from the robust design for a straight maximum range flight will be used in the guidance law for an optimal HAC turn and to investigate the influence of changing initial states on the energy management capabilities.

Banking at maximum bank angle

During one of the test runs to check the implementation of the guidance algorithms in the planning algorithm (described in chapter 11), it was observed that a deviation occurred from the reference equivalent airspeed during the HAC turn. Figure 9.26 shows the ground track for this particular test run, which had the goal of test run was to check whether the lateral guidance was able to guide HORUS to the tangent to a HAC which was placed at a random position. During the HAC turn and when HORUS reaches a heading of 90°, a switch must be made to a straight flight.

During the complete flight, a maximum range strategy is applied. Figures 9.28(a) and 9.28(b) presents the control variables during the flight. Below, focus is on the part of flight starting at the point where the HAC turn starts. At the start of the HAC phase, the bank angle is increased to track the surface of the cylinder. After a few seconds, the bank angle hits the maximum bank

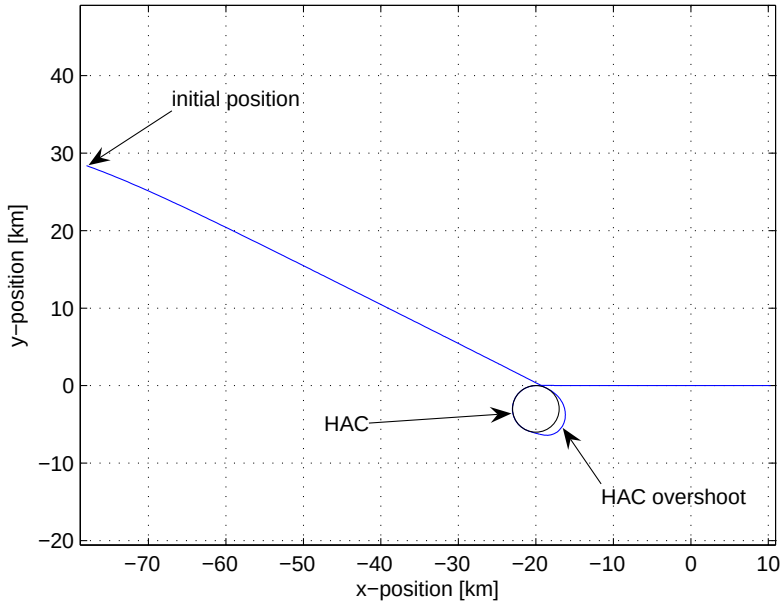

Figure 9.26: Ground track of a simulation with an overshoot of the HAC.

angle limit of 60°. This bank angle is insufficient to follow the HAC surfaces at the current velocity and HORUS overshoots the HAC. During this overshoot, the lateral guidance calculates a new tangent trajectory to the HAC. When HORUS is flying again toward the HAC, the bank angle is lowered until the HAC is reached for a second time. Then the bank angle increases to track the HAC. This time, HORUS is able to track the HAC because it reaches the HAC at a lower velocity. These different phase can also be seen in the trajectory in the energy space as presented in figure 9.27. When HORUS starts the HAC turn for a second time, it is able to track the HAC at a moderate bank angle and the longitudinal guidance is able to track the reference dynamic pressure. During the first attempt to track the HAC, it can be seen that in the beginning, the velocity is also decreased and tends toward the reference equivalent airspeed. But when HORUS is in a banked situation with a maximum bank angle, a falling motion occurs. Due to the extreme banked situation, the longitudinal guidance law should calculated a larger angle of attack to increase the lift force such that the falling motion does not occur. The current gains as obtained using robust design are not sufficient to increase the angle of attack in such a way that the falling motion does not occur. This phenomena of a falling motion during the overshoot can be seen especially at small turn radii. Although it can still be present at a larger turn radius, increasing the radius makes this phenomena less pronounced and harder to detect.

The gains should be adapted in case of high bank angles close to the boundary values. Unfortunately, this is out of the scope of this thesis. But it is recommended that further research is performed, especially to the implementation of an MRAC guidance/control system which changes the gains such that a reference trajectory is followed in case of changing conditions. Another recommendation or solution might be to use a different guidance or control law. The control law from equation 9.9 directly regulates the angle of attack. A better option might be to use a control law that regulates the vertical component of the lift force (or lift coefficient). The angle of attack is then determined from this required vertical component of the lift force.

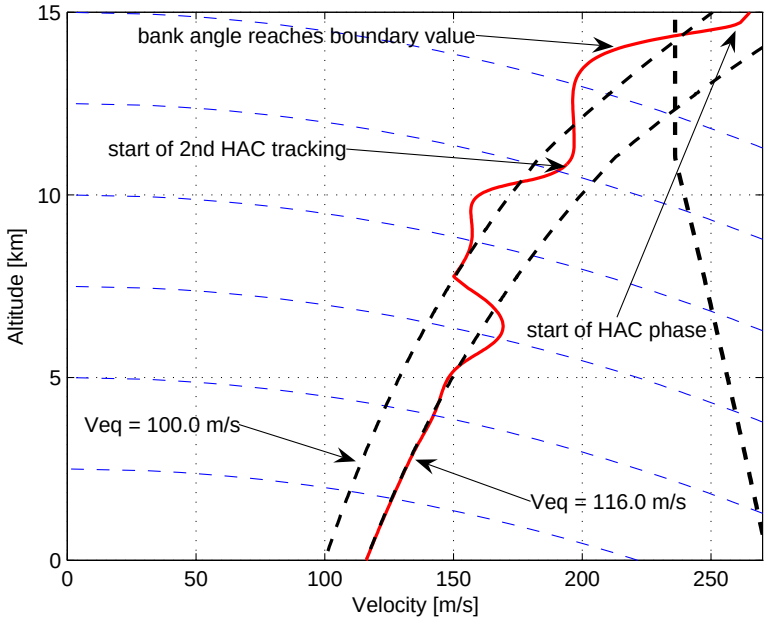

Figure 9.27: Trajectory in the energy space for a HAC overshoot

Also note that the reference dynamic pressure during an overshoot might be different than during the HAC turn. During the HAC turn, the reference equivalent airspeed is based on the minimum drag path for a specific turn radius. But during the HAC overshoot, HORUS turns with a different turn radius and hence, a different reference equivalent airspeed might be necessary. This is also a recommendation for further research.

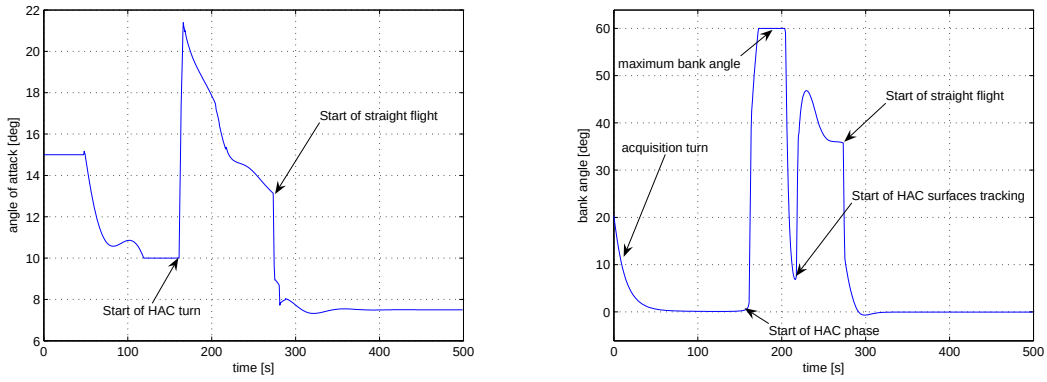

(a) (b)

Figure 9.28: Control variables during a trajectory with a HAC overshoot (a) angle-of-attack (b) bank angle

This phenomena can be seen especially at small turn radii. Although still present at a larger turn radius, increasing the radius makes this phenomena less pronounced and harder to detect.

9.6.2 Maximum dive guidance

Similar to a maximum dive during a straight flight, a maximum dive during a HAC turn will be performed at the maximum dynamic pressure of 13800 Pa. The guidance system tracks this reference dynamic pressure and hence, the guidance law for the maximum dive during a turn is also given by equation 9.9.

open-loop α^*

In a straight flight, the open-loop angle of attack had a constant value. During a turn, the α^* changes both with respect to the energy height and the turn radius. Figure 9.29 indicates the variation of the open-loop α^*. These values are the required angle-of-attack values for a steady-state situation at the combination of a particular energy height and the maximum dynamic pressure. Since the speedbrake can be used in a subsonic HAC turn, the steady-state values are calculated for a maximum dive speedbrake deflection of 25°. The α^* is stored in the guidance system by using a second-order polynomial as given in equation 9.14. The coefficients for the maximum dive turn are presented in table 9.13.

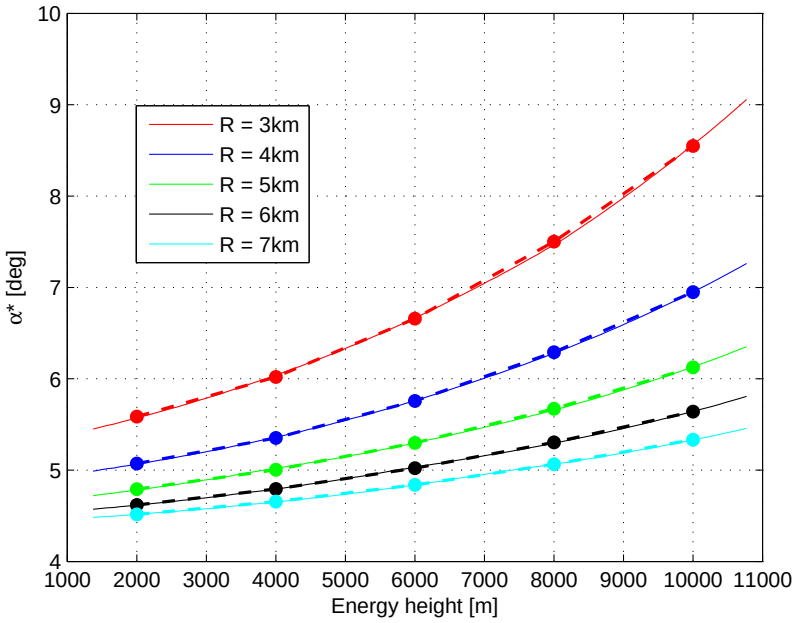

Figure 9.29: Open-loop angle-of-attack α as a function of energy and turn radius for a maximum dive turn. The dotted lines and data points corresponds to an approximation using a second order polynomial.

Adaption of the gains

In section 9.5, the gains were calculated for a maximum dive during a straight flight, both for a subsonic and supersonic dive. During an initial simulation for a HAC turn flight, these gains were used to calculate the angle-of-attack and the trajectory during a diving flight, including the turn around a HAC. Figure 9.30 shows the ground track for this simulation. A random

Table 9.13: Open-loop α^* for a maximum dive HAC turn

HAC radius [km]	c_1	c_2	c_3
3.0	$2.5597{\cdot}10^{-8}$	$6.3353{\cdot}10^{-5}$	5.3560
4.0	$1.5744{\cdot}10^{-8}$	$4.5606{\cdot}10^{-5}$	4.9172
5.0	$1.0121{\cdot}10^{-8}$	$4.5300{\cdot}10^{-5}$	4.6606
6.0	$6.7774{\cdot}10^{-9}$	$4.6437{\cdot}10^{-5}$	4.4989
7.0	$5.3866{\cdot}10^{-9}$	$3.7759{\cdot}10^{-5}$	4.4169

HAC radius of 4 km was chosen. HORUS performs an acquisition turn to fly into a direction tangent to the HAC. During the HAC turn, a small HAC overshoot occurs. When HORUS flies with a heading of 90°, the bank angle is reduced to zero and a straight flight is performed. The used lateral guidance will be discussed in chapter 11.

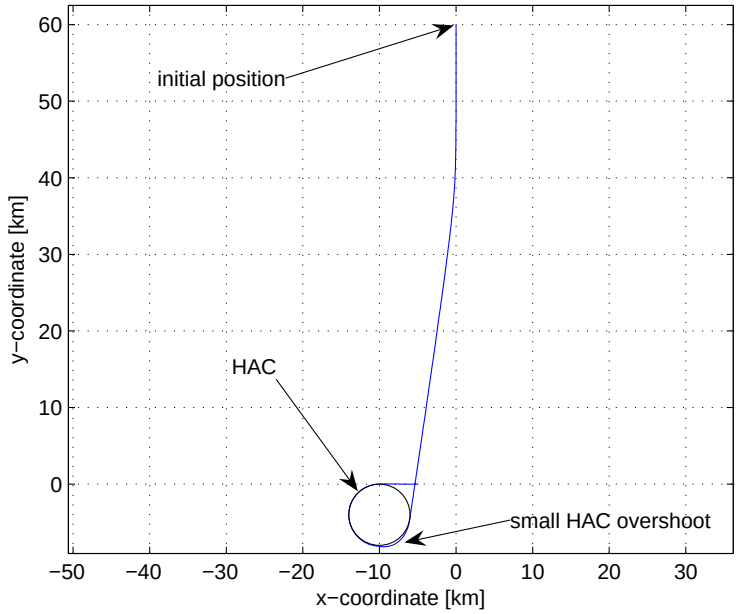

Figure 9.30: Ground track of a simulation with a maximum dive around a HAC.

Figure 9.32 shows the angle-of-attack profile during the maximum dive. In this figure, the start and the end of the HAC turn is indicated. At the start of the HAC turn when the guidance law for a HAC turn is switched on, a spike occurs in the α profile. This is because the guidance law is used without an input filter. A filter will eliminate a sudden change in the input (q or $\dot{q}$) to the guidance law when this guidance law is switched on. Using a filter, a smoother input profile will be transfered to the guidance law. The design of such a filter is left as future work. Moreover, during the peak, $\dot{\alpha}$ is never larger than 3°/s, since an output filter is used on the output of the guidance law. After this peak, some high amplitude oscillations occur. This means that both K_p and K_d should be increased. Besides these oscillations, also high frequency oscillations occur near the end of the flight. It was previously shown that to eliminate the high frequency oscillations, K_p and K_d should be decreased.

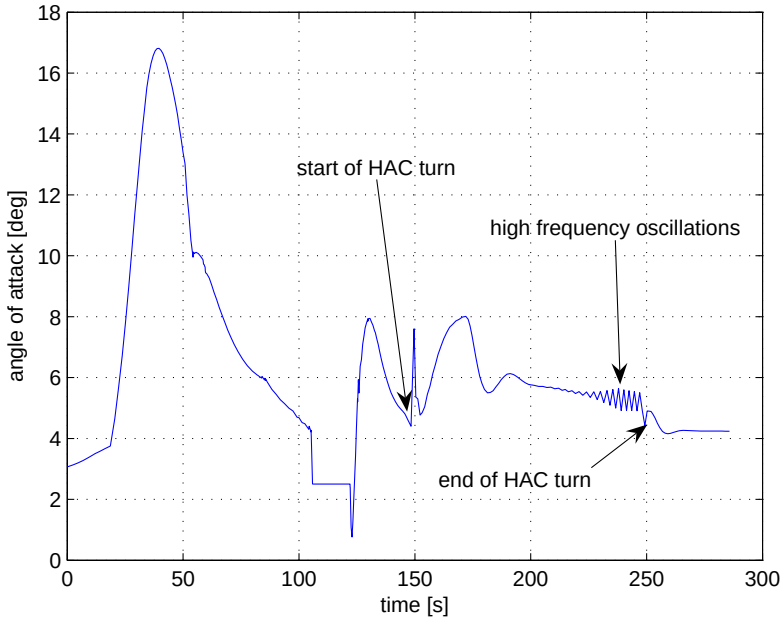

Figure 9.31: Angle-of-attack profile for maximum diving flight around a HAC, using the original gains

It is clear that the same gains as the ones for a straight gliding flight cannot be used during a turning flight. The discussion above indicates a contradiction in the required change of the gains values. To eliminate the high frequency oscillations, the gains should be decreased, while for the oscillations with a larger amplitude, the gains should be increased. The oscillations cannot be eliminated with a single change of the gains. An adaptive system is required that would change the gains such that the fluctuations are eliminated as much as possible in both cases. This is out of the scope of this thesis, but it is recommended to do further research on the implementation of an MRAC system to solve the problem. In this thesis, it was decided to eliminate the high frequency oscillations.

It was observed that the high frequency oscillations decreased when the HAC radius is increased. Hence, the required change for K_p and K_d depends on the turn radius and corresponding bank angle. A new simulation was performed where the original gains of the subsonic dive are multiplied by the cosine of the bank angle. Figure 9.32 shows the new angle-of-attack profile. The high frequency oscillations are eliminated, but the high amplitude oscillations are still present. Figure 9.33 presents the dynamic pressure profile. In the beginning of the HAC turn, the dynamic pressure fluctuated around the required dynamic pressure due to the oscillations in α. Further research is needed to eliminate these oscillations using an MRAC system.

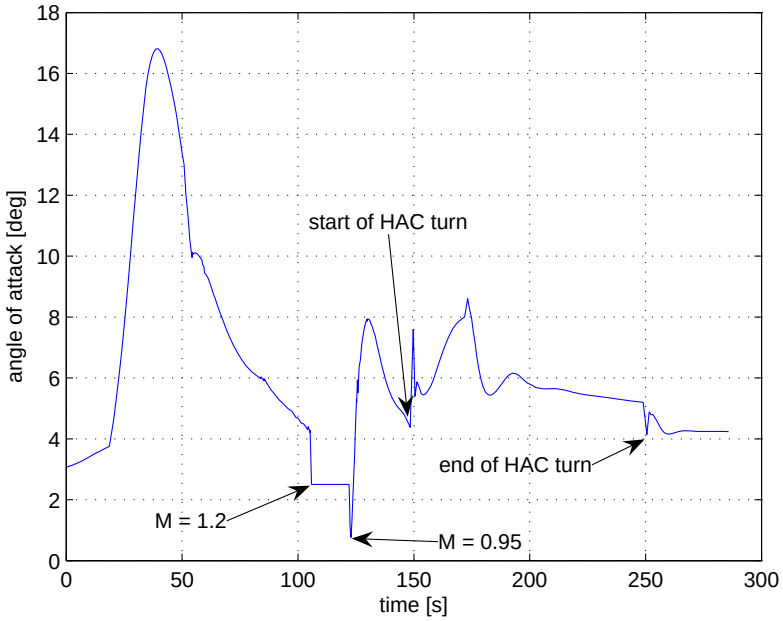

Figure 9.32: Angle-of-attack profile for maximum diving flight around a HAC, using the adapted gains

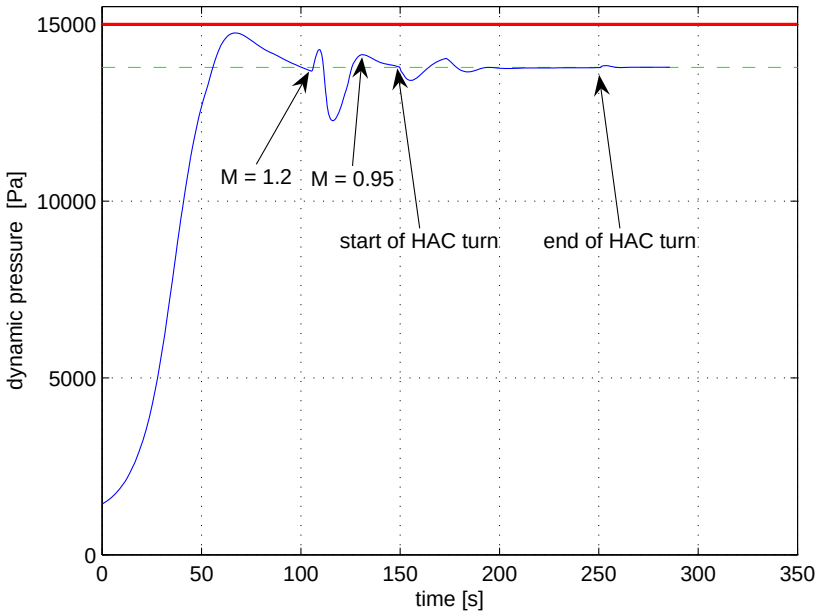

Figure 9.33: Dynamic pressure profile using adated maximum dive guidance for turning flight. RED: maximum dynamic pressure GREEN: reference dynamic pressure BLUE: actual dynamic pressure

Chapter 10

Energy management using the energy-tube concept

The previous chapters considered the optimal trajectories and strategies for a maximum-range and a maximum-dive trajectory. Also the influence of changing initial states was investigated. These strategies can be used to give an answer to the question: given a specific amount of initial energy, what is the maximum and minimum range that can be achieved? But for the purpose of energy management and energy estimation, it is more valuable to know the minimum amount of energy that is required to fly a specific range or the maximum amount of energy with which a specific range can be flown without overshooting the target range. It is also important to investigate the influence of a change in the initial state on these energy levels. This chapter introduces the energy tube concept for a straight flight. In the next chapter, this concept is used to design a planning algorithm for the complete terminal area.

10.1 Minimum required energy

An important boundary of the capabilities of HORUS is the minimum required energy needed to fly a specific range. It is common to use only one specific value for this minimum energy height. If the energy state of the vehicle falls below this boundary value, the targeted range cannot be reached. This is stated in (Buechner, 2003). This can also be observed in the energy profiles as used by the Space Shuttle, see figure 10.1. For a specific range, only one value for the corresponding nominal energy height is used.

However, both steady-state solutions from chapter 6 and the optimization results from chapter 7 indicate that although initial points have the same initial energy height, the obtained maximum range is different. Consider, for example, the subsonic steady-state solutions from chapter 6. The largest maximum range is equal to 34.88 km, obtained for an initial state situated in the drag valley. Figure 10.2 presents all the initial points for which it is possible to fly at least 34.88 km using the maximum range steady-state solution (blue area), indicating the minimum required energy or maximum range boundary. If an initial point is situated below the maximum range boundary (lower energy), then it is not possible to reach the target range of 34.88 km, not even with the maximum range strategy. This figure clearly indicates that not all

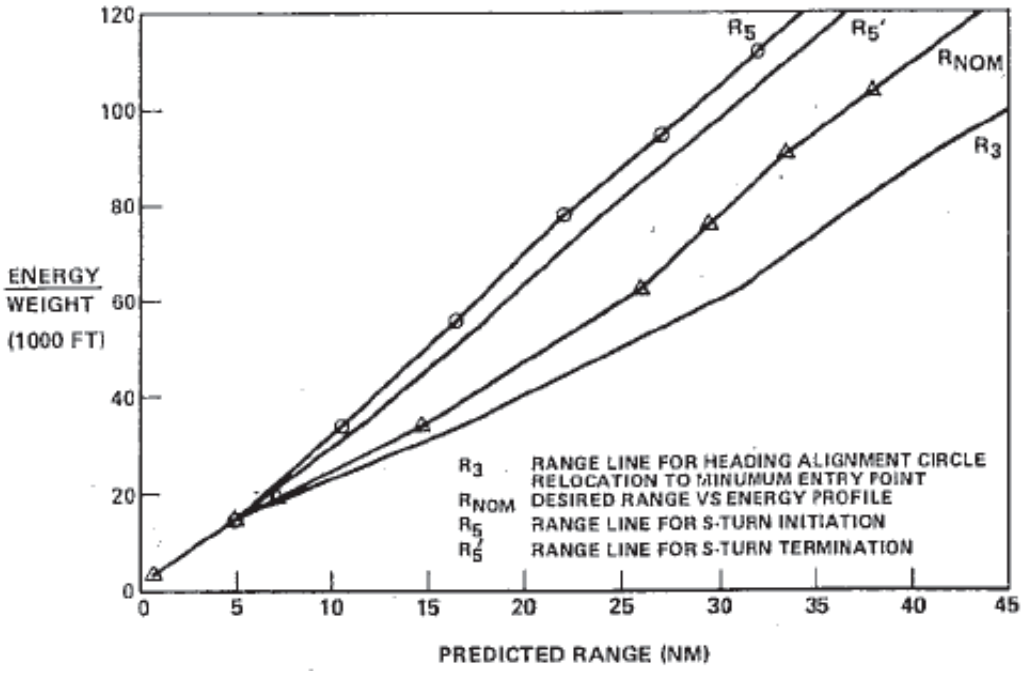

Figure 10.1: Energy profiles as used in the Space Shuttle guidance (Kraemer & Ehlers, 1975)

combinations of initial altitude and velocity with an initial energy height of 10.0 km will yield a maximum range of at least 34.88 km. The maximum-range boundary or minimum required energy boundary does not follow the lines of constant energy. The same trends are observed for the supersonic flight, see figure 10.3. Also in this figure, the maximum range boundary does not follow the lines of constant energy height.

This is an important observation, because this means that in case a guidance system must be able to cope with off-nominal conditions, it is not possible to specify only a single minimum required energy value for a particular range, for all initial states. Next to specifying the minimum required energy for a specific range, it is also necessary to specify for which combination of altitude and velocity this is valid.

Energy profiles as the one from the Shuttle are still valid if they are used in combination with altitudes and velocity profiles. The altitude and velocity profiles then indicate for which combination of altitude and velocity the energy profiles are valid. But when off-nominal conditions arise, these energy profiles need to be adapted, together with the altitude and velocity profiles.

10.2 Energy tube cross-section

Next to the minimum required energy boundary, also the maximum energy boundary or the maximum energy height with which the vehicle can fly to a specific target runway without overshoot, depends on the distribution of the total energy in potential and kinetic components. Initial conditions situated on this maximum energy boundary require the use of the maximum dive strategy to reach the target range, without overshoot. The maximum energy boundary or maximum dive boundary is indicated in figure 10.3.

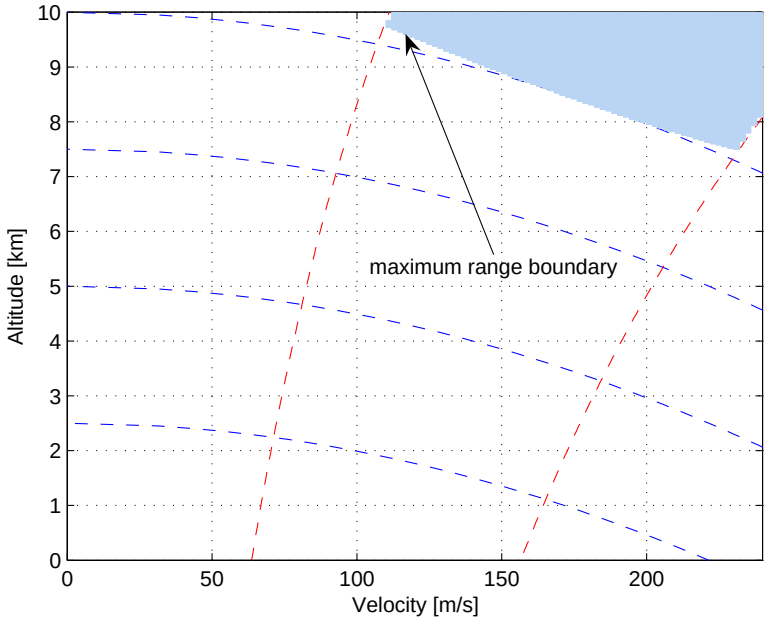

Figure 10.2: Combinations of initial altitude and velocity which yield a maximum range of at least 34.88 km (blue area), indicating the maximum range boundary

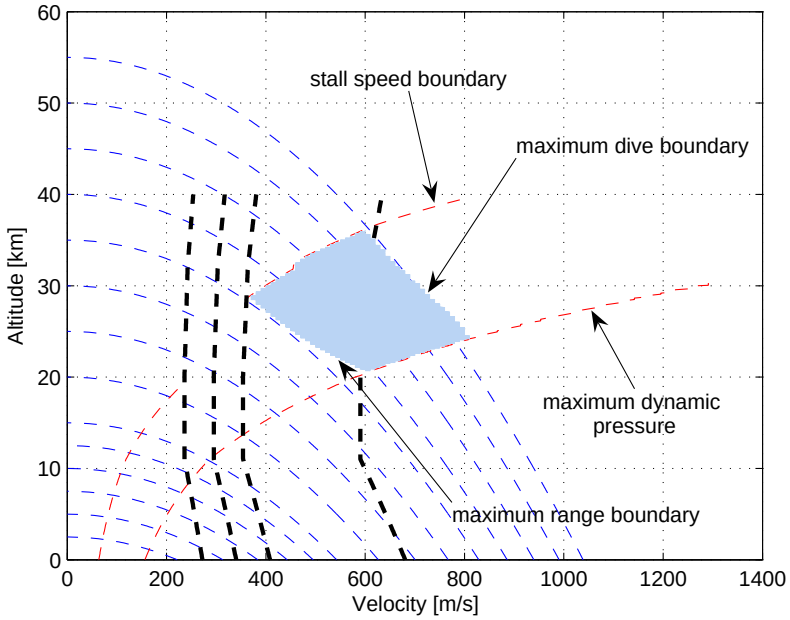

Figure 10.3: Cross-section of energy tube for a target range of 100 km

Now, the capabilities of the vehicle can be expressed by the energy tube concept. The boundaries of the energy tube are required by the minimum required energy needed to fly a specific range (maximum range strategy) and the maximum energy with which the vehicle is able to fly a specific target range, without overshooting the target (maximum dive strategy). Combining

all the points in the energy space for which the maximum distance is larger or equal to the target range and for which the minimum distance is smaller or equal to the target range, yields an area in the energy space for which there is one strategy to fly a distance equal to the target range. This energy area is defined as the cross-section of the energy tube corresponding to the target range. Figure 10.3 shows the energy tube cross-section for a target range of 100 km, together with the corresponding boundaries. For an initial state situated on the maximum range boundary, a maximum range strategy is required to reach the 100 km target range, while an initial state on the maximum dive boundary requires a maximum dive strategy to not overshoot the target range. For all initial conditions between these two extremes, a different specific strategy is required to reach a range of exactly 100 km, depending on the position in the cross-section. Figure 10.4(b) shows the maximum range and maximum dive trajectories for three initial conditions as specified in figure 10.4(a). The maximum range when starting at point A is larger than 100 km, while the minimum distance using the maximum dive strategy is smaller than 100 km. Hence, the target range is within the range boundaries of point A and there is one strategy between the boundary strategies which yield a range of exactly 100 km. For points B and C, the target range of 100 km is situated outside the boundaries of the possible ranges. Starting at point B, HORUS has not enough maximum range capabilities to reach the target, while starting at point C, HORUS does not have enough dive capabilities to not overshoot the target.

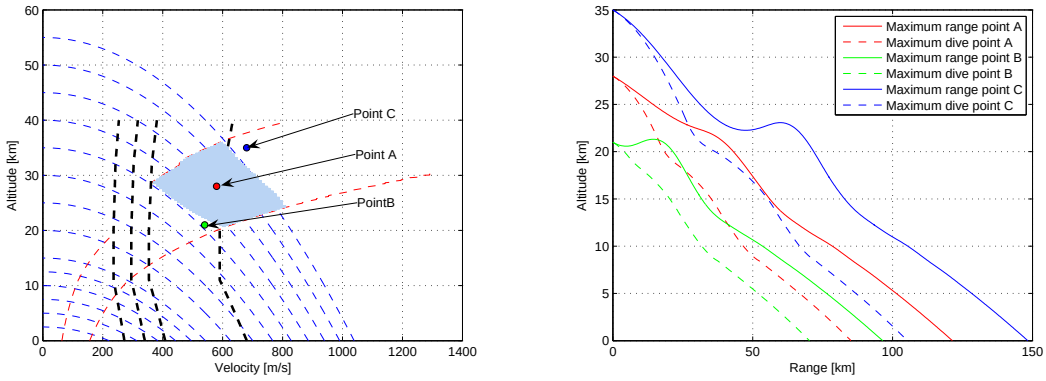

(a) (b)

Figure 10.4: (a) Three initial states in the supersonic energy space (b) maximum range and maximum dive trajectories for three different supersonic points in the energy space

10.3 Applications of the energy tube concept

Every different target range has a different energy tube cross-section. If the cross-section would be calculated for a large interval of target ranges, an energy tube would be obtained. In the above discussion, the concept of the energy tube is explained for a straight flight. This concept can be extended to the complete terminal area by incorporating maximum range and maximum dive strategies in a turning flight. Including turns results in a similar type of an energy tube cross-section, where the boundaries do not follow the lines of constant energy. An example of an energy tube cross-section for a complete terminal area flight, including the turn around the HAC, can be found in figure 12.2. The energy tube concept and the corresponding cross-section can be used for several purposes:

- **Analyzing terminal area flights**
  The energy tube cross-section can be used to investigate and analyze for which initial conditions it is possible to safely reach the runway. Another possibility is to investigate how a TAEM trajectory is situated inside the energy tube. In the TAEM flight, it is important to fly with enough energy control margins. Using the energy tube concept, it is possible to study how well a specific guidance algorithm leaves enough energy control margins by investigating how far the resulting TAEM trajectory is located from the centerline of the energy tube.

- **Vehicle design**
  An energy tube cross-section indicates for how many off-nominal conditions the vehicle is capable of safely reaching a specific target. The larger the cross-section, the more off-nominal conditions the vehicle can handle. Changing the aerodynamic characteristics of the vehicle (gliding capabilities) will alter the cross-sections. The vehicle can be designed such that a satisfying performance is obtained.

- **Implementation in guidance algorithm**
  The previous application areas describe the energy tube concept as a pre-flight analyzing tool. It is unpractical and unnecessary to calculate the complete energy tube on-board, because also the flight-path angle has an influence on the cross-section. The cross-section presented in this section was calculated for an initial flight-path angle of 10°. Changing this value results in a different cross-section. Since γ changes during flight, every time γ changes, a complete different energy tube must be calculated. Another reason is that a lot of the information calculated to define the energy tube, is not used. A practical implementation of the energy tube concept in on-board guidance consists of:

  - TAEM planner
  - energy estimation, generation of control commands and checking energy management boundaries

The energy tube concept can be used to design the HAC configuration when both nominal and off-nominal conditions occur. The HAC is changed until the required range is within the range boundaries of the vehicle at the current state. The next chapter describes the working principle of such a planning algorithm, while the analysis results of the energy management capabilities of HORUS, using the HAC planning algorithm, are described in chapter 12. Note that the algorithm as described in the next chapter is used in this thesis to give a pre-flight analysis of the energy management capabilities of HORUS. The planning algorithm can be used for pre-flight planning, but the goal is to use the same principle in an on-board system. Hence, the theory of the energy tubes and the HAC planning algorithm must be converted to a quick on-board algorithm. The next chapters investigates how well the principle of the planning algorithm works and if it proves to be satisfying, the same principles could be used in an on-board system.

Next to planning, the energy tube concept can also be used for checking the energy management capabilities on-board. Using a guidance law for the maximum range and maximum dive (see previous chapter) and checking on-board if the target range is still within the range boundaries of the current state, similar to the examples given in figure 10.4(b), gives an indication on what the energy control margins of the vehicle are. Based on the current position in the energy tube cross-section or the position of the target range within the range boundaries, the energy excess can be estimated, and the required commands can be generated to dissipate more or less energy in order to reach the target.

Chapter 11

HAC planning algorithm

The energy management capabilities of HORUS determine how well HORUS can handle both nominal and off-nominal conditions. These energy management capabilities depend on the maximum-dive and maximum-range capabilities of HORUS. In the previous chapter, the energy tube concept was introduced for a straight flight. The energy tube cross-section depends on the same vehicle performance capabilities. Next to the longitudinal strategy, also the used ground track geometry and lateral strategy determine the energy-management capabilities. By changing the ground track, these capabilities can be changed. The ground track is characterized by the HAC. In this chapter, a HAC planning algorithm is designed that uses the energy tube concept to plan the position of a HAC for nominal and off-nominal conditions. The performance of the planning algorithm and a study on the energy management capabilities using this planning algorithm, are presented in the next chapter.
Section 11.1 describes the ground track geometry as used for the HAC planning algorithm. In section 11.2, the lateral guidance required to follow the chosen ground track geometry is presented. The HAC planning algorithm also needs a nominal longitudinal strategy. This is described in section 11.3. Finally, the working principle of the HAC planning algorithm is discussed in section 11.4.

11.1 Ground track geometry

11.1.1 HAC shape

Two possibilities exist for the shape of the HAC: a cylinder or a cone. During the first Shuttle flight, a cylinder was used. Also some recent studies use a cylindrical HAC, see for example (Kluever & Horneman, 2005). During later Shuttle missions, a conical HAC was used and resulted in a spiral ground track instead of circular one. This conical HAC shape was also used in terminal area studies for HORUS, see (Helmersson, 1988b). Some advantages and disadvantages of both shapes are discussed below

No explicit reason for the change to HAC cone in the Shuttle guidance was given in (Moore, 1991). But a possible explanation is the reduction of the overshoot. At higher velocities, the maximum attainable turn radius is larger than at lower velocities, at a constant bank angle.

By using a spiral ground track around the HAC cone, the radius is larger at high altitudes where the vehicle reaches the HAC at higher velocities. As the vehicle turns around the HAC and reduces its velocity, the turn radius can be decreased. Another modification was to use an energy dump phase to reduce the velocity with which the Shuttle reaches the HAC. Hence, the combination of the energy dump phase and the change to a HAC cone reduces the overshoot. Also, by using an inward spiral, the vehicle is forced to a tighter turn and consequently needs to fly closer to the runway when it loses its energy.

On the other hand, a cone makes it more complicated to calculate the heading toward a direction tangent to the HAC. The heading should be chosen such that the vehicle joins the HAC with a radius corresponding to the altitude at which the HAC is joined. In is not possible to predict exactly at which altitude the HAC will be joined and hence it is not possible to exactly determine the correct heading. In (Helmersson, 1988b), an approximation is used to predict the altitude at which the HAC is joined by using a constant lift-to-drag ratio. Moreover, a cone makes it also difficult to plan the optimal position of the HAC in the y-direction. The HAC should be placed such that when the vehicle leaves the HAC at a direction towards the runway, the lateral deviation with the runway centerline should be as small as possible. The center of the HAC should be placed such that the outer surface of the HAC touches the extension of the runway centerline. Because the altitude at which the HAC will be left is not known beforehand, it is not possible to know the correct radius at that time and the corresponding optimal y-coordinate of the HAC center.

The main advantage of a cylindrical HAC is simplicity. This is the main reason why such a HAC is still used in (Kluever & Horneman, 2005). Simple equations can be used to calculate the heading towards a tangent to the HAC. The constant HAC radius during a turn makes it also easy to determine the y-coordinate of the HAC, such that the surface of the HAC touches the extension of the runway threshold. The required y-coordinate is equal to the HAC radius. Using a HAC planning algorithm makes it also possible to move the HAC closer to the runway and hence, energy could be dissipated closer to the runway when necessary. This has the same effect of a spiral HAC. The disadvantage that remains is the overshoot in the beginning of the HAC turn at high velocities.

For the HAC planning algorithm as described in this thesis, the cylindrical HAC is used for sake of simplicity. In further research studies, the HAC shape could be modified to a cone, if required.

11.1.2 Type of ground track

Next to the shape of the HAC, other characteristics determine the ground track as well. These include the radius of the HAC, the number of HACs that is used and how the trajectory to the HAC looks like.

In the guidance of the shuttle and during most of the terminal area studies, a single HAC is used. But it is possible to use multiple HACs. Using multiple HACs, several possibilities for the ground track exist. Figures 11.1(a), 11.1(b) and 11.1(c) show several possibilities, based on (Moore, 1991). These include a race track, a spiral and a cylindrical geometry. These are all complex ground track geometries. One can even think of many other possibilities.

When using a single HAC, another possibility to change the ground track is to include the

possibility of a diverting turn before flying to the HAC. One can argue that this diverting turn can be modeled by the ground track as a race track using multiple HACs. Another possibility to include diverting turns is to specify a reversal switch time as was done in (Kluever & Horneman, 2005) for a vehicle with limited bank capabilities. Upon the entry of the terminal area, the vehicle performs a full-bank turn opposite to the direction towards the HAC. At a particular switch time, a bank reversal is performed and the vehicle flies towards the HAC.

In this thesis, the most simple geometry will be used for the HAC planning. First, the principle of the HAC planning method must be tested with a simple geometry before more complicated geometries could be included. Moreover, it is necessary to establish the shortcomings of a simple geometry before improvements can be proposed by using other geometries. Hence, a simple geometry with a single HAC is selected in combination with a direct flight to the HAC without a diverting turn. Figure 11.1(d) shows the simple geometry as used in this study. Using this geometry, the HAC planning algorithm can adapt two parameters:

- HAC center position along the extension of the runway centerline (x-direction), x_{HAC}
- HAC radius or HAC center position in the y-direction, y_{HAC}

11.2 Lateral guidance

Now that a ground track geometry is chosen, a lateral guidance system must be designed such that the ground track geometry is followed. This lateral guidance computes the commanded bank angle, σ_c. After a guidance law has calculated σ_c, this value is passed through two filters: a σ filter (or limiter) and a $\dot{\sigma}$ filter. The bank angle filter assures that the commanded bank angle is not larger than the limits imposed on the maximum allowable bank angle. These limits for HORUS are flight phase depended and are given in section 3.4. The bank rate filter assures that the change in commanded bank angle is not larger than $15^\circ/s$. All the derivative terms as used in the lateral guidance laws are calculated numerically.

Before the different lateral guidance laws are described, an overview on the flight phases as used for the selected simple ground track geometry is given.

11.2.1 TAEM flight phases

Based on the Shuttle guidance and the HORUS guidance described in section 5.3 and 5.4 respectively, the terminal area can be divided into three main phases with an additional phase in case of a HAC overshoot:

- **Phase 1: Acquisition phase**
  The vehicle will rarely enters the terminal area with a heading toward the tangency point to the HAC. In the acquisition phase, HORUS first makes a turn to acquire a heading which is tangent to the HAC. Then a wings-level flight follows until the HAC turn phase is reached.
- **Phase 2: Heading alignment phase**
  In the heading alignment phase, the vehicle is controlled to directionally track the heading

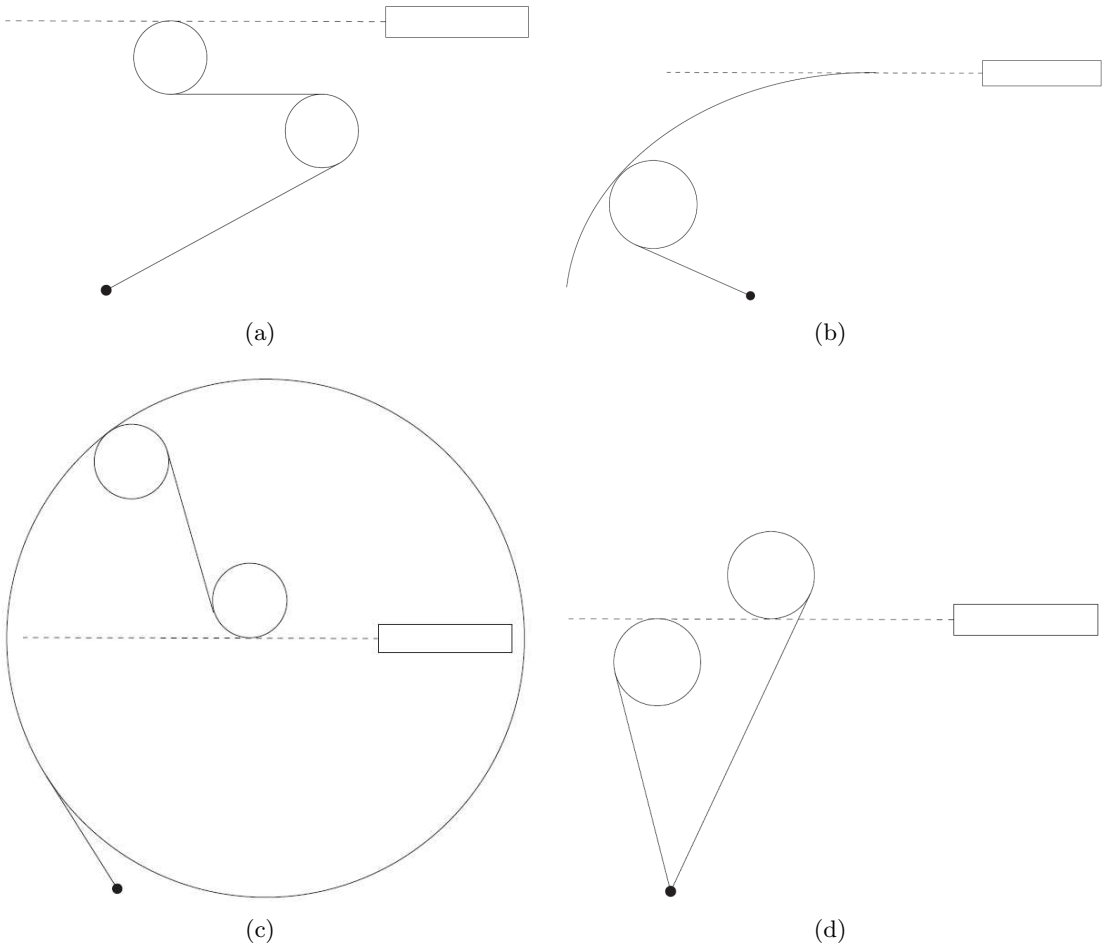

Figure 11.1: Several possible ground track schemes (a) race-track geometry (b) spiral geometry (c) cylindrical geometry (d) simple geometry with a single variable HAC position

alignment cylinder. This phase is continued until the heading is within 5° of the final approach plane. Then, a switch is made to the pre-final guidance phase. The final approach plane is a vertical plane through the extended runway centerline.

- **Phase 3: Pre-final phase**
  During the prefinal guidance phase, the lateral guidance steers the vehicle toward the final approach plane.

- **Phase 4: 2nd acquisition phase**
  In case the vehicle overshoots the HAC, the heading alignment guidance is not sufficient to assure a smooth trajectory toward the HAC. When the difference between the vehicle and the HAC outer surface gets larger than 500 m during a HAC overshoot, a switch is made to a second acquisition phase. The lateral guidance during this phase calculates a new trajectory tangent to the HAC. The lateral guidance algorithm used in this phase is identical to the normal acquisition lateral guidance. When the HAC is reached, the heading alignment guidance is used again. If required, it is also possible to go from the second acquisition phase directly to the pre-final phase.

11.2.2 Prefinal guidance

In the pre-final phase, the bank angle command is generated from a linear combination of the vehicle's lateral deviation Δy and its derivative $\Delta \dot{y}$, from the extension of the runway centerline:

$$\sigma_c = K_p \, \Delta y + K_d \, \Delta \dot{y} \tag{11.1}$$

The gains are presented in table 11.1 and correspond to the gains as used in (Kluever, 2007). Figure 11.2 presents the y-coordinate as a function of time for two pre-final trajectories. This figure indicates that the chosen gains give satisfying results. They are able to guide HORUS to the extension of the centerline (x-axis). Two trajectories are given, one in which HORUS approaches the runway with a negative y-coordinate (pre-final trajectory 1) and one with a positive y-coordinate (pre-final trajectory 2). In both cases, a slight overshoot is present (only 5 meters), after which HORUS tracks the x-axis. Representative initial states for a pre-final trajectory are used. The flight starts at a distance of 300 m perpendicular to the extension of the centerline, with a heading of 85° or 95° for pre-final trajectory 1 and 2, respectively. An initial altitude, velocity and flight-path angle of respectively 3 km, 125 m/s and -15° are used.

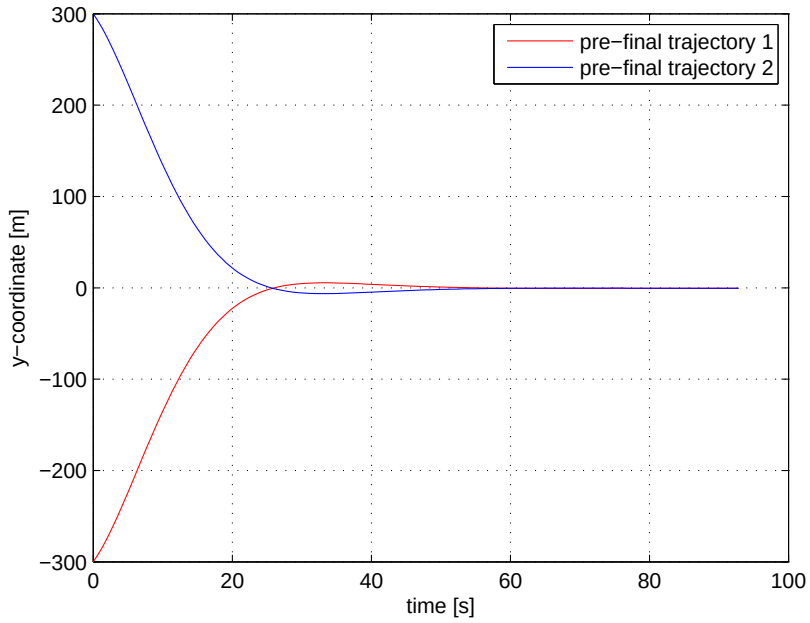

Figure 11.2: y-coordinate as a function of time for two pre-final trajectories

Table 11.1: Gains as used in the lateral guidance laws for the different flight phases. n.a. = not applicable

	K_p	K_d
pre-final	0.001717 [rad/m]	0.02003 [rad/m/s]
heading alignment	0.002 [rad/m]	0.03 [rad/m/s]
acquisition	0.06109 [rad/deg]	n.a.

11.2.3 HAC guidance

In the heading alignment phase, a bank command is generated to assure that HORUS executes a turn which follows the HAC. The commanded bank angle is proportional to the position error and the position rate error:

$$\sigma_c = Y_{HAC}(-\sigma^* + K_p \Delta R - K_d \Delta \dot{R}) \tag{11.2}$$

The steady-state bank angle σ^* is the bank angle required for a turn radius equal to the reference HAC radius at the current state. Equation 11.3 presents this steady-state bank angle and is obtained from equation 6.17. Figure 11.3 represents the lateral guidance geometry during the heading alignment phase. The position error ΔR is expressed by the difference in distance towards the center of the HAC, see equation 11.4. The actual distance between HORUS and the center of the HAC is indicated by R_c, while R_{HAC} represents the reference HAC radius. The position rate error is given by equation 11.5, in which no $\dot{R}_{HAC}$ term is present because this term is equal to zero for a constant cylindrical HAC with a constant radius.

$$\sigma^* = tan^{-1}(\frac{V^2 cos\gamma}{g\, R_{HAC}}) \tag{11.3}$$

$$\Delta R = R_{HAC} - R_c \tag{11.4}$$

$$\Delta \dot{R} = \dot{R}_c \tag{11.5}$$

Y_{HAC} determines the sign of the steady-state bank angle and the gains. Different values are required for a left or a right turn. A right turn is characterized by a positive σ value. Figure 11.3 indicates that a HAC with a positive y-coordinate of the HAC center always requires a left turn to track the HAC and align with the extension of the runway centerline, with the correct heading. A negative y-coordinate of the HAC center requires a right turn. The signs as indicated in equation 11.2 represents a left turn (Y_{HAC} = 1). Multiplying this equation with a negative Y_{HAC} (Y_{HAC} = -1) represents a right turn.

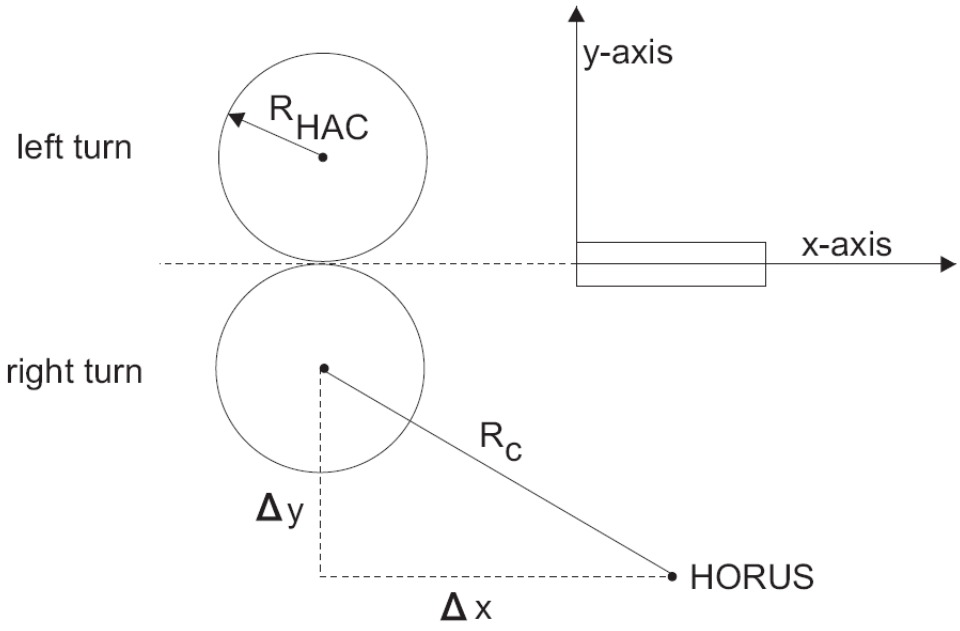

Figure 11.3: Geometry as used during the heading alignment phase

Figure 11.4 shows the variation of the turn radius R_c for three different sets of gains. The reference HAC radius is equal to 5 km. HORUS starts at an initial position that is situated at 500 m from the HAC surfaces (R_c = 5.5 km), with h_0 = 9.4 km, V_0 = 125.0 m/s and γ_0 = -10°. The first set of gains corresponds with the values as used in (Kluever, 2007). Figure 11.4 indicates that in the beginning, the turn radius is even increased. Hence, for HORUS, a higher proportional gain K_p value is required. Set 2 indicates that using a larger K_p results in a reduction of the rise time and an increase of the overshoot. Set 3 reduces the overshoot and increases the damping by increasing the derivative gain K_d. Other simulations performed using this set of gains for a different initial R_c, flight path angle, velocity and reference R_{HAC} indicate that this set is a valid set of gains for the heading alignment phase. Hence, the values from set 3 are used during the rest of this study and are indicated in table 11.1. Note that although the response is acceptable, it is not yet optimal and improvements could still be made in further studies.

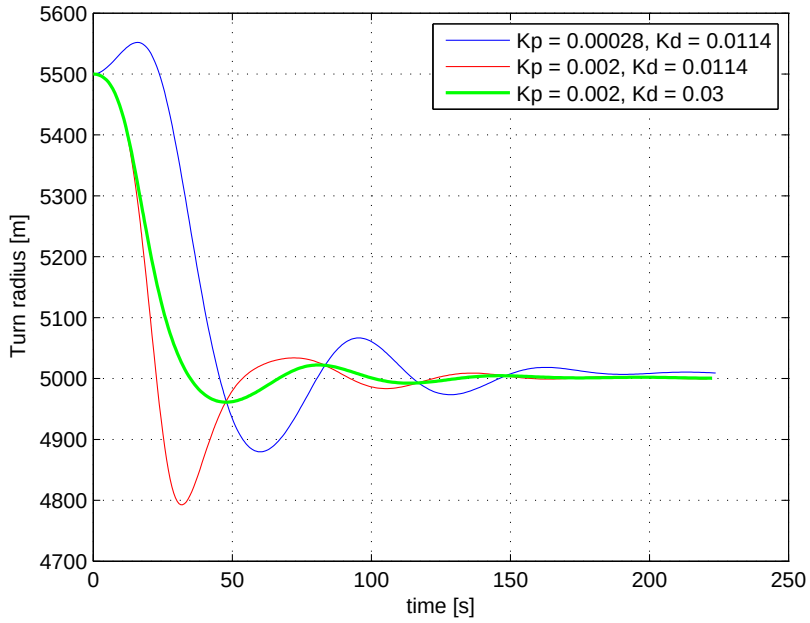

Figure 11.4: Variation of the turn radius for three different sets of gains; R_{HAC} = 5 km.

11.2.4 Acquisition guidance

The lateral guidance during the acquisition phase consists of both a guidance law and a function that calculates the required heading. This required heading serves as an input to the guidance law. Note that the lateral guidance as presented in this section does not resemble an optimal supersonic turn to a specific heading. The guidance law only gives a good performance in terms of flying to the HAC, but perhaps another guidance law might do this in a more optimal way in terms of energy consumption. In chapter 9, it was not possible to design an optimal supersonic longitudinal guidance law. Instead, a constant α-profile is used. Therefore, it was also pointless to study the influence of a supersonic turn on the supersonic longitudinal guidance law. During a supersonic turn, the constant α-profile is still used. Hence, also the optimal lateral guidance

for a supersonic turn was not studied. Further studies on optimal supersonic turns for winged re-entry vehicles are therefore recommended.

guidance law

During the acquisition phase, a bank command is given which is proportional to the vehicle's heading deviation from the tangent to the HAC:

$$\sigma_c = K_p(\chi_{req} - \chi) \tag{11.6}$$

in which χ is the actual heading of HORUS and χ_{req} is the required heading. The value for K_p is equal to 0.06109 rad/deg, which corresponds to the value as used in (Kluever, 2007). The input to the guidance law is the actual heading and the required heading, both expressed in degrees. The output is a bank angle expressed in radians.

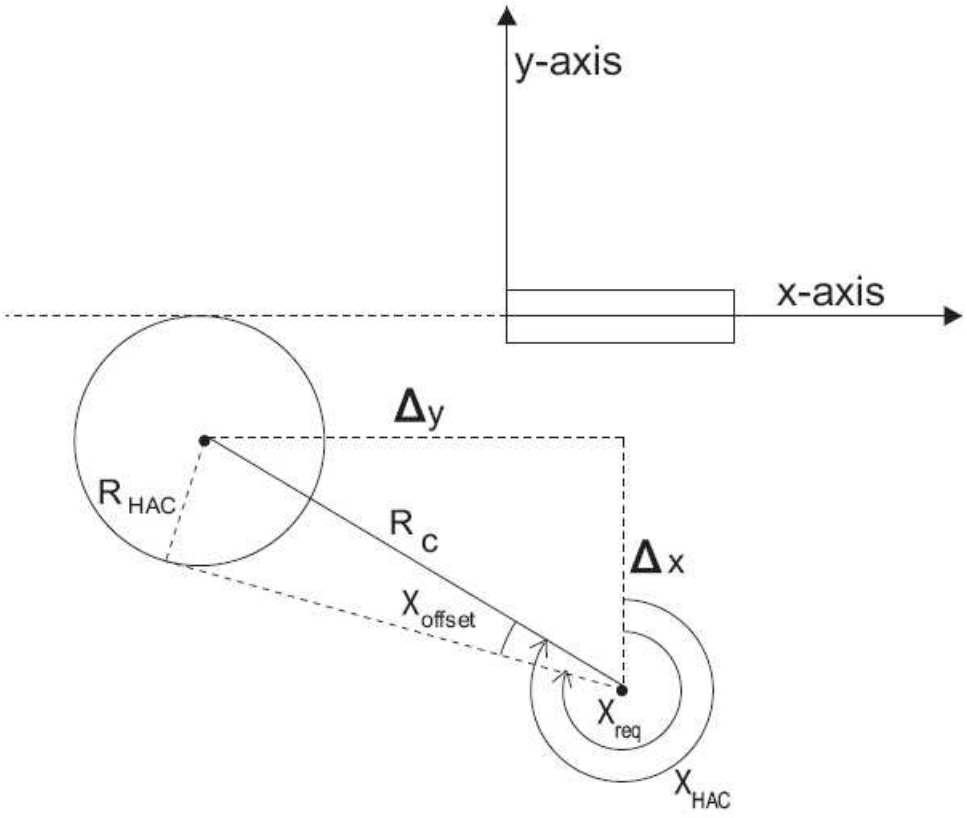

Figure 11.5: Geometry as used during the acquisition phase

calculation of the required heading

The required heading during the acquisition phase is the heading towards the correct tangent to the HAC. Figure 11.5 gives a schematic overview of the geometry during the acquisition phase to determine this required heading. The required heading angle is determined by equation 11.7 and equation 11.8, for respectively a HAC center with a negative y-coordinate requiring a left tangent and with a positive y-coordinate requiring a right tangent. Figure 11.5 presents the

geometry for a HAC center with a negative y-coordinate.

$$\chi_{req} = \chi_{HAC} - \chi_{offset} \tag{11.7}$$

$$\chi_{req} = \chi_{HAC} + \chi_{offset} \tag{11.8}$$

The offset angle χ_{offset} is the angle between the HAC tangent and the heading towards the center of the HAC. χ_{offset} can be calculated by:

$$\chi_{offset} = sin^{-1}(\frac{R_{HAC}}{R_c}) \tag{11.9}$$

The heading towards the HAC center is calculated using Δx and Δy, which are defined as:

$$\Delta x = x_{vehicle} - x_{HAC} \tag{11.10}$$

$$\Delta y = y_{vehicle} - y_{HAC} \tag{11.11}$$

For the geometry as presented in figure 11.5, a simple *tan* function would be sufficient to calculate the heading towards the HAC center. But for other positions of the vehicle with respect to the HAC center, this *tan* function results in incorrect headings due to quadrant ambiguities. To take quadrant information into account, a function or decision scheme is used based on the *atan2* function. Table 11.2 presents this scheme as used in this thesis study. Another problem is the definition of the heading angle as expressed in figure 11.6. Figure 11.6(a) presents the conventional coordinate axis and angle direction as used for trigonometric functions. The center of the coordinate system coincides with the HAC center and the angle is defined positive counterclockwise, starting from the x-axis. For the terminal area problem, the y-axis is directed to the North and the heading angle is defined positive clockwise starting from the y-axis, see figure 11.6(b). Hence, the calculation of the heading towards the HAC center is calculated in two steps. First, an intermediate angle χ_{int} is calculated in the coordinate system as defined in figure 11.6(a), using table 11.2. Then, this intermediate angle is transformed to the correct heading toward the HAC center, defined in the runway coordinate system, using the transformation equation:

$$\chi_{HAC} = -(\chi_{int} + 90^\circ) \tag{11.12}$$

Knowing both the offset angle and the heading towards the center of the HAC, χ_{req} can be calculated. Note that the shortest way to the tangent must be selected. This means that the required heading change is never larger than 180°.

Table 11.2: Function to resolve the problem of quadrant ambiguities for the determination of the heading toward the center of the HAC. n.a. = not applicable

		χ_{int}
$\Delta y > 0$	$\Delta x > 0$	atan($\Delta y/\Delta x$)
	$\Delta x < 0$	180° - atan(-$\Delta y/\Delta x$)
	$\Delta x = 0$	90°
$\Delta y < 0$	$\Delta x > 0$	-atan(-$\Delta y/\Delta x$)
	$\Delta x < 0$	atan($\Delta y/\Delta x$) - 180°
	$\Delta x = 0$	270°
$\Delta y = 0$	$\Delta x > 0$	0°
	$\Delta x < 0$	180°
	$\Delta x = 0$	n.a.

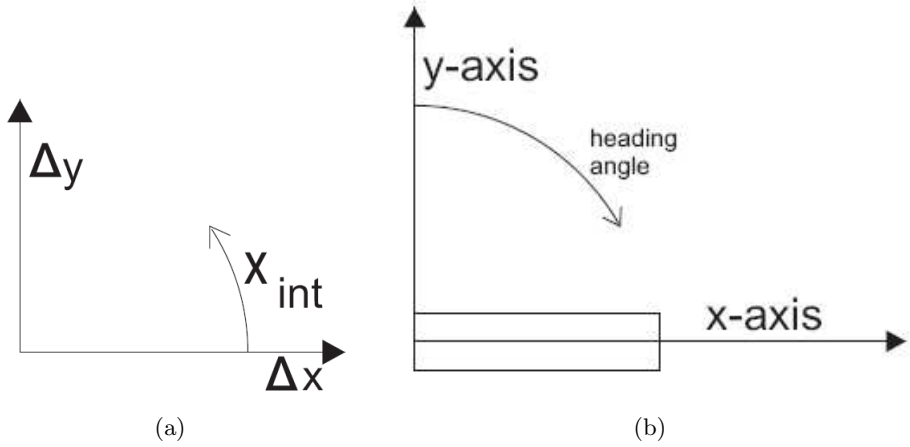

Figure 11.6: Definition of the measurement of an angle (a) conventional coordinate system used for trigonometric functions (b) runway coordinate system

11.2.5 Phase transitions

Based on the state of the vehicle and the position in the ground plane, phase transitions are initiated without using the second acquisition phase for a HAC overshoot:

- The terminal area is entered in the acquisition phase => TAEMphase 1
- if TAEMphase = 1 .and. $\Delta R < 500$ m .and. $\Delta\dot{R} < 20$ m/s => switch to heading alingment phase, TAEMphase = 2
- if TAEMphase = 2 .and. $85° < \chi < 95°$ => switch to pre-final phase, TAEMphase = 3

The transition criteria of $\Delta\dot{R} < 20$ m/s to switch to the heading alignment phase is used to reduce the input on the lateral guidance law. Since no input filter is used in this study, the unfiltered value of $\Delta\dot{R}$ is given to the guidance law which results in a peak in the bank angle at the switch to the heading alignment phase. The effect of a filter is that high input peaks with a high frequency are reduced to lower values. Instead of designing a filter, a more practical solution is used and the switch to the heading alignment phase is postponed until the value for $\Delta\dot{R}$ is reduced. But it is recommended that a input filter is designed for further studies.

If an overshoot is presents, additional phase transitions are used:

- if TAEMphase = 2 .and. $\Delta R > 500$ m => HAC overshoot, TAEMphase = 4
- if TAEMphase = 4 .and. $\Delta R < 500$ m .and. $\Delta\dot{R} < 20$ m/s => switch to heading alingment phase, TAEMphase = 2
- if TAEMphase = 4 .and. $85° < \chi < 95°$ => switch to pre-final phase, TAEMphase = 3

When the vehicle overshoots the HAC, a second acquisition phase is initiated. During this phase, HORUS has the possibility to directly enter the pre-final phase without entering the heading-alignment phase, if required.

11.3 Longitudinal nominal strategy

Till now, only the boundary capabilities of HORUS were discussed based on the maximum and minimum range longitudinal strategies. In the HAC planning algorithm, these strategies are used in combination with the lateral ground track geometry as described above. But when designing a HAC planner, one has to keep in mind that the winged re-entry vehicle is unpowered and has poor gliding capabilities. The vehicle has only one go to reach the runway and no fly-around is possible. The vehicle must be able to cope with off-nominal conditions, both at the start and during the terminal area. Therefore, flying at one of the boundary capability strategies is not a good idea. Instead, a nominal strategy must be used and hence, the HAC planner requires a nominal longitudinal strategy. This nominal strategy must be chosen such that it results in a trajectory in between the maximum range and maximum dive boundary capabilities. The vehicle must fly through the terminal area with sufficient margins left to dissipate more or less energy, if required.

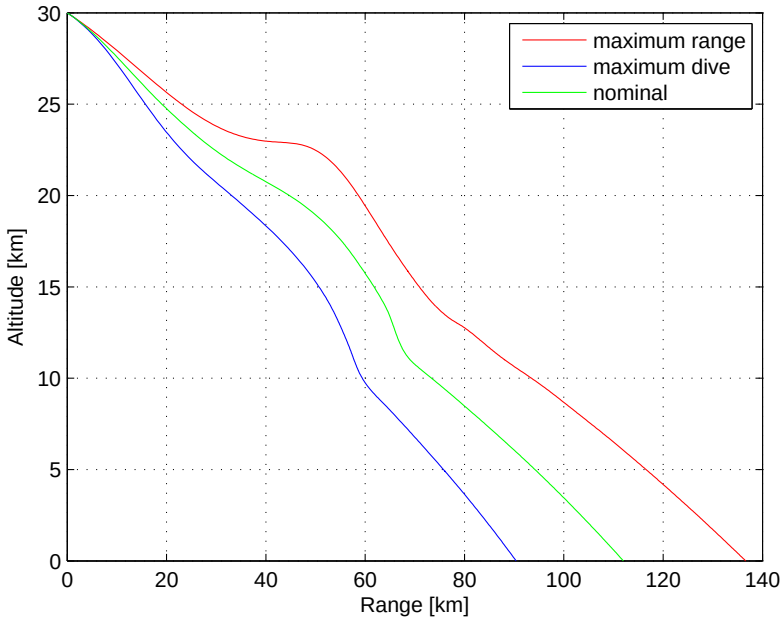

Figure 11.7: Range profiles for wings-level flights using a maximum range, a maximum dive and a nominal strategy.

The nominal strategy requires a reference dynamic pressure and a speedbrake setting in between the values used for the maximum and minimum range strategy. But several combinations of dynamic pressure and speedbrake setting might result in a trajectory in between the maximum range and maximum dive trajectories. Moreover, the energy dissipation is determined by both the steady-state drag levels and the transient maneuvers to intercept the reference dynamic pressure. Hence, the calculation of a combination of the reference dynamic pressure and the speedbrake setting is done by trial and error. The same control law and gains are used as for the maximum dive strategy, see chapter 9.

After several simulations, the reference equivalent airspeeds and speedbrake deflections as presented in table 11.3 gave satisfying results, both during a straight flight and during turning

Table 11.3: Reference equivalent airspeed and speedbrake deflection for the nominal strategy.

	Equivalent airspeed [m/s]	speedbrake deflection [deg]
subsonic	135.0	15.0
supersonic	120.0	0.0

flight around the HAC. Note that other combinations might be possible as well, but for the planning algorithm as described in this study, the values from table 11.3 will be used. Figure 11.7 shows three trajectories for a flight in the vertical plane. This figure indicates that the nominal strategy results in a trajectory and range in between the maximum range and maximum dive. Figure 11.9 shows the results when a HAC turn is included. In this figure an HAC radius of 5 km is used as an example. Also in this case, the nominal trajectory lies in between the maximum range and the maximum dive.

Next to the reference dynamic pressure and the speedbrake setting, the longitudinal control law also requires an open-loop angle of attack α^*. For a subsonic wings-level flight at the nominal strategy, α^* has a constant value of 5.5°. But for a subsonic turning flight and a supersonic flight, α^* is no longer a constant. Figure 11.8 indicates the calculated steady-state α^* values at the required equivalent airspeed or dynamic pressure and the speedbrake setting, as a function of the energy height. The figure presents data for a straight supersonic flight and a subsonic turning flight. The obtained data are stored by using a second-order polynomial. The coefficients are summarized in table 11.4.

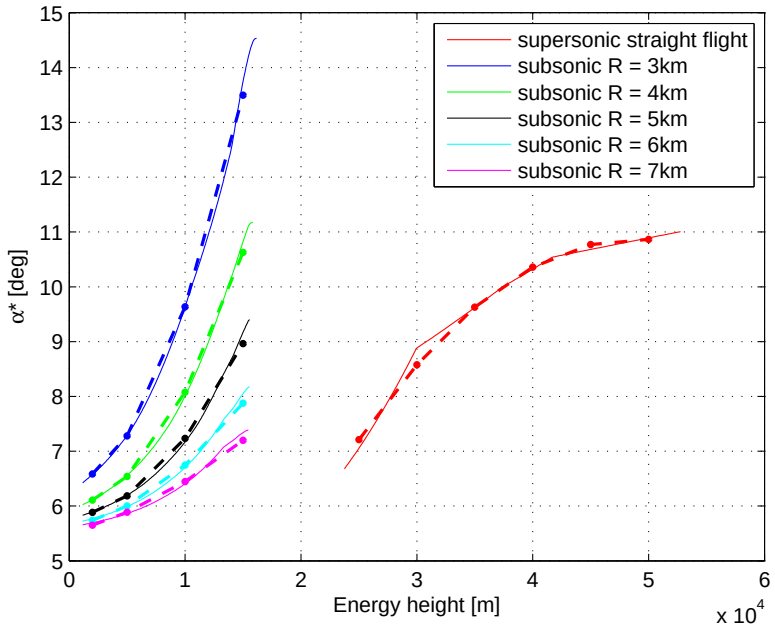

Figure 11.8: Open-loop angle-of-attack for a nominal strategy. DASHED lines indicate the approximations using a second-order polynomial. R = R_{HAC}

As a final note, consider table 11.5. It was already stated that the optimal turn trajectories obtained in chapter 7 only considers the optimal angle-of-attack profile (optimal longitudinal

Table 11.4: Coefficients to calculate α^* with a second-order polynomial

	c_1	c_2	c_3
supersonic	-6.3647·10^{-9}	0.0006237	-4.4023
subsonic R_{HAC} = 3km	3.0074·10^{-8}	2.0360·10^{-5}	6.4243
subsonic R_{HAC} = 4km	2.0344·10^{-8}	1.9135·10^{-6}	6.0225
subsonic R_{HAC} = 5km	1.3640·10^{-8}	4.9924·10^{-6}	5.8190
subsonic R_{HAC} = 6km	7.6209·10^{-9}	3.4824·10^{-5}	5.6378
subsonic R_{HAC} = 6km	3.9373·10^{-9}	5.2345·10^{-5}	5.5286

strategy) such that for a specific HAC radius, the minimal energy is dissipated during the turn. The combination of the angle of attack and the HAC radius, which results in the minimum energy dissipation was not considered. Table 11.5 presents the obtained ranges after a HAC turn using the maximum range strategy, for different HAC radii. Each center of the HAC has a fixed x-coordinate of -8 km. The same initial state is used for the simulations, i.e., h_0 = 30 km, V_0 = 661.64 m/s and γ_0 = -10°, respectively. The ground track geometry is similar to the one indicated in figure 11.9. The results from table 11.5 indicate that the radius does have an influence on the obtained range. From the listed radii, a HAC radius of 4 km gives the best result in terms of traveled distance after the HAC or minimum energy dissipation during the HAC. This is in line with the discussion at the end of chapter 6. A larger bank angle results in a larger instantaneous drag level. A larger turn radius than the optimal radius requires a lower bank angle and hence results in a lower instantaneous drag and energy dissipation. But due to the larger turn radius, the distance around the HAC and hence the interval in which energy is dissipated, increases. This results in a lower obtained range after the turn. For a lower turn radius than the optimal radius, the distance around the HAC decreases but the instantaneous drag increases due to the increased required bank angle. Table 11.5 indicates that there is an optimal balance between the range around the HAC or the interval in which energy is dissipated and the instantaneous drag corresponding to the required bank angle for a particular turn radius.

Table 11.5: Ranges after a HAC turn for different HAC radii. Results are presented for both a longitudinal maximum range strategy and a longitudinal nominal strategy. The center of the HAC has a fixed x-coordinate of -8 km.

HAC radius [km]	**maximum range strategy [km]**	**nominal strategy [km]**
3	36.25	14.58
4	36.91	14.75
5	36.70	14.15
6	36.15	13.39
7	35.34	12.57

11.4 Working principle of HAC planner

The goal of the HAC planning algorithm is to determine the best position of the HAC center, such that the vehicle enters the terminal area with the maximum possible of margin to dissipate more or less energy during the rest of the terminal area. Hence, the HAC position is calculated

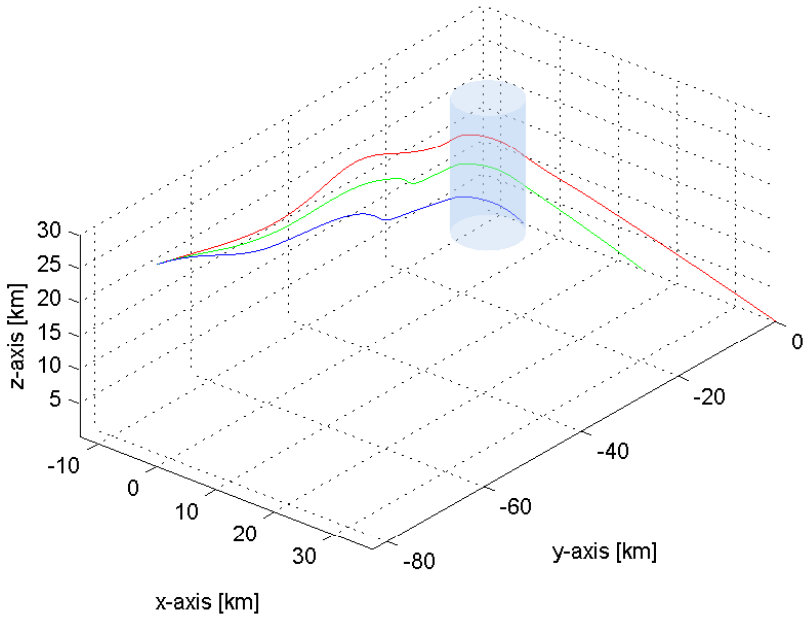

Figure 11.9: Flight trajectories including a HAC turn with a radius of 5 km, using a maximum range, a maximum dive and a nominal strategy. RED = maximum range; BLUE = maximum dive; GREEN = nominal

at the beginning of the terminal area phase while in the terminal area, energy is controlled by deviating from the nominal longitudinal strategy. The planning algorithm must calculate a HAC position such that when the maximum and minimum range boundaries are plotted in the energy space, the initial state is situated in the middle of these boundaries. This leaves enough margin left to anticipate to situations that require more or less energy dissipation. The working principle of the HAC planner is based on the energy tube concept by shifting the HAC until the initial state is situated in between the capability boundaries.

Figure 11.11 presents a flow diagram of the HAC planning algorithm. The two HAC planning parameters, x_{HAC} and y_{HAC}, are computed by iteration and trajectory propagation. A fixed grid of possible HAC positions is used. Using a nested do-loop method, all HAC positions are evaluated. For a single HAC position, three trajectories are calculated: a maximum range trajectory, a maximum dive trajectory and a nominal trajectory. Based on these trajectories, the feasible, nominal and optimal HAC positions are updated. After the evaluation of all possible HAC positions, the best or optimal HAC position is obtained for a particular initial state. Below, more information is given on several aspects of the planning algorithm.

grid of possible HAC positions

Similar to (Kluever, 2007), a fixed interval of possible parameter values is used, all the combinations are evaluated and the best combination is selected. For this study, the following intervals are selected for the planning parameters:

$$x_{HAC} = [-7.0km \ -20.0km] \tag{11.13}$$

$$y_{HAC} = [3.0km \ 7.0km], [-3.0km \ -7.0km] \tag{11.14}$$

The step size in between these boundary values is set to 0.5 km. Hence, a total of 486 combinations are possible. Figure 11.10 shows all the possible HAC center positions using these intervals and step sizes. This figure indicates two HAC center grids. In the energy management analysis as described in the next chapter, only terminal area entry points are used with a negative y-coordinate. Hence, a HAC in the upper grid corresponds to an overhead approach, while a HAC in the lower grid requires a direct approach. Note that the grids are only placed at one side of the runway. In reality, the grids could also be placed on the other side, depending on the wind conditions. In this study, it is assumed that the vehicle's heading during landing is 90°.

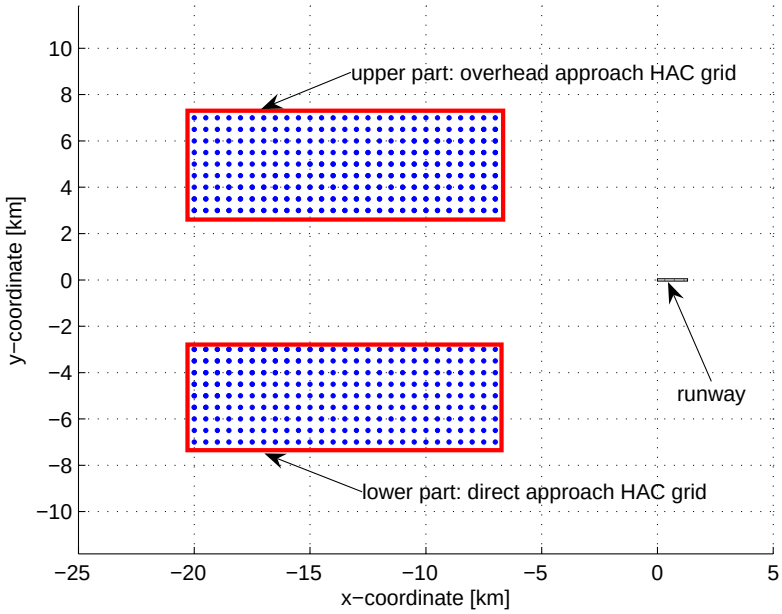

Figure 11.10: Possible positions of the HAC center.

Cost function

The best HAC position is determined by evaluating the state of the vehicle when it touches the ground. Normally, the terminal area is terminated at ALI and the goal is to find a trajectory that brings the vehicle to the nominal ALI. Then, a trajectory from this nominal ALI must be calculated for the approach and landing phase. In (Hull et al., 2005), it is stated that under certain off-nominal conditions, this requirement of passing through the nominal ALI point is an overly-limiting constraint that makes it more difficult to find feasible solutions. A better option is to combine the TAEM segments to form a single trajectory. Also in (Helmersson, 1988b), the trajectory is continued until the vehicle reaches the ground. Hence, in this study, the pre-final phase of the TAEM is combined with the final approach and landing phase, but no flare maneuvers are taken into account.

The cost function consists of the state of the vehicle and the final position in the ground plane, with respect to the runway threshold. For a single HAC position, three cost functions are calculated using the maximum-range strategy, the maximum-dive strategy and the nominal strategy.

- **maximum range strategy**
  If the vehicle overshoots the runway threshold and aligns with the extension of the runway centerline with the correct heading, the current HAC position is feasible in terms of maximum range that can be achieved by HORUS.
- **maximum dive strategy**
  If the vehicle undershoots the runway threshold, the current HAC position is feasible in terms of minimum range that can be achieved by HORUS.
- **nominal strategy**
  If the vehicle aligns with the extension of the runway threshold with the correct heading, the current HAC is feasible. The x-coordinate of HORUS when it touches the ground determines how optimal the current HAC position is.

Feasible, nominal and optimal HAC

Based on the three cost functions, a distinction is made between a feasible, a nominal or an optimal HAC:

- **Feasible HAC**
  A feasible HAC is a HAC position which yields both a feasible maximum range and a maximum dive. The HAC as indicated in figure 11.9 is a feasible HAC. Using the maximum range strategy, the vehicle overshoots the runway threshold (situated in the origin of the coordinate system), while using a maximum dive strategy, the vehicle undershoots the runway threshold. The runway threshold is situated in between the range capabilities of the vehicle. In between the boundary capabilities, there is a longitudinal strategy which results in a trajectory that exactly reaches the runway threshold.
- **Nominal HAC**
  If a HAC is feasible, then a trajectory is calculated using the nominal strategy. If the vehicle is aligned with the extension of the runway threshold with the correct heading and if the final x-coordinate is situated between [-500m 500m], then the current HAC position is a nominal HAC.
- **Optimal HAC**
  If a HAC position results in a final point of the nominal trajectory closer to the runway threshold, the best HAC position is updated. After the complete HAC grid has been searched, the overall best or optimal HAC position is obtained. The optimal HAC is the HAC that results in the nominal trajectory with a final position as close as possible to the runway threshold.

Trajectory calculation

The trajectories are calculated using the lateral guidance laws as described earlier in this chapter and the longitudinal guidance laws from chapter 9. The trajectory propagation is done using the RK45 integrator. The vehicle model as described in chapter 3 is used in combination with the equations for the translational motion with respect to a rotating Earth and the US76 model for the atmosphere. When the proposed HAC planning algorithm is to be used in an on-board system, simplifications in the models and a simpler integrator must be used. But for the current purpose of the analysis on the energy management capabilities, the more complex planner can

be used. Even with this planner using the more complex building blocks, it takes less than 30 seconds to calculate an optimal HAC position for a particular initial state.

constraints

The HAC planning algorithm must take into account several path constraints:

- dynamic pressure boundaries (minimum and maximum boundaries), see chapter 3
- α and σ limits, including rate of change limits, see chapter 3
- load factor < 2.5
- M < 0.95 at start of HAC

The first two constraints do not have to be monitored during the HAC planning because they are already taken into account in the design of the guidance laws. Due to the choice of the reference dynamic pressures, nor the minimum nor maximum dynamic pressure boundaries are violated. Filters are incorporated such that the absolute values and the rate of change values of α_c and σ_n do not cross the boundaries. The last two constraints are monitored during the HAC planning. If these constraints are violated during a maximum range, maximum dive or nominal trajectory for a particular HAC, then that HAC is eliminated from the possible HAC positions.

The net result of the complete HAC planning algorithm is that the HAC is shifted until the final point of the trajectory using the nominal longitudinal strategy is as close as possible to the runway threshold. By doing so, the runway is situated in the middle between the maximum range and minimum range that can be achieved by HORUS. In the energy space, this corresponds to a shift of the energy tube cross-section such that the initial state is situated in the middle of the maximum-range and maximum-dive boundary. This leaves sufficient margin to dissipate more or less energy by adapting the longitudinal strategy if required by off-nominal conditions that occur during the rest of the terminal area.

In the next chapter, the planning algorithm, as described in this chapter, is used to analyze the energy management capabilities in both nominal and off-nominal conditions. Also, the shift in the energy tube cross-section will there be discussed in more detail.

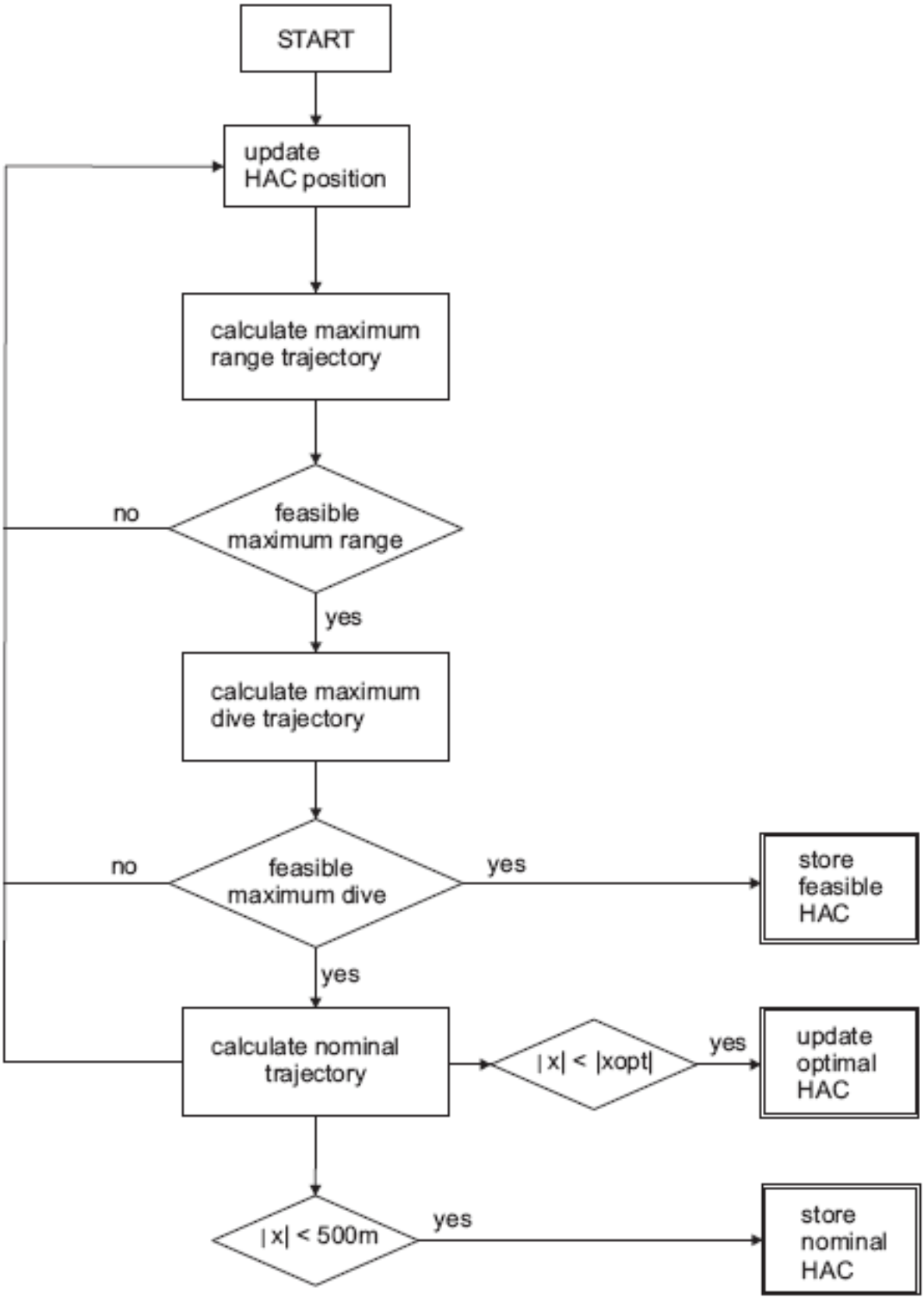

Figure 11.11: Flow diagram of HAC planning algorithm

Chapter 12

Analysis results of energy management capabilities

The previous chapter describes a HAC planning algorithm based on the energy tube concept. In this chapter, the HAC planning algorithm is used to investigate the energy management capabilities of a winged re-entry vehicle, HORUS, in case of both nominal and off-nominal conditions. The more conditions HORUS can handle, the larger the Terminal Entry Gate (TEG).
Section 12.1 describes the output of the planning algorithms for the nominal terminal entry point, the nominal energy tube cross-section and the nominal trajectory. The influence of initial energy variations, heading variations and flight path angle variations are described in section 12.2, 12.3 and 12.4, respectively. In these sections, the influence of change of a single parameter is investigated. Section 12.5 describes the influence of a combination of several parameter changes. The output of the planning algorithm for different initial positions on the terminal area entry circle is described in section 12.6. Section 12.7 gives an overview of possible applications of the energy tube concept base HAC planning algorithm.

12.1 Nominal Terminal Area entry point

In the nominal reference case, HORUS starts the Terminal Area Phase 83 km from the runway at an altitude of 25 km (Mooij, 1998) and with a velocity of 732.0 m/s (Helmersson, 1988b).
It is common to approach the runway in a direction that is perpendicular to the runway centerline, see (Helmersson, 1988b), (Kluever & Horneman, 2005) and (Mooij, 1998). Using an initial negative y-coordinate (-83 km), a zero x-coordinate and a nominal initial heading toward the runway centerline results in $\chi_0 = 0$ (or 360°). γ_0 is set to -10.0°.

In summary, the nominal initial states are:

- x-coordinate: 0.0 km
- y-coordinate: -83.0 km
- z-coordinate: 25.0 km

- velocity: 732.0 m/s
- flight-path angle: -10°
- heading angle: 0°

12.1.1 HAC planning output

The output of the HAC planning algorithm in terms of feasible, nominal and optimal HAC positions is shown in figure 12.1.

The blue dots indicate all the feasible HAC center positions. It is interesting to see that for the nominal TAEM entry point, no feasible HAC positions are available in the top left part of the grid. Using the maximum range strategy, a HAC situated in that part results in an undershoot of the runway threshold. The maximum range capabilities of the HORUS are insufficient to use a HAC situated in the top left part the grid.

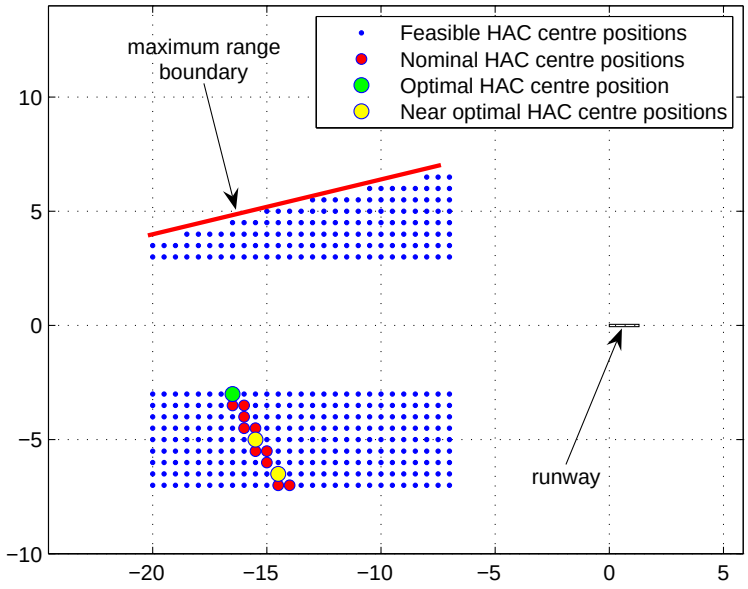

Figure 12.1: Heading Alignment Cylinder center positions for the nominal TAEM entry point

The green dot indicates the optimal HAC position as found by the planning algorithm. Using this HAC position and the nominal longitudinal strategy, the difference between the final x-position of HORUS and the runway threshold is only 21.97 m. There were also two other HAC position which gave a final x-coordinate close to the runway threshold, see table 12.1. These HAC positions are indicated in figure 12.1 by two yellow dots. Relatively large changes in HAC position results in only minor changes of the final x-coordinate. Taking small calculation errors into account, using only one optimal HAC position is not suitable to study the influence of changing conditions on the optimal HAC position. So rather than only specifying one HAC position as 'the optimal', it is better to indicate a 'region of nominal HAC positions' which result in a final position close to the runway threshold. This nominal HAC region is shown in

figure 12.1 by the red dots (and green and yellow dots). All the trajectories using the nominal longitudinal guidance and the HAC centers indicated by the region of nominal HAC positions, yield a trajectory with a final x-coordinate within a distance of 500.0 m of the runway threshold. By using a 'nominal HAC region', it is possible to study the influence of changes in the initial state on the shifting of this region within the grid.

The geometry of the nominal HAC positions can be explained by the range around the HAC. The larger the HAC radius, the larger the range around the HAC and hence, the HAC must be situated closer to the runway to yield a more or less equal total terminal area range than for a HAC with a lower radius. The influence of the optimal turn radius, as described in section 11.3, cannot be distinguished in the geometry, as the influence is too small.

Table 12.1: HAC positions which result in a final x-coordinate close to runway threshold for nominal TAEM entry

x_{HAC} [km]	y_{HAC} [km]	R_{HAC} [km]	$\lvert\Delta x\rvert$ [m]
-16.5	-3.0	3.0	21.9
-15.5	-5.0	5.0	64.4
-14.5	-6.5	6.5	85.4

12.1.2 Energy tube cross-section

Knowing the optimal HAC position, it is possible to calculate all combinations of altitude and velocity for which is possible to reach the runway threshold, using the obtained optimal HAC position. These combinations define the cross-section of the energy tube for that particular point in the ground plane (x =0.0 km, y = -83 km). This cross-section is calculated for the heading angle, flight path angle, x-coordinate and y-coordinate as specified above.

Figure 12.2 shows the obtained energy tube cross-section and the nominal TAEM entry point. This figure indicates that the nominal entry point is situated in the middle between the upper and lower boundary of cross-section defined by the maximum dive and maximum range capabilities of HORUS, respectively. By modifying the HAC position, the HAC planning algorithm shifts the boundaries of the maximum range and dive boundaries of the cross-section until the nominal entry point is situated in the middle of the cross-section. This allows HORUS to adapt to changes in flight condition during the rest of the terminal area, both in situations that require higher or lower energy dissipation, by adjusting the longitudinal strategy (angle of attack and speedbrakes).

Initial states which are situated on the maximum range boundary require the maximum range strategy to reach the runway threshold, while initial states situated on the maximum dive boundary will require the maximum-dive strategy to prevent overshooting the runway. An initial combination of altitude and velocity situated above the maximum dive boundary, will overshoot the runway threshold using the current HAC position, while a initial combination situated below the maximum range boundary will not reach the runway threshold.

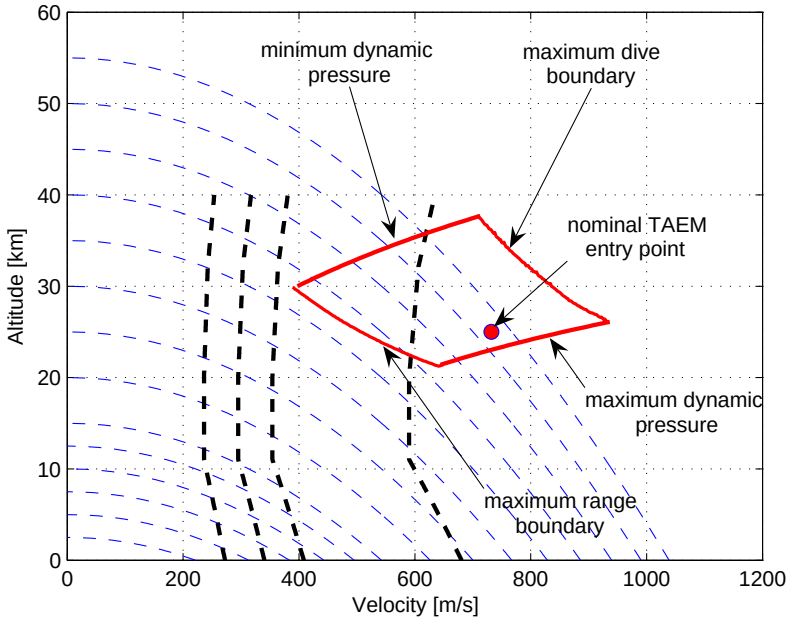

Figure 12.2: Energy tube cross-section for the nominal TAEM entry point. DASHED BLACK lines indicate Mach boundaries (0.8, 1.0, 1.2 and 2)

12.1.3 Nominal reference trajectory

Figure 12.3 shows the nominal trajectory for the nominal terminal area entry point. The runway threshold is situated on the origin of the reference frame. A vertical bar is given at a 20 seconds interval. The total flighttime for the terminal area down to touching the runway threshold is 383.0 seconds (6.4 minutes). The actual ground track as flown by HORUS has a length of 103.86 km.

The control history, angle of attack and bank angle, is shown in figure 12.4.
initially, the bank angle is set to its maximum of 30° in the acquisition phase in order to align with a tangent to the HAC. After 237 seconds, the HAC is reached. During this HAC phase, the bank angle if first equal to its maximum value of 60 degrees, followed by a decrease after which it increases again. As already explained, this behavior indicates an initial small overshoot of the HAC, followed by a second acquisition and a HAC tracking without overshoot.
The angle-of-attack profile shows that after the transonic phase with constant angle-of-attack, a subsonic straight flight occurs before the HAC is reached. In order to reach the nominal equivalent airspeed of 135.0 m/s, first a dive followed by a pull-up maneuver is required. Also the influence of the bank maneuver on the nominal angle of attack is clearly visible.
The speebrake deflection is not plotted. Until the Mach number reaches a value of 0.95, the speedbrakes are not used and are fully retracted. After the Mach number reaches 0.95, the speebrakes are partially deployed and are set to 15°.

The velocity and the flight-path angle for the nominal entry point are indicated in figure 12.5. The velocity at the end of the flight is equal to 135.0 m/s, which corresponds to the nominal equivalent airspeed in a straight flight. For the subsonic straight flight towards the HAC and during the prefinal, the flight path angle is only slowly decreasing. The HAC turn is clearly

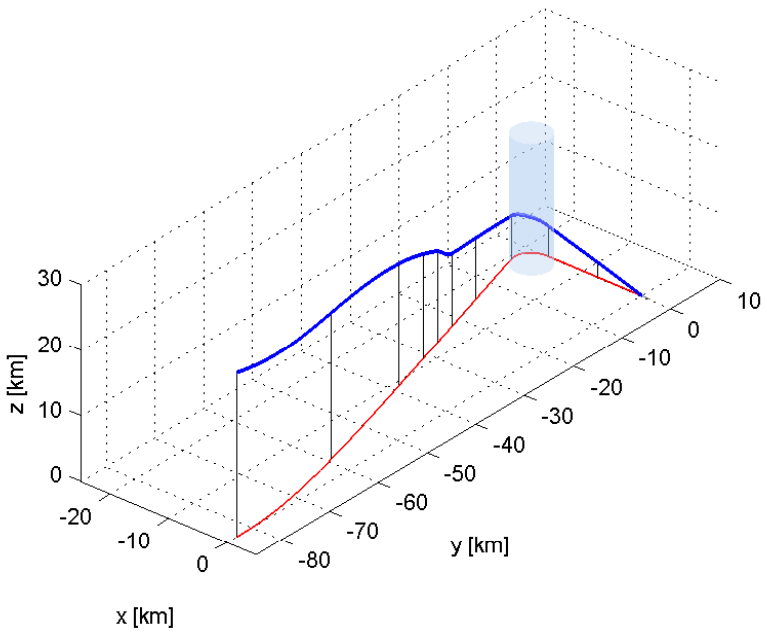

Figure 12.3: 3-D reference trajectory for the nominal TAEM entry point

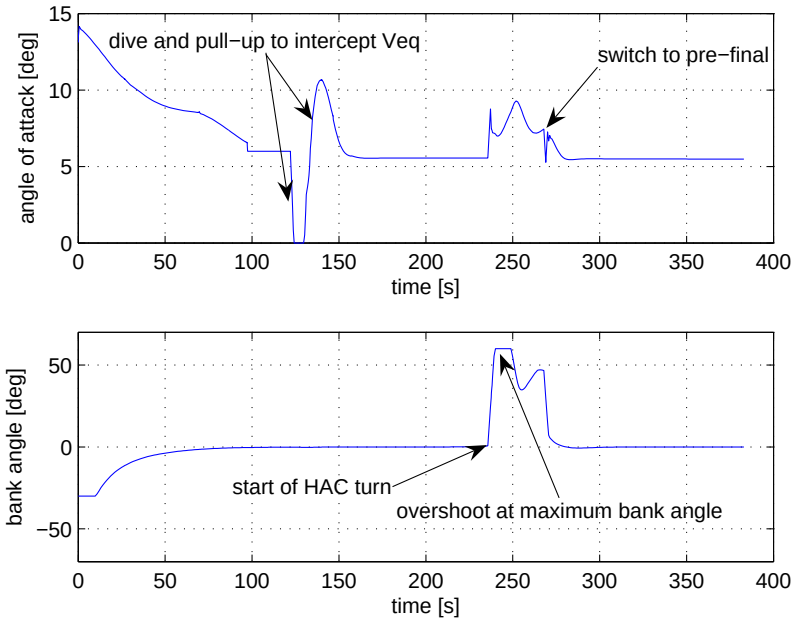

Figure 12.4: Angle-of-attack and bank angle history for the nominal TAEM entry point

visible in the flight path-angle profile as a jump, increasing the flight path angle to more than 20°.

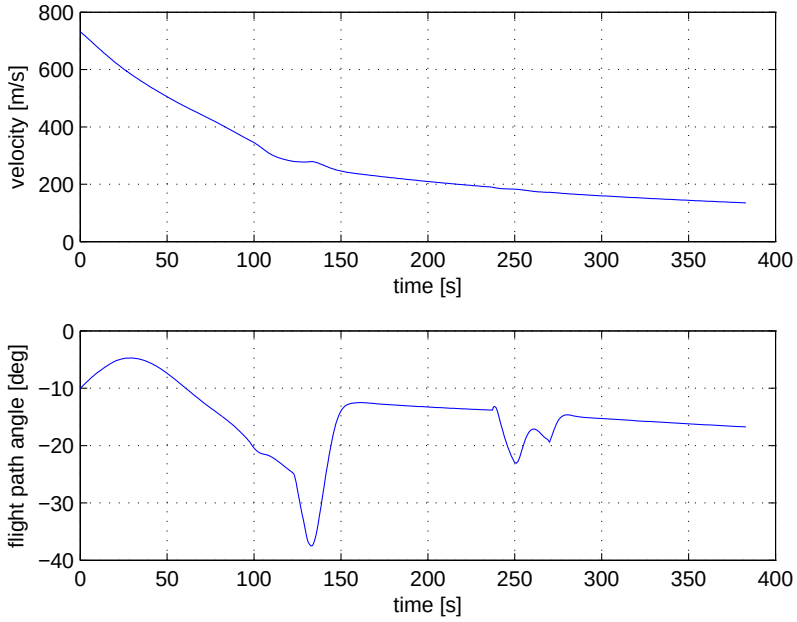

Figure 12.5: Velocity and flight path angle history for the nominal TAEM entry point

12.2 Initial energy variations

This section describes the influence on the HAC position due to changes in the initial energy, i.e., both high and low energy cases. Because of the position of the nominal entry point in the energy space, high energy cases will be achieved by increasing the altitude, while low energy cases are obtained by lowering the velocity to prevent exceeding the maximum-dynamic pressure boundary.

12.2.1 High energy case by increasing altitude

Three simulations with an increased altitude were performed. The altitude is increased with steps of 2.5 km. The values for the x-coordinate, y-coordinate, velocity, flight path angle and heading angle are equal to ones used as the nominal entry point. The obtained optimal HAC positions with the HAC planning algorithm are shown in table 12.2.

Table 12.2: Optimal HAC positions for 3 TAEM entry point with High Energy

	altitude [km]	x_{HAC} **[km]**	y_{HAC} **[km]**	$\lvert\Delta x\rvert$ **[m]**
HE case 1	27.5	-7.5	3.5	35.8
HE case 2	30.0	-8.5	4.5	73.2
HE case 3	32.5	-15.5	3.5	2.7

The HAC planning algorithm copes with energy and altitude variations by modifying the HAC. Figure 12.6 shows the nominal trajectory, ground track and calculated HAC position for an initial altitude of 30.0 km. The HAC is now situated at the other side of runway such that an

overhead approach is required. The ground track distance covered by HORUS is now equal to 117.15 km. The overhead approach elongates the ground track, enabling HORUS to dissipate more energy. Also, the ground track distance of the HAC phase is longer, which means that HORUS is in a banked situation for a longer period of time with respect to the situation of the nominal terminal area entry point.

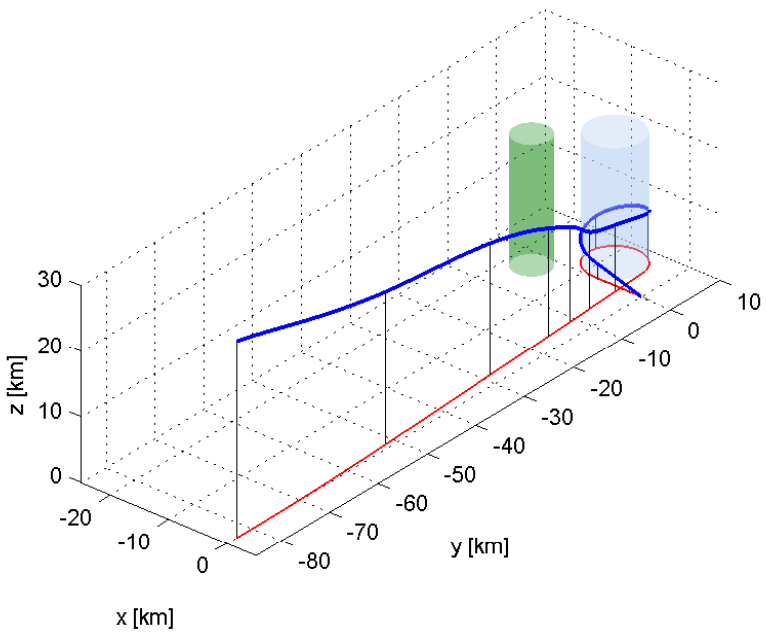

Figure 12.6: 3-D reference trajectory for an energy high situation; alt = 30 km. The green HAC is the optimal HAC for the nominal terminal area entry point

Figures 12.7(a), 12.7(b) and 12.7(c) show the feasible, nominal and optimal HAC positions for an initial altitude of respectively 27.5 km, 30.0 km and 32.5 km. Comparing these figures with the nominal entry point, see figure 12.1, it is possible to indicate and discuss general trends in the variation of feasible and nominal HAC positions.

Influence on feasible HAC positions

In the nominal case, the region of feasible HAC positions is bounded by the maximum range boundary, situated in the top left part of the HAC grid. If a HAC position is selected beyond this boundary, the maximum-range capability of HORUS is insufficient to reach the runway. If the energy is increased, this maximum-range boundary is shifted higher to the left top corner. This means that there are more feasible HAC positions for which the maximum-range capability is sufficient to reach the runway. For an initial altitude of 32.5 km, all the HAC positions in the upper part of HAC grid (positive y-coordinate) are available and there is no longer a maximum-range boundary.

At an initial altitude of 30 km, two new boundaries appear: the maximum dive boundary and a Mach = 0.95 boundary. If a HAC position is selected beyond the maximum-dive boundary, the maximum-dive capability of HORUS is insufficient, and HORUS will overshoot the runway threshold. Increasing the energy shifts the maximum-dive boundary downward, to the

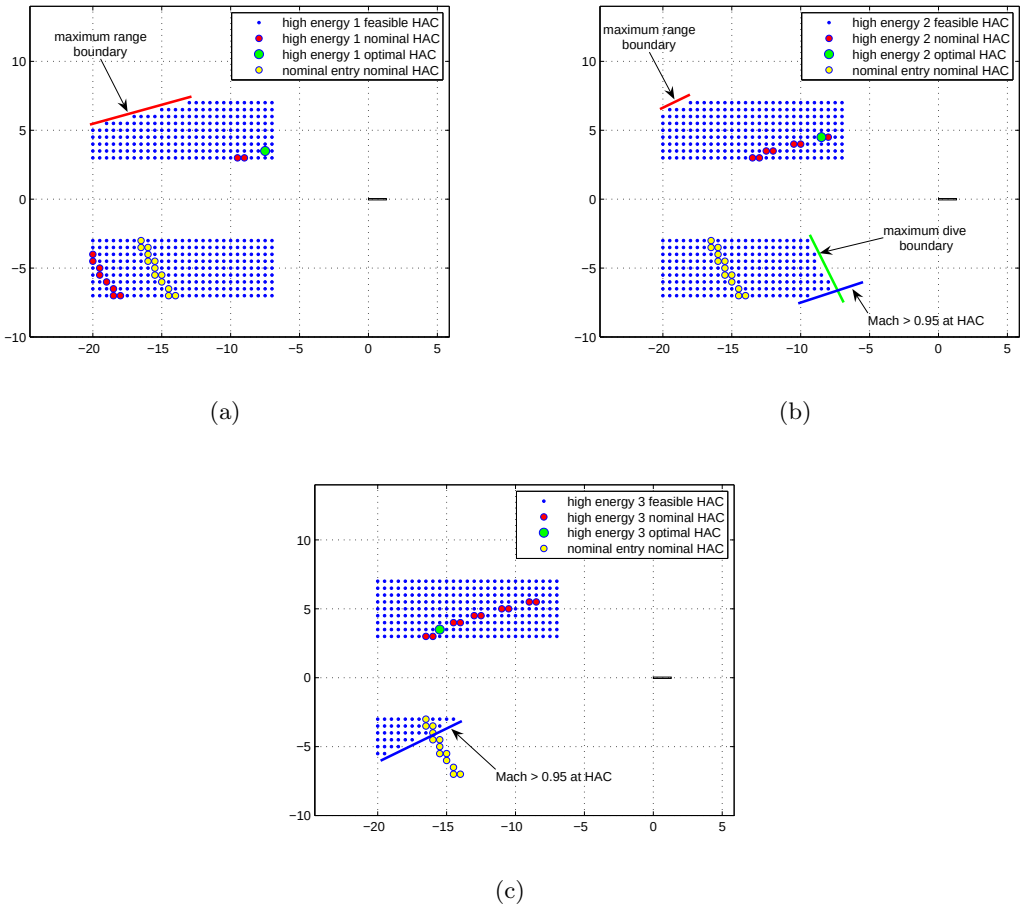

Figure 12.7: Heading Alignment Cylinder center positions for high energy (a) altitude 27.5 km (b) 30.0 km (c) 32.5 km

left corner of the lower part of the HAC grid. Selecting a HAC position beyond the Mach = 0.95 limit results in a trajectory that reaches the HAC at a velocity higher than Mach 0.95. Increasing the energy shifts this boundary upward to the left corner of the lower part of the HAC grid. Note in figure 12.7(c) that for an altitude of 32.5 km, the Mach = 0.95 boundary is dominant, while the maximum dive boundary is situated outside the Mach = 0.95 boundary and hence is not visible.

Influence on nominal HAC positions

The HAC planning algorithm copes with an initial energy increase by increasing the ground track. This is visible in the moving pattern of the nominal HAC positions as the energy is increased. Increasing the altitude to 27.5 km results in downward shift of the nominal HAC positions to the left lower corner of the lower part of the HAC grid, but it also result in three nominal HAC positions which appear in the right lower corner of the upper part of the HAC grid. Both regions result in an increased ground track with respect to the nominal HAC positions for the nominal entry point. If the energy is further increased, no nominal HAC positions appear any more in the lower part of the HAC grid. The nominal points in the upper part of the HAC grid shift upward to the upper left corner of the upper part of the HAC grid.

The most dominant effect of an increased energy on the nominal HACs and therefore, on the optimal HAC, is the larger resulting ground track by shifting the complete nominal HAC area. The influence of the optimal turn radius within this nominal HAC area, as discussed in section 11.3, cannot be distinguished. Again, the effect of the change in radius is too small.

Influence on energy tube cross-section

Figures 12.7(a), 12.7(b) and 12.7(c) also indicate that the original optimal HAC position for the nominal entry point is still a feasible HAC position for all the three cases of high initial energy. But if this HAC would be used in case of an energy high situation, it would be no longer possible to fly at the nominal longitudinal strategy. A strategy with a higher energy dissipation (closer to maximum dive strategy) would be required in order to reach the runway threshold without overshoot.

This is also indicated by the energy tube cross-section, see figure 12.8. The blue dot represent an high energy case (30 km altitude). If the optimal HAC position for the nominal entry is used, which has a corresponding energy tube cross-section boundary represented by the red line, the new energy high case (blue dot) is close to the maximum dive capabilities. This is undesirable, because HORUS would have a smaller capability to react to off-nominal conditions that would require a strategy with more energy dissipation. Therefore, the planning algorithm shifts the HAC position until the new initial state is again in the middle of the maximum dive and maximum range capabilities and energy tube cross-section boundaries. By changing the HAC, the planning algorithm assures that HORUS has maximum of capabilities to react to both situations that would either require more or less energy dissipation during the rest of TAEM flight. The minimum-dynamic pressure and the maximum-dynamic pressure boundaries do not change.

Another advantage of an adaptive HAC configuration is the increase of the total cross-section of the energy tube. Figure 12.8 shows that by using two possible HAC positions, the effective total cross-section is increased with respect to one fixed HAC position. A variable HAC position means that more initial conditions can be handled by HORUS.

Hence, figure 12.8 indicates that a variable HAC position has two advantages:

- It enables HORUS to start the TAEM phase in the 'middle' of the energy tube such that HORUS can react to both off-nominal reactions that would require more or less energy dissipation.
- The effective total energy tube cross-section is larger than for a single HAC position.

12.2.2 Low energy case by decreasing velocity

Three simulations with a decreased velocity were performed. The velocity was decreased with steps of 40 m/s. The values for the altitude, x-coordinate, y-coordinate, flight path angle and heading angle are equal to ones used for the nominal entry point. Table 12.3 gives the obtained optimal HAC positions for the three energy low cases.

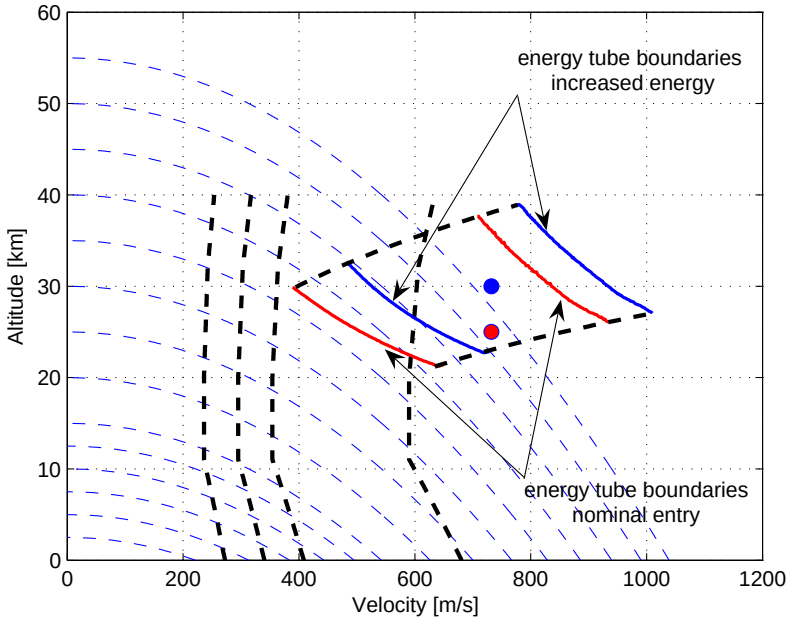

Figure 12.8: Energy tube cross-section for the nominal TAEM entry point and energy high situation. The red dot indicates the nominal entry point, while the blue dot indicates an entry point with a higher energy (alt = 30 km).

Table 12.3: Optimal HAC positions for 3 TAEM entry point with Low Energy

	velocity [m/s]	x_{HAC} **[km]**	y_{HAC} **[km]**	$\|\Delta x\|$ **[m]**
LE case 1	692.0	-11.0	-7.0	24.36
LE case 2	652.0	-9.0	-5.0	65.15
LE case 3	612.0	-7.0	-3.0	113.01

Figure 12.9 shows the nominal trajectory, ground track and calculated HAC position for an energy low case with an initial velocity of 652.0 m/s. The HAC is now situated closer to then runway than for the nominal terminal area entry point. This decreases the ground track distance to a value of 96.28 km and hence, the total energy dissipation is decreased. The HAC planning algorithm copes with low energy cases by adjusting the HAC positions such that the ground-track distance is shortened in order to dissipate less energy.

Figure 12.10(a), 12.10(b) and 12.10(c) show the feasible, nominal and optimal HAC positions for an initial velocity of 692.0 m/s, 652.0 m/s and 612.0 m/s respectively. Comparing these figures with the nominal entry point, it is possible to discuss general trends in the movement of the feasible and nominal HAC positions.

Influence on feasible and nominal HAC positions

In case of an energy-low situation, the feasible HAC positions are only bounded by the maximum-range boundary. The maximum-range capability of HORUS determines the feasible HAC positions. The maximum dive capability of HORUS is always sufficient and not critical in low-energy cases. If the initial energy is decreased, the maximum range boundary is shifted to the right

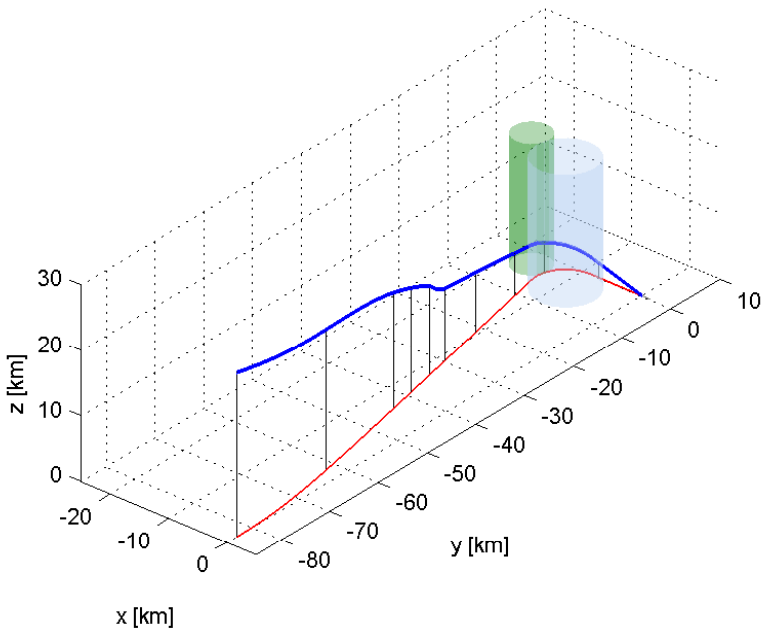

Figure 12.9: 3-D reference trajectory for an energy low situation; v = 652.0 m/s. The green HAC is the optimal HAC for the nominal terminal area entry point

lower corner of the upper HAC grid. This means that there are less possible HAC positions in the upper HAC grid for which the maximum-range capability of HORUS is sufficient to reach the runway.

The moving pattern of the nominal HAC positions show that the planning algorithm copes with an energy-low case by decreasing the ground track distance. If the energy is decreased, the nominal HAC positions are shifted to the left part of the lower HAC grid. Figure 12.10(c) shows that for an initial velocity of 612.0 m/s, there are only four nominal HAC positions available. If the velocity is decreased even further, no more nominal HAC positions are available without adapting the HAC grid.

Influence on energy tube cross-section

Similar to the high energy situations, the HAC position corresponding with the nominal entry point is still a feasible HAC position in all three low energy cases. But if this HAC would be used, than it would no longer be possible to fly at the nominal longitudinal strategy. A strategy with less energy dissipation (closer to the maximum range strategy) would need to be used. Figure 12.11 shows the energy tube cross-section boundaries (red lines) for the HAC position corresponding to the nominal entry point (red dot) and the low energy situation (blue dot). The low energy situation is situated closer to the maximum range boundary and hence requires less energy dissipation with respect to the nominal strategy in order to reach the runway. As before, this is undesirable, because HORUS would have a smaller capability to react to off-nominal conditions. Therefore, the HAC planning algorithm shifts the HAC position, and hence the boundaries of the energy tube, such that the nominal longitudinal strategy can be used. The adapted boundaries of the energy tube cross-section corresponding to the HAC position for the low energy case, are shown by the blue lines. The HAC position is chosen such that

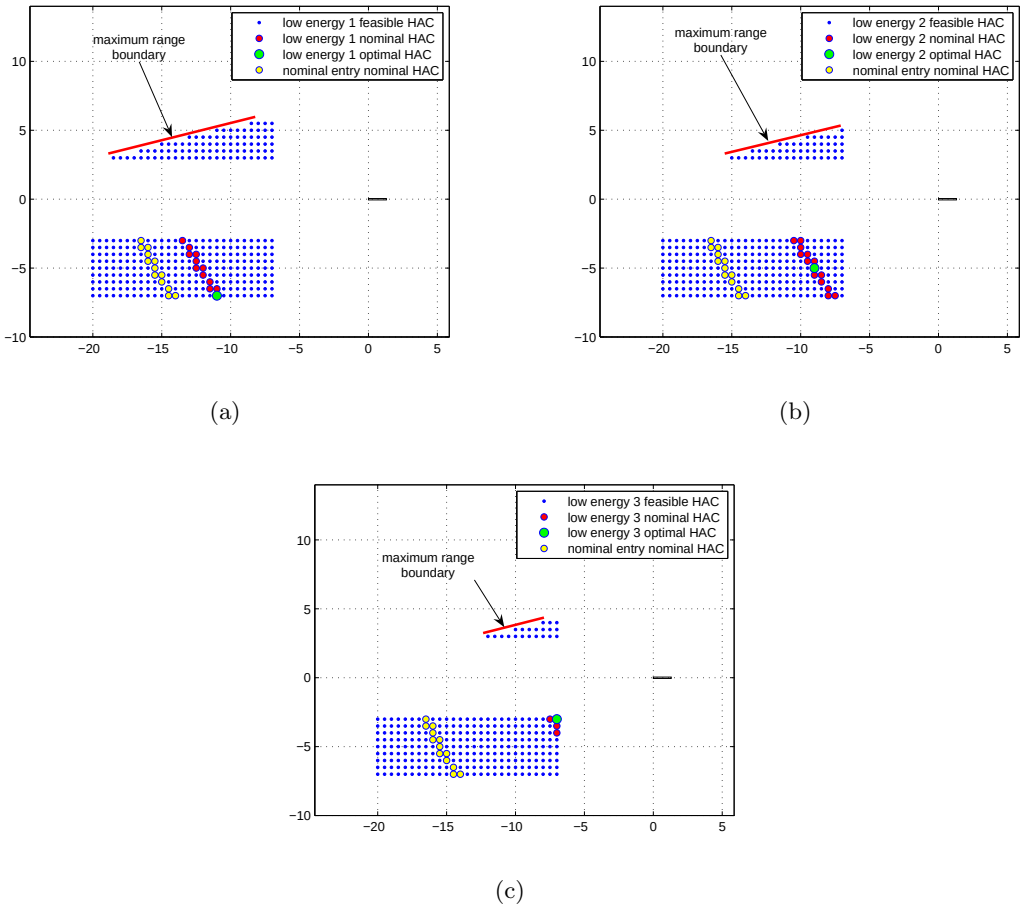

Figure 12.10: Heading Alignment Cylinder center positions for low energy (a) velocity 692.0 m/s (b) 652.0 m/s (c) velocity 612.0 m/s

HORUS starts the TAEM phase in the middle between the maximum-range and maximum-dive boundary of the energy-tube cross-section. Figure 12.11 also indicates that the effective cross-section for a variable HAC position is larger than for a single fixed HAC position.

12.3 Initial heading variations

This section describes the changes in nominal trajectories and HAC positions due to a change in the initial heading angle. Both heading increasements and decreasements are considered. Table 12.4 gives the optimal HAC positions for several cases with a heading variation. The values used for the x-coordinate, y-coordinate, velocity, altitude and flight path angle are equal to the nominal entry-point values.

The HAC planning algorithm is capable of calculating nominal HAC positions for a large heading angle variation. The initial energy of all these cases is equal to the energy value for the nominal terminal area entry point and hence, the same amount of energy must be dissipated during the terminal area. The planning algorithm copes with a heading deviation by computing a new trajectory during which the same amount of energy can be dissipated. Since the nominal

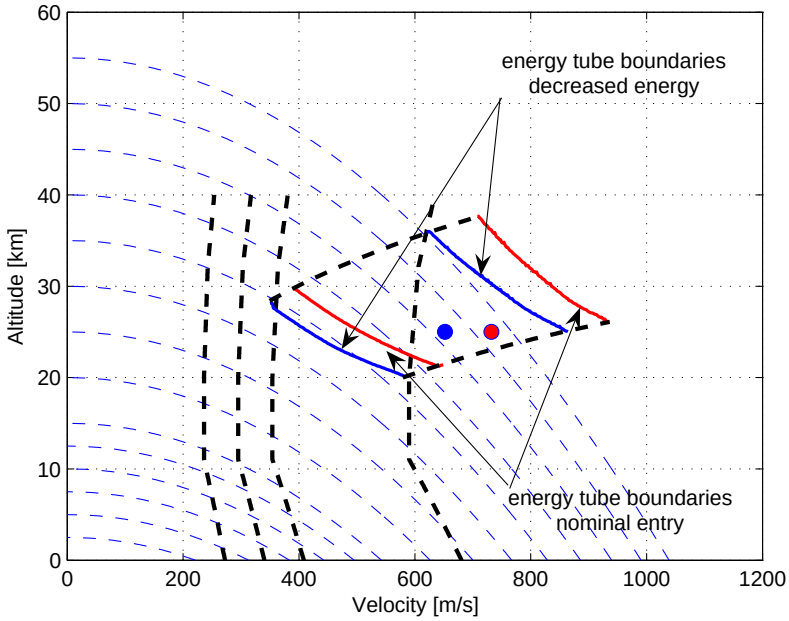

Figure 12.11: Energy tube cross-section for the nominal TAEM entry point and energy low situation. The red dot indicates the nominal entry point, while the blue dot indicates an entry point with a lower energy (V = 652.0 m/s).

longitudinal strategy is used, the amount of energy that can be dissipated is determined by the length of the ground track, the length of the HAC turning phase and the applied bank angles. The bank angle during the supersonic acquisition phase does not influence the drag or energy dissipation. Normally, the angle of attack is increased during a turn. An increased angle of attack means an increased drag. But during the supersonic turn, the angle of attack is equal to the value during a straight flight. Hence, a supersonic turn does not increase the drag and thus energy dissipation.
Figure 12.12 shows the resulting nominal trajectory, ground track and calculated HAC position for an initial heading of 30°. The length of the ground track is equal to 102.54 km. The planning algorithm positions the HAC closer to the runway. During the supersonic acquisition turn, the angle-of-attack is not influenced by the bank angle and hence, the value of the lift is smaller than the value required for equilibrium. The small zoom maneuver is no longer present.

Cases 1 till 4 describe an heading-angle increase (rotation clockwise), while cases 5 till 10 consider a heading-angle decrease (rotation counterclockwise). Below, the influence on the feasible and nominal HAC positions is discussed for each of these cases.

12.3.1 Heading angle increase

Figures 12.13(a), 12.13(b) and 12.13(c) show the feasible and nominal HAC positions for a heading increase of 20°, 30° and 40°, respectively.
Increasing the heading results in a shift of the maximum-range boundary to the right lower corner of the upper HAC grid and hence, decreases the amount of feasible HAC positions. For an $\chi = 40°$, the maximum-range boundary also appears at the left side in the lower part of the HAC grid. The maximum dive capabilities of HORUS are always sufficient during a heading

Table 12.4: Optimal HAC positions for initial states with Heading Variations. n.a. = not applicable

	heading [deg]	x_{HAC} [km]	y_{HAC} [km]	$\|\Delta x\|$ [m]
HV case 1	10.0	-14.0	-5.0	33.56
HV case 2	20.0	-12.0	-5.0	93.44
HV case 3	30.0	-8.0	-6.0	24.75
HV case 4	40.0	n.a.	n.a.	n.a.
HV case 5	-10.0	-17.5	-4.0	67.30
HV case 6	-20.0	-16.5	-6.0	33.41
HV case 7	-30.0	-15.5	-5.0	27.88
HV case 8	-40.0	-14.0	-4.0	43.62
HV case 9	-50.0	-9.5	-5.5	15.20
HV case 10	-60.0	n.a.	n.a.	n.a.

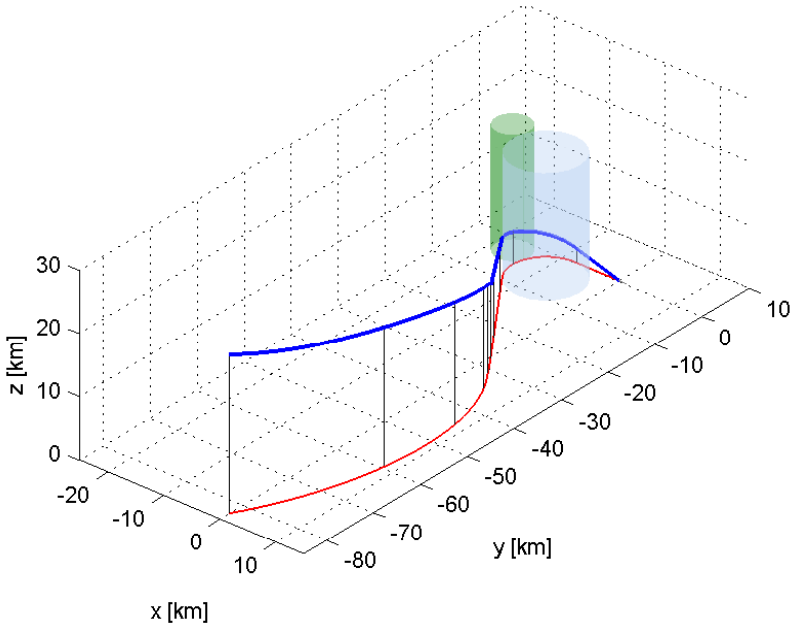

Figure 12.12: 3-D reference trajectory for a heading variation; $\chi = 30°$. The green HAC is the optimal HAC for the nominal terminal-area entry point

increase and is not critical in determining the feasible HAC positions.
The moving pattern of the nominal HAC positions indicates a shift to the right part of the lower HAC grid. No nominal HAC positions are available for a situation with an initial heading of 40°. The HAC position which results in a trajectory using the nominal longitudinal strategy has an x- and y-coordinate of respectively -7.0 km and -3.0 km, i.e., the HAC position closest to the runway with a straight-in approach using the smallest HAC radius possible. The difference between the end point of HORUS and the runway threshold is more than 800.0 m. In order to reach the runway threshold, a strategy with less energy dissipation must be followed. It is no longer possible to only adapt the lateral or ground track geometry and to use a single nominal longitudinal strategy. Both the lateral and the longitudinal strategy must be adapted to reach the runway.

During a heading-angle increase, the ground track distance during the acquisition turn is increased. To compensate for this increase, the nominal HAC positions are shifted closer to the runway. Similar to the case of an energy increase, it is also impossible to distinguish the influence of an optimal turn radius on the nominal HAC positions.

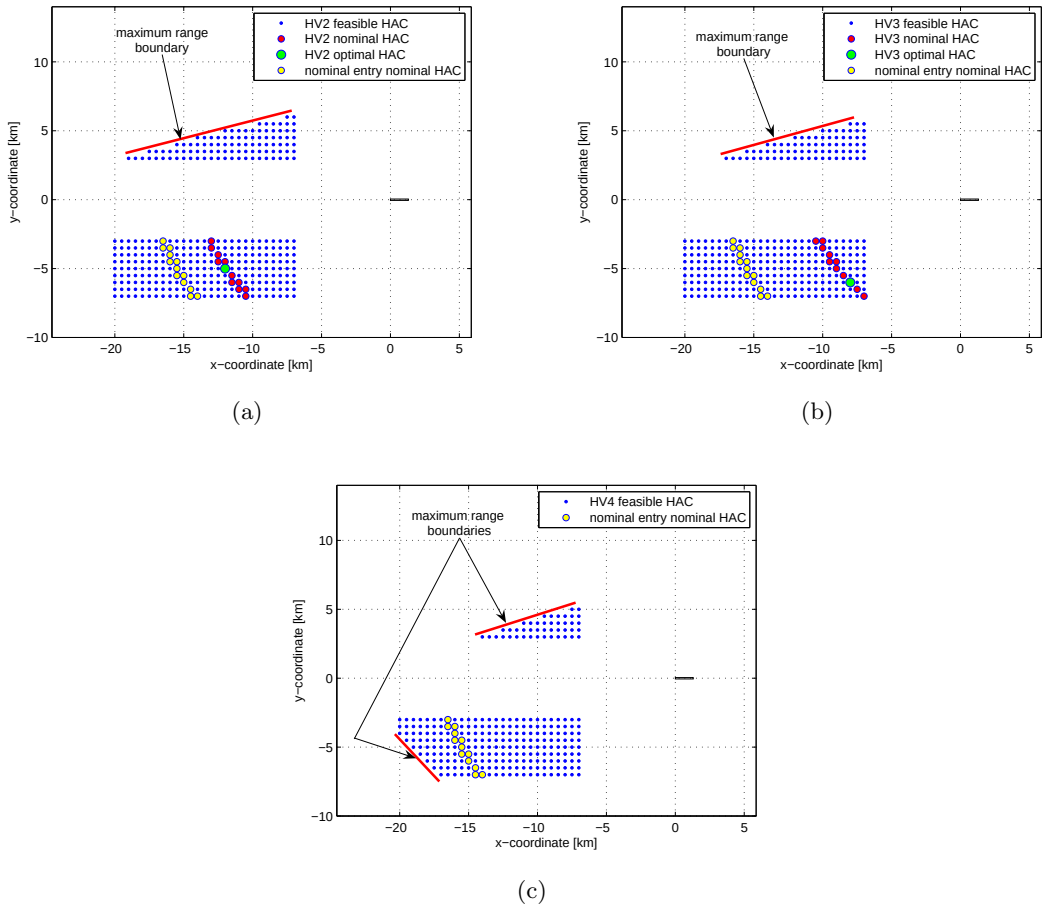

Figure 12.13: Heading Alignment Cylinder center positions for heading angle increase (a) heading = 20° (b) heading = 30°(c) heading = 40°

12.3.2 Heading angle decrease

In contrast to a heading increase, a heading decrease to -10° and -20° results is a shift of nominal HAC positions to the left with respect to the nominal entry case. This can be seen in figure 12.14(a), where the feasible and nominal HAC positions are shown for an heading angle of -20°. Decreasing the heading angle further shifts the nominal HAC positions again to the right. Figure 12.14(b) indicates that for a heading angle of -30°, the nominal HAC positions coincide with the nominal HAC positions of the nominal terminal area entry conditions. Decreasing the heading angle even further results a shift of nominal HAC positions the right with respect to the nominal entry situation. For an initial heading of -15 degrees, it is possible to fly a trajectory with no acquisition turn. This gives a HAC location which is situated the furthest from the runway. A deviation to the right or left will decrease the distance from the HAC to the runway. Starting with an initial heading angle of 60°results in a situation similar to the

one shown in figure 12.13(c). There are no nominal HAC positions available for this situation. Again the HAC with an x- and a y-coordinate of respectively -7.0 km and -3.0 km gives the smallest difference between the endpoint of HORUS and the runway threshold. The difference is now more than 4.0 km. Hence, a strategy with less energy dissipation is required. Also in this case, both the lateral and the longitudinal strategy must be adapted to reach the runway.

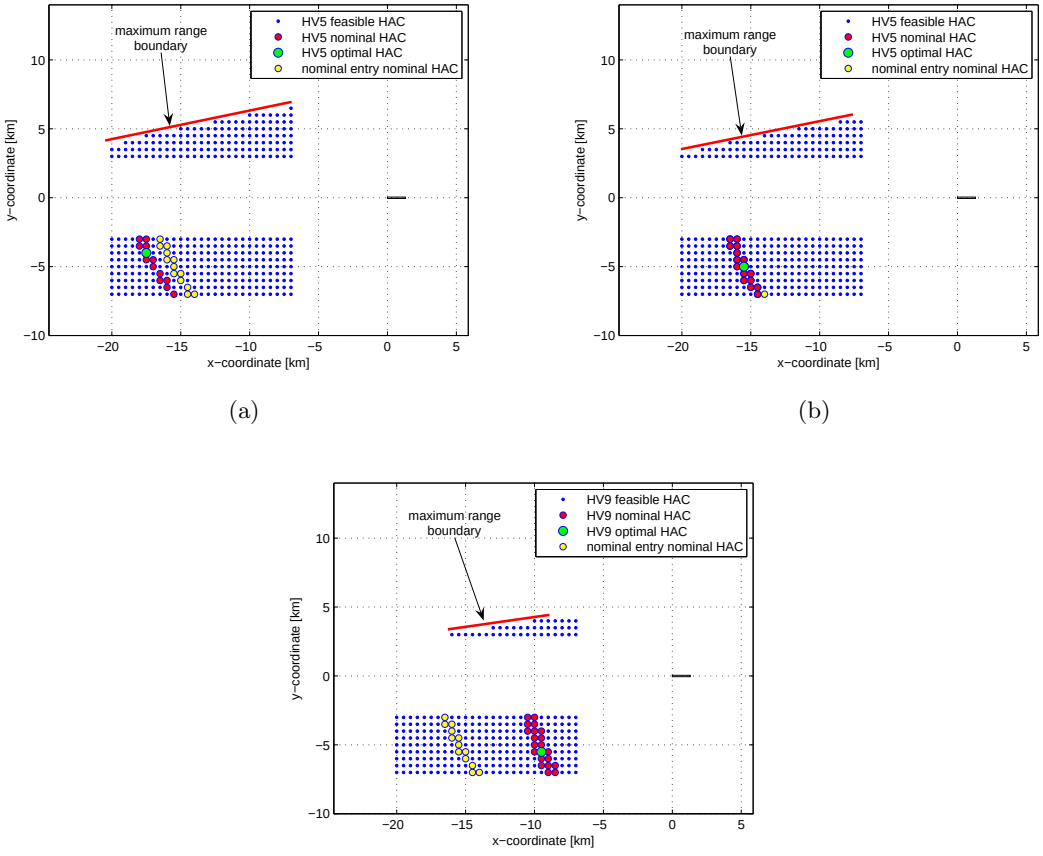

Figure 12.14: Heading Alignment Cylinder center positions for heading angle decrease (a) heading = -10° (b) heading = -30° (c) heading = -50°

12.4 Initial flight path angle variations

This section presents the influence on the HAC position due to changes in the flight path angle. The other parameters of the initial state are unchanged and equal to the values as used in the nominal case. Two simulations were performed, i.e., one with a flight path-angle decrease, and one with an increase. Table 12.5 presents the obtained optimal HAC positions for these two simulations.

Figure 12.15(a) and 12.15(b) indicate the feasible, nominal and optimal HAC positions for a flight path angle of -5° and -15°, respectively. The planning algorithm copes with a flight-path angle change by modifying the HAC position. If the flight-path angle is decreased, i.e., a

Table 12.5: Optimal HAC positions for 2 TAEM entry point with a change in Flight-Path angle

	γ[deg]	x_{HAC} [km]	y_{HAC} [km]	$\lvert\Delta x\rvert$ [m]
FP case 1	-5.0	-18.5	-4.0	55.61
FP case 2	-15.0	-13.5	-4.5	23.77

shallower entry, the range which can be covered with the same amount of energy is increased with respect to a the steeper entry. Therefore, the nominal HAC positions are shifted to the left to increase the ground track distance. In case of a flight-path angle increase, the opposite occurs and the planning algorithm shifts the nominal HAC positions closer to the runway.

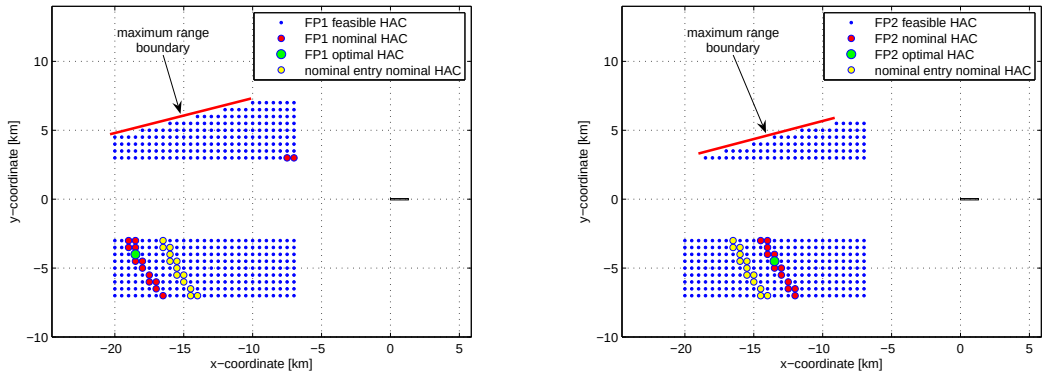

(a) (b)

Figure 12.15: Heading Alignment Cylinder center positions for flight path angle change (a) γ = -5 degrees (b) γ = -15 degrees

Clearly, a change in flight-path angle does has an effect on the resulting trajectory. This is in contrast to the statement in (Helmersson, 1988b) indicating that a change in flight path angle has only a minor influence on the trajectory and can therefore be ignored.

12.5 Combination of several parameter changes

Till now, only one parameter was changed at a time. This section investigates the influence of combining several parameter changes at ones. A Monte Carlo analysis is performed using 100 different initial off-nominal conditions. Changes in altitude, velocity, heading angle and flight-path angle were taken into account. For each off-nominal initial state, the values for these parameters are determined randomly in a parameter-dependent interval. The x- and y-coordinate of the initial state were not changed and are still equal to 0 km and -83 km, respectively.

Table 12.6 indicates for each parameter the interval boundaries. The boundaries are selected to present a reasonable set of initial states which could occur at the beginning of the terminal area. Figure 12.16 indicates the spread of the 100 random selected initial states, both in the (V,h) space and the (χ, γ) space.

Table 12.6: Interval boundaries as used during the Monte Carlo analysis on the initial state

	minimum boundary	maximum boundary
Altitude [km]	25.0	30.0
Velocity [m/s]	652.0	732.0
Heading angle [deg]	-20	20
Flight path angle [deg]	-15	-5

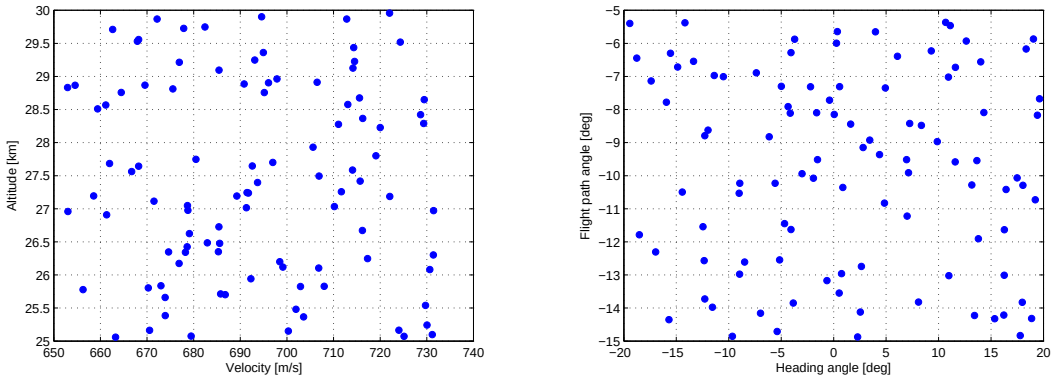

(a) (b)

Figure 12.16: Spread of the 100 random initial states of the Monte Carlo analysis in the (a) (V,h) space and (b) (χ, γ) space

The HAC planning algorithm copes with initial off-nominal conditions by adjusting the HAC. The optimal HAC configuration is the one which yields a proper alignment with the runway centerline (y-coordinate), at the correct direction (final heading) and with a final x-position as close to the runway threshold as possible, using the nominal longitudinal strategy. The optimization criteria used to select the optimal HAC is the difference in x-position between the final state HORUS and the runway threshold. Figure 12.17 presents a histogram of this difference for the 100 initial off-nominal cases, using the optimal HAC as calculated by the HAC planning algorithm for each initial state. For most initial off-nominal conditions, the difference is smaller than 50 meters. Few cases have a larger difference, with a maximum for single point of only 170 meters. Hence, the planning algorithm is able to calculate a HAC position such that it is possible to reach the runway threshold using the nominal longitudinal strategy in case of a combination of several initial state parameter changes. In some cases, only very small deviations from the nominal longitudinal strategy is required. Because HORUS is able to start the terminal area with a nominal longitudinal strategy, it is able to cope with off-nominal conditions which occur along the terminal area by adapting the longitudinal strategy.

Figure 12.18 shows the resulting ground track for the 100 cases of the Monte-Carlo analysis. Different initial states require a different ground track (HAC position) to reach the runway threshold using the nominal longitudinal strategy. Because HORUS is able to start the terminal area with a nominal longitudinal strategy, it is able to cope with off-nominal conditions which occur along the terminal area by adapting the longitudinal strategy and using the HAC position as calculated at the beginning of the terminal area.

It should be noted that, in principle, 100 simulations are not enough to identify critical com-

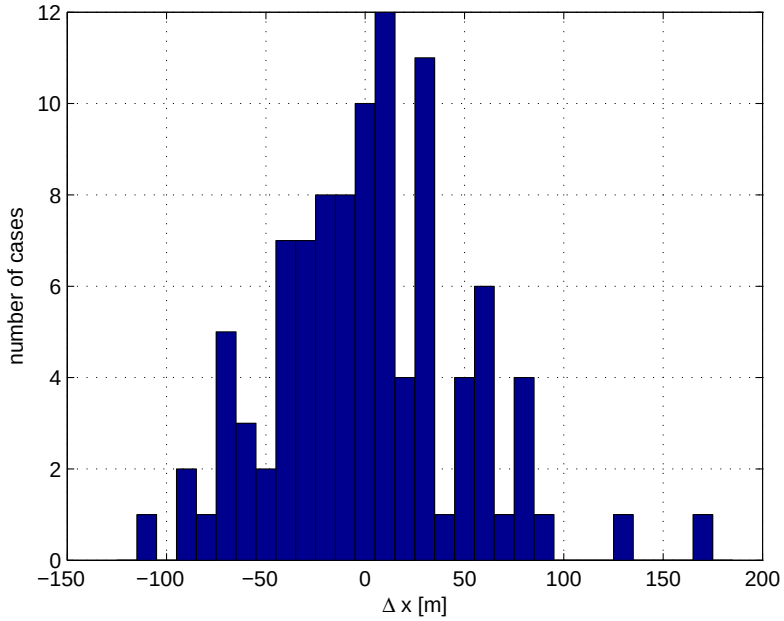

Figure 12.17: Histogram of the difference between the final position of HORUS and the runway threshold on x-direction for a Monte-Carlo analysis of 100 different initial states

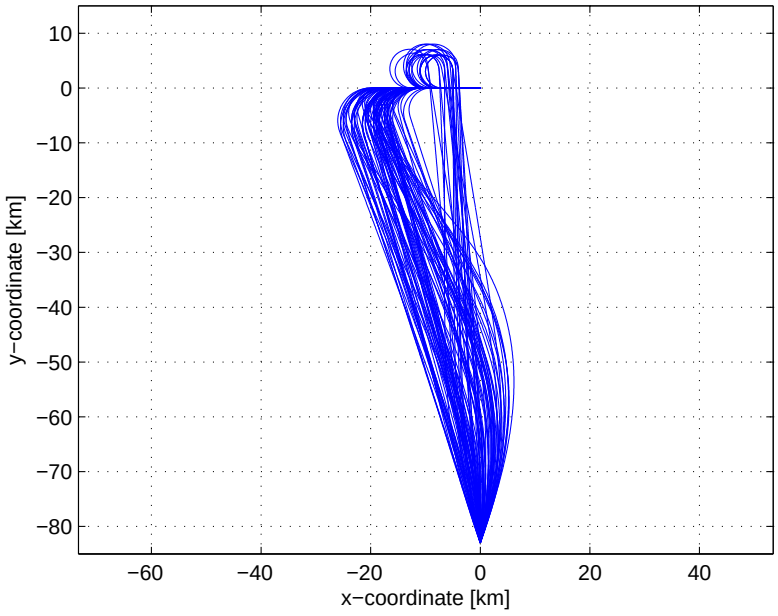

Figure 12.18: Resulting ground tracks of the Monte-Carlo analysis

binations and to draw general conclusions. Hence, more simulations should be performed in further studies.

12.6 TAEM entry circle

The previous sections all considered an initial state at a fixed position in the xy-plane. Both nominal and off-nominal states started at an x- and y-coordinate of 0.0 km and -83.0 km, respectively. The initial distance to the runway threshold is hence equal to 83 km. In this section, the influence on the optimal HAC position is investigated for initial states with a different x- and y-coordinate, but with an constant value for the distance to the runway threshold of 83 km. Hence, the initial points are situated on a circle centered around the runway threshold with a radius of 83 km. Only positions with a negative y-coordinate (half of the circle) are studied. Assuming a zero-wind condition, the solution for the other half can be obtained by taking the mirror image. If wind would be present, this situation would no longer be correct. The initial altitude, velocity and flight path angle are equal to 25.0 km, 732.0 m/s and -10.0°, respectively. The initial heading angle is chosen such that the HORUS is flying toward the runway threshold. These values are identical to the nominal values.

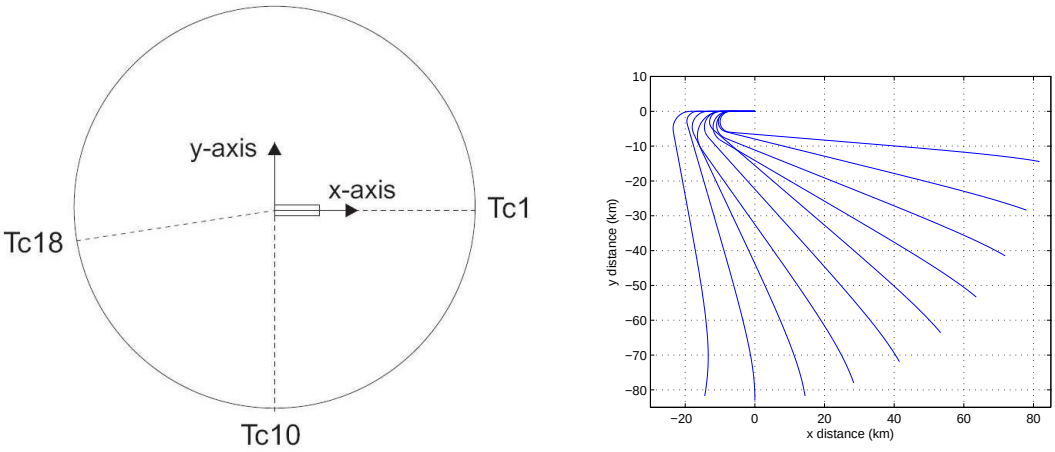

(a) (b)

Figure 12.19: (a) Initial positions on the TAEM entry circle. Initial positions situated between the shown boundary values are situated on the circle, with an angle shift of 10°(b) resulting ground track using optimal HAC position and nominal longitudinal strategy for TC 2 - TC 11

Figure 12.19(a) shows the initial positions as used for the analysis while table 12.7 present the obtained optimal HAC positions using the HAC planning algorithm. Consider the initial positions with a positive x-coordinate (TC 1 - TC 10). For all these positions, the HAC planning algorithm is able to calculate nominal HAC positions ($|\Delta x| < 500.0$ m), except for initial position 1. Figure 12.20 indicates the feasible, nominal and optimal HAC positions for four initial positions on the TAEM entry circle with a positive x-coordinate. For initial position 1, no nominal HAC positions are possible and the feasible HAC positions in the upper and lower grid are symmetrical. Using initial point 2, two nominal HAC positions appear in the top right part of the lower HAC grid. The feasible HAC positions in the upper and lower grid are no longer symmetrical. Going along the TAEM entry circle shifts the maximum range boundary in the upper HAC grid to the right while in the lower HAC grid, the maximum range boundary is shifted to the left. Next to this shift, also a small clockwise rotation is present. The nominal HAC positions shift to the left side of the lower HAC grid. Figure 12.19(b) presents the result-

ing ground tracks.

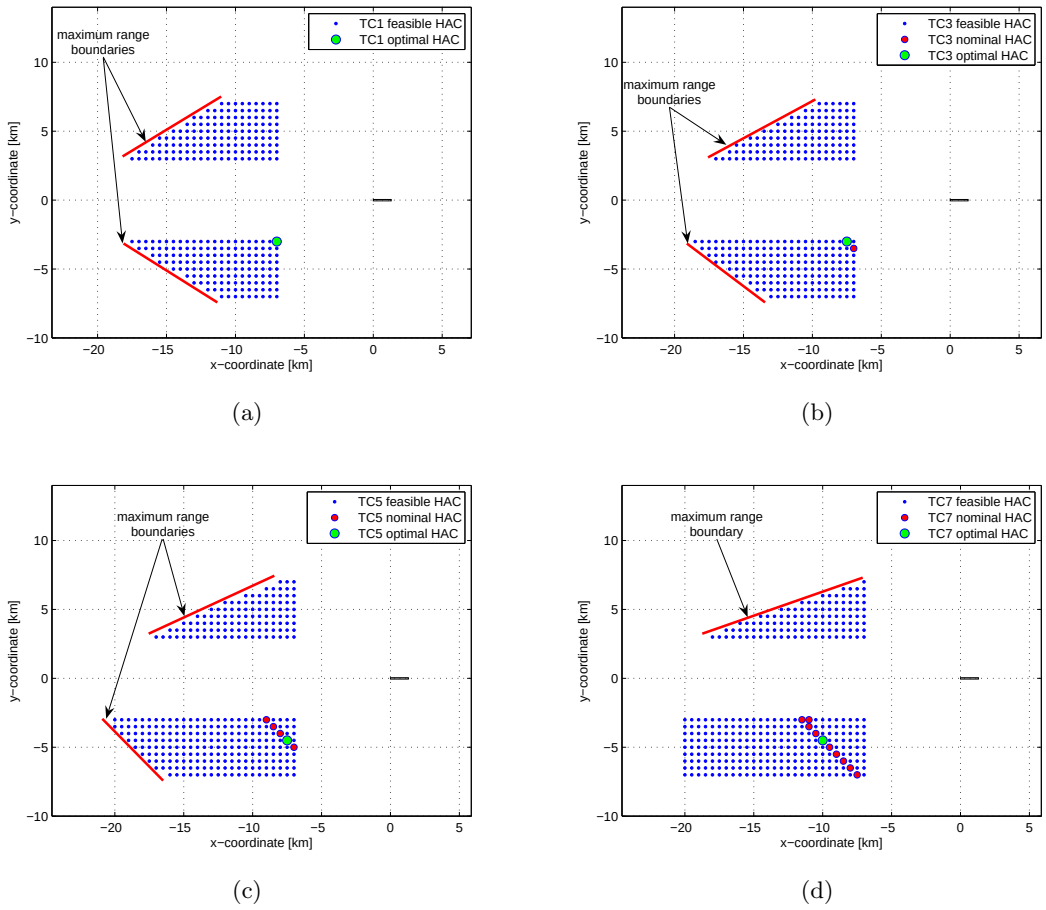

Figure 12.20: Heading Alignment Cylinder center positions for positions of TAEM circle (a) TC 1 (b) TC 3 (c) TC 5 (d) TC 7

Table 12.7 shows that for initial points on the TAEM entry circle with a negative x-coordinate (TC 12 - TC 18), it is not possible to position the HAC such that the difference between the runway threshold and the final position of HORUS is sufficiently small using a nominal longitudinal strategy, except for initial position 11. For the last three positions, it is possible to find nominal HAC positions, but with a relative large difference between the final position of HORUS and the runway threshold. It is important to note that for all the initial position on the TAEM entry circle with a negative x-coordinate, it is still possible to reach the runway threshold if a different longitudinal strategy is used and not the nominal longitudinal strategy, i.e., more or less energy dissipation.

Consider initial position TC 13, which resulted in the largest difference between the final HAC position and the runway threshold using the nominal longitudinal strategy. It uses an overhead approach and does not reach the runway threshold (undershoot). Hence, the initial energy is insufficient to reach the runway threshold using the nominal longitudinal strategy and a HAC position in the upper part of the HAC grid. Using a HAC position in the lower part of the HAC grid results in an overshoot of the runway threshold, and a final difference which is larger

Table 12.7: Optimal HAC positions for initial states on the TAEM entry circle

	x_{HAC} **[km]**	y_{HAC} **[km]**	χ_0 **[deg]**	$\lvert\Delta x\rvert$ **[m]**
TC 1	-7.0	-3.0	270	1264.1
TC 2	-7.0	-3.0	280	224.6
TC 3	-7.5	-3.0	290	16.52
TC 4	-7.0	-4.0	300	200.5
TC 5	-7.5	-4.5	310	17.1
TC 6	-10.0	-3.0	320	53.8
TC 7	-10.0	-4.5	330	31.2
TC 8	-9.5	-7.0	340	29.5
TC 9	-13.5	-4.5	350	33.4
TC 10	-16.5	-3.0	0	21.9
TC 11	-18.5	-5.0	10	31.7
TC 12	-20.0	-7.0	20	1351.0
TC 13	-7.0	3.0	30	1481.8
TC 14	-7.0	3.0	40	1028.5
TC 15	-7.0	3.0	50	592.4
TC 16	-7.0	3.0	60	265.7
TC 17	-7.0	3.0	70	162.1
TC 18	-7.0	3.0	80	197.8

than during the undershoot. This suggest that the runway threshold could be reached using the nominal longitudinal strategy if a different initial energy occurs. Therefore, the optimal HAC position was again calculated for initial position 13, but for three different initial energy values, see table 12.8. In case of an energy increase (TC 13b), it is possible to find an optimal HAC position which results in an overhead approach that reaches the runway using the nominal longitudinal strategy. Sufficiently reducing the initial energy (TC 13d) results in an optimal HAC position that reaches the runway threshold using an direct approach. Apparently, there is some kind of 'energy dead band' for which it is not possible using the current nominal guidance strategy to find an optimal HAC position, within the currently used HAC grid. Above or below this 'energy death band', it is possible. Some recommendation can be made in case HORUS starts the terminal area on the TAEM entry circle with a negative x-coordinate:

- start at an initial energy value outside the 'energy dead band' if the nominal longitudinal strategy and the current HAC grid are to be used. The best energy region to start the terminal area at the TAEM entry circle will differ for each point on the circle.
- fly at a different longitudinal strategy if the terminal area is started at the an energy value within the 'energy death band' and using the current HAC grid.
- use a different ground track geometry or use a different HAC grid. The latter could be used, for example, in TC 12. Enlarging the HAC grid to even smaller values for the x-coordinate might result in a better solution. A different ground track can consists of multiple Heading Alignment Cylinders instead of a single HAC or some extra turns can be included.

The position on the TAEM entry circle and the values for heading angle and flight-path angle will have an influence on the boundaries of the energy dead band. Therefore, a Monte Carlo

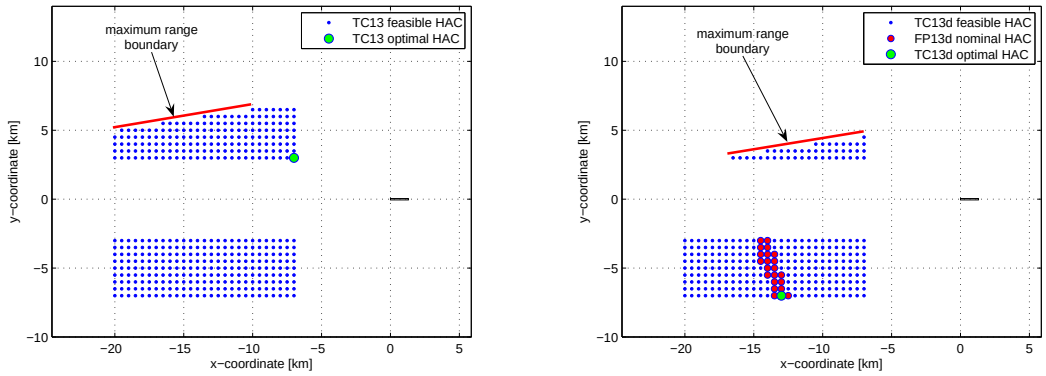

(a) (b)

Figure 12.21: Heading Alignment Cylinder center positions for positions of TAEM circle (a) TC 13 (b) TC 13D

analysis similar to the one performed in the previous section is required for each initial position on the TAEM entry circle, to study the change in the energy death band and the optimal initial energy region as a function of the position on the TAEM entry circle. This is beyond the scope of this thesis, but it is recommended for further research.

However, it is possible to conclude from the TAEM circle analysis that the best region on the TAEM entry circle to start the terminal area is between point TC 5 and TC 11 for the current combination of nominal longitudinal strategy, the current HAC grid, and the nominal energy value to start the terminal area.

Table 12.8: Optimal HAC positions for 3 initial states at position TC 13 with initial energy variations

	altitude [km]	**velocity [m/s]**	x_{HAC} **[km]**	y_{HAC} **[km]**	$\lvert\Delta x\rvert$ **[m]**
TC 13b	27.5	732.0	-9.5	3.5	27.3
TC 13c	25.0	692.0	-20.0	-7.0	1683.4
TC 13d	25.0	612.0	-13.0	-7.0	20.3

12.7 Application possibilities

The results as presented above indicate that the HAC planning algorithm successfully works and hence, several applications are possible. These can be categorized in off-board and on-board applications.

The HAC planning algorithm can be used to perform pre-flight analysis of the energy management capabilities. The simulations can be extended by incorporating different ground-track geometries. Also the influence of off-nominal conditions in terms of vehicular changes or atmospheric changes, can be investigated. Next to the use an analysis tool, the algorithm can also be used to design nominal trajectories.

As stated in section 11.4, on-board applications are possible, if some simplifications are introduced. The on-board applications can be categorized in planning, monitoring and estimation.

- **planning**
  The planning algorithm can be used to determine the optimal HAC, based on the initial state. This HAC is then used during the rest of the terminal area. The optimal HAC position is calculated at the beginning of the terminal area. Off-nominal conditions that occur during the rest of the terminal area are coped with by adapting the longitudinal strategy. If a TAEM guidance algorithm is used that requires a reference trajectory, the nominal trajectory as calculated during the HAC planning (with possible small changes) can be used as an input to the guidance system.

- **monitoring**
  The same HAC planning principle and energy tube concept can be used to monitor the boundary capabilities during the terminal area using the current HAC. Calculating the maximum range and maximum dive trajectory on-board on regular intervals during the terminal area indicates the current energy management boundaries. If the required longitudinal strategy comes close to one of the boundary capabilities, the HAC planning algorithm can be used again to calculate a new optimal HAC position. This shifts the HAC such that the current state is situated again in the middle of the energy tube cross-section such that enough margins are again available.

- **estimation**
  When a terminal area guidance system based on predicting capabilities is used, the energy excess can be estimated by numerically propagating a trajectory using the nominal strategy. The difference in distance between the final point in the ground plane and the runway threshold determines the energy excess. Based on this difference, commands can be generated such that more or less energy is dissipated with respect to the nominal trajectory.

The HAC planning algorithm, and the monitoring and estimation function can be used for re-entry vehicles during the terminal area, either after a normal hypersonic re-entry or after a launch abort. Next to these space-related applications, the planning algorithm could also be extended to commercial aircrafts. On 23 July 1983, a Boeing 767-200 from Air Canada ran out of fuel at an altitude of 12.5 km about halfway between Montreal and Edmonton. The crew was able to glide the aircraft to an emergency landing at Gimli Industrial Park Airport, hence the nickname of the aircraft, the Gimli Glider (GimliGlider, 2009). No system was available to aid the pilots with the energy management. The pilots estimated the speed for the best glide ratio (maximum range) and flew toward the airfield. When approaching the runway, it became clear that the aircraft was too high (high energy). Since no turn-around option was available, the pilots had to perform a so called forward-slip maneuver. This maneuver is regularly used for normal gliders to descend more rapidly (increased energy dissipation). But with a large commercial aircraft that close to the ground, this maneuver is not the best option. But, except for a collapsed unlocked nose wheel, the aircraft made it safely to the runway and luckily, none of the passengers was seriously hurt. A HAC planner and estimation and monitoring system could have assisted the pilots to make the correct in-flight decision regarding the energy-management and hence, the use of a forward-slip maneuver could have been avoided. Several similar incidents occurred. Not all cased ended as well as the Gimli Glider and several persons were killed during gliding approach and landing attempts (GimliGlider, 2009).

Chapter 13

Conclusions and recommendations

The main question of this thesis work was formulated as follows:

Can the safe return of a winged re-entry vehicle through the terminal area be guaranteed for a wide range of initial conditions?

This problem definition was transformed into four study goals, i.e., to:

- investigate current terminal area studies and identify their strong and weak points.
- calculate optimal trajectories and analyze the influence of changing initial conditions on these trajectories in terms of energy.
- assess the use of guidance systems to approximate the optimal trajectories.
- analyze the energy management capabilities in case of both nominal and off-nominal conditions, using the obtained strategies.

Based on the results of the literature study, which are discussed below, the last three study goals are further specified, resulting in main research questions. These research questions, together with the main question, are answered in this study and the conclusions are presented in section 13.1. Section 13.2 provides an overview of the recommendations for future work and terminal area studies.

The literature study on terminal area trajectories indicates that the guidance algorithm of the Space Shuttle uses pre-flight computed reference trajectories. An important disadvantage of the Shuttle algorithm is the limited flexibility to off-nominal conditions. To solve this problem, several terminal area studies use an onboard trajectory planner, which calculates the reference trajectories based on the initial state. Off-nominal conditions are dealt with by adapting the lateral ground track, while the longitudinal strategy remains fixed. The advantage of these systems is that a variable ground track is designed based on the initial state and hence, it is more flexible to off-nominal conditions than the Space Shuttle. A disadvantage is that a single reference dynamic pressure or even a fixed dynamic pressure profile is used as the longitudinal strategy, without investigation the influence of off-nominal conditions on this profile. It is also

not investigated if adapting both the lateral ground track and the longitudinal strategy would yield better results when off-nominal conditions occur.

Another possibility to deal with off-nominal conditions is to use a guidance system based on predicting capabilities. Such a system is proposed by Saab Space and forms the basis of this terminal area study. This method yields a high flexibility regarding variations in the initial state because no reference trajectories are required. Analyzing the proposed guidance system indicates two important improvements that must be made:

- improved energy estimator to estimate the required energy more accurate
- design of an automatic HAC selection algorithm

Both the energy estimator and the HAC planner require knowledge about the correct vertical corridor. This vertical corridor determines the longitudinal capabilities of the vehicle in terms of the maximum range that it can fly and the maximum dive that it can perform. This results in the following questions related to the second study goal and consider only the longitudinal motion:

- What are the optimal strategies to perform a maximum-range flight and a maximum-dive flight?
- What is the influence of variations in initial altitude and velocity on these strategies?

The optimizations in this study indicate that it is impossible to onboard optimize a trajectory in terms of steering commands. Hence, guidance laws have to be designed that approximate the real optimal solutions. This corresponds with the third study goal.

Using the obtained guidance laws, the boundaries of the energy-management capabilities can be estimated. This is corresponds with the fourth study goal and questions related to energy estimation include:

- What are the minimum and maximum energy boundaries that define the capabilities of HORUS?
- What is the influence of a change in initial state and velocity on these boundaries?

Using all the gained information, a HAC planning algorithm has been designed. This algorithm has been used to analyze the HAC placement and trajectories in the terminal area. This analysis answers the main question of this thesis study.

13.1 Conclusions

Calculation and characterization of optimal trajectories

Using energy as the independent variable, three possibilities have been studied to represent the control vector during the optimization. The best results, in terms of optimal range, were obtained using a control vector representation with fixed grid points. A representation using variable grid points can reduces the computational time significantly (40 percent for subsonic

cases), but the obtained solution, in terms of optimal range, is problem dependent. In some cases, the solution is only slightly less optimal with respect to the solution for the fixed grid points, while a large decrease in performance is obtained for other situations. The biggest problem is the determination of the grid spacings in between the grid points, especially if an optimal trajectory requires a control profile with several changes (maneuvers) in a relative short energy interval. Problem-dependent information is required before the optimization to steer the GA in selecting the best grid spacings. The third option, a Chebyshev polynomial is also not a suitable option. The obtained results are far from optimal and requires a large computational time. Using this representation, it is difficult to implement angle-of-attack constraints and $\dot{\alpha}$ constraints. The vector with fixed grid points is used to calculate optimal trajectories throughout the thesis study.

Although it is commonly stated that a maximum lift-to-drag ratio (steady-state approximation) results in a maximum range flight in the vertical plane, the optimal solutions obtained using the genetic algorithms indicate that it is possible to obtain larger ranges. For subsonic initial states, the increase in range can be as large as 6 percent. The optimal results indicate that the largest part of a subsonic optimal maximum range glide is effected at an angle of attack near the required value for a maximum lift-to-drag ratio, except for the initial and the final phases of the flight. At the end of the flight, a pull-up or flare maneuver is performed. The amplitude of the variations in the altitude, velocity and flight-path angle are much smaller for the optimal solutions, with respect to the steady-state solutions. In case of a supersonic initial state, the range is increased by a maximum of 3 percent. A glide at maximum lift-to-drag ratio provides a good initial guess, especially for moderate initial altitudes (20-25 km), but if accurate predictions of the maximum range are required, the optimal solutions must be used. Oscillations are still present in the altitude, velocity and flight-path angle profiles of the optimal solutions, but with a lower amplitude as compared with the steady-state solution.

The optimal strategy to perform a maximum range flight is to fly at minimal drag. For a supersonic aircraft that has relative good gliding capabilities ($L/D_{max} \approx 10$), the optimal maximum range trajectory can be visualized with the energy-state approximation. Contours of constant drag, which are calculated using an equilibrium flight situation, yield a maximum range glide path in the energy space. If the vehicle starts at an initial state, which is not situated on this path, transient maneuvers are performed to intercept the maximum range glide path. Near the end of the flight, an improvement in range can is obtained by performing a final flare maneuver to convert kinetic energy into potential energy. If the gliding capabilities of the supersonic aircraft are reduced ($L/D_{max} \approx 4$) to resemble the characteristics of a winged re-entry vehicle, the optimal trajectories do not follow the drag valley in the supersonic region. The trajectories indicate a large overshoot of the drag valley. Due to the combination of the high velocities and the poor gliding capabilities, the drag encountered during the maneuver to intercept the drag valley is not optimal.

The energy-state approximation, using equilibrium flight conditions, is a valid approximation to the real optimal solutions for a subsonic maximum range flight of HORUS. But in case HORUS starts at a supersonic velocity, the energy-state approximation using equilibrium flight conditions, is no longer valid because the transient maneuvers have a large impact on the optimal maximum-range trajectory of a winged re-entry vehicle with poor gliding capabilities at supersonic velocities. The principles of dissipating the least amount of energy with respect to flown range and flying at minimum integrated drag are still valid, but the angle of attack for an equilibrium stationary situation can no longer be used to visualize the drag valley in the energy

space.

The optimal dive is obtained by flying at a minimum dynamic pressure, without stalling. Near the end of the flight, the velocity is increased to transform potential energy into kinetic energy. This is opposite to the maximum diving flights at maximum dynamic pressure as stated throughout the literature. The energy-state approximation indicates that the drag encountered at the minimum dynamic pressure boundary is larger than at the maximum dynamic pressure boundary. Also, when the speedbrakes are used, the maximum dive is obtained by flying at the minimum dynamic pressure. The extra decrease in range due to a full speedbrake deflection ranges from 6 to 9 km. The natural instinct is to lower the nose of the vehicle and to perform a dive at maximum dynamic pressure. This dive strategy is also used in the current study, while the strategy of minimum dynamic pressure can be used as back-up to enlarge the dive capabilities.

The longitudinal strategy during an optimal turn around the HAC with minimum energy dissipation, is different than during a wings-level flight. An optimal turn is performed at a larger angle of attack and a lower velocity. The smaller the HAC radius, the lower the optimal velocity and the higher the required angle of attack. The energy-state approximation is extended to the optimal turn problem. To calculate the drag contours, an angle of attack is now used for an equilibrium banked flight situation. The bank angle is equal to the required bank angle at a particular altitude and velocity resulting in the required turn radius. This yields new drag valleys for different HAC radii which. The drag valleys are shifted to lower dynamic pressures as the turn radius decreases. The optimal trajectories again intercept the drag valley, followed by a flight along the minimum drag path.

An important conclusion from the optimal subsonic and supersonic trajectories is that the optimal dynamic pressure profile changes for different initial states. A different initial state requires a different dynamic pressure profile to reach an optimal trajectory. Hence, it is not possible to use a single fixed dynamic pressure profile in case the maximum range or the minimum range must be predicted for off-nominal conditions.

Guidance system design

The proposed guidance law for a subsonic maximum range guidance law uses a simple PD control law with the dynamic pressure in the drag valley as the reference input. It is possible to calculate a set of gains which approximates the real optimal subsonic maximum trajectory very well. It is not possible to use the same gains for a different initial state because than, an incorrect trajectory is followed. A different initial state requires a different set of optimal gains. By simultaneously optimizing a single set of gains for multiple conditions (robust design), a suboptimal set of gains is found that can be used for several initial states. This results in an acceptable approximation to subsonic maximum range trajectories.

For a supersonic maximum range flight, the dynamic pressure at the start of the transonic regime is used as a reference. Using a PD law, it is possible to find an optimal set of gains for a specific initial supersonic state. A different initial state requires again a different set of gains. The attempt to design a single set of gains for several initial states, using the robust design method, did not succeed. For a supersonic maximum range flight, it is necessary to optimize the gains for each initial state.

The obtained suboptimal gains for the subsonic maximum range flight in a vertical plane can also be used during an optimal turning flight. Using the PD law, the trajectories intercept the required drag valley. The reference dynamic pressure corresponds with the drag valley and depends on the required HAC radius.

For a maximum-dive flight, it is also possible to use a PD control law to intercept and follow the maximum-dive reference dynamic pressure. The gains do not have to be obtained using robust design. By using several simulations, a good set of gains is obtained. For a maximum dive during a turn, the gains for a diving flight in the vertical plane must be multiplied by the cosine of the bank angle. Otherwise, high frequency oscillations occur in the angle-of-attack profile.

Boundaries of energy capabilities

The minimum and maximum energy boundaries are defined by the maximum range and maximum dive capabilities. The minimum energy boundary corresponds to the initial states for which HORUS is able to fly a specific distance, using the maximum range strategy. The maximum energy boundary corresponds to the initial states for which HORUS is able to fly to a specific target range without overshoot, using a maximum dive strategy.

Although it is common to specify a single value for the minimum required energy that is needed to reach a specific range, simulations indicate that the maximum range differs for initial states with the same initial energy. The maximum range also depends on the combination of the components of the initial energy (altitude and velocity). Hence, it is not possible to only specify the minimum required energy for a specific target, but it is also necessary to specify for which combination of altitude and velocity this is valid. The same holds for the maximum energy boundary.

All the combinations for which it is possible to fly a desired range, without overshoot or undershoot, form an energy area in the energy space. This energy area is the cross-section of the energy-tube at the desired range. Every different target range has a different cross-section. The larger the cross-section, the more off-nominal conditions, in terms of variation in velocity and altitude, the vehicle is able to deal with.

Analysis of energy management capabilities

Using the energy-tube concept, a planning algorithm has been designed which adapts the position of a single cylindrical HAC such that a flight using a nominal longitudinal strategy results in a trajectory with an end point as closely as possible to the runway threshold. The HAC position is adapted until the initial state (start of the terminal area) in the energy space is positioned in the middle of the energy tube, such that enough energy control margins are left to anticipate off-nominal conditions during the rest of the flight.

Considering the nominal entry point, in terms of position with respect to the runway, the HAC planning algorithm is able to successfully cope with initial energy variations, initial heading variations and flight-path angle variations by adapting the HAC position. In these cases, the nominal longitudinal strategy can be used.

For some cases which start the terminal area in a different initial position with respect to the runway, it is no longer possible to use the nominal longitudinal strategy. The HAC planner is unable to find and optimal HAC which results in a trajectory that ends at the runway threshold using a nominal longitudinal strategy. But it is still possible to safely reach the runway, if a different longitudinal strategy is used.

The main conclusion is that it is possible to guarantee the safe return of a winged re-entry vehicle through the terminal area for a wide range of initial conditions, if an onboard HAC planning is used, in combination with a variable longitudinal strategy determined by the output of the energy estimator.

13.2 Recommendations

The terminal area study, as described in this thesis report, leads to several recommendations regarding research topics that were not considered in the current study. Below, the recommendations for further research are divided into several groups.

Simulation models

- The current aerodynamic data of HORUS are only a rough description of major aerodynamic effects. In further studies, a more elaborate and accurate vehicle model should be used, preferable data which is validated through wind tunnel tests or test flights.
- Include a navigation to use state measurements and determine the effect of measurement errors.
- Include a control model to investigate the effects of control delays and errors in actuator settings.
- Use 6 degrees of freedom to include the simulation of the rotational dynamics. This is related to the control model (control delays due to the rotational inertia).

Calculation and characterization of optimal trajectories

- Investigate the use of a control-vector representation with a variable number of grid points.
- Use a local optimizer that refines the output of the GA.
- Investigate optimal supersonic turns.
- Investigate the overshoot trajectories of the HAC.
- Investigates the flight around a conical HAC (spiral turn).

Guidance system design

- Study the implementation of a Model Reference Adaptive Control (MRAC) system to approximate the optimal trajectories more closely. In a MRAC system, the gains are adapted, based on the state error.

- Design input filters for the guidance system to eliminate peaks in the control profiles.
- Use a different longitudinal guidance law that controls the vertical component of the lift force, rather than the angle of attack.

Energy estimation and HAC planner

- Implement the energy estimator in an onboard system, by numerically propagating a trajectory using the nominal strategy. The difference between the final position of the vehicle and the runway threshold serves as the reference to determine the required control commands to adapt the longitudinal strategy.
- Implement the HAC planning algorithm in an onboard system.
- Implement simplified models (atmosphere, vehicle aerodynamics, simplified dynamic equations) and simple integration methods to assure fast calculations in both the energy estimator and the HAC planning.

Analysis of energy management capabilities

- Investigate the use of other ground track geometries by using multiple HACs, or by introducing other parameters such as, for example, a bank-reversal switch time.
- Include off-nominal conditions in the environment (wind, density).
- Include off-nominal conditions in the vehicle aerodynamics and banking capabilities.

Mission

- Consider the terminal area and landing phase as one single phase, by including more refined landing guidance algorithms, especially for the flare maneuver.
- Include launch mission abort scenarios by extending the use of an estimation and planning algorithm to launch abort flights.
- Investigate if the energy-tube concept, the energy estimator and the planning algorithm can be extended to vehicles which use parafoils during the re-entry.

References

Alemany, K., & Braun, R. D. (2007). Survey of global optimization methods for low-thrust, multiple asteroid tour missions. Georgia Institute of Technology.

Alenia. (2003, June 30). *Sphynx, flight mechanics notes-1.*

Anon. (1980, June). *Mcc level c formulation requirements. shuttle taem guidance and flight control (sts-1 baseline)* (Tech. Rep. No. NASA-TM-81100). NASA.

Arora, R. K. (2002, September). Reentry trajectory optimization: Evolutionary approach. *American Institute of Aeronautics and Astronautics*(AIAA-2002-5466).

Belau, W., & Sommer, J. (2006). *Definition of rsts reference scenarios, missions, vehicle configurations and s/s layout* (Tech. Rep. No. RIBRE-HMS-TN-0001). Astrium-ST GmbH.

Betts, J. (1998). Survey of numerical methods for trajectory optimization. *Journalof Guidance, Control and Dynamics*, *21*(2), 193-207.

Bletsos, N. (2007). *Launch vehicle guidance, navigation and control.* http://www.aero.org/publications/crosslink/winter2004/06.html. Available from `http://www.aero.org/publications/crosslink/winter2004/06.html` (online; accessed on 28 September 2007)

Boom, T. van der, & Schutter, B. D. (2007). *Optimization in systems and control, lecture notes.* Delft University of Technology.

Bryson, A., Desai, M., & Hoffman, W. (1968, 12-14 August). The energy-state approximation in performance optimization of supersonic aircraft. In *Aiaa guidance, control and flight dynamics conference pasadena, california.*

Buechner, T. (2003). *Trajectory generation strategy for the terminal area of a reusable launch vehicle.* Unpublished master's thesis, Universitt Stuttgart, Institut fr Flugmechanik und Flugregelung.

Camara, F. (2003). *Development and design of the terminal area energy management guidance for a reusable launch vehicle.* Unpublished master's thesis, Delft University of Technology.

Chartres, J. T. A. (2007). *Trajectory design, optimisation and guidance for reusable launch vehicles during the terminal area flight phase.* Unpublished doctoral dissertation, The University of Adelaide.

Costa, R. da. (2003, 11-14 August). Studies for terminal area gnc of reusable launch vehicles. In *Aiaa guidance, navigation and control conference and exhibit austin, texas.*

Cucinelli, G. (1987, 31 March). *Summary on reference vehicle definition and orbit/trajectory constraints* (Tech. Rep. No. TN-ESA 6718/85-1). MBB.

Demeyer, J. (2007). *Orbital design for a formation flying mission in the distant retrograde*

orbits. Unpublished master's thesis, Delft University of Technology.

Elias, A. (1974, Januari 30-February 1). A new guidance strategy for unpowered space shuttle orbiter flight. In *Aiaa 12th aerospace sciences meeting, washington, d.c.*

Fehlberg, E. (1968). *Classical fifth-, sixth-, seventh- and eight-order runge-kutta formulas with stepsize control* (Tech. Rep. No. NASA TR-R-287). Washington: NASA.

FESTIP. (1998, August). *Festip system concepts description* (Tech. Rep.). Ottobrun: Daimler-Benz Aerospace, Space Infrastructure.

Filipe, N. (2008a). *Survey about taem guidance tools and techniques* (Tech. Rep. No. TEC-ECM-TAEM-NF-TN-0801). European Space Agency.

Filipe, N. (2008b). *Taem tool software requirements document* (Tech. Rep. No. TEC-ECM-TAEM-NF-SRD-0802). European Space Agency.

Fortescue, P., Stark, J., & Swinerd, G. (Eds.). (2003). *Spacecraft systems engineering*. Wiley.

GimliGlider. (2009). *Gimli glider.* http://en.wikipedia.org/wiki/Gimliglider. (online; accessed on 20 June 2009)

Girerd, A., & Barton, G. (2000, 14-17 August). Next generation entry guindance-onboard trajectory generation for unpowered drop tests. In *Aiaa guidance, navigation and control conference and exhibit denver, co.*

Goldberg, D. (1989). *Genetic algorithms in search, optimization and machine learning*. Addison-Wesley Publishing Company, Inc.

Grallert, H. (1988). *Executive summary on re-entry guidance and control study* (Tech. Rep. No. TN-ESA 6718/85-0). MBB.

Helmersson, A. (1988a). *Software requirements document of the terminal area energy management phase* (Tech. Rep. No. SP/TNOT/8774/M). Saab Space.

Helmersson, A. (1988b). *Terminal area guidance strategies* (Tech. Rep. No. TN-ESA 6718/85-8). Saab Space.

Hull, J., Gandhi, N., & Schierman, J. (2005, 26-29 September). In flight taem/final approach trajectory generation for reusable launch vehicles. In *Infotech@aerospace, arlington, virginia.*

Jarmark, B. (1988, March). *Terminal area energy management* (Tech. Rep. Nos. TN-ESA 6718/85-4, Revision B). Aircraft Division Saab-Scania AB.

Kirpischikov, V. (2007). *Trajectories of buran orbiters descent and landing, algorithms of the automatic guidance and control.* http://www.buran-energia.com/documentation/documentation-akc-guidance-control.php. (online; accessed on 28 December 2007)

Kluever, C. (2007, January-February). Terminal guidance for an unpowered reusable launch vehicle with bank constraints. *Journal of Guidance, Control and Dynamics*, *30*(1), 162-168.

Kluever, C., & Horneman, K. (2005, 15-18 August). Terminal trajectory planning and optimization for an unpowered reusable launch vehicle. In *Aiaa guidance, navigation and control conference and exhibit san francisco, california.*

Kraemer, J., & Ehlers, H. (1975). Shuttle orbiter guidance system for the terminal flight phase. *Instrument Society of America*, 6.5 1-6.5 10.

Lee, K., & Roh, M. (2001). An efficient genetic algorithm using gradient information for ship structural design optimization. *Ship Technology Research*, *Vol.48*.

Linden, O. van der. (1994, november). *Navigatie en besturing van een gevleugeld re-entry voertuig in de terminal area* (internship report). TH Rijswijk.

Mayanna, A., Grimm, W., & Well, K. (2006, 21-24 August). Adaptive guidance for terminal area energy management (taem) of reentry vehicles. In *Aiaa guidance, navigation and control conference and exhibit keystone, colorado.*

Michalewicz, Z. (1996). *Genetic algorithms+data structures=evolution programs.* Springer.

Mooij, E. (1997). *The motion of a vehicle in a planetary atmosphere.* Delft University Press.

Mooij, E. (1998). *Aerospace-plane flight dynamics.* Unpublished doctoral dissertation, Delft University of Technology.

Moore, T. E. (1991, November). *Space shuttle entry terminal area energy management* (Tech. Rep. No. NASA-TM-104744). National Aeronautics and Space Administration.

Mora, M. B., & Martin, M. B. (1995). Moderate lift/drag vehicle reentry "ratt" final report. GMV S.A.

Mulder, J., Staveren, W. van, Vaart, J. van der, & Weerdt, E. de. (2006). *Flight dynamics, lecture notes.* Delft University of Technology.

NOAA, NASA, & USAF. (1976). Us standard atmosphere 1976 [Computer software manual]. Washington, D.C..

Noomen, R. (2007). *Mission geometry and orbit design.* Delft University of Technology.

Ogata, K. (2002). *Modern control engineering* (Fourth edition ed.). Prentice Hall.

Pesch, H. (1993, October). *Optimization methods for control and guidance* (Tech. Rep.). Technische Universitat Munchen.

Press, W. H., Teukolsky, S. A., Vetterling, W. T., & Flannery, B. P. (2007). *Numerical recipies.* Cambridge University Press.

Ranasinghe, M. (2003). Mixing paradigms: A genetic operator that approximates gradient-descent. *Stanford University, Stanford Electrical Engineering Departement*.

Regan, F., & Anandakrishnan, S. (1993). *Dynamics of atmospheric re-entry*. American Institute of Aeronautics and Astronautics, Inc.

Reichmann, H. (1976). *Zum problem der fahroptimierung im streckensegelflug*. Unpublished doctoral dissertation, Universitt Karlshruhe, Institut fr Praktische Mathematik.

Ruijgrok, G. (1996). *Elements of airplane performance*. Delft University Press.

Safipour, E. (2007). *Trajectory optimization for a mission to neptune and triton*. Unpublished master's thesis, Delft University of Technology.

Spaans, J. (2009). *Optimization of optimization techniques*. Unpublished master's thesis, Delft University of Technology.

Stengel, R. (1974, March). Optimal guidance for the space shuttle transition. *Journal of Spacecraft*, *11*(3), 173-179.

Vinh, N. (1981). *Optimal trajectories in atmospheric flight*. Elsevier scientific publishing company.

Vinko, T., Izzo, D., & Bombardelli, C. (2007, 24-28 September). Benchmarking different global optimisation techniques for preliminary space trajectory design. In *58th international astronautical congress*. IAF.

Visser, H. (2007). *Aircraft performance optimization part 1 lecture notes*. Delft University of Technology.

Wakker, K. (2002). *Astrodynamics i & ii lecture notes*. Delft University of Technology.

Welch, A., Welch, L., & Irving, F. (1970). *New soaring pilot*. Butler & Tanner Ltd.

Wertz, J. (Ed.). (2001). *Mission geometry; orbit and constellation design and management*. Microcosm Press and Kluwer Academic Publishers.

Yokoyama, N., & Suzuki, S. (2003, 11-14 August). Trajectory optimization via modified genetic algorithm. In *Aiaa guidance, navigation and control conference and exhibit austin, texas.*

Zak, A. (2006). *Kliper*. http://www.russianspaceweb.com/kliper.html. (online; accessed on 9 January 2008)

Appendix A

Aerodynamic data of HORUS-2B

This appendix gives the trimmed aerodynamic data of the HORUS-2B, version 7, as provided by MBB. This data is given in graphical form and was copied from (Cucinelli, 1987). Only information about the lift and drag forces in the subsonic and supersonic regime are given. The data set in (Cucinelli, 1987) also contained data about the required deflections of the body flap and elevons to assure a trimmed flight condition. The interested reader is referred to this document.

The data was obtained using a specific set of vehicle parameters :

- reference area FREF: 110 m^2
- reference length, pitch: 23 m
- reference length, yaw and roll: 12 m
- moment reference center about x: 13 m
- moment reference center about z: 0m

Below, the different terms as used in the graphs are explained.

- ALFA = angle of attack
- Mach = Mach number
- ETA1 = left rudder deflection angle
- ETA2 = left wing flap (elevon) deflection angle
- ETA3 = body flap deflection angle
- ETA4 = right wing flap (elevon) deflection angle
- ETA5 = right rudder deflection angle
- ALT = altitude

- DH = drag decrement altitude: 20km - actual altitude

On the next pages, the data for the trimmed lift, the trimmed lift-to-drag ratio and trimmed drag polar are given, both for the subsonic and the supersonic regime. Also the drag decrement altitude is given.

TRIMMED LIFT

FREF= 110. [MM] LREF= 23. [M] BREF= 12. [M]

XREF= 13. [M] ZREF= 0.0 [M]

ALFA	MACH	ETA1	ETA2	ETA3	ETA4	ETA5
VAR1	VAR2	0	TRIM	-20.	TRIM	0.

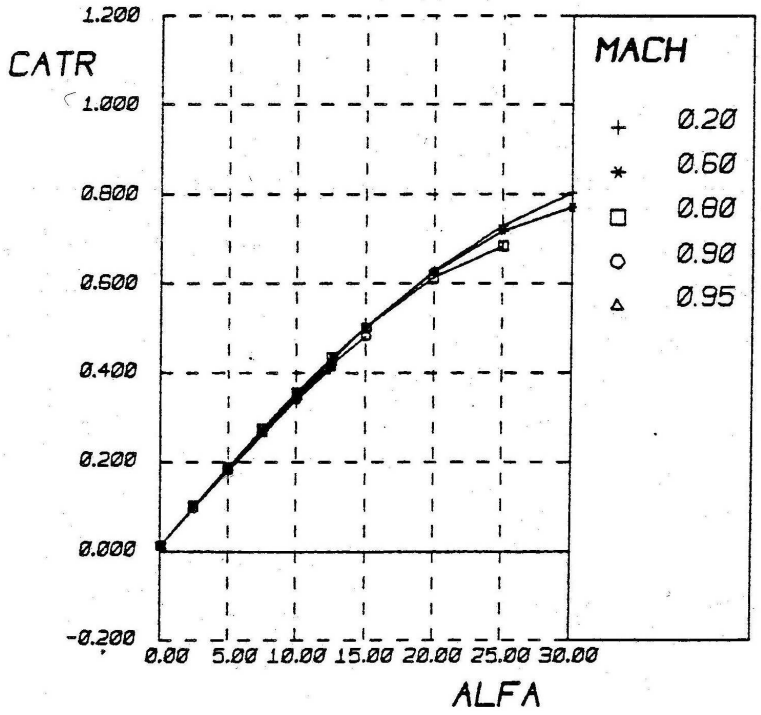

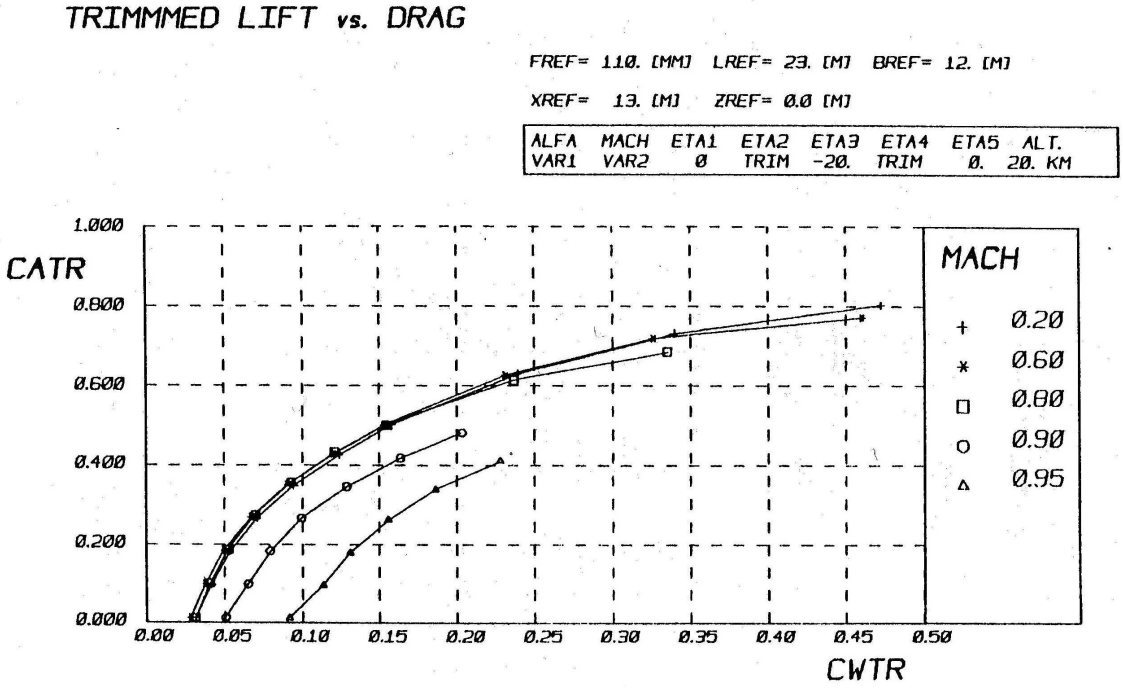
TRIMMMED LIFT vs. DRAG
FREF= 110. [MM] LREF= 23. [M] BREF= 12. [M]
XREF= 13. [M] ZREF= 0.0 [M]
ALFA MACH ETA1 ETA2 ETA3 ETA4 ETA5 ALT.
VAR1 VAR2 0 TRIM -20. TRIM 0. 20. KM
CATR
1.000
0.800
0.600
0.400
0.200
0.000
0.00 0.05 0.10 0.15 0.20 0.25 0.30 0.35 0.40 0.45 0.50
CWTR
MACH
0.20
0.60
0.80
0.90
0.95

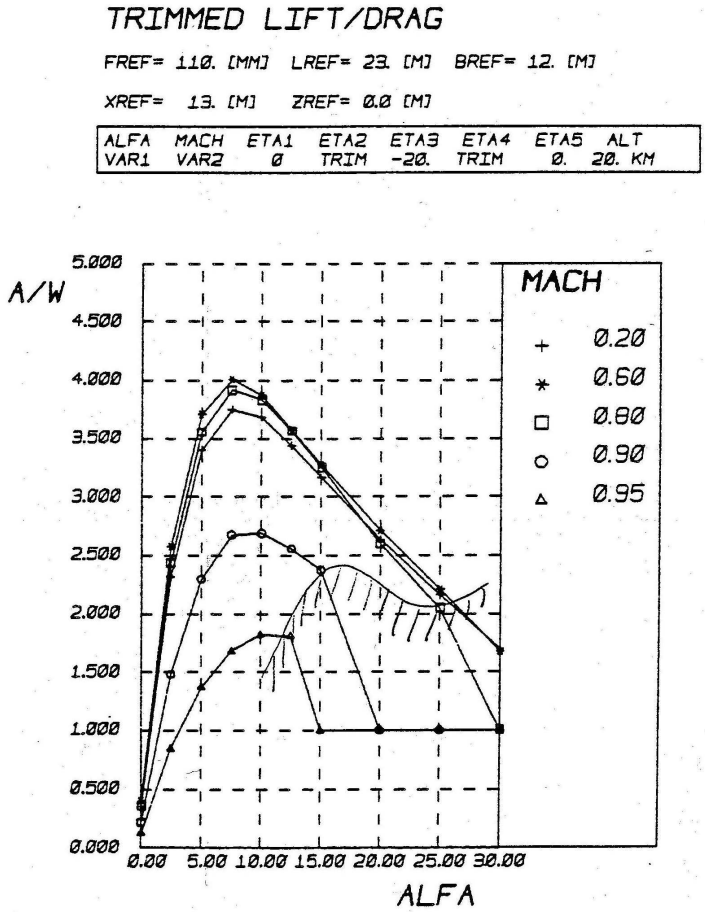
TRIMMED LIFT/DRAG
FREF= 110. [MM] LREF= 23. [M] BREF= 12. [M]
XREF= 13. [M] ZREF= 0.0 [M]
ALFA MACH ETA1 ETA2 ETA3 ETA4 ETA5 ALT
VAR1 VAR2 0 TRIM -20. TRIM 0. 20. KM
A/W
5.000
4.500
4.000
3.500
3.000
2.500
2.000
1.500
1.000
0.500
0.000
0.00 5.00 10.00 15.00 20.00 25.00 30.00
ALFA
MACH
0.20
0.60
0.80
0.90
0.95

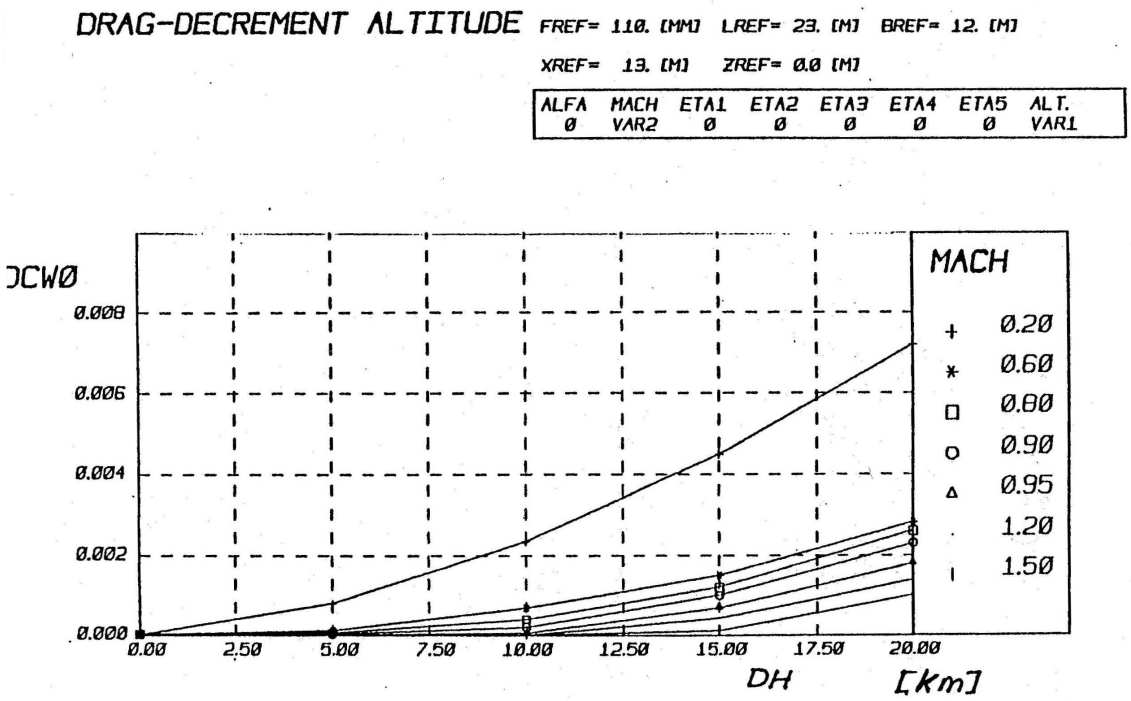
DRAG-DECREMENT ALTITUDE FREF= 110. [MM] LREF= 23. [M] BREF= 12. [M]
XREF= 13. [M] ZREF= 0.0 [M]
ALFA MACH ETA1 ETA2 ETA3 ETA4 ETA5 ALT.
0 VAR2 0 0 0 0 0 VAR1
DCW0
0.008
0.006
0.004
0.002
0.000
0.00 2.50 5.00 7.50 10.00 12.50 15.00 17.50 20.00
DH [km]
MACH
0.20
0.60
0.80
0.90
0.95
1.20
1.50

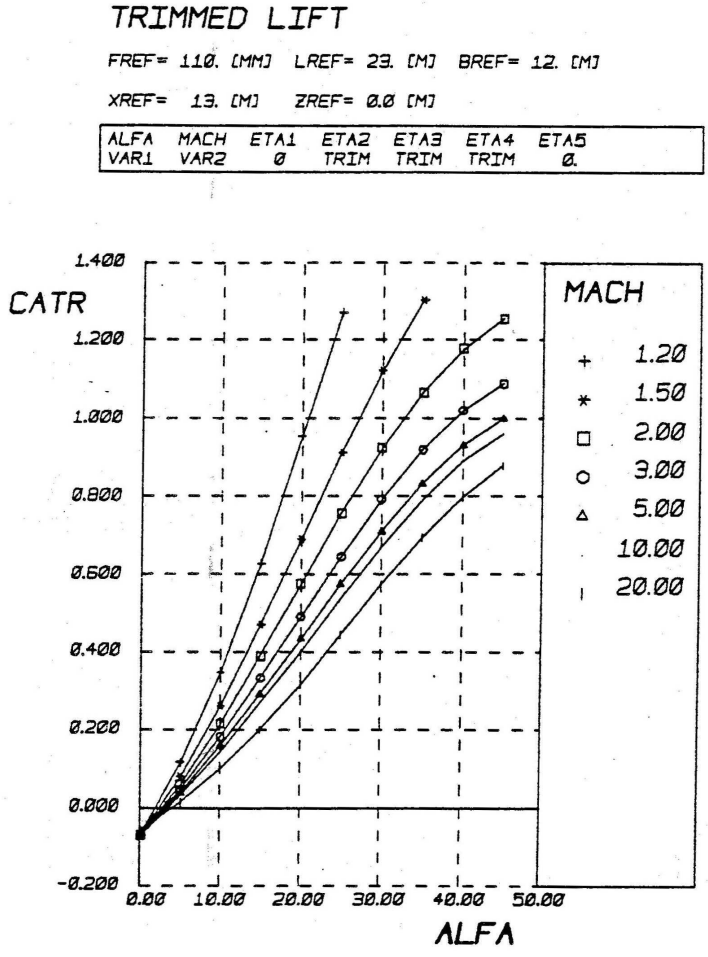
TRIMMED LIFT
FREF= 110. [MM] LREF= 23. [M] BREF= 12. [M]
XREF= 13. [M] ZREF= 0.0 [M]
ALFA MACH ETA1 ETA2 ETA3 ETA4 ETA5
VAR1 VAR2 0 TRIM TRIM TRIM 0.
CATR
1.400
1.200
1.000
0.800
0.600
0.400
0.200
0.000
-0.200
0.00 10.00 20.00 30.00 40.00 50.00
ALFA
MACH
1.20
1.50
2.00
3.00
5.00
10.00
20.00

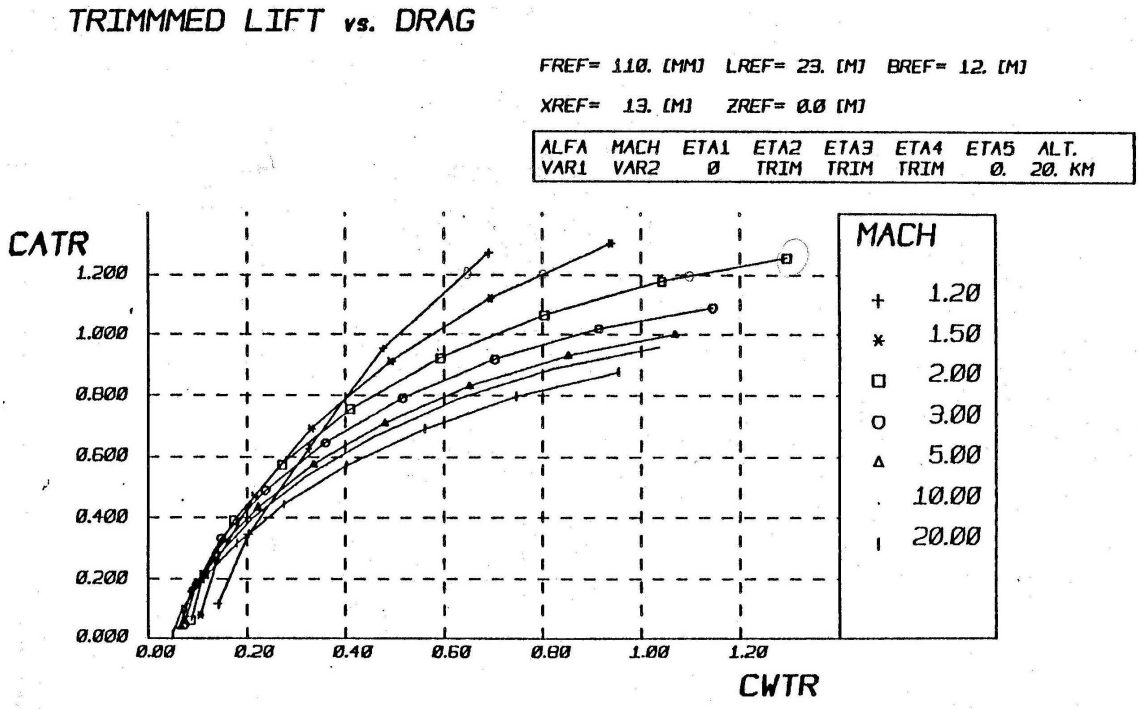
TRIMMMED LIFT vs. DRAG
FREF= 110. [MM] LREF= 23. [M] BREF= 12. [M]
XREF= 13. [M] ZREF= 0.0 [M]
ALFA MACH ETA1 ETA2 ETA3 ETA4 ETA5 ALT.
VAR1 VAR2 0 TRIM TRIM TRIM 0. 20. KM
CATR
1.200
1.000
0.800
0.600
0.400
0.200
0.000
0.00 0.20 0.40 0.60 0.80 1.00 1.20
CWTR
MACH
1.20
1.50
2.00
3.00
5.00
10.00
20.00

TRIMMED LIFT/DRAG

FREF= 110. [MM] LREF= 23. [M] BREF= 12. [M]

XREF= 13. [M] ZREF= 0.0 [M]

ALFA	MACH	ETA1	ETA2	ETA3	ETA4	ETA5	ALT
VAR1	VAR2	0	TRIM	TRIM	TRIM	0.	20. KM

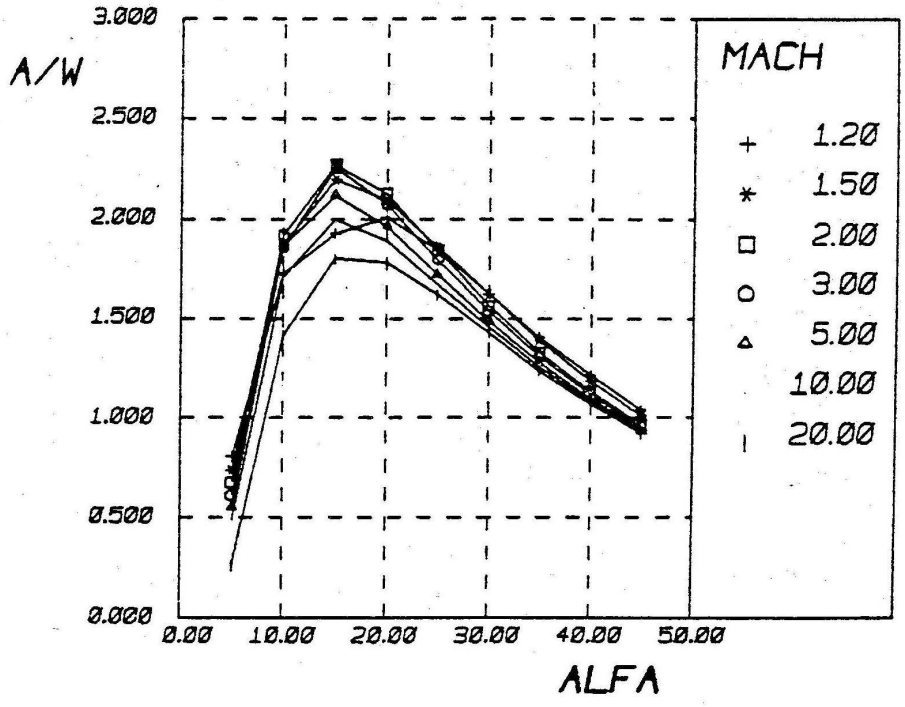

Appendix B

Numerical integration techniques

This appendix describes numerical integrations techniques that can be used to integrate the equations of motions. Section B.1 gives an short overview of possible integration techniques, while the Runge-Kutta method is described in section B.2. This technique is a good competitive method, especially if used in combination with adaptive stepsize. This adaptive stepsize is described in section B.3.

B.1 Different Integration methods

The basic idea of all integration methods is to add small increments to a state. The small increments corresponds to the derivatives of the state multiplied by a stepsize. The most basic implementation of this is The Euler method. Considering only one state variable x instead of the a state vector $\overline{x}$, the Euler method is given as:

$$x_{n+1} = x_n + hf\left(t_n, x_n\right) \tag{B.1}$$

The difference between the exact solution and the numerical solution is called the local truncation error. This truncation error is a measure for how well a method approximates the solution. The truncation error of a step in the integration will be carried over to the next step.

The Euler method is not recommended for any practical use because the method is not as accurate as other methods using the same stepzize. The Euler method only uses derivative information at the beginning of the interval. There are three other major types of numerical integration techniques which have a practical use for solving initial value problems: Runge-Kutta methods, Richardson extrapolation methods and predictor-corrector methods. All three are briefly discussed below.

- **Runga-Kutta methods**
  Runga-Kutta methods propagate a solution over an interval by combining the information from several Euler-style steps and then using the obtained information to match a Taylor series expansion up to some higher order (Press et al., 2007).

- **Richardson extrapolation methods**
  Richardson extrapolation uses the powerful idea of extrapolating a computed result to the value that would have been obtained if the stepsize had been very smaller than it actually was. Extrapolation to zero stepsize is the desired goal. This idea was first implemented in a practical way by Bulirsch and Stoer and so this method is often called Burlisch-Stoer methods (Press et al., 2007).

- **Predictor-corrector methods**
  Predictor-corrector or multistep methods store the solution along the way and use those results to extrapolate the solution one step advanced and they then correct the extrapolation using derivative information at the new point (Press et al., 2007).

The higher-order Runge-Kutta methods are competitive with the other integration methods. Runge-Kutta almost always succeeds and it is usually the fastest method when the computation of the derivative function is not to difficult and when only a moderate accuracy (10^{-5}) is required (Press et al., 2007). Bulrisch-Stoer or predictor-corrector methods can be more efficient for problems where very high accuracy is required. (Linden, 1994) describes the use of a Runge-Kutta method for the problem of TAEM guidance and this Runge-Kutta method seems to work, so this integration method will also be used during the thesis. In the next section, the Runge-Kutta method will be further explained. More information about the other methods can be found in (Press et al., 2007).

B.2 Runge-Kutta methods

As already explained, the Euler method only uses derivative information at the starting point of each interval. The derivative at the starting point is extrapolated to obtain the next point. This method has a first-order accuracy and an error term equal to $O(h^2)$ [1].

An extra point can be selected at the midpoint of each interval and the derivative information at this point can be used to reduce the error. This is called the midpoint method or second-order Runge-Kutta method. This method has a second-order accuracy and an error term of $O(h^3)$. The derivative at the starting point of the interval at each step is used to find a point halfway across the interval. The derivative information at this midpoint is then used across the full width of the interval to compute the real step across the full interval.

This principle can be extended to more intermediate points of which the derivative information is used to calculate the new point. The method which is by far the most often used is the fourth-order Runge-Kutta method. Figure B.1 illustrates this method. The derivative is evaluated four times during each step: once at the initial point, two times at trial midpoints and once at the trial endpoint. The derivatives are used to calculate the new point according to the following scheme (Press et al., 2007):

$$\begin{aligned} x_{n+1} &= x_n + \frac{1}{6}k_1 + \frac{1}{3}k_2 + \frac{1}{3}k_3 + \frac{1}{6}k_4 + O\left(h^5\right) \\ k_1 &= hf\left(t_n, x_n\right) \\ k_2 &= hf\left(t_n + \frac{1}{2}h, x_n + \frac{1}{2}k_1\right) \end{aligned} \tag{B.2}$$

[1] A method is called nth order if it has an error term $O(h^{n+1})$ (Press et al., 2007)

$$
\begin{aligned}
k_3 &= hf\left(t_n + \frac{1}{2}h, x_n + \frac{1}{2}k_2\right) \\
k_4 &= hf\left(t_n + h, x_n + k_3\right).
\end{aligned}
$$

In (Press et al., 2007), this Runge-Kutta method is referred to as the old workhorse and it is stated that it is quite competitive as long as very high accuracy is not required. It is possible to get pretty far with this method, especially if it is combined with an adaptive stepsize algorithm. This adaptive stepsize algorithm will be discussed in the next section.

The fourth-order Runge-Kutta can be extended to higher order methods (fifth, sixth, seventh and height-order Runge-Kutta methods) but it should be noted that although higher order methods are more efficient, higher order doesn't always mean higher accuracy (Press et al., 2007). More efficient higher-order methods will often have higher accuracy, but surely not always.

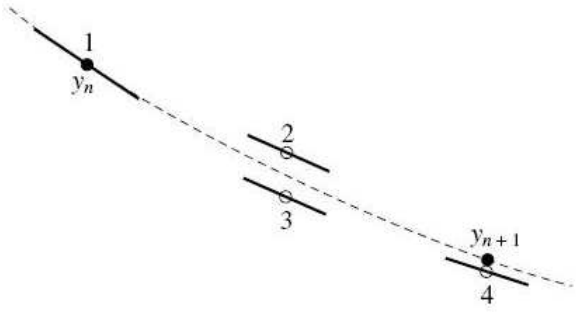

Figure B.1: Fourth-order Runge-Kutta method; filled points indicate points on boundary of step interval and open dots are point from where information is used to calculate new point (Press et al., 2007)

B.3 Adaptive stepsize

The accuracy of the solution depends on the stepsize. The smaller the step size, the larger the accuracy. But a smaller step size means more calculations and thus longer running times. So a good balance should be found in order to reach a predetermined accuracy with minimum computational effort. Long integration steps can be used for smooth uninteresting countryside, while many small steps should be used through treacherous terrain (Press et al., 2007). For the TAEM problem, this translates in long steps when the change in required maneuvers is small (straight steady flight) and small steps when maneuvers are required (turns, dive and pull-ups).

The working principle of the adaptive stepsize control is based on estimating the truncation error. For implementation of the adaptive stepsize control in the fourth-order Runge-Kutta method, two options exist:

- **Step doubling**
  In this method, each step is taken twice: once as a full step and then as two half steps. The difference between the two numerical estimates for the new point is an indicator of the truncation error. The difference is used to keep a desired degree of accuracy by adjusting the stepsize (Press et al., 2007). This method is not much used because the next option is more efficient.

- **Embedded Runge-Kutta methods**
  Fehlberg found a fifth-order method with six function evaluations [2] where another combination of this six functions gives a fourth-order method. The difference between the two obtained estimates of the new point can be used to estimate the truncation error and to adjust the stepsize.
  In document (Press et al., 2007), the fifth-order Runge-Kutta method with the embedded fourth-order Runge-kutta formula is described. The used values for the constants in the formulas differs from Fehlberg's original values, because they give a more efficient method (Press et al., 2007). It is also explained how the the truncation error can be used to determine the required stepsize.
  This way of error control is a local error per step method. It controls the local error and not the global accumulation of errors.

The fifth-order Runge-Kutta method with the embedded fourth-order Runge-Kutta formula is used in the genetic optimization program OPTIDUS. Hence, this RK45 method will also be used during this study on the terminal area.

[2] It should be noted that M-order Runge-Kutta methods, where M is higher than four, requires more than M function evaluations.

Appendix C

Aerodynamic data of supersonic aircraft

This appendix presents the aerodynamic data of the supersonic aircraft used in the energy-state approximation as described in chapter X. Both models for the original supersonic aircraft with good gliding capabilities and the adapted version with poor gliding capabilities are described.

C.1 Original supersonic aircraft

The aerodynamic coefficients of the supersonic aircraft which was used in (Bryson et al., 1968) in the maximum glide range problem, are calculated using:

$$C_L = C_{L\alpha}\alpha \tag{C.1}$$
$$C_D = C_{D0} + C_{L\alpha}\alpha^2 \tag{C.2}$$

where the parameters $C_{L\alpha}$ and C_{D0} are Mach dependent. Table C.1 shows the used values as given in (Bryson et al., 1968). The reference surface is equal to 500 ft^2 or 46.45 m^2 and the mass of the aircraft is equal to 34200 lb or 15513 kg.

Table C.1: Mach dependent parameters used to calculate the lift and drag coefficients of a supersonic aircraft as used in (Bryson et al., 1968)

M	$C_{L\alpha}$	C_{D0}
0.0	2.240	0.0065
0.4	2.325	0.0055
0.8	2.350	0.0060
1.2	2.290	0.0118
1.6	2.160	0.0110
2.0	1.950	0.0086
2.4	1.700	0.0074
2.8	1.435	0.0069
3.2	1.250	0.0068

In order to get a feeling of the gliding capabilities of this supersonic aircraft, the lift-to-drag ratio for different angles of attack and Mach numbers is indicated in figure C.1. This figure shows that the subsonic and supersonic maximum lift-to-drag ratio are respectively 10.3 and 7.6.

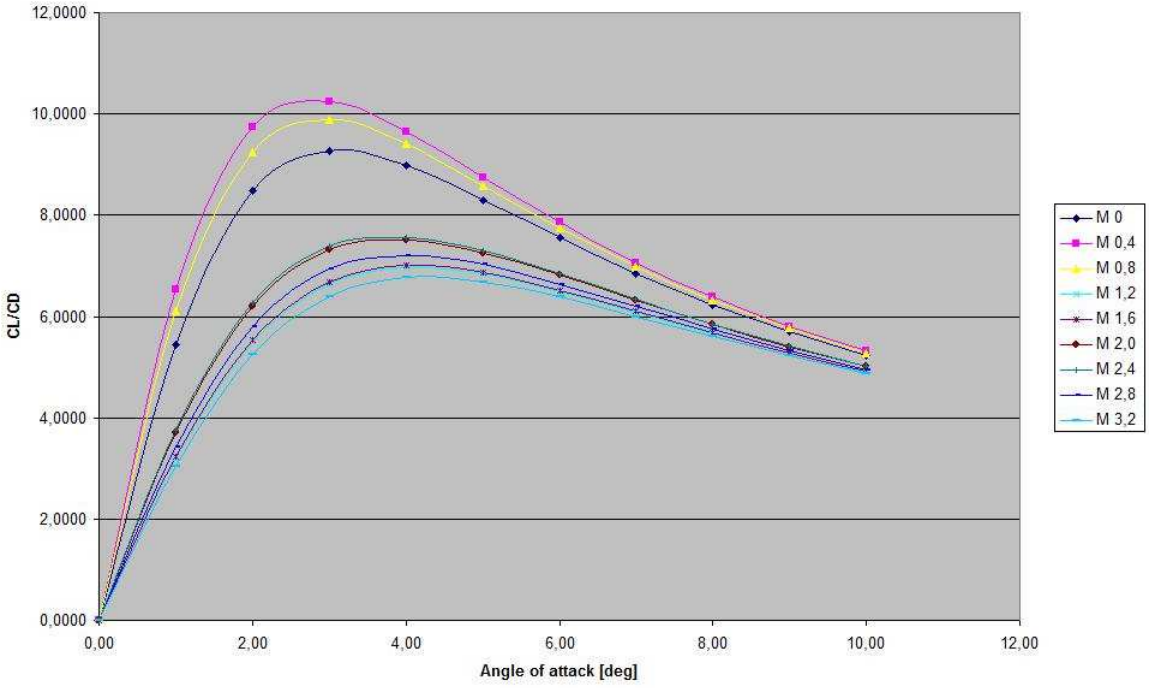

Figure C.1: Lift-to-drag ratio for different angles of attack and Mach number of the supersonic aircraft as used in (Bryson et al., 1968)

C.2 Adapted supersonic aircraft

To simulate a supersonic aircraft with poor gliding capabilities, the Mach dependent parameters of the supersonic aircraft as given in table C.1 were adapted such that the lift-to-drag ratio was lowered. The best result was obtained by lowering the values of $C_{L\alpha}$. Scaling down the values for $C_{L\alpha}$ by a factor of 5.6 and keeping the other parameters constant resulted in respectively a subsonic and a supersonic maximum lift-to-drag ratio of 4.3 and 3.2. This resulted in a supersonic aircraft with lower gliding capabilities. The new Mach dependent parameters are given in table C.2, while the lift-to-drag ratio for different Mach numbers and angles of attack is given in figure C.2. The data was extended up to an angle of attack of 30°.

Table C.2: Mach dependent parameters used to calculate the lift and drag coefficients of a supersonic aircraft with poor gliding capabilties

M	$C_{L\alpha}$	C_{D0}
0.0	0.400	0.0065
0.4	0.415	0.0055
0.8	0.420	0.0060
1.2	0.409	0.0118
1.6	0.386	0.0110
2.0	0.384	0.0086
2.4	0.304	0.0074
2.8	0.256	0.0069
3.2	0.233	0.0068

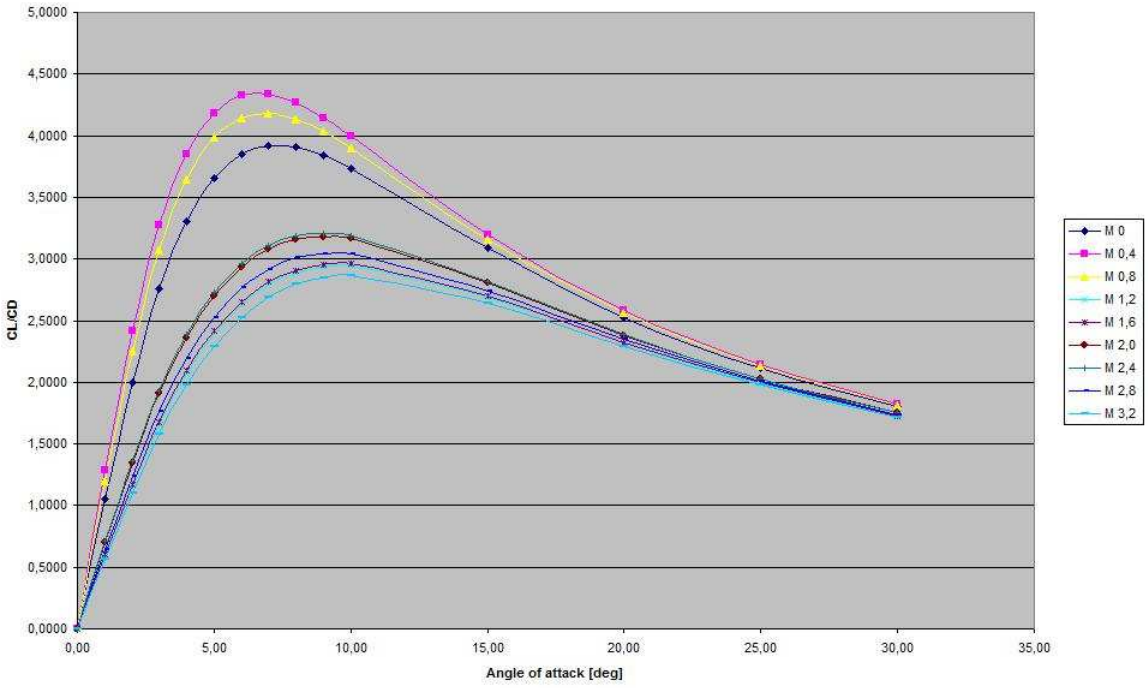

Figure C.2: Lift-to-drag ratio for different angles of attack and Mach number of a supersonic aircraft with poor gliding capabilities